THE EFFECT OF SHEARING ON FULLY-GROUTED REBAR ROCK BOLTS IN SASKATCHEWAN POTASH MINES

A Thesis Submitted to the College of

Graduate Studies and Research

In Partial Fulfillment of the Requirements

For the Degree of Master of Science

In the Department of Civil, Geological, and Environmental Engineering

University of Saskatchewan

Saskatoon

By

GARRETT SNELL

PERMISSION TO USE

In presenting this thesis in partial fulfillment of the requirements for a Postgraduate degree from the University of Saskatchewan, I agree that the Libraries of this University may make it freely available for inspection. I further agree that permission for copying of this thesis in any manner, in whole or in part, for scholarly purposes may be granted by the professor or professors who supervised my thesis work or, in their absence, by the Head of the Department or the Dean of the College in which my thesis work was done. It is understood that any copying or publication or use of this thesis or parts thereof for financial gain shall not be allowed without my written permission. It is also understood that due recognition shall be given to me and to the University of Saskatchewan in any scholarly use which may be made of any material in my thesis.

Requests for permission to copy or to make other uses of materials in this thesis/dissertation in whole or part should be addressed to:

Head of the Department of Civil, Geological and Environmental Engineering
University of Saskatchewan
Saskatoon, Saskatchewan S7N 5A9
Canada

OR

Dean
College of Graduate Studies and Research
University of Saskatchewan
107 Administration Place
Saskatoon, Saskatchewan S7N 5A2
Canada

ABSTRACT

Reinforcing bar (rebar) is a common method of ground support in underground potash mines in Saskatchewan. The rebar is anchored into the potash rock to provide support using resin and the system is referred to as a fully-grouted rebar rock bolt. The rebar can be subjected to tensile deformation and shear deformation due to the geomechanical properties of potash and the presence of relatively weak interbedded clay seams.

This research project focussed on determining the magnitude of shear plane displacement that a rebar rock bolt can withstand before failure. Secondary objectives of the project were:

- To confirm that the distributed optical sensing technology, also known as fibre-optic instrumentation, can endure the harsh conditions present in a potash mine and can accurately measure strain within rebar undergoing shear deformation.
- To identify any existing models that can be applied to predict the rebar behaviour under shear displacement in underground potash mines.
- To investigate the effect shear plane separations have on the rebar behaviour and ultimate strength in shear.

The objectives of this research were achieved using a combination of laboratory testing, field testing, and in situ instrumentation for monitoring field behaviour. Laboratory testing was conducted to determine the behaviour of rebar in a controlled environment and to investigate the effect of different shear plane apertures. A novel testing apparatus was developed and used to determine rebar behaviour when installed in potash. Last, instrumented rebar was installed across an in situ shear plane, in three different underground potash mines, to confirm our interpretation of the general behaviour of the rebar.

Laboratory test results showed that shear plane separation can have a large effect on the magnitude of shear displacement a rebar rock bolt can undergo before failing. The laboratory testing has also suggested that the fibre-optic instrumentation used can accurately measure the strain within the rebar. However, the lateral loads applied to the rebar were not able to be accurately back-calculated

from the fibre-optic instrumentation results when the rebar was subjected to shear in laboratory testing.

Field testing successfully demonstrated the interaction of potash and the rebar rock bolt and showed the potash allows for additional shear displacement compared to hardrock environments. The testing apparatus is a promising design, but improvements have been suggested for future design iterations.

The instrumented rebar installed across in situ shear planes provided valuable information on the behaviour of the rebar. This was accomplished due to the high resolution strain measurements provided by the distributed optical sensing technology. The fibre-optic instrumentation performed very well in the harsh conditions of the underground potash mines. Unfortunately, without additional instrumentation, the strain results could only show the general rebar behaviour.

Using the results of the laboratory testing and the field testing, a design chart was generated to estimate the shear displacement capacity of rebar rock bolts under varying shear plane apertures. This chart helps mine engineers determine re-bolting requirements to maintain safe drift access for mine personnel. Initial steps have been taken towards understanding the behaviour of rebar rock bolts. Further research should be conducted to increase this understanding, which would lead to reduced ground support costs and, most importantly, increase safety in our underground mines.

ACKNOWLEDGEMENTS

Acknowledgement is given to the following groups and individuals:

Department of Civil, Geological and Environmental Engineering at the University of Saskatchewan for their advice, assistance, and patience during this research project:

- Doug Milne, Ph.D., P.Eng., Professor (Co-Supervisor)
- Lisa Feldman, Ph.D., P.Eng., Professor (Co-Supervisor)
- Chris Hawkes, Ph.D., P.Geo., Associate Professor
- Donna Benneteau, M.Sc., P.Eng., Assistant Professor
- Zig Szczepanik, M.Sc., P.Geo., Geological Lab Chief Technician
- Brennan Pokoyoway, Structures Lab Technician
- Evan Kuley, Geological Lab Assistant
- Brandon Fell, Geological Lab Assistant

Nutrien Ltd. for their guidance, assistance, and financial support:

- Darren Neely, Mine Engineer
- Cole Smith, Chief Mine Engineer
- Mike Bartsch, Chief Mine Engineer
- Craig Funk, Director, GeoServices and Land
- Tanner Smith, Mine Engineer
- Jesse Prefontaine, Mine Engineering Intern
- Tristin MacDonald, Mine Engineering Intern

The Mosaic Company for their guidance, assistance, and financial support:

- Dean Gerhardt, Chief Mine Engineer
- Nathan Morgan, Geologist

International Minerals Innovation Institute for their guidance and financial support:

- Al Shpyth, Executive Director
- Marylou Langridge, Finance and Operations Coordinator

Grant Powell and Jeff Thompson from DSI Canada in Saskatoon for their advice and supplies to carry out the research project.

NSERC for providing additional funding.

DEFINITIONS

Back – The ceiling or roof of an underground drift.

Clay Seam – A relatively weak and thin layer of various fine grained insoluble minerals separating thicker layers of rock.

Drift – A tunnel in an underground mine. Drifts are typically created by continuous mining machines or roadheaders in potash mines.

Dywidag Threadbar – A specific type of rebar manufactured by Dywidag Systems International with rebar deformations forming coarse threads. It is often referred to as a “dywidag”.

Grout – Typically refers to a cementitious fluid that solidifies to anchor rock bolts and provide ground support. The term is often used interchangeably with resin that does not contain significant cement material.

Potash – A rock composed primarily of Halite (NaCl) and Sylvite (KCl). The rock may also contain minor amounts of clay minerals.

Rebar – Reinforcing bar of varying steel grades and diameters used as ground support in underground mining. It may refer to industry standard rebar or dywidag threadbar.

Resin – A polyurethane based fluid that solidifies to anchor rock bolts and provide ground support.

Rib – The sidewall of an underground drift.

Rock bolt – The broad range of ground support including grouted rebar, mechanically anchored rock bolts, and grouted dywidag threadbar.

NOTATIONS AND SYMBOLS

a_{strain} = the slope of the linear strain distribution across the rebar cross-section in fibre-optic instrumented rebar

d_C = horizontal displacement of the testing apparatus in a lateral pull test

d_O = horizontal displacement of point O in a lateral pull test

d_{rebar} = diameter of a rebar

EM = penetration modulus of rock or resin (kN/mm) according to Schubert (1984)

E_{rebar} = Young's Modulus of a rebar

h = chassis radius of 63.5 mm (2.5 in.) for the apparatus in a lateral pull test

i = dilation angle for shear plane movement

I_{Exp} = experimentally determined area moment of inertia for a rebar

I_{Rebar} = theoretical area moment of inertia for a rebar

K = some load factor greater than or equal to 1 (assumed to be equal to 1 by Pellet and Egger, 1996)

l = distance between the outer rebar supports in a beam bending test

l_e = length of the rebar between its intersection with the shear plane, point O, and its point of maximum bending moment, point A, at the yield stress of point O

l_f = length of the rebar between its intersection with the shear plane, point O, and its point of maximum bending moment, point A, at the failure stress of point O

L_i = initial distance between the chassis of the apparatus and the string potentiometers in a lateral pull test

ΔL_B = change in length of the bottom string potentiometer in a lateral pull test

ΔL_T = change in length of the top string potentiometer in a lateral pull test

$M_{internal}$ = the internal bending moment at a given distance along fibre-optic instrumented rebar

N_{oe} = axial force acting at point O at the yield stress of the rebar

N_{of} = axial force at point O at failure of the rebar

p_u = bearing force of surrounding rock/grout along length l_a of a rebar assuming a constant distribution

P = load being applied to rebar in various experiments

Q_{oe} = shear force acting at point O at the yield stress of a rebar

T_{Ult} = ultimate tensile load of a rebar (kN)

U_{oe} = shear displacement of point O parallel to the shear plane at the yield stress of a rebar

U_{of} = shear displacement of point O at the failure of a rebar

ΔU_{op} = additional shear displacement of point O between the yield stress and the failure stress of a rebar

U_{Ult} = shear displacement of the shear plane at the maximum shear resistance (mm)

$v_{internal}$ = the shear force within a rebar at a given distance along the rebar

V = maximum shear resistance provided by a rebar to a shear plane (kN)

α = the angle of a rock bolt towards a shear plane measured from perpendicular to the shear plane

β = angle between initial bolt axis and a shear plane

δ_{centre} = deflection at the centre of a rebar during a beam bending test

ε_{Axial} = the axial strain within a fibre-optic instrumented rebar

ε_{Lower} = the strain at the lower extreme edge of a fibre-optic instrumented rebar (label bottom is arbitrary and simply indicates it is diametrically opposite of the top)

$\varepsilon_{failure}$ = strain of a rebar at failure

ε_{Upper} = the strain at the upper extreme edge of the rebar (the label top is arbitrary and simply indicates it is diametrically opposite of the bottom)

ε_1 = strain measured by the first fibre-optic strand in a fibre-optic instrumented rebar at a specific distance along the rebar length

ε_2 = strain measured by the second fibre-optic strand in a fibre-optic instrumented rebar at a specific distance along the rebar length

ε_3 = strain measured by the third fibre-optic strand in a fibre-optic instrumented rebar at a specific distance along the rebar length

σ_c = uniaxial compressive strength of rock or resin

$\sigma_{failure}$ = failure stress of rebar

σ_{yield} = yield stress of rebar

ω_{oe} = rotation of the rebar axis at point O at the yield stress of point O

$\Delta\omega_{op}$ = additional rotation of point O from the yield stress to the failure stress

ω_{of} = rotation of point O at the failure of the rebar

θ_{fi} = angle between the first fibre-optic strand and the centroidal axis perpendicular to the bending direction in a fibre-optic instrumented rebar

$\theta_{Rotation}$ = rotation of testing apparatus in a lateral pull test

φ = friction angle of a shear plane

$\frac{\Delta M_{internal}}{\Delta x}$ = change in internal bending moment with respect to the change in distance along a rebar

TABLE OF CONTENTS

LIST OF FIGURES

LIST OF TABLES

LIST OF EQUATIONS

1 INTRODUCTION

This research project focusses on the shear behaviour of fully-encapsulated resin grouted rebar rock bolts in underground potash mines. This section discusses the mine geology, mining methods, ground control issues commonly encountered, and the ground support methods used. The testing sites used in this research project are also described. Last, this section discusses the research objectives, scope, and methodology.

The research project was conducted using three main approaches:

- Laboratory testing was conducted to measure rebar behaviour and failure in a controlled environment.
- A field testing apparatus was designed and used to measure rebar behaviour installed in potash at Saskatchewan mines.
- Instrumented rebar was installed in the field to monitor deformation along active shearing planes at Saskatchewan mines.

All testing used distributed optical sensing technology which was capable of high resolution strain readings within the rebar rock bolts.

1.1 Background

This project analyzed the behaviour of rebar crossing a shear plane in a potash mine. The research was carried out through a combination of laboratory testing, field testing, and in situ instrumentation.

The field testing and in situ instrumentation was completed at four potash mines within roughly 80 km of Saskatoon (Figure 1.1): Nutrien's Vanscoy, Cory, and Allan mines and Mosaic's Colonsay mine. Every mine in this project is producing from the same stratigraphic layer and the potash exhibits little variation in properties across these mines. Every mine investigated in this

research project uses a similar mining method, has similar ground control issues, and stands to benefit from any substantial findings.

All of the mines in the Saskatoon area are excavating the Upper Patience Lake Formation at a depth of around 1 km. Every mine has been mining this formation for roughly 50 years. The mines are all owned and operated by either Nutrien or Mosaic. Due to the different ownership and unique history of each mine, the mining method, equipment, and ground support procedures at each mine are slightly different.

Figure 1.1. Saskatchewan and test site locations – based on Google Maps (2017)

1.1.1 Geology and Mining

Potash deposits in Saskatchewan are part of the Prairie Evaporite Formation. This formation was precipitated from an inland sea during the Middle Devonian Period roughly 400 million years ago (Worsley and Fuzesy, 1979). The formation is quite extensive and as a result, the depth to the formation can vary significantly. The general stratigraphy (Figure 1.2) extends from the Nutrien Vanscoy Mine to the Nutrien Rocanville Mine in eastern Saskatchewan. The main members of the Prairie Evaporite Formation, which contain the potash, are the Esterhazy, Belle Plaine, and Patience Lake (Upper and Lower) Members.

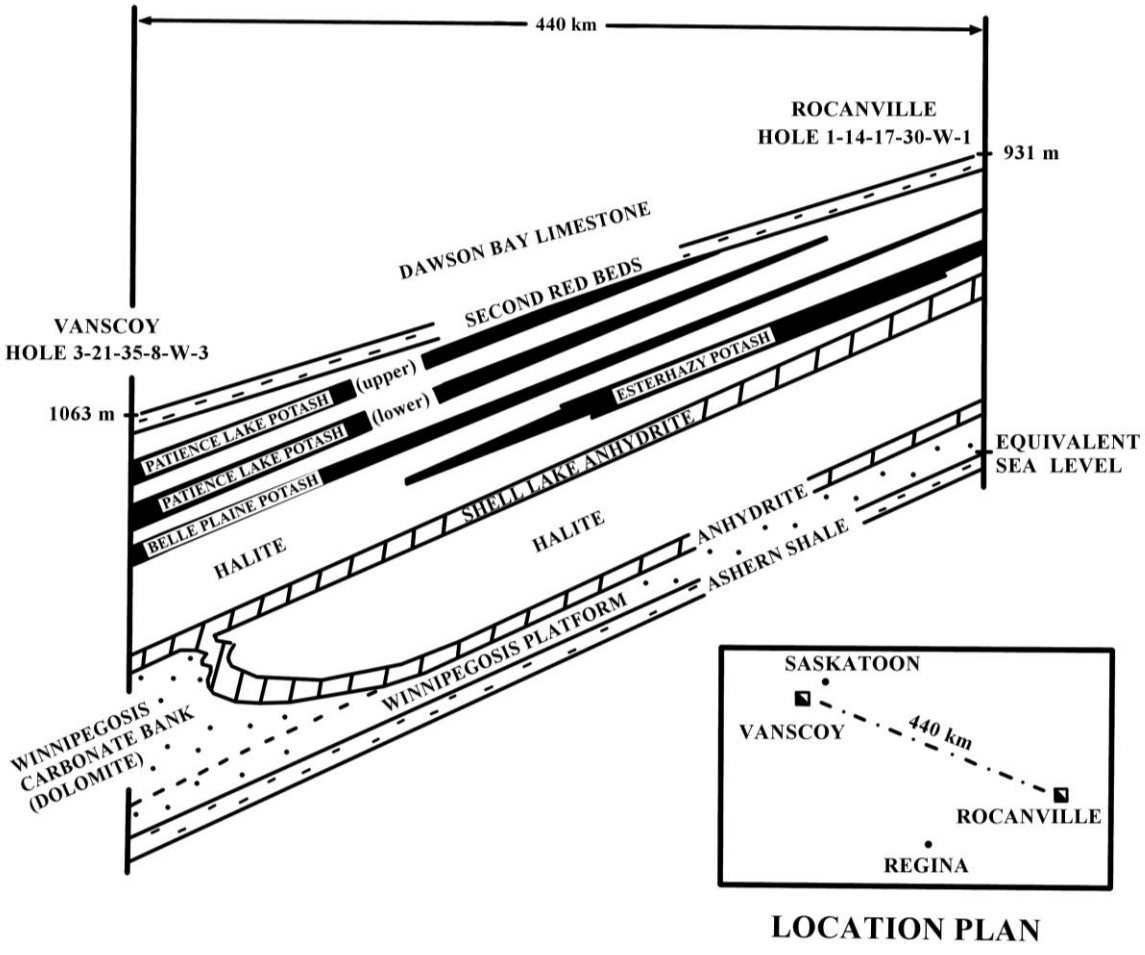

Figure 1.2. General Stratigraphy of the Prairie Evaporite Formation across Saskatchewan (after Jones and Prugger, 1982)

Generally, the Prairie Evaporite Formation is mined at a depth of approximately 1 km. The formation dips to the south-southwest at about 2 m to 8 m per horizontal kilometer (Duncan, 1990). Figure 1.2 is a section showing the main members in the vicinity of the formation and provides an indication of their depth across Saskatchewan.

The Dawson Bay Limestone lies above the Prairie Evaporite Formation and the Winnipegosis Formation underlies it. Both the Dawson Bay and Winnipegosis Formations are composed of dolomitic limestone. The Esterhazy Member and the Belle Plaine Member are mined in central and south-eastern Saskatchewan. The Patience Lake Member (Upper and Lower considered together) extends further west than the lower two and is mined in the Saskatoon area. The mines in this area are the focus of this research.

Figure 1.3 shows this interbedding and a typical stratigraphy surrounding a mine opening in the Patience Lake Member. The potash, highlighted in Figure 1.3, consists of sylvite, halite, carnallite, and anhydrite (calcium sulphate) mineral grains, along with some insoluble particles of clay, dolomite, quartz, calcite, iron oxides, and hydroxides. The exact composition of the economic potash rock varies significantly from one stratigraphic layer and member to another, but they generally contain 15-30 % sylvite (Duncan 1990).

The clay layers, highlighted in Figure 1.3, affect mining operations because the clay is a relatively weak layer within the potash rock. Failure of the potash rock, either by shear or tension, often occurs along these clay layers. The clay layers occur as thin seams 3 cm to 5 cm thick, but are occasionally nearly 1 m thick (Worsley and Fuzesy, 1979).

Potash mining near Saskatoon employs a unique room-and-pillar mining method. Drifts are mined using mechanical excavation in three to five parallel drifts. Figure 1.4 shows a cross section of five parallel drifts. These drifts can be up to 1.6 km (1 mile) long and are regularly connected by cross-cuts. This mining pattern is often referred to as stress-relief mining or a “chevron pattern”.

The term stress-relief mining is used to describe mining since the outer most drifts are designed to fail and relieve the stress around the inner drifts. As shown in Figure 1.4, the outer most drifts are

mined first followed by the inner drifts. Over a few days to weeks after excavation, the outer drifts will fail due to higher induced stress. The horizontal stress must then migrate further away from the outer drifts and the inner drifts are protected from high horizontal stress.

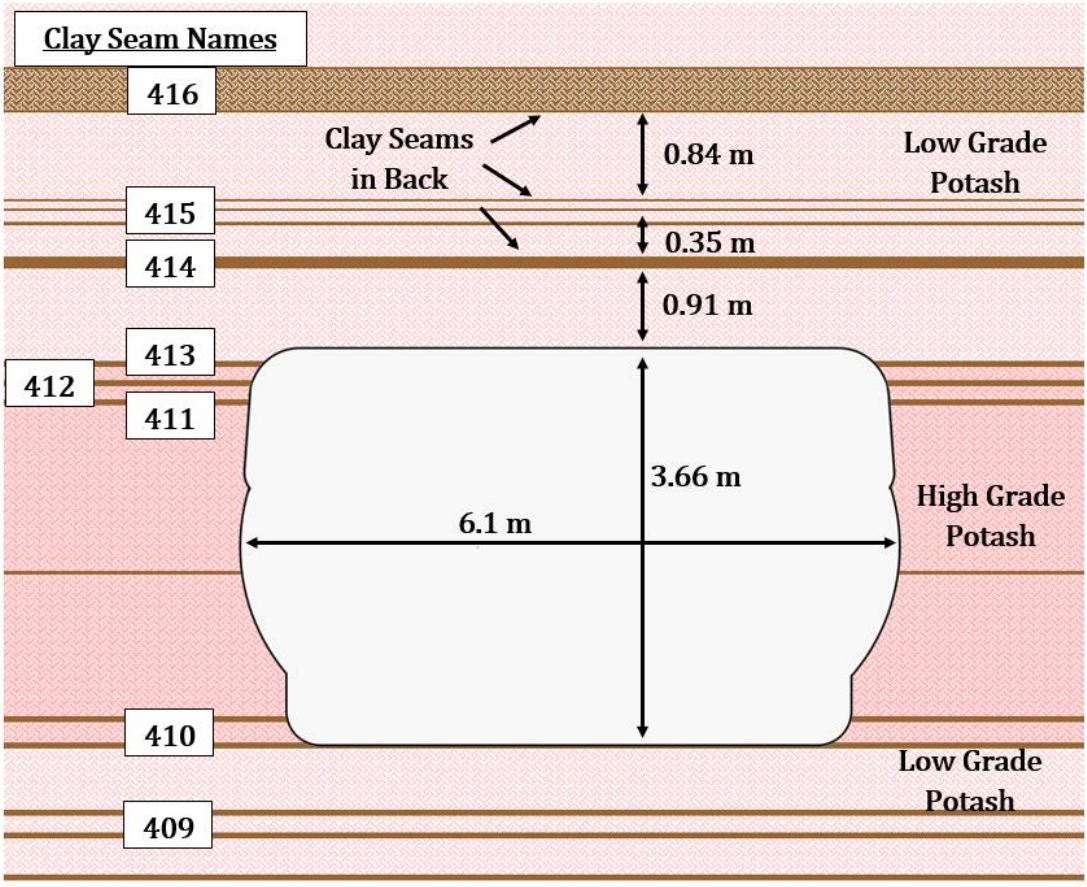

Figure 1.3. Stratigraphy around a typical mine opening in the Upper Patience Lake Member

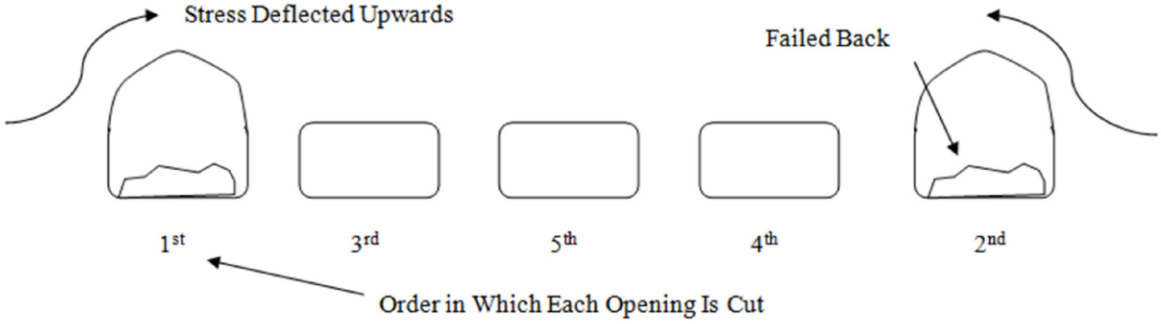

Figure 1.4. Cross-sectional view of parallel drifts in potash mining (from Neely, 2014)

1.1.2 Ground Deformation

Large ground deformations are common in potash mines near Saskatoon and can lead to instabilities if ground is not supported. Various types of instabilities can arise in potash mines, most of which are associated with the clay seams interbedded within the potash. Although this dissertation refers to these features as instabilities, there is generally no immediate risk to mine workers and equipment. The slow and gradual creep associated with potash rock allows time to address any developing concerns.

The most common deformation mechanism in Saskatoon area potash mines is tensile separation in the back of a drift (Figure 1.5). Prior to mining, the potash in the Upper Patience Lake Formation is under hydrostatic in situ stress conditions. When a drift is mined horizontally through the potash, the in situ stresses must reorient around the newly mined cavity. It is the horizontal induced stresses that cause tensile separations in the back. The increased horizontal stresses cause the potash "beam" to flex inward into the drift. These flexing beams of potash have the potential to buckle into the drift if they flex inwards enough. The stress relief mining method is designed to reduce the horizontal stress, however circumstances still arise where tensile separations are created and rock bolts must be installed.

Tensile separations can also occur in the floor of a drift if clay seams lead to the creation of potash beams. The upward deflection of beams of potash is regularly encountered in the floors of potash mines. However, the deflections of potash beams in the floor are not typically a concern, since there is no risk of rock falling on personnel or equipment. Figure 1.6 shows a tensile separation in the floor of a cross-cut drift.

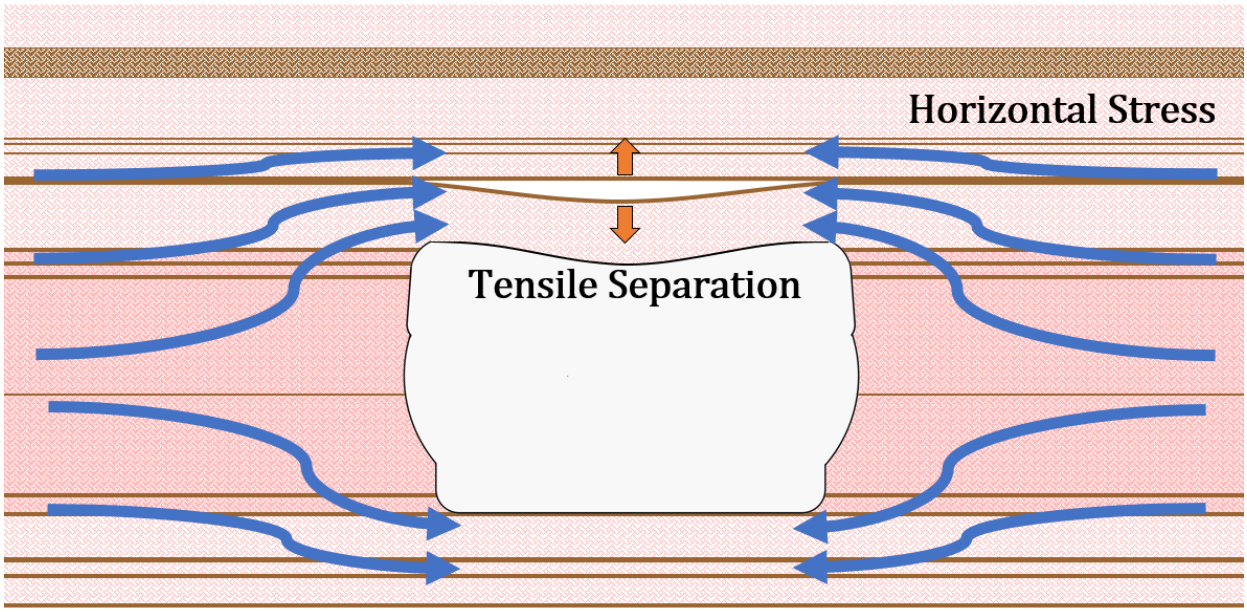

Figure 1.5. Typical tensile separation of back beam due to high horizontal stresses

Figure 1.6. Beam Separation observed in the floor of a cross-cut

Another instability encountered is shear movement along clay seams (Figure 1.7). Not only are clay seams weak in tension, they are also weak in shear. Stress conditions can drive shear movement along these clay seams. Figure 1.7 shows four common scenarios where shear movement can occur in potash mines.

Figure 1.7a shows a traditional tensile separation. Although most of the movement is tensile due to deflection of the potash beam, there is often a component of shear movement near the ribs of the drift as well.

If the horizontal stresses in the back are large enough, the potash beam can fail. Figure 1.7b shows a failure of the potash beam that has caused a dipping shear plane. The newly formed failure plane through the potash beam can allow unimpeded shear movement to take place. A failure such as this causes a cantilever of potash in the back.

Some mines choose to “slot cut” the back of some drifts (Figure 1.7c). This is meant to relieve the horizontal stresses immediately in the back of the drift by redistributing the stress deeper into the rock. The slot cut introduces a free face in the potash and the rock will shear into the slot cut, eventually closing it altogether. Although slot cutting will prevent potash beams from deflecting and buckling, they also introduce potentially unstable cantilevers into the back. A similar scenario could easily exist anytime there is a cavity adjacent to potash layers.

Last in Figure 1.7d, wedge failures can be encountered in potash mines. High horizontal stress can fail the potash in the back and cause two dipping shear planes. These planes form a wedge in the back that is squeezed out. Shear movement along the dipping shear planes is often accompanied by a tensile separation in the apex of the wedge (Figure 1.7d).

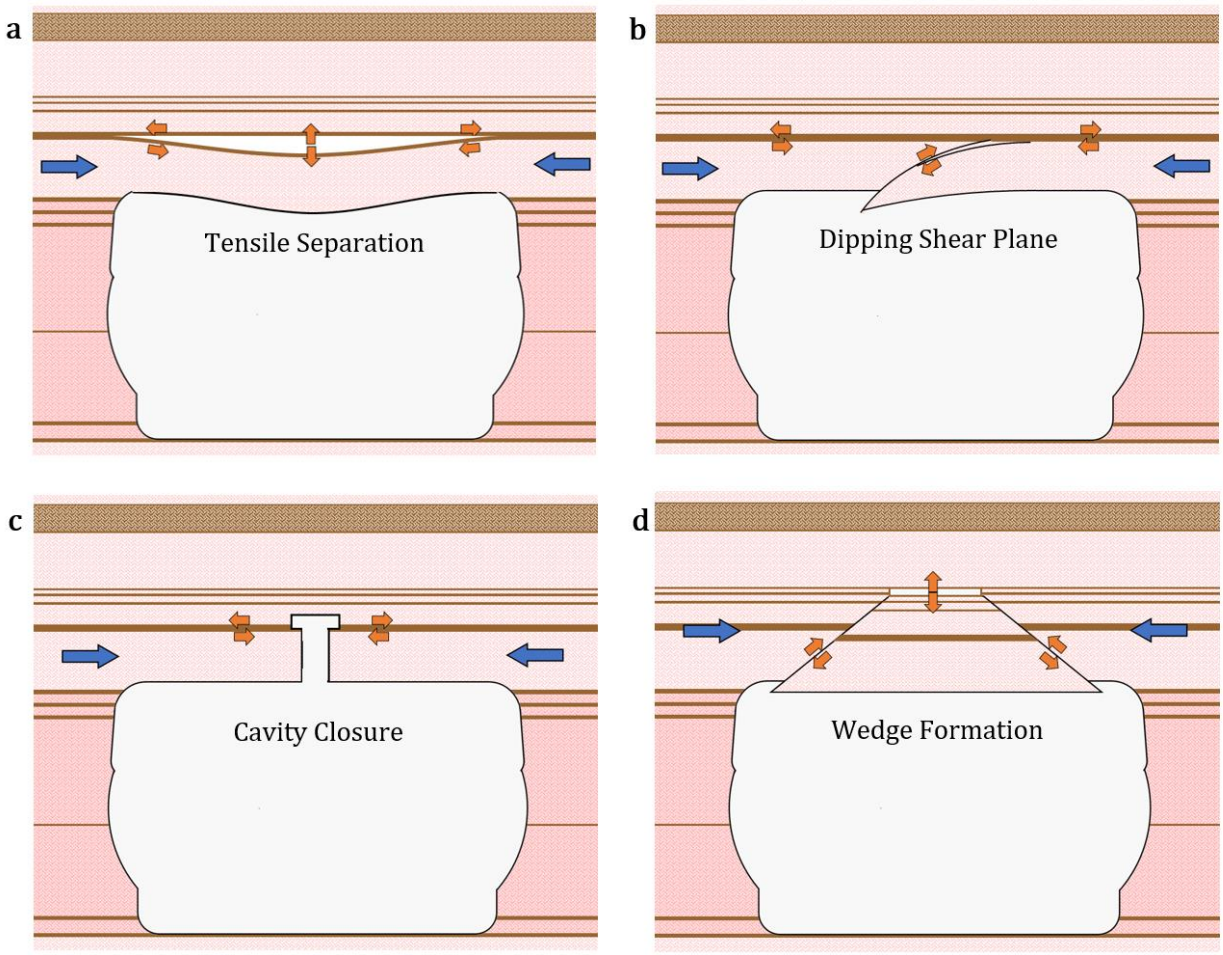

Figure 1.7. Various scenarios where shear movement can be observed in the back where blue arrows indicates driving force and orange arrows indicate local relative movements a) Tensile separation of the back beam showing a gap forming b) Shear failure of the back beam c) Movement into an adjacent cavity such as a slot cut d) Wedge-type failure

1.1.3 Ground Support Methods and Mechanisms

There are many types of rock bolts used throughout the world and at potash mines in Saskatchewan. Currently, two of the most commonly used types in potash mines are mechanical rock bolts and fully-encapsulated resin grouted rebar. Mechanical rock bolts are used to support tensile separations and not to resist shear movement in Saskatchewan potash mines, so they are not discussed further.

Fully-encapsulated resin grouted reinforcing bars are commonly used in potash mines. This type of reinforcement is commonly referred to as fully-grouted rebar within the mining industry and this terminology will be used. Theoretically, the potash surrounding an opening is reinforced by bonding the potash layers together across clay seams. Figure 1.8 shows how rebar installed in the back of a drift will bond the potash layers into thicker and more stable beams.

As shown in Figure 1.9, the rebar support system can be broken down into six main components: rebar, resin, surrounding potash, clay seam(s), plate, and bolt head or nut. The rebar is made of steel and provides the strength to the system. The resin acts to bond the rebar to the surrounding potash across the weak clay seam(s). Commonly, a metal plate is placed between the forged head or nut on the end of the rebar and the potash surface.

The fully-grouted rebar rock bolt is installed by first drilling a hole. Cartridges of a two-part polyester resin are inserted into the hole. The rebar is then pushed into the hole and cartridges and spun for several seconds to break and mix the resin cartridges, as per the manufacturer instructions. The resin will typically harden within minutes and the rebar will be bonded to the potash.

Ground support is installed in areas of potash mines that exhibit a potential instability such as a separation in the back (Figure 1.5) or another type of instability (Figure 1.7). When the potash layers separate, the fully-grouted rebar is loaded in a nearly pure tensile manner. This situation and the internal tensile forces are shown in Figure 1.9.

When the potash rock separates, load is transferred to the rebar rock bolt through the resin bond. There are two interfaces in the rebar support system: the potash-resin interface and the resin-rebar interface. The load is transferred across these interfaces via shear stress. This shear stress and its distribution along the support system will be discussed further in Section 2.3.

The other type of potential instability encountered is shear movement of potash. The shear movement causes the potash rock to apply a lateral force to the resin and rebar. Figure 1.9 shows the forces being applied to the rebar. This lateral force results in shear stress and bending stresses within the rebar and the rebar deforms into a characteristic “S” shape. As shear displacement

occurs, a component of tensile force is also introduced into the rebar. Ultimately, the rebar failure is dependent on a complex combination of shear stress, bending stress, and tensile stress.

The shear, bending, and tensile forces are dependent on a wide variety of the variables present within the shearing system. For example, the behaviour of the system is dependant on the strength of the surrounding rock, the strength of the resin, the size of the rebar, the bond strength between the rebar and resin, etc. A review of previous investigations of this behaviour is presented in Section 2.2.

Although tensile separations and shear movement are presented as separate concepts here, they are commonly seen together in potash mines. To simplify the concepts and behaviours, tensile separation and shear movement are considered as isolated situations.

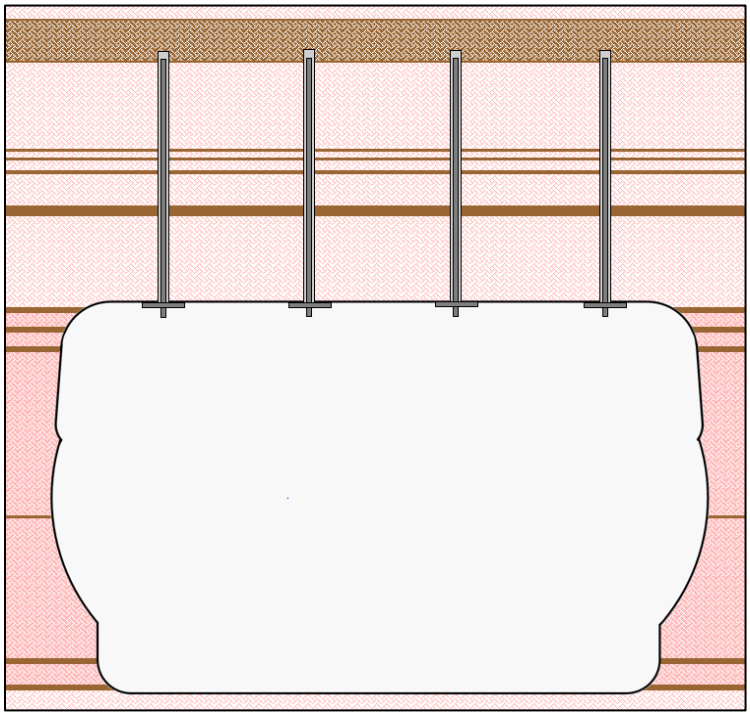

Figure 1.8. Resin grouted rebar installed in the back of a drift

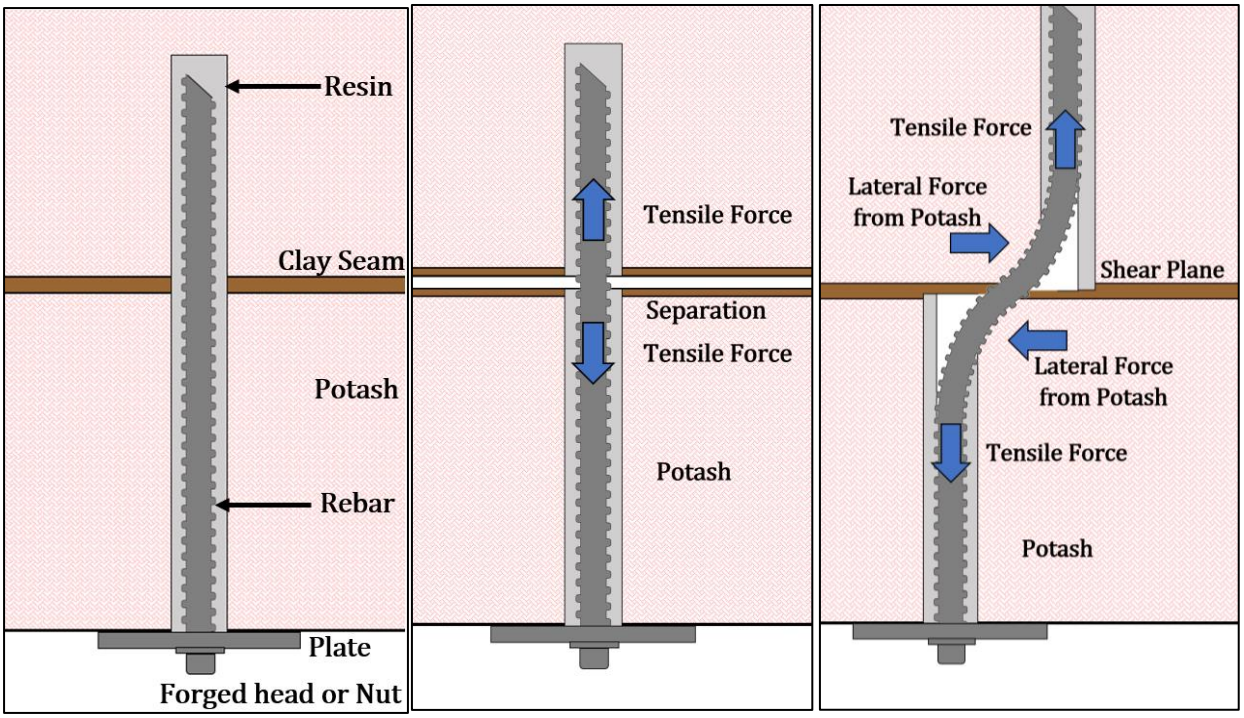

Figure 1.9. Components of fully-encapsulated resin grouted rebar (left), rebar loading during separation of potash layers (centre), and rebar loading during shear movement across potash layers (right)

1.2 Testing Sites

All laboratory testing was performed at the University of Saskatchewan Saskatoon campus. The university is equipped with the required loading frames, materials, and expert personnel required. All laboratory testing occurred in the Civil Engineering Laboratory and the Geological Engineering Laboratory. Dywidag Systems International (DSI) is the primary supplier of rock bolts at each mine and supplied the steel used in the laboratory experiments.

Field pull testing experiments occurred at the Nutrien Cory mine, as it was the author's place of work. Fibre-optic in situ instrumentation was installed at Nutrien Vanscoy, Nutrien Allan, and Mosaic Colonsay mines. The instrumentation sites were chosen based on the instabilities that arose at each site throughout the course of this project. All four of these mines are near Saskatoon, Saskatchewan and produce from the Upper Patience Lake Formation. The geology of each testing

site was visually assessed on a case by case basis as to whether it would be representative of the typical Upper Patience Lake potash geology.

1.3 Objectives of Research

The primary objective of this research project was to correlate the displacement of a shear plane in potash to the failure of commonly used fully-grouted rebar rock bolts. Reaching this objective will allow mine engineers to estimate the support integrity in the Saskatoon area potash mines.

The secondary objectives of this thesis can be summarized as:

- To confirm if fibre-optic instrumented rebar can endure the harsh conditions present in a potash mine and can accurately measure strain within rebar.
- To identify any existing models that can be applied to predict the rebar behaviour under shear displacement in underground potash mines.
- To investigate the effect that shear plane separations have on the rebar behaviour and strength.

1.4 Scope and Methodology

The research and resulting conclusions presented in this dissertation are based on a combination of laboratory tests, field tests, and field monitoring. The laboratory tests were used to determine various properties of the rebar, grout, and potash in a controlled environment. These laboratory tests were also used to determine the suitability of the fibre-optic strain instrumentation for monitoring strain in rebar rock bolts. The field testing and monitoring was conducted to determine the in situ rebar behaviour and compare it with the rebar behaviour in the laboratory testing.

The type of rebar investigated only covered the types commonly found in Saskatoon area potash mines. Rebar in Saskatchewan potash mines is commonly supplied by Dywidag-Systems International (DSI) so all rebar tested in this research was supplied by this company. The samples tested were not from the same “heat-batch”. Although different batches can mean the samples have slightly different properties, the large number of experiments conducted meant controlling for this

variable was not feasible. Both linear-elastic and plastic behaviour of the rebar steel was considered in the analysis of this research.

The time-dependent behaviour of potash rock was not considered beyond a simple awareness of its existence and a general prediction of its effect on the support behaviour. Additionally, the potash investigated was limited to the Upper Patience Lake Formation that is mined in the Saskatoon area.

Last, the shear of potash was assumed to be perfect shear displacement. The shear plane was assumed to have no change in its aperture or "gap" after the rebar is installed. The effect of an existing shear plane separation was, however, investigated since the presence of such a separation is often what prompts support installation in the first place.

1.5 Thesis Overview

Section 1 provides the background, scope, and research objectives of this thesis.

Section 2 is the literature review which discusses similar projects and some background information pertaining to the project. Steel and potash properties are discussed based on previous research and data. The behaviour of fully-grouted rebar in various loading conditions are discussed based on previous research projects. As this project made use of fibre-optic instrumented rebar, a review of this technology is also included.

Section 3 discusses the laboratory testing undertaken to measure the strengths and behaviours of the steel rebar investigated. The tests undertaken were beam bending tests and double shear tests. In addition to measuring material properties, these tests also allowed for verification of the fibre-optic instrumentation used in this research. The theory and results of these tests are presented in this section.

Section 4 presents the observations and results of newly developed testing procedures. These tests were designed for measuring and understanding the shear behaviour of rebar in the field. Fibre-optic instrumentation was also used and analyzed in these tests.

Section 5 presents the fibre-optic instrumented rebar that was installed in actively shearing potash rock. The section summarizes and discusses the data gathered from three different mine sites over the course of this research project.

The findings from all tests are discussed in Section 6. This section attempts to combine the various test results. This section also discusses implementing the results in ground support procedures at mine sites.

Last, the formal conclusions of this project are summarized in Section 7. Recommendations for future work are also discussed.

2 LITERATURE REVIEW

Previous studies related to fully-grouted rebar rock bolts are described in this section. These studies included investigations related to rebar mechanical properties, including behaviour in shear and tension. Potash geomechanical behaviour is an important variable in rock bolt behaviour, so studies on potash behaviour are also briefly presented. General characteristics about the rock bolts being studied and previous studies using distributed optical sensing technology are also discussed.

2.1 Rebar Types, Geometries, and Properties

The rebar types being investigated in this project are widely used in potash mining in Saskatchewan and were donated by Dywidag-Systems International (DSI). DSI supplies most of the rebar rock bolts and resin to Saskatoon area potash mines. Three commonly encountered rebar types were investigated:

- Grade 400 22M forged-head rebar (approximately equivalent to an imperial Grade 60 #7 forged-head rebar)
- Grade 400 25M forged-head rebar (approximately equivalent to an imperial Grade 60 #8 forged-head rebar)
- Grade 500 22M dywidag threadbar (approximately equivalent to an imperial Grade 75 #7 rebar)

The rebar can be divided into different types and sizes of rebar. The size of a rebar refers to its nominal diameter to the nearest millimeter. The rebar sizes most commonly used in potash mines are 22M (22 mm diameter) and 25M (25 mm diameter). These sizes are often referred to at mine sites by their approximate imperial equivalents of #7 and #8, respectively.

Forged-head rebar and dywidag threadbar are the two types of rebar readily available from DSI. All rebar is produced in accordance with ASTM Standard F432-13 (ASTM International, 2013) and CSA Standards M430-90 (CSA, 2011) and G30.18-M92 (CSA, 2007) according to DSI (2015). Forged-head rebar has a minimum tensile yield strength of 400 MPa (60 ksi) while

dywidag threadbar has a minimum yield strength of 500 MPa (75 ksi). These yield strength values relate directly to the assigned steel grades. The Grade 400 rebar has a minimum ultimate tensile strength of 590 MPa (85 ksi) and the Grade 500 threadbar has a minimum ultimate tensile strength of 690 MPa (100 ksi) (ASTM International, 2013).

The geometries of the three rebar types are very similar (Figure 2.1). Each rebar has a solid cylindrical core with deformations or "ribs". A major difference is that forged-head rebar has a line running down its length while the dywidag threadbar does not. Additionally, the ribs on the dywidag threadbar form a coarse thread, while the forged-head deformations do not. The threads of the dywidag threadbar allow for a specialized nut to be threaded onto the rebar.

Table 2.1 summarizes the differences in steel grade, minimum diameter, yield strengths, and ultimate tensile strengths of the three different rebar types. The size of the solid cylindrical core of the rebar is called the "minimum diameter" herein. This minimum diameter was used in all calculations, such as for calculating the minimum cross-sectional area of the rebar. The strengths were taken directly from the properties advertised by DSI (2015).

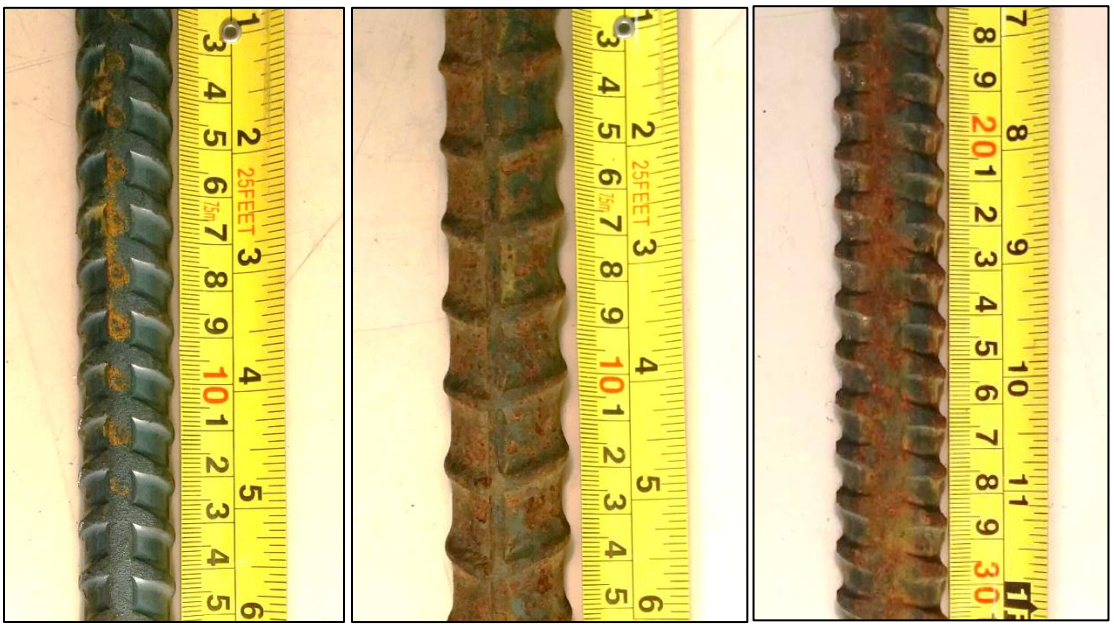

Figure 2.1. Geometry of a 22M (#7) Grade 400 rebar (left), 25M (#8) Grade 400 rebar (centre), and 22M (#7) dywidag threadbar (right)

Table 2.1. Summary of Rebar Properties

Rebar Sample	Minimum Diameter mm [inches]	Expected Young`s Modulus GPa [ksi]	Minimum Tensile Yield Stress MPa [ksi]	Advertised Tensile Yield Load* kN [tonnes]	Minimum Ultimate Tensile Stress MPa [ksi]	Advertised Ultimate Tensile Load* kN [tonnes]
22M (#7) Grade 400 (60) forged-head rebar	21.1 [0.831]	200 [29000]	400 [60]	155 [15.8]	600 [85]	232 [23.6]
25M (#8) Grade 400 (60) forged-head rebar	23.1 [0.909]	200 [29000]	400 [60]	200 [20.4]	600 [85]	300 [30.6]
22M (#7) Grade 500 (75) dywidag threadbar	21.0 [0.827]	200 [29000]	500 [75]	200 [20.4]	660 [100]	270 [27.5]

*Advertised in Dywidag-Systems International (2015)

2.2 Rebar Behaviour in Shearing Rock

The effect of shear plane movement on rebar rock bolts has been studied for over 40 years and many contributions to the understanding of rock support behaviour during shear plane movement have been made. Bjurstrom (1974) and Dight (1982) studied how much resistance to shear plane movement rock bolts can provide before failing. They also investigated how much displacement can occur on the shear plane before the rock bolts fail. All previous researchers assumed there were no shear plane separations present prior to shear movement. Shear movement in potash mines often occurs along shear planes with some amount of separation.

2.2.1 Past Rock Bolt Shear Experiments

Bjurstrom (1974) was one of the first researchers to analyze the behaviour of rock bolts crossing a shear plane. Bjurstrom studied fully-grouted rock bolts in both the lab and the field. Bjurstrom installed fully-grouted rebar rock bolts across two granite blocks at various angles, α in Figure 2.2, measured from perpendicular. The angles ranged from 0 degrees to 60 degrees from perpendicular. A force was applied to one granite block parallel to the joint between the two blocks to move one in shear relative to the other, as depicted in Figure 2.2. Haas (1976), Spang and Egger (1990), Chen and Li (2015), and Chen (2014) all performed similar experiments to Bjurstrom (1974) where ground support was installed across two blocks of rock or concrete and then one block was moved in shear relative to the other block.

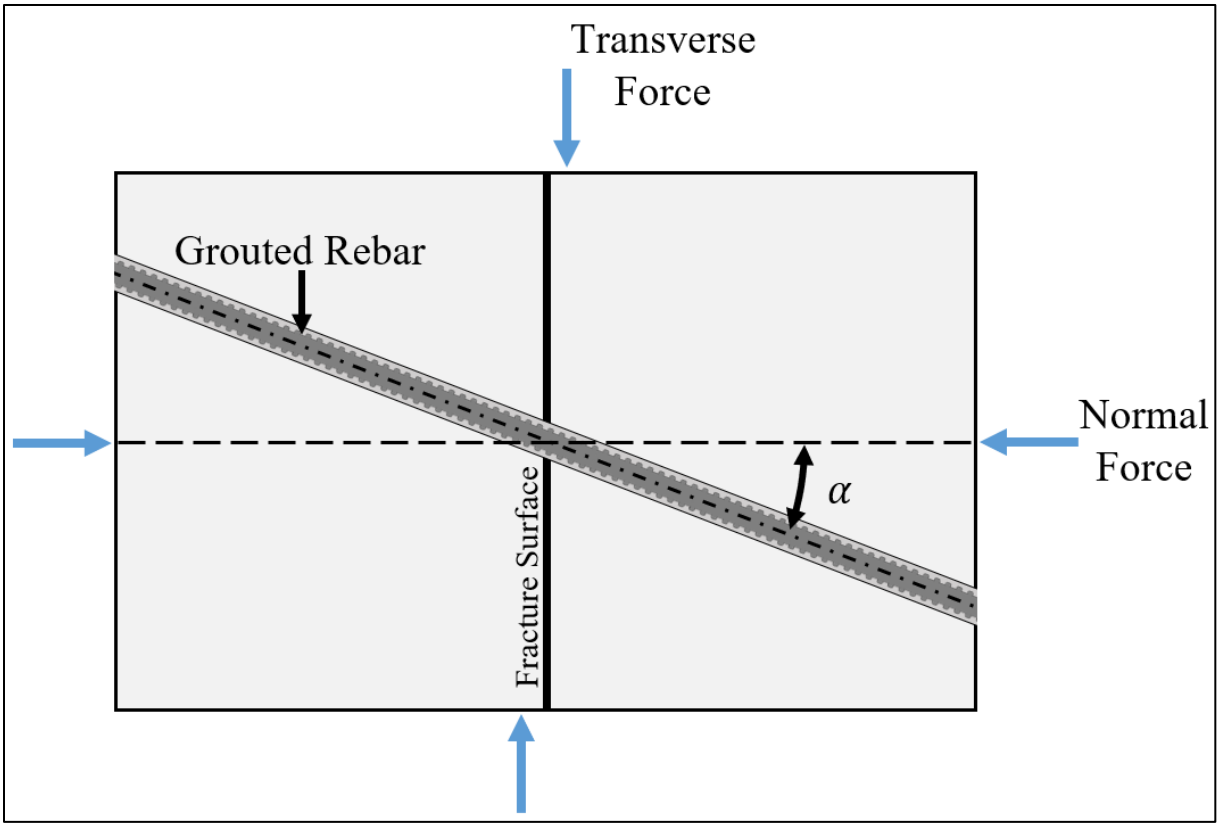

Figure 2.2. Two block shear test (after Haas, 1976)

Bjurstrom (1974) found that the full strength of the rebar rock bolts were mobilized at 15-30mm of shear displacement. Bjurstrom also found the contribution of the rock bolts to the shear resistance of a shear plane is dependent on the inclination of the rock bolts, the relative shear displacement of the shear plane, the strength of the surrounding rock, and the roughness of the shear plane.

Haas (1976) encountered unanticipated problems when shearing 60 cm cubic blocks of limestone and shale. He found the rebar would sometimes get wedged between the blocks and force them apart, or the blocks of rock would split in half. Stillborg (1984) also encountered blocks splitting when shearing 30 cm x 40 cm x 55 cm blocks of granite. Based on these findings, testing rebar in the laboratory using blocks of rock requires relatively large blocks to conduct a valid experiment.

Some researchers (Grasselli, Kharchafi, and Egger, 1999; Aziz, Pratt, and Williams 2003; Jalalifar et al., 2006; and Li et al., 2015) investigated the shear behaviour of rebar using three blocks of

concrete instead of just two. In these tests, the rebar rock bolts were installed across three blocks and a lateral load was applied to the centre block. This test setup can be seen in Figure 2.3 and it had the benefit of balancing the moments imparted on each side of the central block due to the symmetry of the test setup. As a result of balancing the moments, the centre block is not likely to tilt and affect the test results.

Grasselli, Kharchafi, and Egger (1999) were among the first researchers to attempt an experiment with two shear planes, referred to as a double shear test set-up in this document. Similar tests were conducted by Aziz, Pratt, and Williams (2003), Jalalifar et al. (2006), and Li et al. (2015). These researchers investigated the effect of pre-tensioning the rock bolts, the effect of different concrete strengths, and conducted numerical modelling.

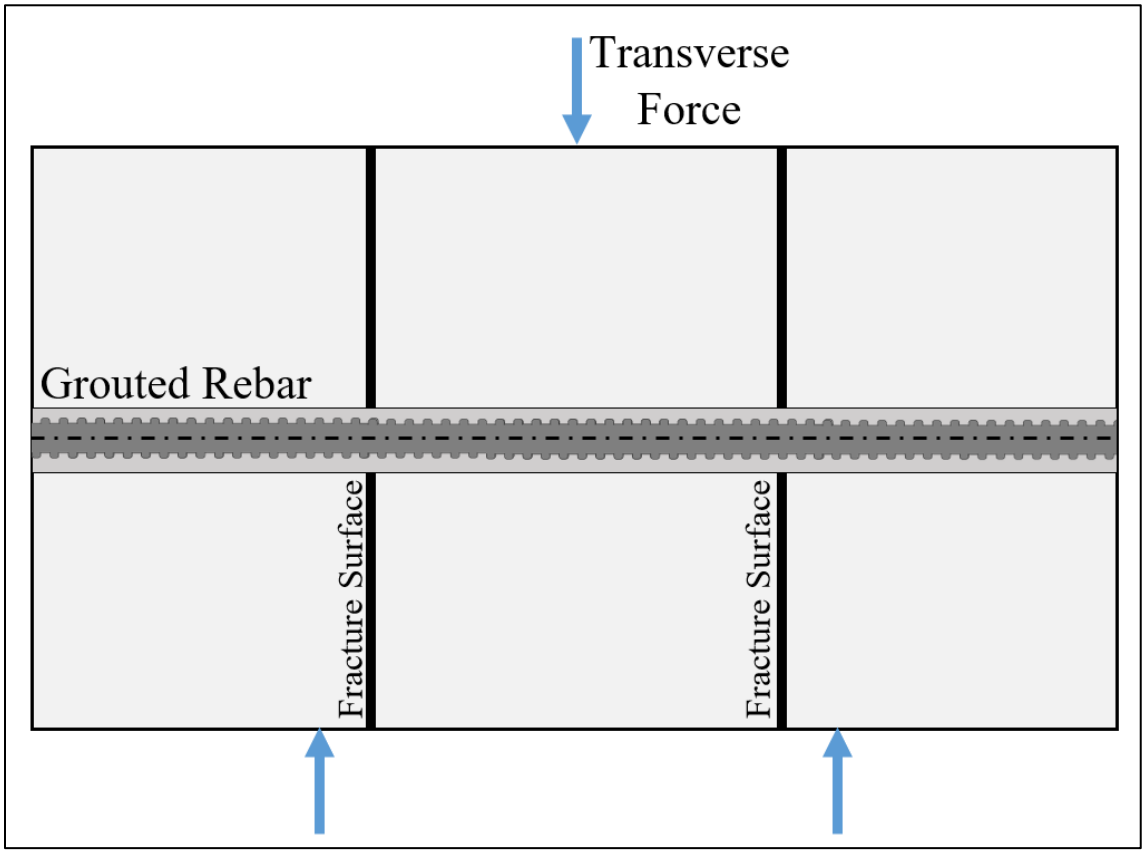

Figure 2.3. Cross-section of double shear test on rebar in three blocks of concrete or rock

Another type of test was designed by Dube (1995) for testing cable bolts with a combination of shear and tensile loading. The bolts were tested by grouting them within two steel pipes as shown in Figure 2.4. One pipe was then displaced at some angle relative to the other by applying a shear force and a tensile force.

Grouting the cable bolts into pipes instead of concrete or rock provided confinement and allowed for consistent and reliable tests. However, these tests did not replicate the way concrete and rock can be crushed by the bolts under high lateral loads. Crushing of the surrounding medium can allow for additional shear displacement prior to failure of the cable bolts. The pipe does not allow for this crushing and causes the results of this test to differ from what would be expected in the field or using concrete blocks.

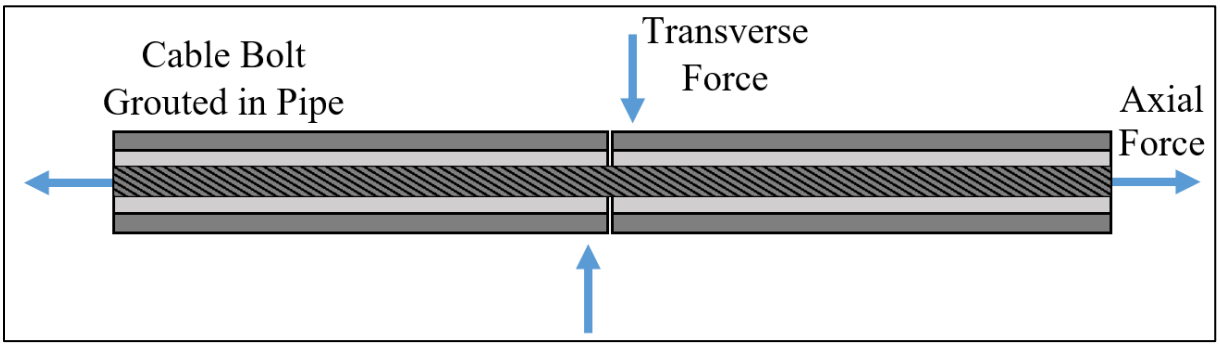

Figure 2.4. Cross-section shear test on cable bolt grouted in pipes and subjected to shear and tensile forces

2.2.2 Rock Bolts Inclined to a Shear Plane

Bjurstrom (1974) investigated the effect of the orientation of rebar rock bolts relative to a shear plane. Bjurstrom found the orientation to be an important factor in the behaviour of the rebar. Similar conclusions were made by Haas (1976), Spang and Egger (1990), and Pellet and Egger (1996).

The orientation of the rebar rock bolt relative to the shear plane was defined using the alpha angle, α, measured from the shear planes perpendicular axis to the rebar's centroidal axis (Figure 2.2 and Figure 2.5). The orientation is also sometimes defined using the complimentary angle, β.

All researchers found that rock bolts installed with an alpha angle closer to 90 degrees had a stiffer shear load – displacement relation than similar rock bolts oriented nearly perpendicular to the shear plane. Rock bolts oriented perpendicular to the shear plane tended to fail in a combination of tension and shear. The rock bolts oriented at an angle towards the direction of shearing failed primarily in tension. Additionally, the inclined rock bolts exhibited greater ultimate loads and lower ultimate displacements when compared to rock bolts oriented perpendicular to the shear plane.

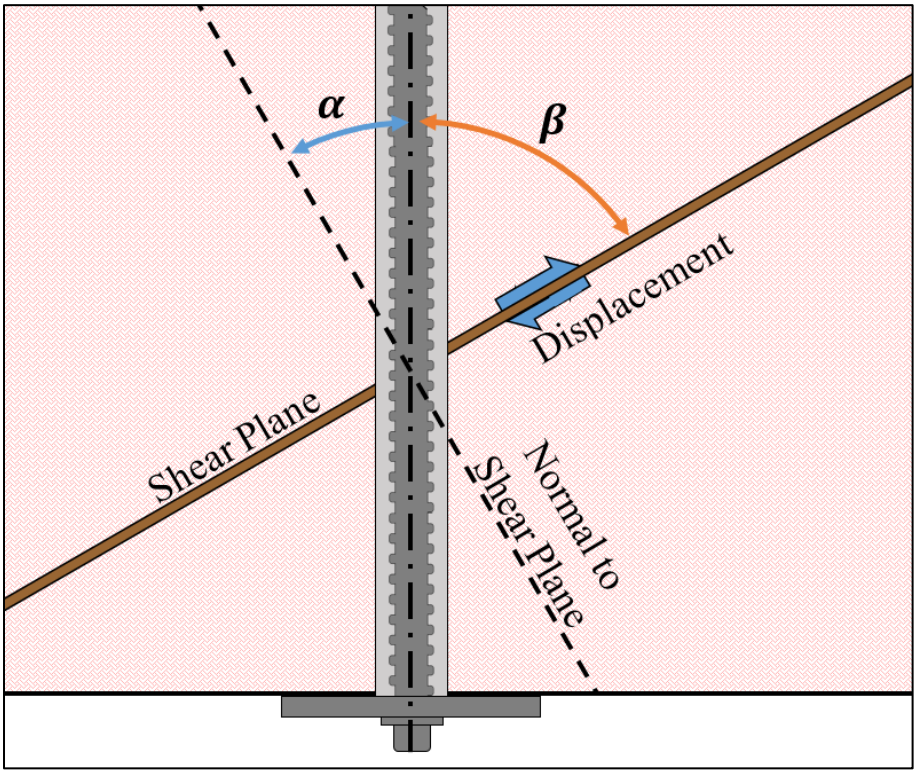

Figure 2.5. Definition of Alpha and Beta angles between the rebar and the shear plane

2.2.3 Effect of Shear Plane Dilation

Dight (1982), Spang and Egger (1990), and Chen and Li (2015) investigated the effect of shear plane dilation on the behaviour of rebar. Shear plane dilation is typically defined by the angle of dilation, i, as shown in Figure 2.6. For clarification, when $i = 0°$ the relative movement of the discontinuity is purely shear movement. The relative movement of the discontinuity is an entirely tensile separation of the discontinuity when $i = 90°$.

These researchers all found that shear plane dilation has a similar effect to rock bolt inclination. A rebar rock bolt installed across a discontinuity with a large component of dilation has a stiffer load-displacement relation than a similar rock bolt subjected to pure shear displacement. Rock bolts subjected to large dilation movements exhibit lower total displacements and higher ultimate loads when the rebar fails. Larger total displacements can occur before the rebar fails when the discontinuity displaces in pure shear ($i = 0°$). This relationship has not been studied extensively and, therefore, has not been quantified.

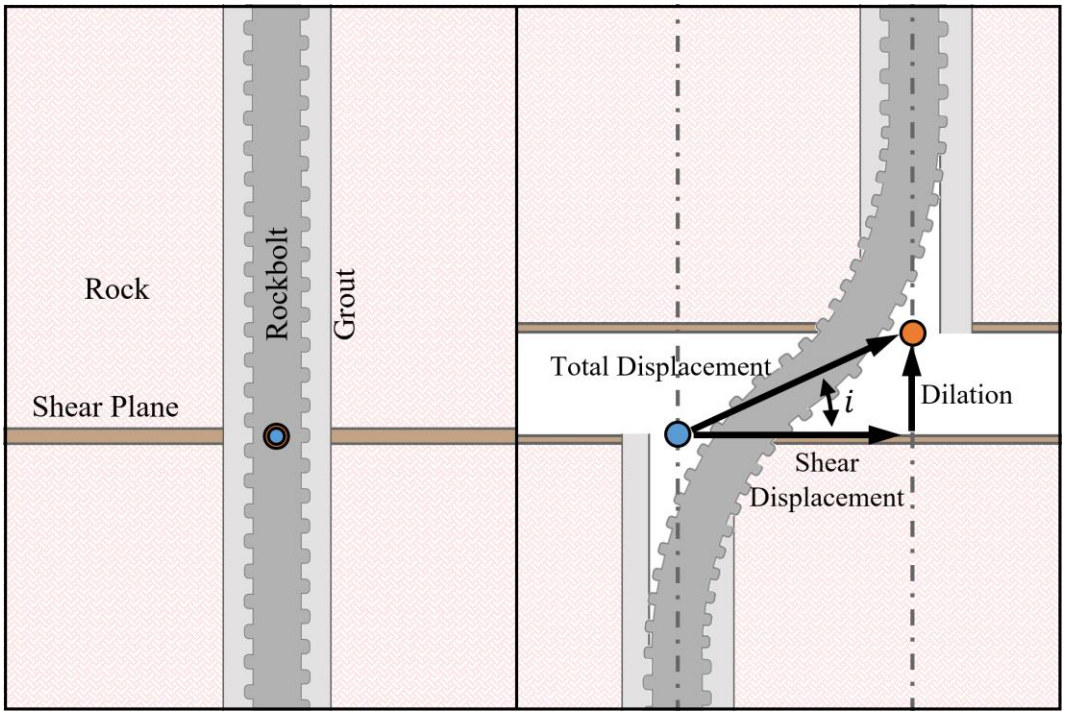

Figure 2.6. Fully-grouted rebar at installation (left) and after shear plane dilation in combination with shear movement (right)

2.2.4 Strength of Surrounding Medium and Effect on Rock Bolt Behaviour

Multiple authors (Dight, 1982; Spang and Egger, 1990; Aziz, Pratt, and Williams, 2003; Chen, 2014) tested rebar rock bolts subjected to shear in blocks of various strengths. The researchers conducted these tests using blocks made of both rock and concrete. All researchers found that weaker rock or concrete resulted in greater displacements before failing the rebar when compared to similar tests with stronger rock or concrete. An example of this relationship can be seen in two tests from Chen (2014) shown in Figure 2.7. These shear tests were conducted on 20 mm diameter rebar installed in two 0.95 m cubic blocks of concrete.

Ferraro (1995) found that the rebar failure can occur in two different ways due to the strength of the rock/concrete. He found that the rebar will fail by a combination of shear and tension when the rock/concrete is relatively strong. The rebar will fail by a combination of tension and bending deeper into the rock/concrete surface on either side of the shear plane when the rock/concrete is relatively weak.

The surrounding rock or concrete exerts a bearing force, p_u, on the rebar as shear movement occurs. This bearing force is the reason the strength of the surrounding medium has such a large impact on the behavior of the rebar rock bolt when subjected to shear movement. This bearing force is distributed along the rebar as shown in Figure 2.8. Although this force likely has some complex distribution due to the inherent heterogeneity of rock, Dight (1982) and Pellet and Egger (1996) assumed it was constant along the rebar length.

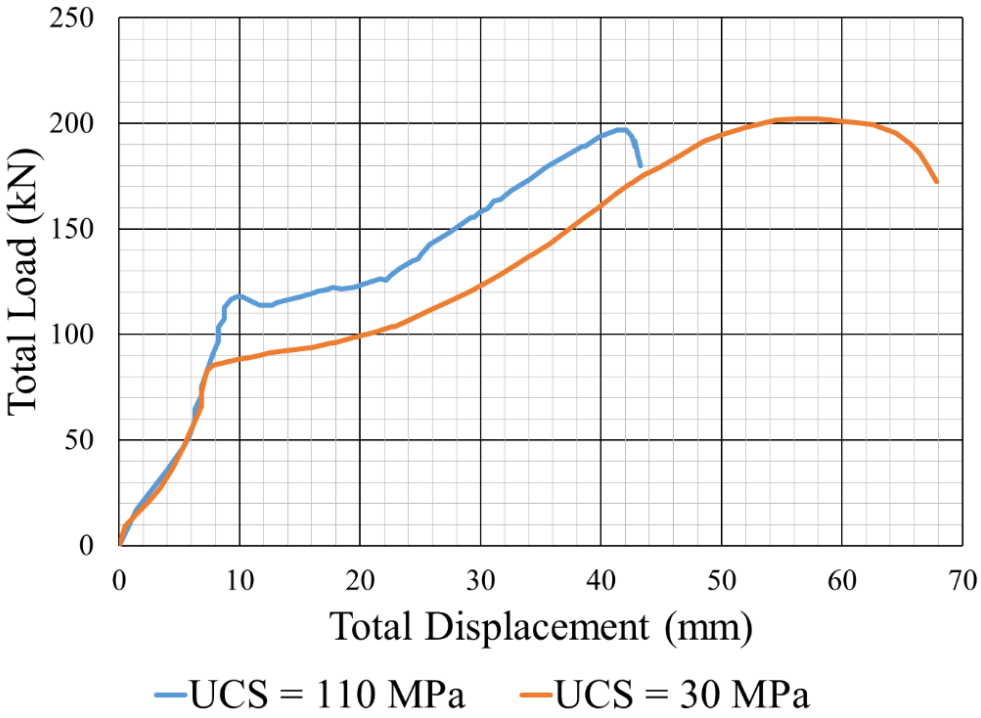

Figure 2.7. Comparison of load vs displacement behaviour of 20 mm diameter rebar in concrete with different uniaxial compressive strengths (UCS) (after Chen, 2014)

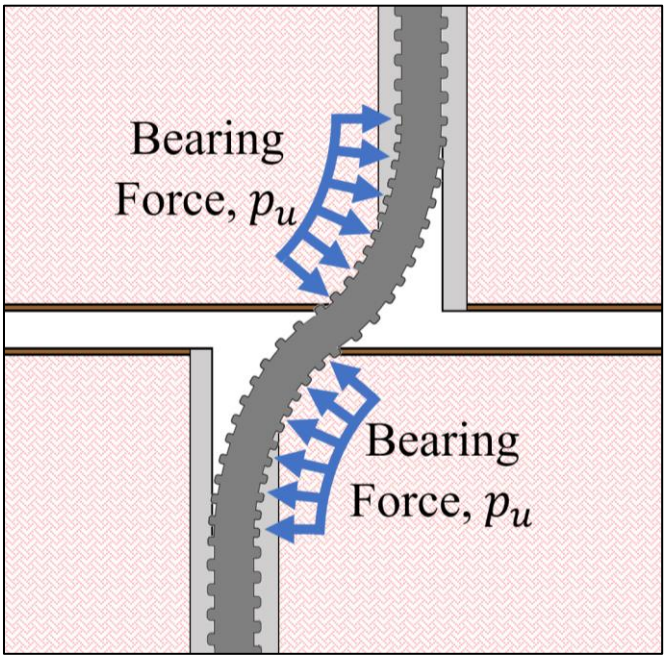

Figure 2.8. Sheared rebar rock bolt showing some distribution of the bearing force, p_u, that the surrounding rock exerts on the rebar

2.2.5 Effect of Shear Plane Aperture

Few researchers considered the possibility of a shear plane already having a gap or aperture when the rock bolts are installed. A shear plane with a gap or aperture is shown in Figure 2.9. Almost all researchers considered the shear plane to be initially closed.

Stimpson (1987) considered a shear plane aperture in his analytical analysis of the rebar behaviour. He concluded that a shear plane aperture would reduce the stiffness of the rebar's load-displacement behaviour. Stimpson developed an analytical model to predict this stiffness, however it was limited to only linear elastic behaviour and very small deformations.

Chen (2014) tested a fully-grouted 20 mm diameter rebar with a 30 mm shear plane aperture in two concrete blocks with a uniaxial compressive strength (UCS) of 110 MPa. The tests had a dilation angle of 50 degrees (Section 2.2.3). The 30 mm aperture test on rebar exhibited an ultimate displacement of 48 mm as opposed to 33 mm when compared with a similar rebar test with an initially tight shear plane. Both tests had a similar ultimate total applied load.

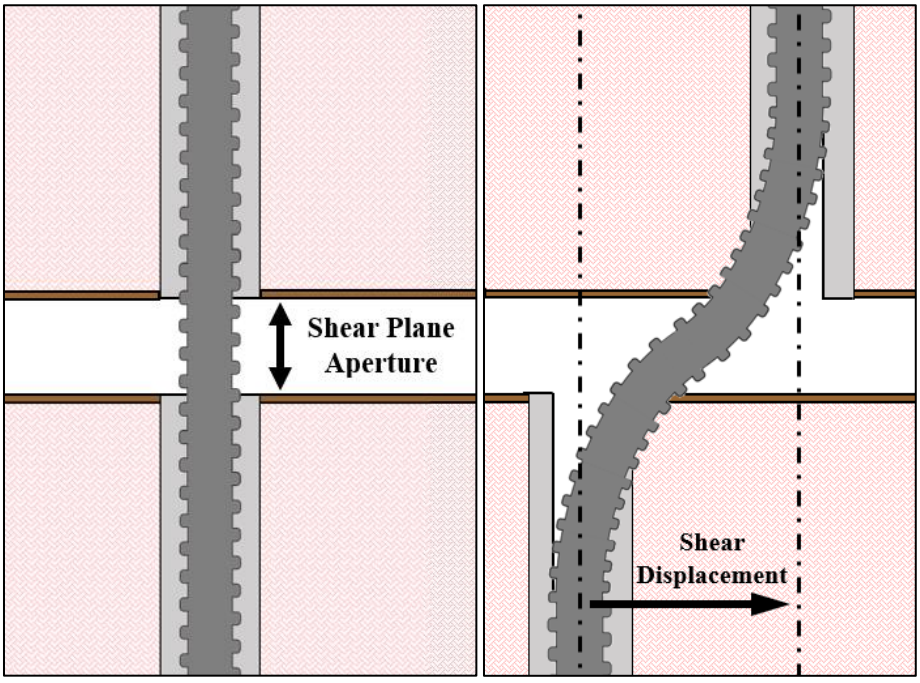

Figure 2.9. Diagram showing unchanged shear plane aperture at installation (left) and after some shear displacement (right)

2.2.6 Rock Bolt Models

There have been multiple models for predicting shear behaviour of fully-grouted rebar presented by past researchers (Bjurstrom, 1974; Dight, 1982; Ferrero, 1995). However, the empirical model from Spang and Egger (1990) and the analytical model from Pellet and Egger (1996) are both simple and representative of their experimental results. These models are presented and discussed in this section.

Spang and Egger (1990) developed an empirical model to predict the maximum shear resistance and shear displacement of fully-grouted rebar crossing a shear plane. The model was developed based on laboratory testing, field testing, and numerical modelling. The model is dependent on the penetration modulus of the surrounding rock or resin as proposed by Schubert (1984).

Schubert (1984) designed a test called the penetration test. This test is conducted by pressing a 20 mm diameter hardened steel ball bearing into a rock sample. The penetration modulus, EM, is the linear relationship between the force applied in kN and the penetration of the ball bearing in mm. Spang and Egger (1990) developed their empirical model to describe fully-grouted rebar rock bolt behavior in shear using this penetration modulus property.

The equations from Spang and Egger (1990) presented here are in terms of the uniaxial compressive strength (UCS) of the rock or resin. These equations were derived using the penetration modulus, but were converted to UCS using the empirical relationship:

$$\sigma_c = EM^{1.43}$$

Equation 2.1

Where σ_c = uniaxial compressive strength of the rock or resin (MPa)

EM = penetration modulus of rock or resin (kN/mm)

The maximum shear resistance of the rock bolt can be calculated by the following empirical relationship:

$$V = T_{Ult}\sigma_c^{-0.14}(0.85 + 0.45\ tan\ tan\ \varphi)[1.55 + 0.011\ \sigma_c^{1.07}\ (\alpha + i)\ ]$$

Equation 2.2

Where V = maximum shear resistance provided by the rebar to the shear plane (kN)

T_{Ult}= ultimate tensile load of the rock bolt (kN)

φ = friction angle of the shear plane

α = the angle of the rock bolt towards the shear plane measured from perpendicular

i = dilation angle for shear plane movement

The shear displacement corresponding to this maximum shear resistance is calculated as follows:

$$U_{Ult} = d_{rebar}(15.2 - 55.2\,\sigma_c^{-0.14} + 56.2\,\sigma_c^{-0.28})\left[1 - \frac{tan\,\alpha}{\sqrt{cos\,\alpha}}\left(\frac{70}{\sigma_c}\right)^{0.125}\right]$$

Equation 2.3

Where U_{Ult} = shear displacement of the shear plane at the maximum shear resistance (mm)

d_{rebar} = diameter of the rebar (mm)

Pellet and Egger (1996) presented an analytical model for the shear behaviour of fully-encapsulated rock bolts. They assumed the rock bolt would behave elastically before developing plastic hinges. These plastic hinges are located along the rebar where elastic deformation is exceeded. After the plastic hinges were formed, the authors assumed the bolt would not develop any further internal shear forces and it would ultimately fail due to the combined shear and tensile forces in the bolt.

Figure 2.10 shows the rebar deformation and loading at the yield point of the rock bolt. Many of the variables and characteristics of Pellet and Egger's (1996) model are shown in this figure. Point O represents the rebar at its intersection with the shear plane. The rebar is subjected to a shear force, Q_{oe}, and an axial force, N_{oe}, being applied at point O at the yield point of the rebar. The rebar's centroidal axis has some amount of rotation, ω_{oe}, and shear displacement, U_{oe}, at point O as a result of the applied forces. The surrounding rock exerts a lateral force on the rebar as it shears called the bearing force, p_u. Pellet and Egger assumed the bearing force is constant along the length, l_e, between point O and point A. Point A is the point of the maximum internal bending moment within the rebar and point B represents the point where the rebar is no longer affected by the shear plane.

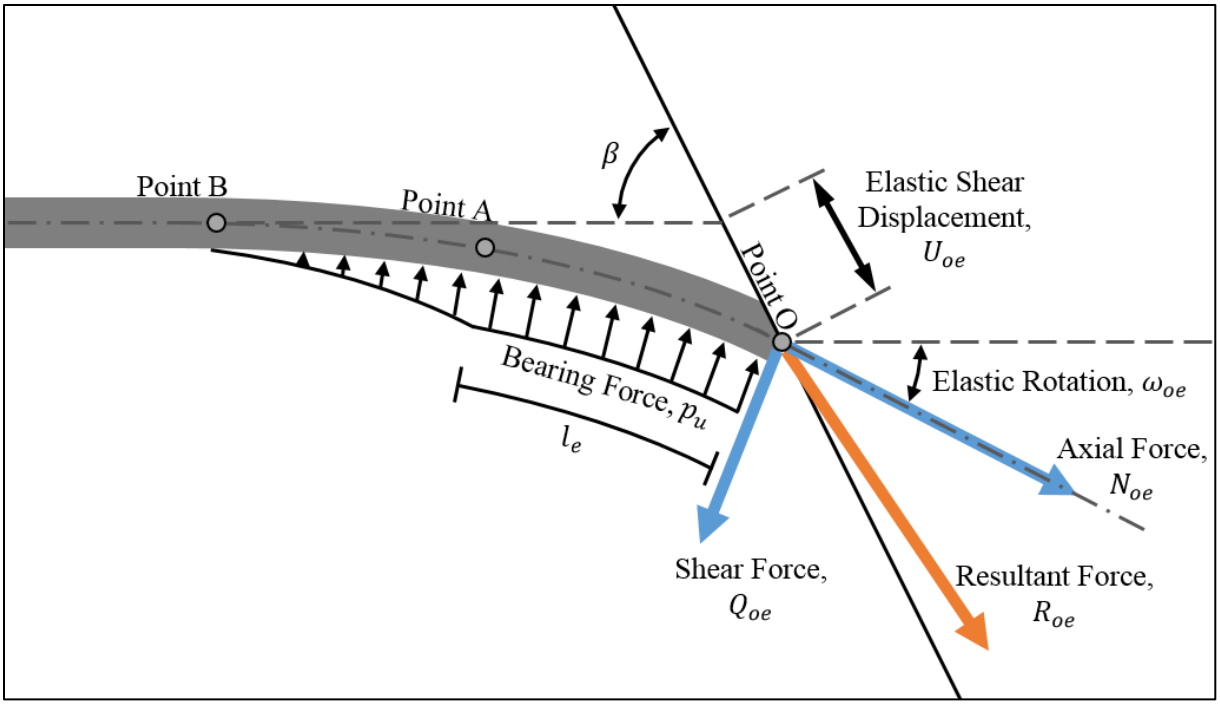

Figure 2.10. Rebar behaviour and variable definitions at the yield point of the rebar (after Pellet and Egger, 1996)

Equation 2.4 can be used to calculate the internal shear force at point O, Q_{oe}, associated with yielding of the rebar. This equation has no straight forward discrete solution, so an iterative approach must be taken to solve for the value of Q_{oe}. Once the shear force is known, Equation 2.5 should be used to determine the corresponding axial force in the rebar.

$$Q_{oe}^3 + Q_{oe}^2\left(\frac{30\pi^3 p_u d_{rebar} tan\,\beta}{693}\right) - \left(\frac{3\pi^4 \sigma_{yield} p_u^2 d_{rebar}^4 tan\,\beta}{1108}\right) = 0$$

Equation 2.4

$$N_{oe} = \frac{\pi d_{rebar}^2 \sigma_{yield}}{4} - \frac{4Q_{oe}^2}{p_u d_{rebar}}$$

Equation 2.5

Where N_{oe} = internal axial force acting at point O at the yield stress of the rebar

Q_{oe} = internal shear force acting at point O at the yield stress of the rebar

p_u = bearing force of surrounding grout/rock acting on rebar assuming a constant distribution

d_{rebar} = diameter of the rebar

β = angle between initial bolt axis and shear plane

σ_{yield} = yield stress of rebar

The displacement of point O parallel to the shear plane at yield of the rebar can be calculated using Equation 2.6. This displacement can be taken as one half of the shear displacement of the shear plane if perfectly symmetric loading conditions and behaviour exist on either side of the shear plane.

$$U_{oe} = \frac{2216\, Q_{oe}^4}{\pi^4\, E_{rebar}\, p_u^3\, d_{rebar}^4\, sin\, \beta}$$

Equation 2.6

Where U_{oe} = shear displacement of point O parallel to the shear plane at the yield stress

E_{rebar} = Young's Modulus of rebar

= 200 GPa

The centroidal axis of the rebar at point O rotates as shear displacement occurs. This rotation angle at yield of point O can be calculated by Equation 2.7. The angle is measured from the initial rebar axis.

$$\omega_{oe} = \frac{554\, Q_{oe}^3}{\pi^3\, E_{rebar}\, p_u^2\, d_{rebar}^4}$$

Equation 2.7

Where ω_{oe} = rotation of the rock bolt centroidal axis at point O at yield of point O relative to the initial centroidal axis orientation

Pellet and Egger (1996) defined a new set of equations to describe the plastic behaviour of the rebar after it has yielded. This model assumes the shear force within the rebar between point O and point A will not increase after yield.

Figure 2.11 shows the rebar profile and the relevant variables that define this plastic behaviour. When the rebar fails, point O is again subjected to a shear force, Q_{oe}, which has not changed since

the rebar yielded. This point is also subjected to an axial force at failure, N_{of}. The axial force can be calculated using Equation 2.8.

$$N_{of} = \frac{\pi \sigma_{failure} d_{rebar}^2}{4} \sqrt{1 - 64 \left(\frac{Q_{oe}}{\pi \sigma_{failure} d_{rebar}^2} \right)^2}$$

Equation 2.8

Where N_{of} = axial force at point O at failure

Q_{oe} = shear force at point O at yield and failure

$\sigma_{failure}$ = ultimate tensile strength of the rock bolt

The additional rotation of the rebar's centroidal axis that occurs at point O between the yield point and the rebar failure is given by Equation 2.9.

$$\Delta\omega_{op} = arccos \left[\frac{l_e}{l_f} \sin^2 \beta \ \pm \sqrt{\left(1 - \left(\frac{l_e}{l_f}\right)^2 \sin^2 \beta\right) \cos^2 \beta} \right]$$

Equation 2.9

Where $\Delta\omega_{op}$ = additional rebar rotation at point O from the yield stress to the failure stress or the rebar

l_e = length of the rebar between its intersection with the shear plane, point O, and its point of maximum bending moment, point A, at the yield stress of the rebar at point O

l_f= length of the rebar between its intersection with the shear plane, point O, and its point of maximum bending moment, point A, at the failure stress of the rebar at point O

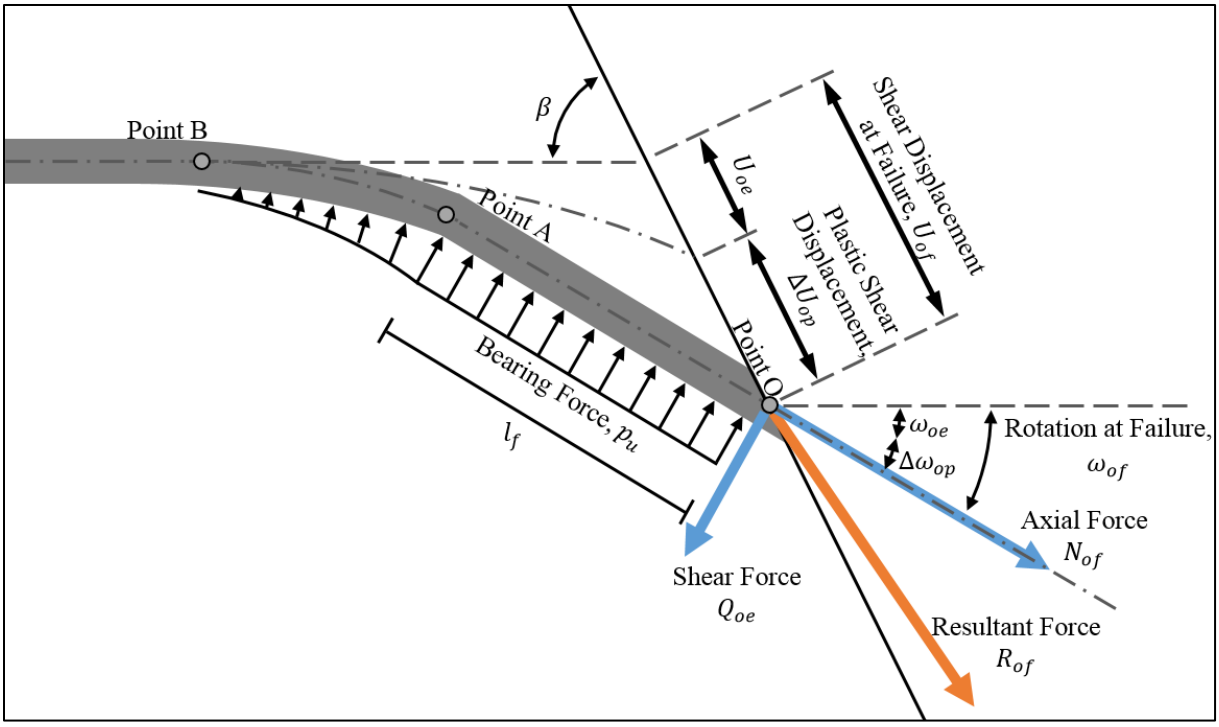

Figure 2.11. Plastic rebar behaviour and variable definitions (after Pellet and Egger, 1996)

The length of the rebar at yield between its intersection with the shear plane, point O, and its point of maximum bending moment, point A, can be calculated using Equation 2.10. The axial strain throughout this length is assumed to be constant at failure. As a result, Equation 2.11 can be used to calculate the length between points O-A at failure.

$$l_e = \frac{Q_{oe}}{p_u}$$

Equation 2.10

$$l_f = l_e(1 + \varepsilon_{failure})$$

Equation 2.11

Where Q_{oe} = shear force at point O at yield

p_u = bearing force of surrounding rock/grout along l_a (assuming a constant distribution of bearing force along rebar length)

$\varepsilon_{failure}$ = strain of the rock bolt at failure.

The additional displacement of point O parallel to the shear plane that occurs between the yield of the rebar and the failure of the rebar is given by Equation 2.12.

$$\Delta U_{op} = \frac{Q_{oe}\, sin\, \Delta\omega_{op}}{p_u\, sin\left(\beta - \Delta\omega_{op}\right)}$$

Equation 2.12

Where ΔU_{op} = additional shear displacement of point O from the yield of the rebar and the failure of the rebar

The total rotation and shear displacement of point O at rebar failure can then be calculated by Equation 2.13 and Equation 2.14.

$$\omega_{of} = \omega_{oe} + \Delta\omega_{op}$$

Equation 2.13

$$U_{of} = U_{oe} + \Delta U_{op}$$

Equation 2.14

Where ω_{of} = rotation of point O at the failure of the rebar

U_{of}= shear displacement of point O at the failure of the rebar

The model and almost all analytical models presented here are dependent on the bearing force per length of the rebar that the surrounding rock/grout exerts on the rebar. Pellet and Egger (1996) assumed this force to be constant between point O and point A and defined it by Equation 2.15.

$$p_u = K\, \sigma_c\, d_{rebar}$$

Equation 2.15

Where K = some load factor greater than or equal to 1 (assumed to be equal to 1)

σ_c = uniaxial compressive strength of the surrounding rock/grout

2.3 Rebar Rock Bolt Behaviour in Tension

Bjurstrom (1974), Aziz et al. (2005), and Chen and Li (2015) found that rebar subjected to shear displacement will also be subjected to tensile force. This tensile force increases with increasing shear displacement. The increasing tensile forces provide a normal force to the shear plane and

increase the friction. Alternatively, the force could serve to close a shear plane aperture when present.

The generation of tensile forces in the rebar engages its bond strength. For this reason, it is important to understand the tensile and bond strength behaviour of fully-grouted rebar rock bolts. A brief review of previous research in this area will be presented in this section.

When loaded in tension, rebar will transfer load to the surrounding rock through its bond with the surrounding grout or resin. The distribution and length over which this load transfer occurs can be quite complex. A simple uniform bond stress model was proposed by Cook (1993) and is shown in Figure 2.12.

The uniform bond stress model is advantageous due to its simplicity. The shear stress engaged by the rebar is assumed to be constant along its length and transfers load from the rebar to the surrounding rock. As a result of the assumed constant bond strength, the load within the rebar decreases linearly along its length.

Figure 2.13 illustrates the method by which tensile loads are transferred to the surrounding rock through shear forces. These shear forces include the rebar–resin interface shear force, and the resin–rock interface shear force, in response to the tensile force applied to the rebar. In the case of the uniform bond stress model, the shear stresses between the rebar–resin and the resin–rock are assumed to be constant along the rebar length.

Feldman and Bartlett (2007) also proposed a bond strength model for rebar cast in concrete and loaded in tension. This model assumed that beyond a certain threshold of load or displacement, the bond strength fails along a certain length and the shear stress is reduced. Models like these can account for deteriorating resin, grout, or concrete and loss of adhesion.

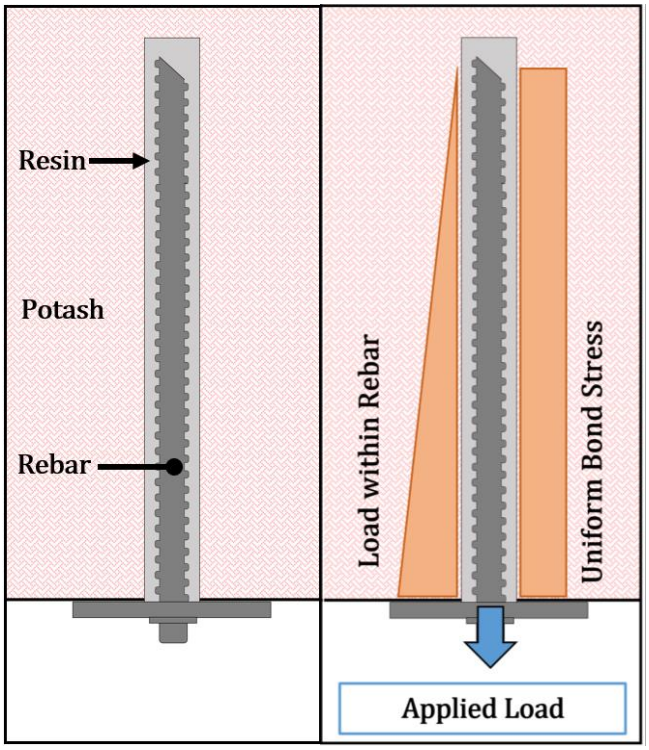

Figure 2.12. The uniform bond stress model proposed by Cook (1993)

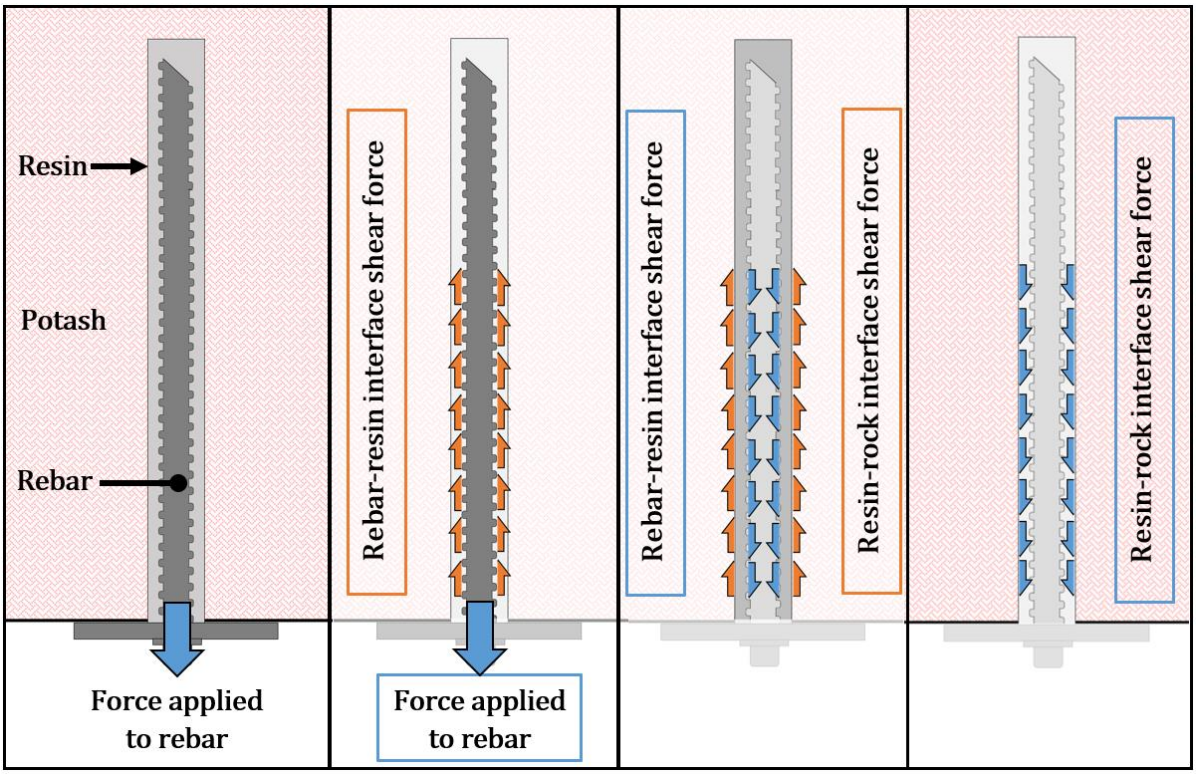

Figure 2.13. Fully-grouted rebar showing how a tensile force is transferred through the various component to the surrounding rock

Stimpson (1994) presented an overview of rock bolts and reinforcement in coal and soft-rock mining. Stimpson explained that rock bolts reinforce ground by allowing load to be transferred across discontinuities and failed regions of rock. Stimpson stated that the shear stress capacities of the rebar-resin and resin-rock interfaces, as shown in Figure 2.13, can be dependent on:

- Reduction in bolt diameter due to axial tension (i.e. Poisson's Ratio)
- Confining stress
- Hole geometry
- Size and surface geometry of the rock bolt
- Grout/resin annulus thickness
- Rock strength
- Grout/resin type
- Grout/resin curing temperature
- Installation procedure
- Mechanical properties of rock bolt

Neely (2014) performed dozens of pull-tests on rebar rock bolts that had been installed in situ in potash mines in Saskatchewan. The pull-tests were conducted on 25 mm diameter Grade 400 forged-head rebar from Dywidag Systems International. The rebar was installed with fast acting resin and the bond length was varied. Neely found that the rebar had an average bond strength of 360 kN/m.

2.4 Potash Properties

Previous researchers have found that the rebar rock bolt behaviour is dependent on the strength of the rock surrounding the rebar. For this reason, a discussion on the material properties of potash follows.

Various researchers have tested the Uniaxial Compressive Strength (UCS) of potash relevant to this research project. The results of tests from two researchers are displayed in Table 2.2. Neely (2014) performed UCS tests on Upper Patience Lake potash samples. These were obtained from the Nutrien Allan Mine and were drilled perpendicular to the depositional stratigraphy. Based on

ten tests, Neely reported an average strength of 25.4 MPa, an average Young's Modulus of 2.8 GPa, and an average Poisson's Ratio of 0.30. Brazilian testing of ten samples resulted in an average tensile strength of 1.75 MPa perpendicular to the bedding. Finally, the potash was estimated to have a cohesion of 7.0 MPa based on guillotine shear testing on ten samples of potash.

Duncan (1990) performed five uniaxial compressive strength (UCS) tests on Patience Lake potash samples from the Nutrien Lanigan Mine with varying strain rates. Sample number UP-6 had a UCS of approximately 29.7 MPa when failed within 30 minutes. This test time is slower than the tests conducted by Neely (2014), but comparable to the maximum specified UCS testing time of 15 minutes set out in ASTM Standard D7012 – 14 (ASTM International, 2014b).

Duncan (1990) also loaded a Patience Lake potash sample slowly over the course of roughly 2 weeks. In this test, the UCS was reduced to approximately 16.5 MPa. This long-term reduction in strength is due to the time dependent property of potash known as visco-plasticity.

Table 2.2. Upper Patience Lake potash uniaxial compressive strengths

	Duncan, 1990		**Neely, 2014**
Approximate Test Duration	30 minutes	2 weeks	10 minutes
UCS	29.7 MPa	16.5 MPa	25.4 MPa

Visco-plastic deformation, also referred to as creep, is a critical component of potash behaviour. Visco-plastic deformation allows for large displacements of potash rock to occur over time. Visco-plasticity is long term non-recoverable deformation where a material retains its final strain state indefinitely after stress is removed.

Goodman (1989) provided a summary of visco-plastic constitutive models. In this text, the three stages typically exhibited by a creeping material (Figure 2.14) are explained. According to Goodman, a visco-plastic material will exhibit similar instantaneous strains as most rocks do. However, immediately after this instantaneous strain occurs, the material will continue to strain

over time. This is the primary creep stage during which creep occurs at a high rate initially and then begins to slow down.

Secondary creep follows primary creep and is characterized by a constant strain rate. In this stage, the material has reached a steady state of deformation and will continue to strain at the same rate so long as the stress state does not change. Finally, the material may or may not enter the tertiary creep stage. During this stage, the material will strain at an accelerating rate until ultimate failure. At this state, the sample has essentially deformed beyond its capacity and so begins to degrade.

Chen (1993) carried out many creep and relaxation tests to quantify the time dependent behaviour of potash. Results of the testing were fit to a constitutive model to predict deformation under tri-axial stress conditions. The laboratory testing was verified by field observations of in situ potash creep. Most notably, Chen concluded that potash has no creep limit. This suggests that under certain stress conditions and a long enough period, potash can deform indefinitely. In other words, under the right conditions potash will remain in the secondary creep stage without entering the tertiary stage.

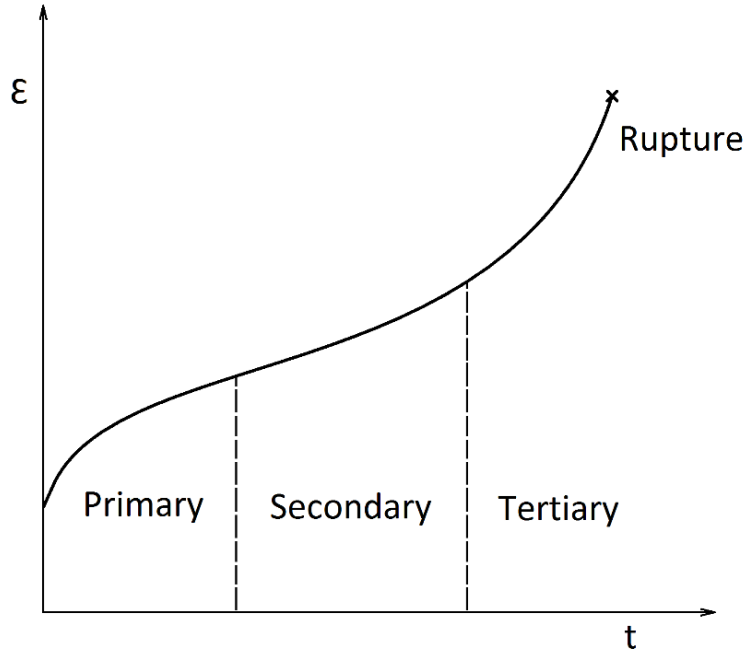

Figure 2.14. General behaviour of material creep where ε is compressive strain and t is time (after Goodman, 1989)

Duncan and Lajtai (1993) performed uniaxial creep tests of potash from the Upper Patience Lake and Esterhazy Formations. The creep tests were performed at constant strain rates with testing periods ranging from two months to eight months. They found that potash will begin to deform visco-plastically at any uniaxial stress. However, the strain rate is insignificant until the uniaxial stress reaches about 10 MPa.

Duncan and Lajtai (1993) also determined that the uniaxial stress at which brittle failure begins is heavily dependent on the strain rate. The onset of brittle failure was identified by dilatational volumetric strains and attributed to micro-fractures forming and propagating within the potash samples. They found that this brittle deformation process could begin at a uniaxial stress as low as 6 MPa if the samples were loaded at 25 με/s and at 24 MPa if loaded at 1.1 με/s. When loaded even slower than 1.1 με/s, this brittle deformation mechanism would not occur at all and all deformation was visco-plastic.

The potash behaviour summarized here could be very important in understanding the behaviour of fully-grouted rebar crossing a shear plane in potash. As was discussed, the strength and deformation of potash is heavily time dependent. Additionally, rebar crossing a shear plane can undergo more shear displacement of the shear plane before failing when installed in weaker and more deformable rock than when installed in stronger rock. Therefore, a relatively slow moving shear plane in potash should allow more shear displacement before failure of rebar rock bolts when compared with an identical shear plane with a faster rate of movement.

2.5 Fibre-optic Instrumented Rebar

This research project makes extensive use of fibre-optic instrumented rebar rock bolts. As was shown by other researchers, fully-grouted rebar rock bolts loaded in shear exhibit complex shear, bending, and tensile deformations. Furthermore, these deformations are very localized near the shear plane. To properly measure and understand the manner in which the rebar is loaded and deforms, high resolution strain measurements must be taken. The fibre-optic instrumentation uses distributed optical sensing to measure the strain at sub-millimeter increments along the length of the rebar.

A commercial system capable of distributed optical sensing was first released by Luna Technologies circa 2010. The system can precisely measure strain and temperature using fibre-optic strands. It can make the measurements with 0.65 mm resolution along a roughly 20 m sensing length. The strain within the fibre-optic strand can be measured within 25 micro-strain (με) accuracy at a maximum rate of 10 Hz (Luna Inc., 2016).

The system uses a laser to send light waves down the fibre-optic strand. Some amount of the light is reflected by natural imperfections within the fibre-optic strand (Samiec, 2012). This reflection is called Rayleigh scattering and occurs along the entire length of the fibre-optic strand. The scattered light is broken down into windows of analysis, as shown in Figure 2.15.

The high-resolution strain sensing is made possible using a technique called optical frequency domain reflectometry (OFDR). This contrasts with various other fibre-optic strain sensing methods that use the flight-time of reflected light waves to determine the distance along the fibre-optic strand. OFDR combines the back-scattered light waves from the fibre-optic strand with the unaltered input light waves. The laser inputs various frequencies of light and, based on the interference of the scattered and unaltered light waves, the strain at each window of analysis can be determined.

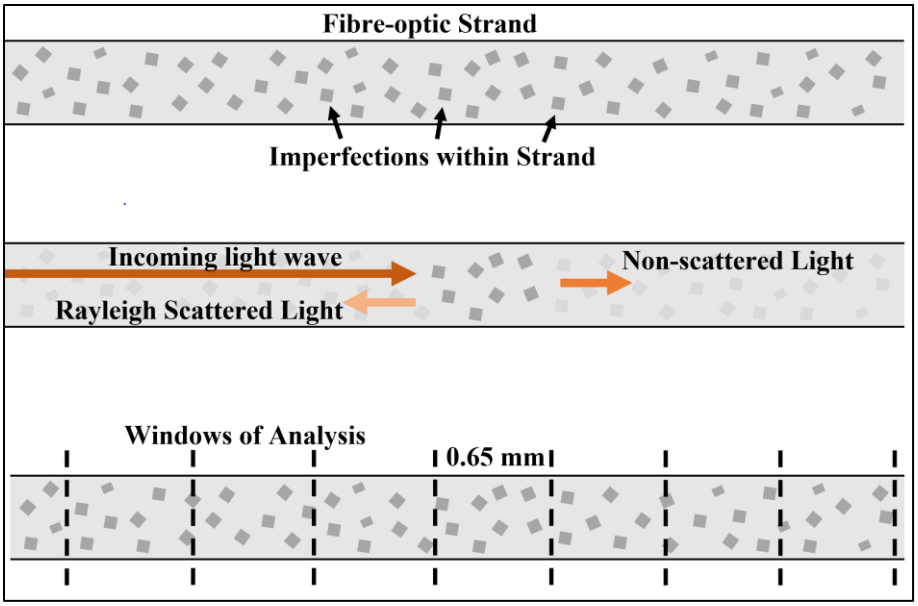

Figure 2.15. Fibre-optic strand and Rayleigh scattering of light that allows 0.65 mm widows of strain analysis along the fibre-optic length

Regier (2013) and Davis (2015) performed multiple tests using the distributed optical sensing technology. Among the experiments, they investigated different bonding agents for instrumenting steel plates, concrete, and rebar with the fibre-optic instrumentation. They conducted tensile tests with instrumented steel plates and reinforced concrete. They also conducted reinforced concrete beam bending tests with fibre-optics bonded to the internal rebar and to the concrete externally.

Regier (2013) and Davis (2015) determined that the fibre-optic instrumentation was able to accurately identify and measure localized strains. They were able to identify areas of concrete beams with tensile cracking in the concrete, poor bonding of the rebar to the concrete, and rebar with significant corrosion or reduced cross-sectional areas.

YieldPoint Inc. manufactures and sells rebar instrumented with the Luna distributed optical sensor. The instrumented rebar are constructed by machining small grooves down the length of the rebar and the fibre-optic strands are epoxied into them. These grooves are roughly 3 mm wide and 3 mm deep into the surface of the rebar. Two configurations of these grooves are available. The first diametric configuration has two grooves machined down the length of the rebar at roughly 180 degrees apart (diametrically opposed). The second three-groove configuration has three grooves

machined down the rebar length at roughly 120 degrees apart. Figure 2.16 shows the cross-sections of diametric instrumented rebar and three-groove instrumented rebar.

The difference between the two configurations becomes clear in the theoretical analysis of instrumented rebar. The three-groove configuration allows for calculation of bending strain, axial strain, and the direction of bending. The diametric configuration allows for calculation of axial strain but requires a known or assumed direction of bending relative to the fibre-optic strand to calculate the bending strain.

It should be noted that using two or three separate fibre-optic strands are not required to instrument the rebar. Instead, a single strand is used and simply looped around the ends of the rebar. A hole is either drilled through the rebar to connect the grooves or a circumferential groove is machined to connect the grooves.

Hyett et al. (2013) used the diametrically instrumented rebar to investigate the bond strengths of rebar and the strain distribution along the rebar in shear. The researchers conducted tensile pull tests on the instrumented rebar after grouting them in concrete. The researchers were able to identify the distribution of strain along the embedment length with a very high resolution using the distributed optical strain sensing technology, compared to previously used strain and displacement gauges. Double shear tests were also conducted on the instrumented rebar after they were installed across three blocks of concrete. The tests showed the rebar exhibited highly concentrated strains near the shear planes.

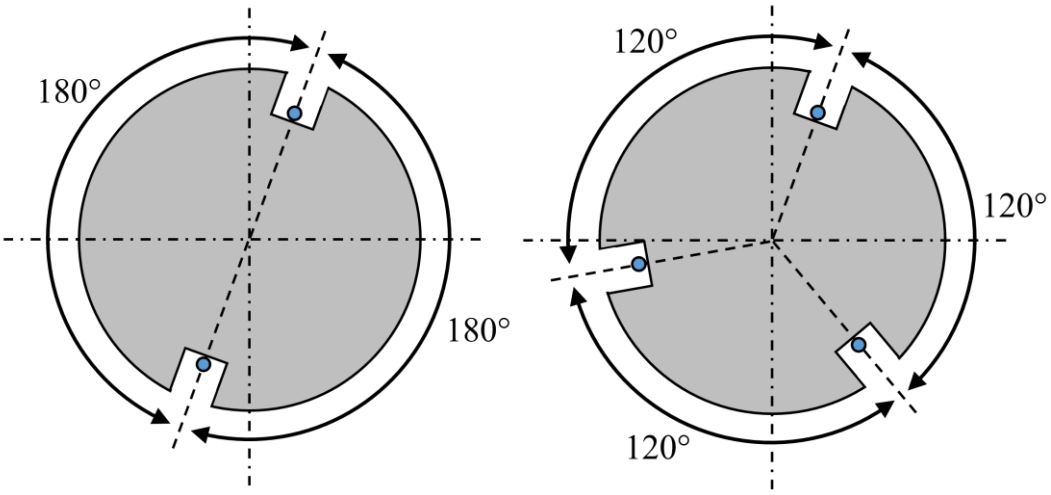

Figure 2.16. Cross-section of fibre-optic instrumented rebar in a diametric configuration (left) and three-groove configuration (right)

Hyett et al. (2013) found strain distributions that agree closely with the findings of the numerical modelling presented by Jalalifar et al. (2006). Specifically, the rebar was found to have high compressive and tensile zones of strain on either side of the shear plane and on either side of the rebar, as in Figure 2.17. Hyett et al. (2013) did not note any slippage of the fibre-optic strand from the rebar, however, they did not explicitly test for this. Slippage of the fibre-optic could be an issue, specifically with double shear testing, since the rebar exhibits a high strain gradient near the shear planes.

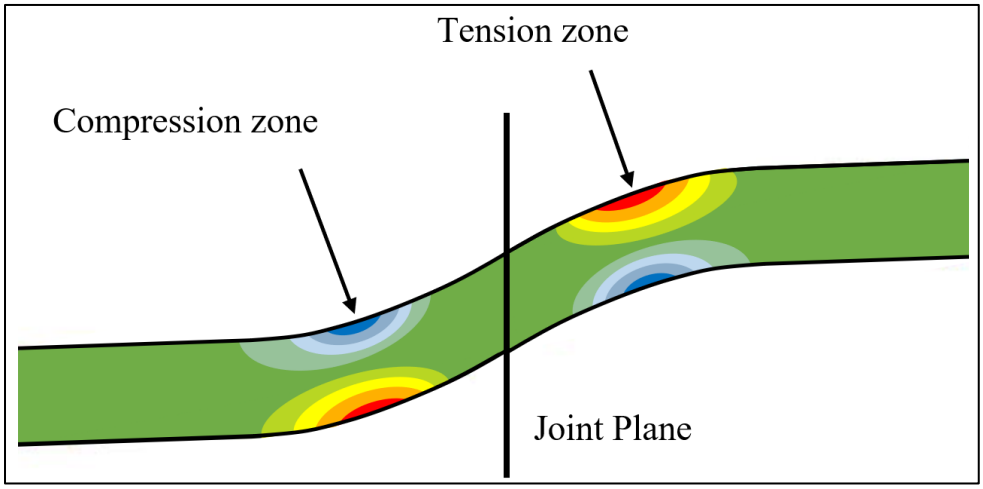

Figure 2.17. Strain contours in rebar crossing a sheared joint (after Jalalifar et al., 2006)

2.6 Discussion

An extensive literature review was conducted and relevant material was summarized in this section. Most notably, rebar rock bolts crossing shear planes in rock have been studied by many different researchers. These researchers found a large number of variables that can affect the shear behaviour of rebar rock bolts.

Unfortunately, almost all researchers only considered shear planes without a shear plane aperture and potash shear planes are regularly observed to be open. Previous researchers have also failed to develop an easily reproducible testing method or apparatus to evaluate the shear behaviour of rebar rock bolts.

Two models have been proposed by previous researchers that will be compared against results in this project in Section 6.3. The models did not consider the presence of a shear plane aperture, however they were still useful for verification of the project results.

The fibre-optic instrumentation used in this research project is relatively new. Previous research has shown the distributed optical sensing technology is effective at measuring the strain in rebar at a very high resolution. Limited information is available on the application of this technology so much of the applied analysis was developed as part of this research. The data from this instrumentation was primarily used to confirm the general behaviour of the rebar in shear.

3 LABORATORY TESTING

This section describes the design, theory, and results for the laboratory experiments conducted in this research project. Two laboratory experiments were carried out to better understand the rebar's behaviour when subjected to lateral loads and the effect of shear plane aperture. The experiment also served to evaluate the accuracy of fibre-optic instrumented rebar. All laboratory testing was conducted at the University of Saskatchewan (USask) in either the Geological Engineering or Civil Engineering Laboratories.

The laboratory testing consists of two experimental set-ups: beam bending tests and double shear tests. The goal of the beam bending tests was to evaluate the accuracy of the fibre-optic instrumentation by comparing the lab results to the theoretical bending behaviour of the different types of rebar.

The goal of the double shear tests was to investigate the load-displacement relationship of the different types of rebar when subjected to shear with varying shear plane apertures. The shear plane apertures were varied from 2 mm to 40 mm across 22 tests. The experiment was designed to be representative of in situ shear loading using readily available testing equipment.

Fibre-optic instrumented rebar is used in both the beam bending tests and the double shear tests. This technology is relatively new and the analysis techniques are not well developed. For these reasons, the technology is tested in this section and the analysis methods developed are verified. Some mathematical theory for analyzing the fibre-optic instrumentation is presented in this section, but a more extensive derivation can be found in Appendix C, Appendix D, and Appendix E.

3.1 Beam Bending Tests

Ten beam bending tests were conducted in order to experimentally determine the area moment of inertia, I, of the various rebar sizes and types, and to quantify any asymmetry of this property. Results were compared against the theoretically determined area moment of inertia to determine

the magnitude of errors that could be introduced when using theoretically determined area moment of inertias.

A total of four tests were conducted on rebar with fibre-optic instrumentation in order to investigate the efficacy of the fibre-optic instrumentation under simply-supported beam bending conditions with purely linear-elastic steel behaviour. The tests allowed for back calculation of the lateral displacement and lateral load from the fibre-optic strain measurement and then comparison of these results with the measured experimental results.

3.1.1 Experimental Design

The simple beam bending test set-up is shown in Figure 3.1. The rebar was supported by two outer supports and a load was applied downward at the midspan. The load and displacement of the centre loading platen were measured throughout the test. The tests were stopped prior to yielding any of the rebar samples.

The test was conducted twice for each sample at a different orientation. As seen in Figure 3.2, the bend test was initially conducted with the rebar's linear deformations oriented horizontally and then repeated with the linear deformations oriented vertically. The two tests were conducted to determine if there was asymmetry in the area moment of inertia. Rebar is often considered to be a solid long cylinder which has a radially symmetric cross-section and, as a result, the area moment of inertia is assumed to be symmetric as well. This assumption was investigated since the direction the rebar is bending could have an impact on its strength.

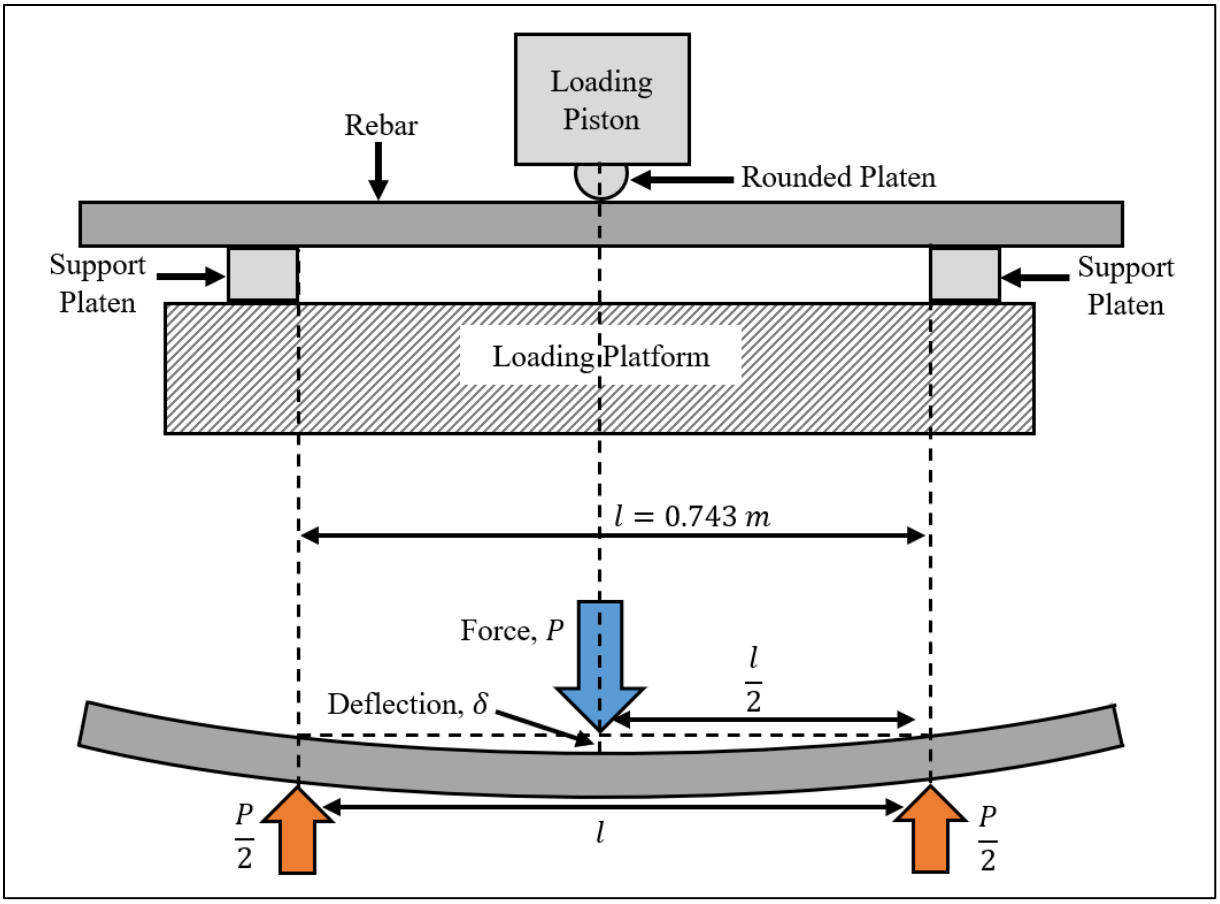

Figure 3.1. Beam bending test set-up.

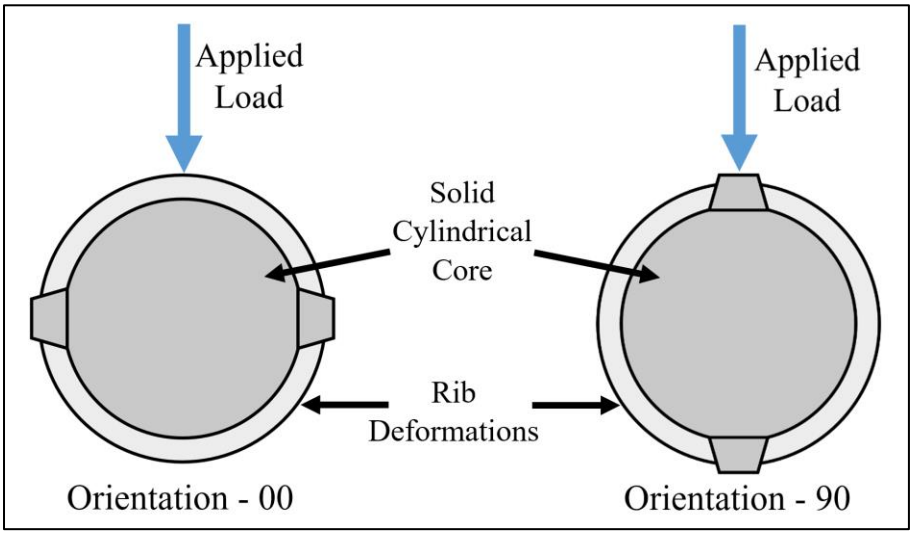

Figure 3.2. Rebar testing orientations to determine effect of asymmetrical geometry on the area moment of inertia.

The area moment of inertia is calculated from the experimental load and displacement data. In order to make this calculation, the Young's Modulus of the material and the distance between the outer supports must first be known. Since the load is centred between the supports, then Equation 3.1 describes the relationship between the area moment of inertia, the load applied, and the deflection where the load is being applied.

$$I_{Exp} = \frac{l^3}{48\,E_{rebar}} \frac{P}{\delta_{centre}}$$

Equation 3.1

Where I_{Exp} = experimental area moment of inertia for the rebar

l = distance between outer rebar supports, 0.743 m

P = load applied at centre

E_{rebar} = Young's modulus of the rebar

δ_{centre} = deflection at the centre of the rebar

The theoretical area moment of inertia for rebar is calculated by assuming the rebar to be a solid cylinder. The diameter of this cylinder is taken to be the minimum diameter of the rebar as measured with calipers. This ignores the effect of the rib deformations of the rebar. Equation 3.2 shows the equation for this theoretical calculation.

$$I_{Rebar} = \frac{\pi\, d_{rebar}^4}{64}$$

Equation 3.2

Where I_{Rebar} = theoretical area moment of inertia for the rebar

d_{rebar} = minimum diameter of the rebar

Calculating the theoretical area moment of inertia for fibre-optic instrumented rebar with notches at 120 degree intervals is more complicated. A full summary of the equations used, and their derivation, is included in Appendix E. At a basic level, the area moment of inertia for the cylindrical, un-notched rebar is calculated, and then the area moment of inertias for each instrumentation notch is subtracted from it.

3.1.2 Beam Bending Test Results

A total of ten beam bending tests were successfully conducted on five different rebar samples. Two of the rebar samples tested were instrumented with fibre-optic strain instrumentation in a three-groove configuration. Additional test results can be found in Appendix I.

The beam bending tests were labelled according to the following system:

Ex. BB-8R-00-FO

BB	- Indicates a beam bending test
7 or 8	- Indicates the rebar size in imperial nomenclature: 22M (#7) or 25M (#8)
R or D	- Grade 400 (60) rebar or Grade 500 (75) dywidag threadbar, respectively
00 or 90	- Orientation of the rebar longitudinal deformations as an angle from horizontal
FO	- Indicates tests on fibre-optic instrumented rebar

One sample of 22M (#7) Grade 400 rebar was tested first and the load versus deflection at the midspan is plotted in Figure 3.3. A linear trendline was fitted to each test using the least sum of squares method and the equations of these lines are displayed. The rebar exhibits nearly the same linear behaviour in both perpendicular loading orientations, suggesting the area moment of inertia is approximately equivalent in both directions for this rebar.

Two samples of the 25M (#8) Grade 400 (60) rebar were tested, one of which was instrumented with fibre-optic instrumentation. The load-deflection plots of these four tests are shown in Figure 3.4. Linear trendlines were fitted to the test data to provide an estimate of the slope and the corresponding equations are shown.

The load-deflection behaviour of the 25M rebar in Figure 3.4 is generally quite linear. Beam bending test BB-8R-90 deviated significantly from the behaviour exhibited by other tests on the 25M rebar, including test BB-8R-00 conducted on the same sample in the perpendicular direction. The difference in behaviour of this one test suggests there could be some asymmetry in the area moment of inertia or an operator error while conducting the test. All other tests overlap

significantly suggesting they have a similar area moment of inertia. This, in turn, means that there is not a substantial effect of instrumenting the rebar with fibre-optics.

Two samples of the 22M (#7) Grade 500 (75) dywidag threadbar were tested. Un-instrumented rebar and fibre-optic instrumented rebar were each tested in two perpendicular orientations. The load-deflection plots of the four tests are shown in Figure 3.5. Once again, linear trendlines were fitted to the test data and the equations are displayed on the plot.

The load-deflection behaviour of the 22M dywidag in Figure 3.5 is again very linear. The two tests on un-instrumented rebar overlap closely, as do the two tests on instrumented rebar. This overlap means there is a very similar area moment of inertia for the rebar in the two directions. The tests on instrumented rebar have a slightly lower slope than those on un-instrumented rebar indicating the fibre-optic instrumentation may reduce the area moment of inertia of the rebar slightly.

The slopes of the linear trendlines were used to calculate the area moment of inertias for each test using Equation 3.1. The results of these calculations are shown in Table 3.1. For ease of comparison, the experimentally determined area moment of inertias as a percentage of the theoretical values are also shown.

As indicated by the graphs in Figures 3.3, 3.4, and 3.5, and summarized in Table 3.1, all experimentally determine values of area moment of inertia are within 13% of the theoretically calculated values. This result supports the assumption that the un-instrumented rebar can be treated as a solid cylinder and that the equations derived for calculating the area moment of inertia for fibre-optic instrumented rebar are adequate for correcting for the altered geometry.

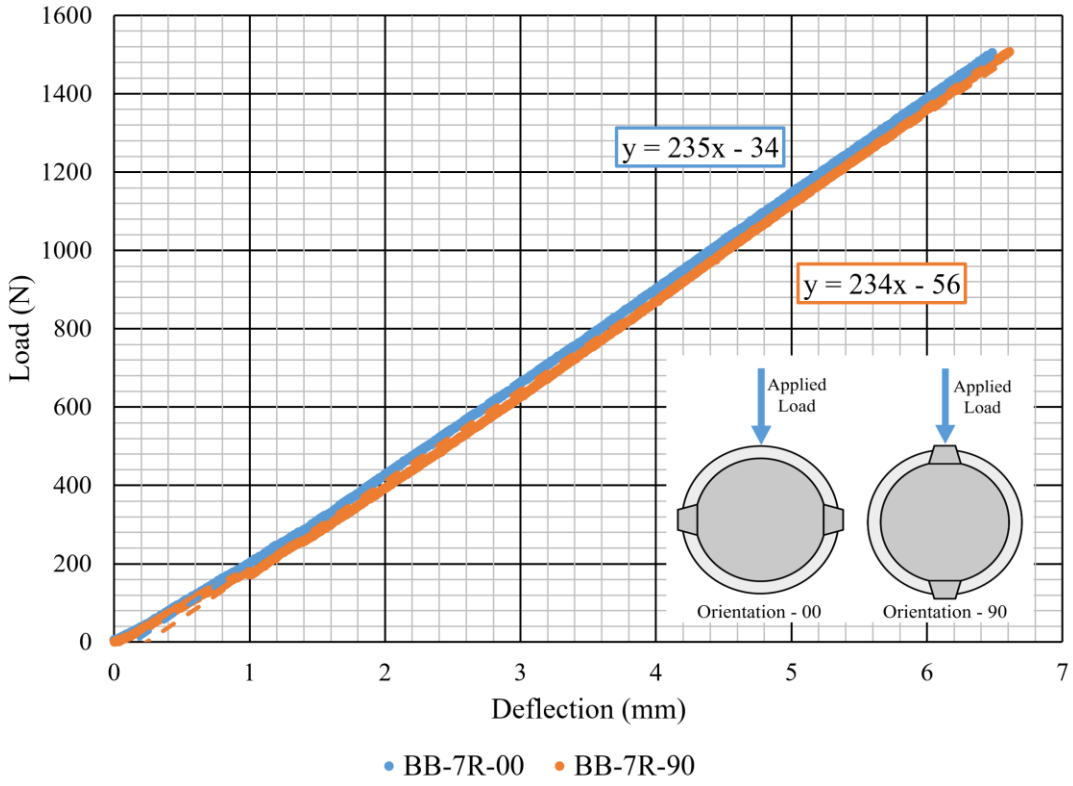

Figure 3.3. Beam bending test results on 22M Grade 400 rebar.

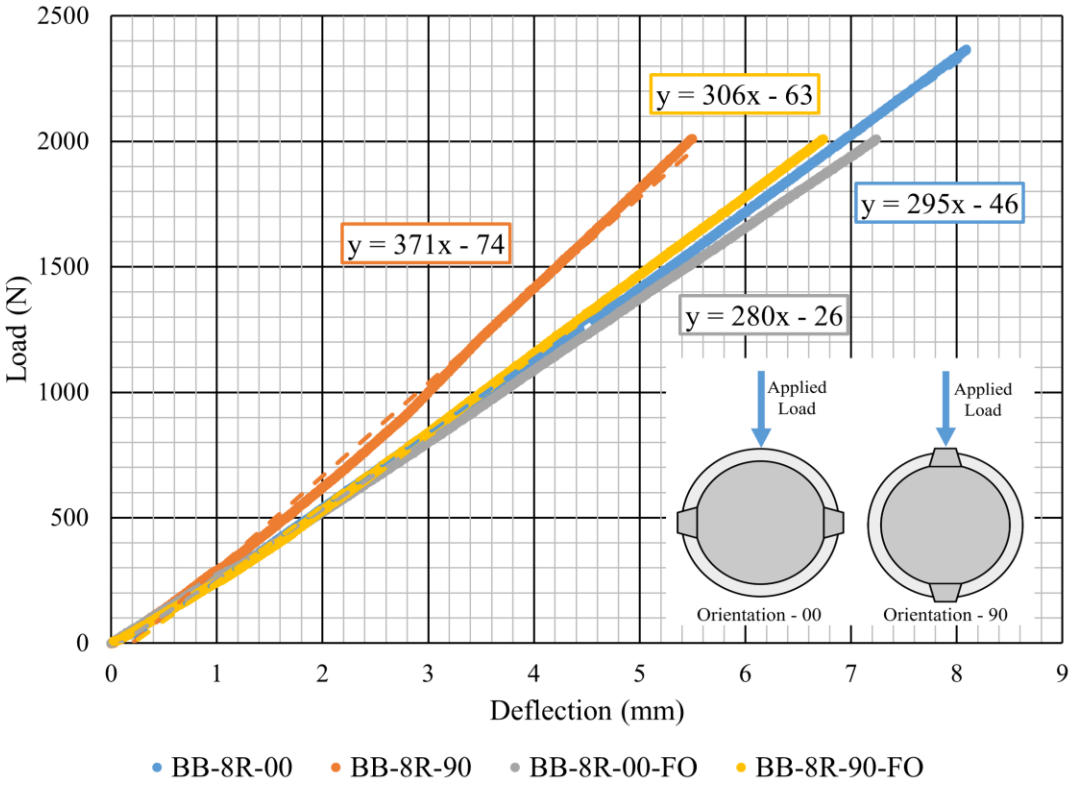

Figure 3.4. Beam bending test results on 25M Grade 400 rebar.

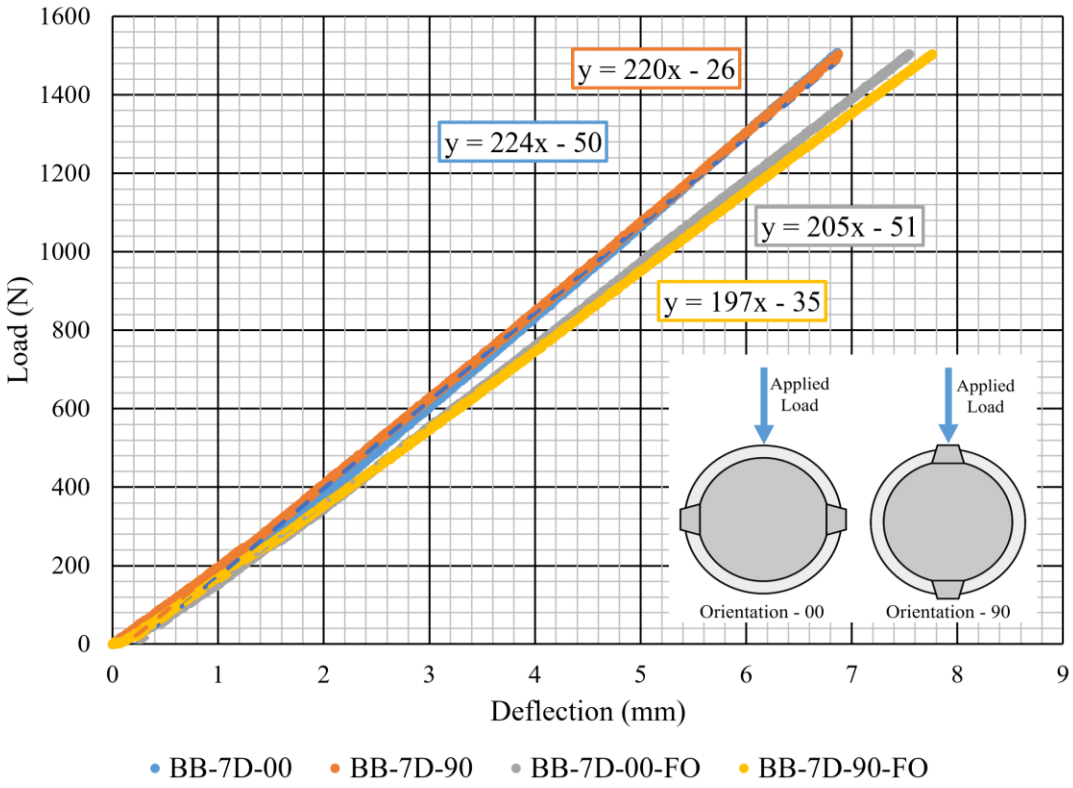

Figure 3.5. Beam bending test results on 22M Grade 500 dywidag.

Table 3.1. Summary of experimental and theoretical area moment of inertias

Rebar Type	Rebar Size	Fibre-Optics?	Theoretical Area Moment of Inertia (m^4)	Experimental			
				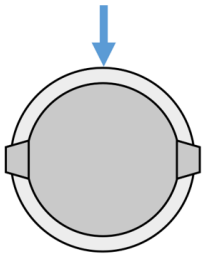 Orientation - 00		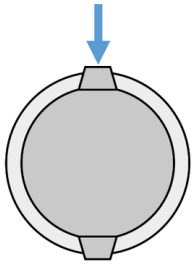 Orientation - 90	
				Area Moment of Inertia (m^4)	As a Percent of Theoretical	Area Moment of Inertia (m^4)	As a Percent of Theoretical
Grade 400 Rebar	22M [#7]	No	9.73E-09	1.01E-08	103%	9.99E-09	103%
	25M [#8]	No	1.41E-08	1.26E-08	90%	1.59E-08	113%
		Yes	1.27E-08	1.19E-08	94%	1.31E-08	103%
Grade 500 Dywidag	22M [#7]	No	9.51E-09	9.55E-09	100%	9.42E-09	99%
		Yes	8.40E-09	8.75E-09	104%	8.43E-09	100%

3.1.3 Analysis Methods of Fibre-optic Instrumented Rebar

Four beam bending tests were conducted on fibre-optic instrumented rebar in a three-groove configuration, as outlined in Section 2. Analysis of the fibre-optic strain data requires application of several equations. Many equations used for analyzing the strain data are listed here, however, a more extensive theoretical derivation can be found in Appendix D and Appendix E.

When viewing a cross-section of a three-groove fibre-optic instrumented rebar, the angle of the first fibre-optic strand from the centroidal axis of the rebar can be calculated with Equation 3.3. This angle is measured counter-clockwise from the centroidal axis and allows for identification of the direction of bending relative to the first fibre-optic strand. Equation 3.3 assumes the fibre-optic strands are all oriented 120 degrees apart around the rebar and are an equivalent distance from the rebar central axis (centre of area ignoring the rib deformations).

$$\theta_{fi} = \text{TAN}^{-1}\left[\frac{1+\frac{\varepsilon_1-\varepsilon_2}{\varepsilon_1-\varepsilon_3}}{\sqrt{3}\left(1-\frac{\varepsilon_1-\varepsilon_2}{\varepsilon_1-\varepsilon_3}\right)}\right]$$

Equation 3.3

Where θ_{fi} = the angle between the first fibre-optic strand and the centroidal axis perpendicular to the bending direction

ε_1 = the strain measured by the first fibre-optic strand at a specific distance along the rebar length

ε_2 = the strain measured by the second fibre-optic strand at a specific distance along the rebar length

ε_3 = the strain measured by the third fibre-optic strand at a specific distance along the rebar length

Once the angle between the first fibre-optic strand and the centroidal axis is known, the distribution of strain across the rebar cross-section can be calculated. The strain is assumed to be linearly distributed across the cross-section of the rebar as in Euler-Bernoulli beam bending theory. The slope of the strain distribution with respect to distance from the centroidal axis, a_{strain}, can be calculated with Equation 3.4. This equation assumes the fibre-optic strands are oriented 120

degrees apart and are embedded 3 mm into the rebar's surface, as was the specification given to the manufacturer.

$$a_{strain} = \frac{\varepsilon_1 - \varepsilon_2}{(0.5 * d_{rebar} - 3mm)\left(sin\,\theta_{fi} - sin\left(\theta_{fi} + 120\right)\right)}$$

Equation 3.4

Where a_{strain} = the slope of the linear strain distribution across the rebar cross-section

d_{rebar} = the minimum diameter of the rebar

$3mm$ = the assumed depth of the fibre-optic within the rebar surface

The axial strain within the rebar (at the centroidal axis) is calculated from Equation 3.5. Once again, this equation assumes all fibre-optic strands are oriented 120 degrees apart.

$$\varepsilon_{Axial} = \frac{\varepsilon_1 + \varepsilon_2 + \varepsilon_3}{3}$$

Equation 3.5

Where ε_{Axial} = the axial strain within the rebar

The strain along the upper edge, or the exterior of the rebar where strain is at a maximum or minimum, can be calculated from Equation 3.6. This upper edge of the rebar has the largest magnitude of compressive strain within the rebar cross-section at any given distance along the rebar length. Since this has the largest compressive strain, it is important to calculate the strain here to ensure no plastic compressive deformation occurs in these tests.

$$\varepsilon_{Upper} = 0.5 * a_{strain}\, d_{rebar} + \varepsilon_{Axial}$$

Equation 3.6

Where ε_{Upper} = the strain at the upper extreme edge of the rebar (the label is arbitrary)

The strain along the lower extreme edge of the rebar is calculated from Equation 3.7. The lower edge of the rebar has the largest magnitude of tensile strain within the rebar cross-section. Once again, calculating the strain here ensures no plastic tensile deformation occurs in these tests.

$$\varepsilon_{Lower} = -0.5 * a_{strain}\, d_{rebar} + \varepsilon_{Axial}$$

Equation 3.7

Where ε_{Lower} = the strain at the lower extreme edge of the rebar (label is arbitrary and simply indicates it is diametrically opposite of the top)

The strain distribution can be used to calculate the internal bending moment within the rebar. The internal bending moment relates the strain exhibited by the rebar with the loads acting on it:

$$M_{internal} = a_{strain} \cdot I_{Rebar} \cdot E_{rebar}$$

Equation 3.8

Where $M_{internal}$ = the internal bending moment within the rebar at a given distance along the rebar

The load being applied to the rebar can be calculated using the fibre-optic strain readings using the internal bending moment. The change in internal bending moment with respect to the change in distance along the rebar is equivalent to the shear force with the rebar. This relation can be seen mathematically in Equation 3.9 and graphically in Figure 3.6.

$$v_{internal} = \frac{\Delta M_{internal}}{\Delta x}$$

Equation 3.9

Where $v_{internal}$ = the shear force within the rebar at a given distance along the rebar

$\frac{\Delta M_{internal}}{\Delta x}$ = change in internal bending moment with respect to the change in distance along the rebar

Since the applied load can be assumed to be a point load near the midspan of the rebar length, the shear force within the rebar will be constant along the length between the midspan and the outer supports. The applied load can be calculated as the difference in this constant shear force, as per Figure 3.6. Alternatively, the applied load can be calculated from the summation of the absolute slopes of the internal bending moments on either side of the applied load. The calculated load will then be compared against the measured load to determine the efficacy of this method.

The deflection of the rebar midspan can also be calculated using the fibre-optic instrumentation. The derivation is long and the solution involves iterating through several equations to calculate the position of the rebar. A full explanation of this analysis is presented in Appendix E. At a basic

level, the position of the rebar's centroidal axis is calculated by determining the curvature of the rebar at thousands of points based on the fibre-optic strain data and then iteratively summing those curves together.

The beam bending test accurately recorded the deflection of the midspan of the beam and the fibre-optic data was also used to calculate this deflection. The two values were compared to determine the accuracy of calculating lateral displacements of rebar from fibre-optic strain measurements.

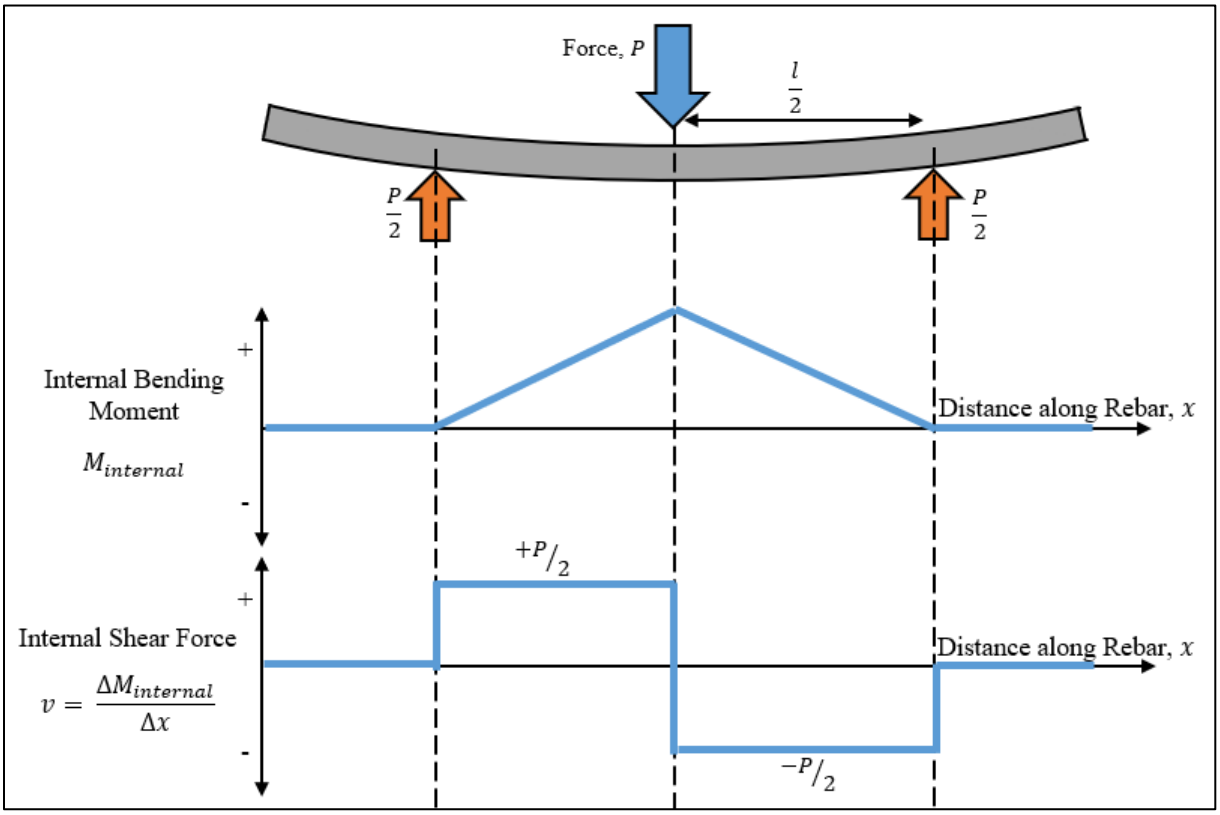

Figure 3.6. Relation between internal bending moment and shear force within rebar.

3.1.4 Results of Fibre-optic Instrumented Rebar

During beam bending tests on fibre-optic instrumented rebar, strain was measured at one second intervals throughout each test. This resulted in approximately 6000 strain measurements taken per second. Each second of strain measurement had a corresponding applied load and measured deflection from the loading machine.

The fibre-optic strain measurements were analyzed for all tests at all measurement times. However, only a single measurement interval for beam bending test BB-8R-00-FO are presented as an example. Similar results were obtained for all tests.

The strain measurements for test BB-8R-00-FO are plotted in Figure 3.7. At the measurement interval displayed, the sample had an applied load of 1995 N. The near-zero strain of Strand 1 indicates the first-pass of the fibre-optic strand is near the neutral bending axis which agrees with observations made during testing. The way Strand 2 and Strand 3 decrease and increase linearly toward the midspan of the sample agrees with what is expected from Euler-Bernoulli beam bending theory.

Knowing the strains at each incremental distance and the angle of Strand 1 from the centroidal axis, the strain at the upper and lower edges of the rebar and at the centroidal axis can be calculated. These strains are shown for test BB-8R-00-FO in Figure 3.8.

Tensile tests, included in Appendix B, suggest the 25M (#8) Grade 400 (60) rebar will yield at roughly 2500 micro-strain. According to Figure 3.8, the maximum strain the rebar exhibited was roughly 1500 micro-strain, which is well under the yield strain of the rebar. These results suggest the rebar behaviour was entirely linear elastic during the beam bending tests, as intended. Similar results were found in all tests on fibre-optic instrumented rebar.

Ideally, the axial strain in a beam bending test would be zero since there should be no axial force in the rebar. Figure 3.8 shows that there is some amount of axial strain within the rebar. This could suggest the test setup is imparting an axial force either due to friction at the loading platens, error in the strain measured by the fibre-optics, or the fibre-optic strands are not perfectly 120 degrees apart.

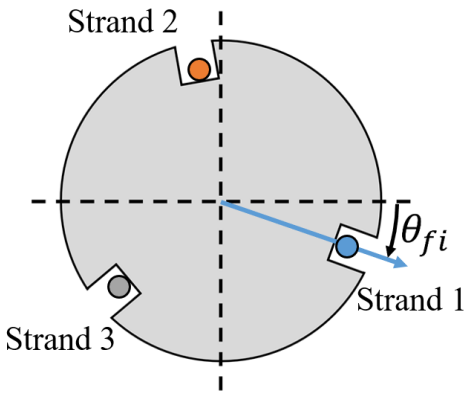

a) Cross-section A-A'

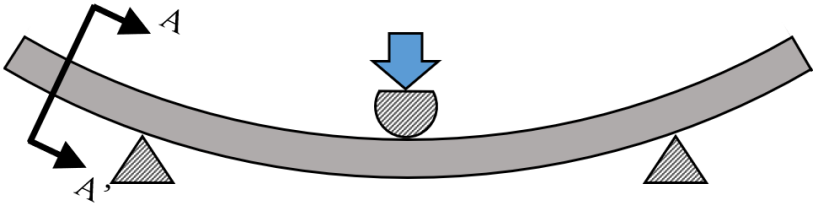

b) Long-section

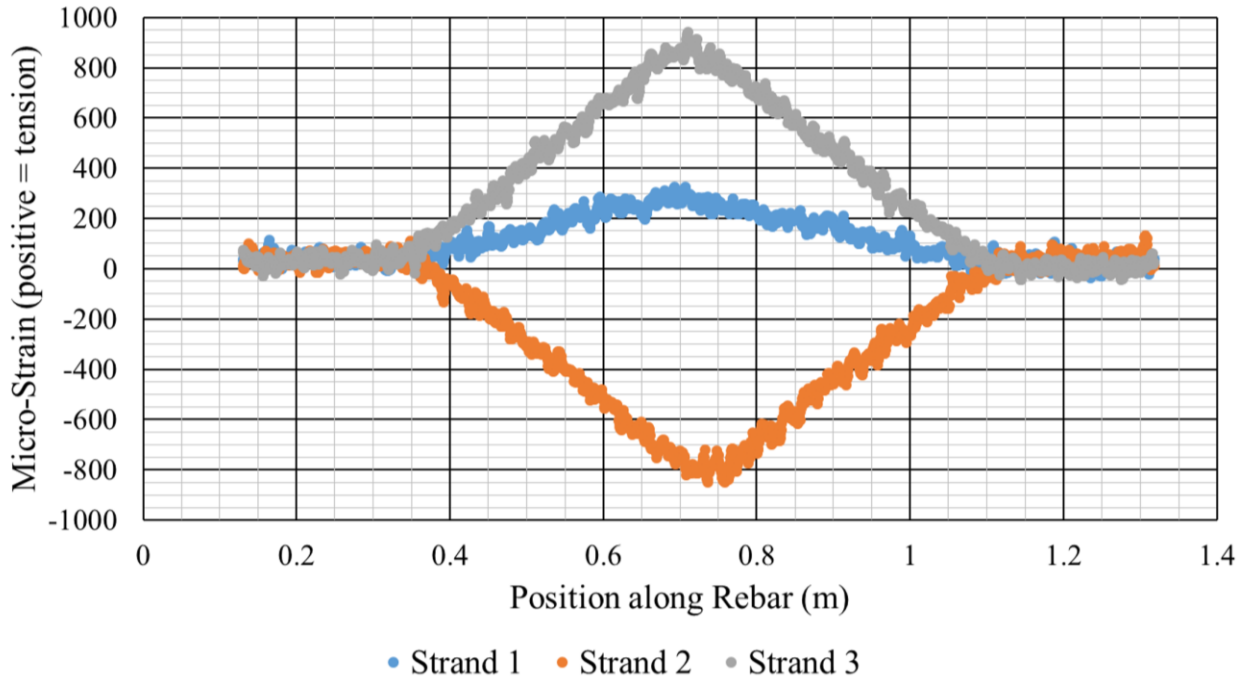

c) Fibre-optic Strain Readings

Figure 3.7. Beam bending test BB-8R-00-FO with 1995 N applied. Figure shows a) the cross-section of instrumented rebar, b) the long-section view of the beam bending test, and c) the strain measured from the fibre-optic instrumentation.

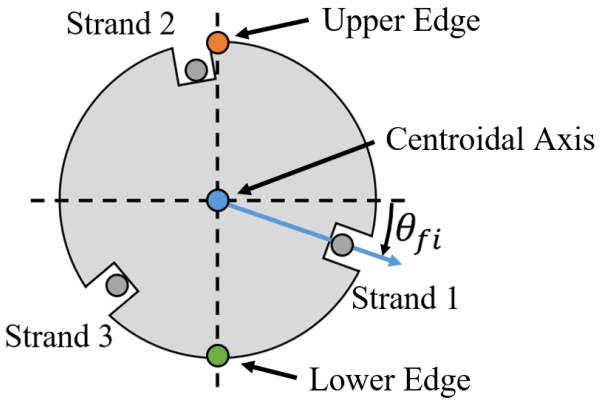

a) Cross-section A-A'

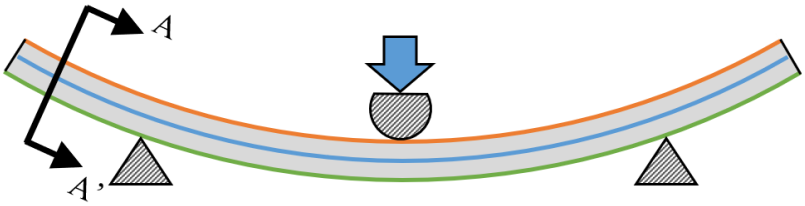

b) Long-section

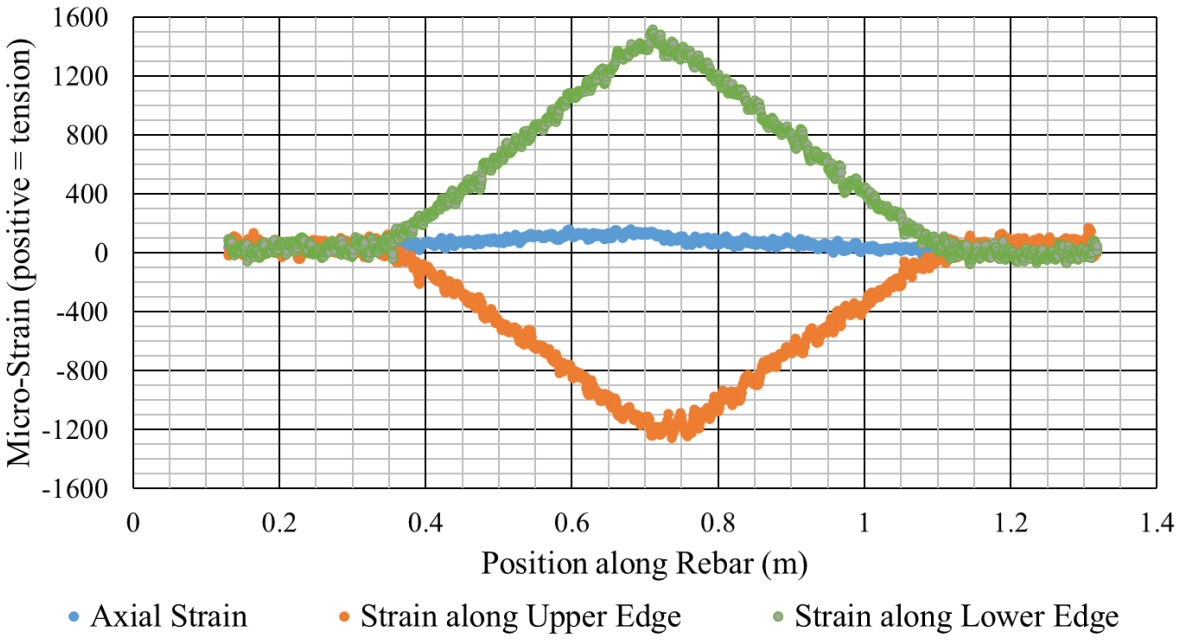

c) Fibre-optic Strain Readings

Figure 3.8. Beam bending test BB-8R-00-FO with 1995 N applied. Figure shows a) the cross-section of instrumented rebar, b) the long-section view of the beam bending test, and c) the strain calculated from the fibre-optic instrumentation.

The internal bending moment was calculated using Equation 3.8 for all fibre-optic instrumented beam bending tests. The theoretical area moment of inertia and the assumed Young's modulus of 200 GPa was used to calculate the internal bending moments along the rebar length. The internal bending moment results for test BB-8R-00-FO at an applied load of 1995 N are shown in Figure 3.9. All beam bending tests on fibre-optic instrumented rebar exhibited a similar distribution of internal bending moments. This distribution matched the expected internal bending moment distribution, shown in Figure 3.6, very well.

A line was fitted to each linear segment of the bending moment diagram. The intersection of these lines was assumed to be the mid-point of the rebar sample where the load was applied. The intersection of the lines with the 0 Nm bending moment axis was assumed to be where the rebar was supported. The slope of the lines should be equivalent to the shear force within the rebar, according to Equation 3.9. For example, addition of the absolute values of the linear slopes yields about 1620 N for test BB-8R-00-FO shown Figure 3.9.

As discussed previously, the strains calculated within the rebar can be used to calculate the relative position of the rebar's centroidal axis. Since all bending should occur in the same direction, a 2-dimensional position analysis was used for calculating the position of the rebar's centroidal axis. Figure 3.10 shows the position of the rebar axis for test BB-8R-00-FO with 1995 N applied at the midspan. The sample midspan and outer supports as approximated from Figure 3.9 are also shown. The deflection of the midspan was calculated as the difference in vertical position of the midspan relative to the outer supports.

In these tests, the position of the midspan and outer supports was approximated from Figure 3.9. The orientation of the rebar was iteratively solved by changing the assumed orientation of the rebar in 2D space until the outer two supports had the same vertical position. Further information and discussion about calculating the centroidal axis position of the rebar from the fibre-optic strain measurements can be found in Appendix E.

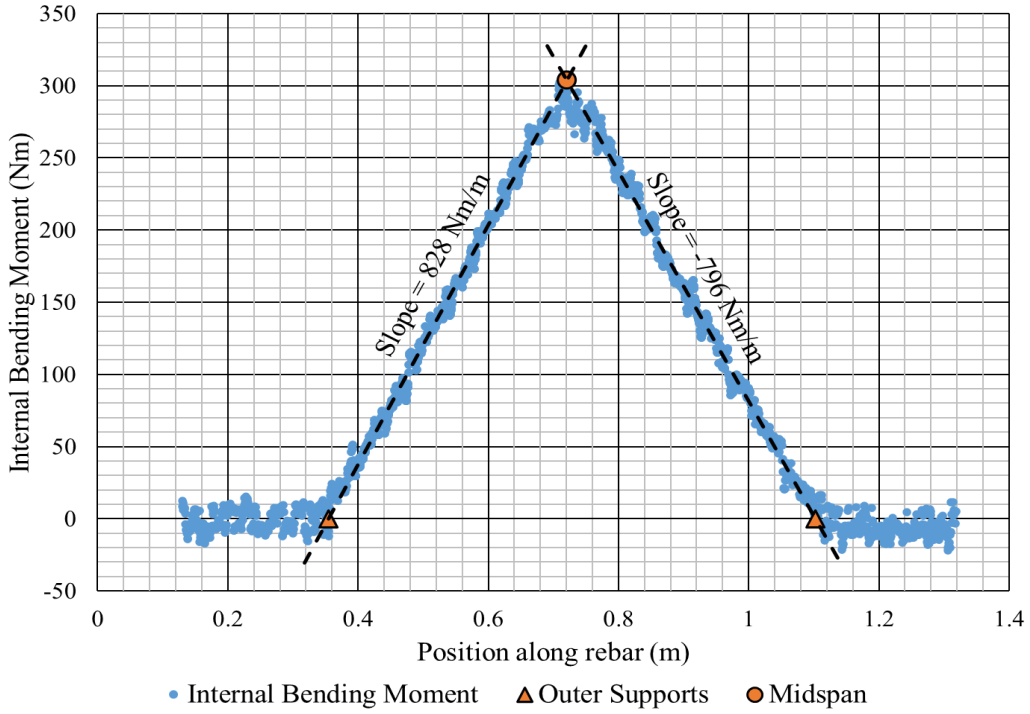

Figure 3.9. Internal bending moment of rebar calculated from fibre-optic instrumentation in beam bending test BB-8R-00-FO with 1995 N applied.

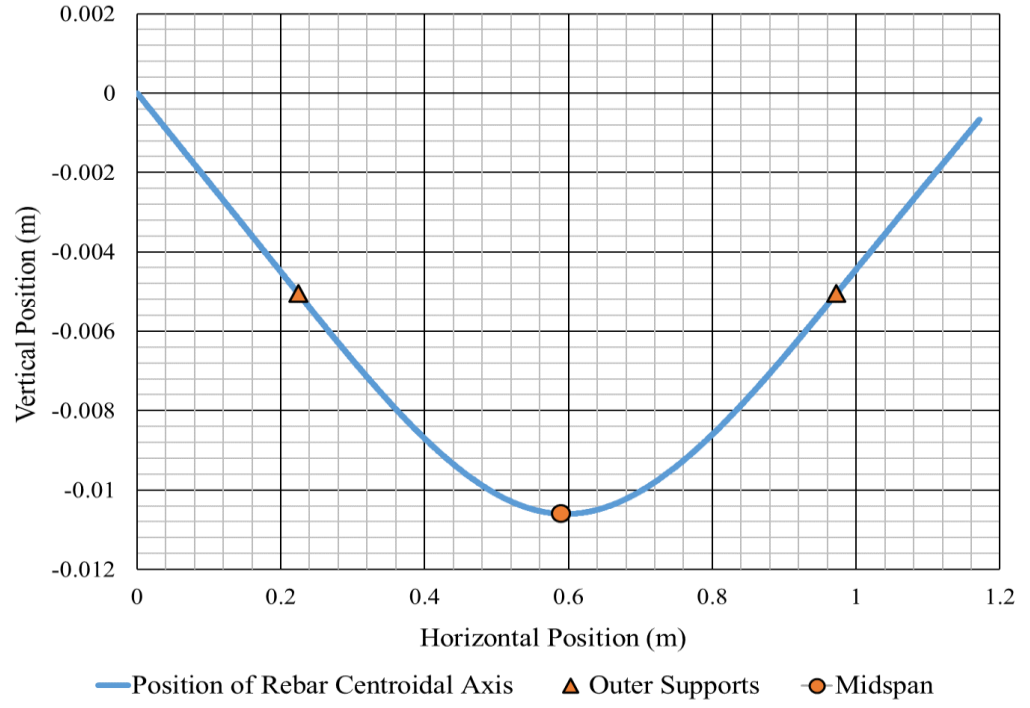

Figure 3.10. Position of the rebar's centroidal axis calculated from fibre-optic instrumentation in beam bending test BB-8R-00-FO with 1995 N applied.

The analysis conducted for test BB-8R-00-FO at 1995 N applied load was also conducted for all beam bending tests on fibre-optic instrumented rebar at every second reading (2 seconds). All tests exhibited similar qualitative behaviour as BB-8R-00-FO above.

The shear effects calculated from the internal bending moment diagrams were plotted against the corresponding applied load in Figure 3.11. All tests exhibit a strong linear correlation between the fibre-optic calculated load and the measured load. However, all tests appear to under-estimate the load using the fibre-optic instrumentation.

The deflection of the midspan of each sample relative to the outer supports was also calculated for all tests at every second measurement (2 seconds). The deflection calculated from the fibre-optic instrumentation is plotted against the deflection measured by the loading frame in Figure 3.12 for all tests on fibre-optic instrumented rebar. Once again, the plot exhibits a strongly linear correlation for all tests but under-estimates the calculated deflection.

The instrumentation exhibited a reasonable accuracy in determining the strain behaviour, internal bending moment, shear force, and relative axial position along the entire length of the rebar in linear elastic bending conditions. The distributed optical sensing technology is relatively new and the results of this testing are very encouraging.

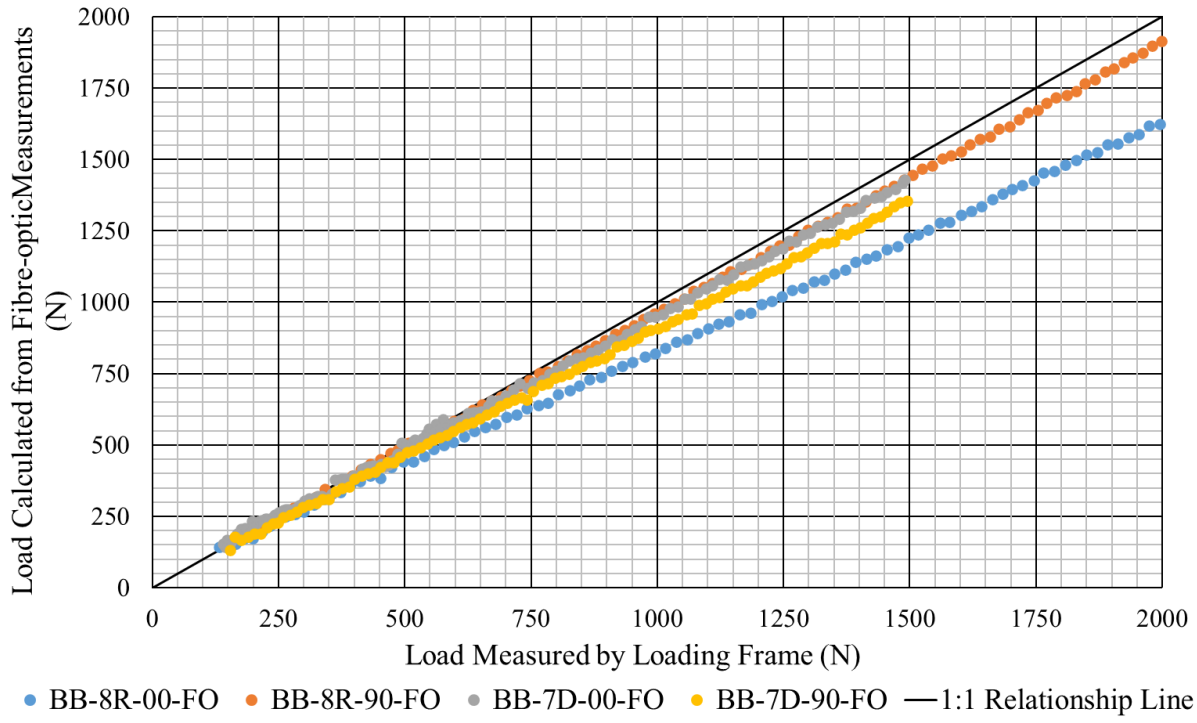

Figure 3.11. Load calculated from fibre-optic instrumentation vs load measured by loading frame for beam bending tests.

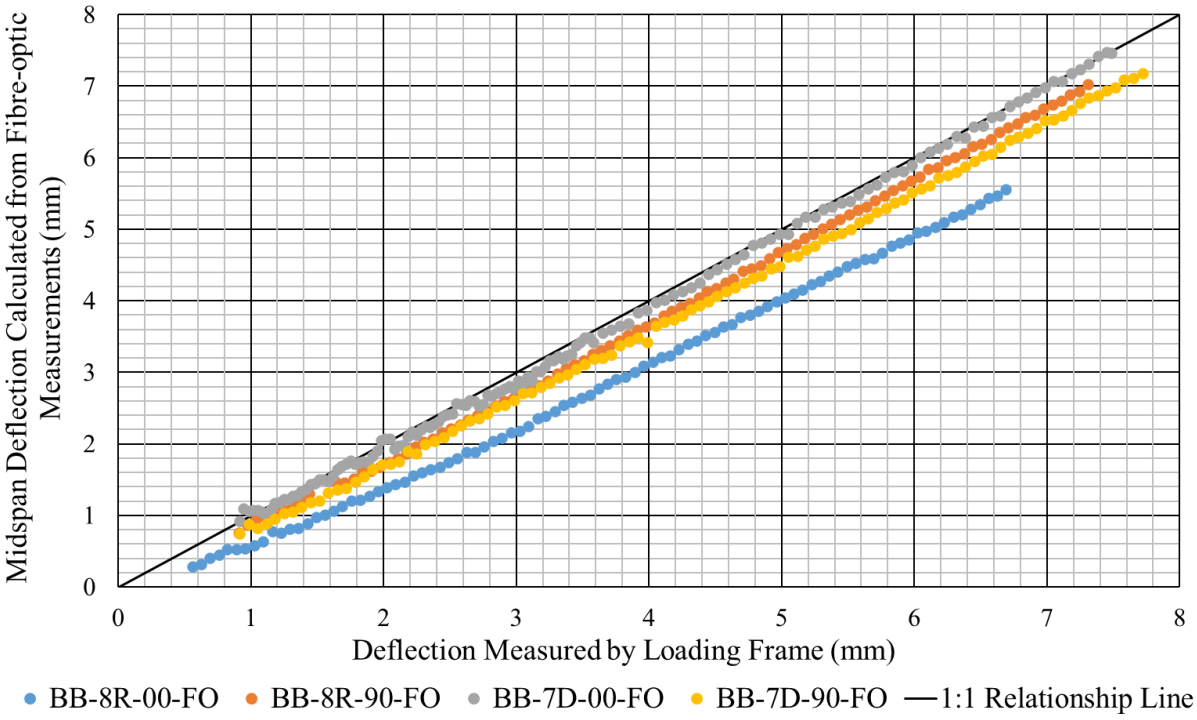

Figure 3.12. Deflection calculated from fibre-optic instrumentation vs deflection measured by loading frame for beam bending tests.

3.2 Double Shear Tests

Double shear tests were conducted with the primary goal of determining the relation between shear behaviour of rebar and the aperture of the shear plane. The aperture of the shear plane was varied from 2 mm to 40 mm in order to investigate its effect on the yield load, displacement at yield, ultimate load, and displacement at ultimate load of the various rebar types being investigated. These double shear tests also provided the opportunity to evaluate the fibre-optic instrumented rebar when crossing a shear plane.

Double shear tests have previously been conducted at the University of Saskatchewan by Beneteau et al. (2019). The tests conducted in this research program were similar except for the variation in gaps between the steel pipes used in this project to simulate shear plane apertures.

3.2.1 Experimental Design and Theory

Rebar samples, both instrumented and un-instrumented, were tested by grouting them into pipes, securing the outer lengths, and applying a lateral load to the centre segment. A cross-section of a prepared rebar sample grouted into three sections of steel pipe is shown in Figure 3.13.

The pipe used was schedule 160 pipe. Previous testing has suggested this size pipe is strong enough to resist deformation throughout these tests and is sufficiently close to being completely rigid. Schedule 160 pipe has an outer diameter of 48.3 mm and an inner diameter of 34.0 mm. This inner diameter approximately matches the hole diameter of rebar installed in Saskatoon area potash mines. Each pipe segment was 406 mm long.

The pipe segments were separated with a thick rubber spacer which had approximately the same outer diameter and a slightly smaller inner diameter than the pipe. The thickness of these rubber spacers was varied from 2 mm to 40 mm to control the shear plane aperture during sample preparation. The rubber spacers were removed prior to testing.

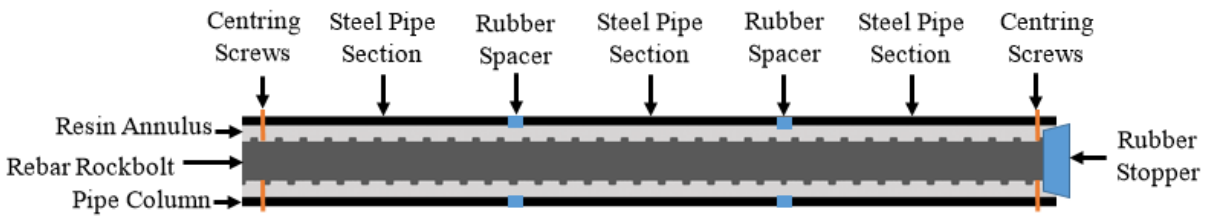

Figure 3.13. Double shear sample preparation.

A Ground Lok resin from Dywidag Systems International (DSI) was used to install the rebar into the pipe. This is a two-part pourable polyester resin with an advertised UCS of 83 MPa (DSI, 2015). However, UCS testing, described in Appendix A, suggests the resin has a strength of roughly 31 MPa. The discrepancy in strength may be due to incomplete mixing of the two components or other issues with sample preparation in the testing described in Appendix A.

To create the testing samples, the steel pipes and rubber spacers were secured against a board to keep them concentrically aligned and in place. The pipes and spacers were held vertically and a rubber stopper was pushed into the bottom end of the pipe column to prevent resin from leaking out the bottom. After pouring the resin into the pipe column, the rebar sample was pushed into the resin and pipe until it hit the rubber stopper. Three centring screws at either end of the pipe column were then tightened to centre the rebar within the pipe. The resin was held stationary under room temperature and humidity to harden for at least one day before testing.

A Tinius Olsen loading frame in the USask Geological Engineering Laboratory was used for most double shear tests. A diagram of the test setup is shown in Figure 3.14. Steel loading platens were placed in line with the outer pipe segments to support them. These platens had the same curvature as the outside of the pipe to ensure they cradled the pipe concentrically.

The ends of the outer pipes were secured against upward deflection by clamping them to the loading platform. The initial clamping force was kept low in order to prevent instigating any initial bending moments in the sample. LVDTs were placed on the centre platens, near each gap, to measure the displacement of the centre pipe segment at a rate of 1 Hz throughout the test. The load

being applied to the central rebar segment was recorded at a rate of 1 Hz using a calibrated load cell (Figure 3.14).

The results of the double shear tests were primarily analyzed by plotting the load against the displacement of the centre pipe. It should be noted that the applied load is distributed between the two shear planes. In analyzing the test results, the applied load was assumed to be evenly distributed between the two planes and has been divided by two in order to determine the shear load on each shear plane. Similarly, the displacement was taken as the average displacement of the two LVDTs at either end of the central loading platen.

The yield point of each test was identified as the point in the load-displacement plot where the behaviour was no longer linear and behaved less stiff by exhibiting a lower slope. The yield loads, ultimate loads, and corresponding displacements of the tests were used to identify the effect that different shear plane apertures had on the rebar behaviour.

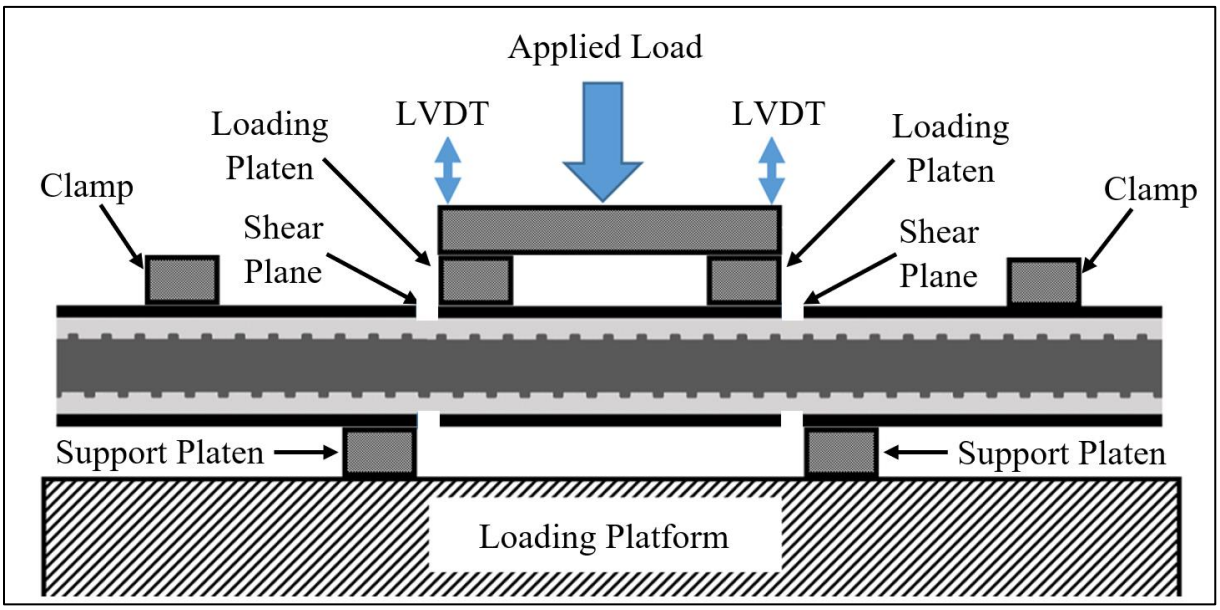

Figure 3.14. Double shear test setup.

3.2.2 Double Shear Test Results

In total, 22 double shear tests were conducted on both fibre-optic instrumented rebar and rebar without any strain instrumentation. The results of these tests are presented and explained in this section. Additional test results can be found in Appendix J. The tests were numbered using the following system:

Ex. DS-8R-305-FO

DS	- Indicates a double shear test
7 or 8	- Indicates the rebar size in imperial nomenclature: 22M (#7) or 25M (#8)
R or D	- Grade 400 (60) rebar or Grade 500 (75) dywidag threadbar
1, 2, or 3	- Arbitrary number used for replicates in a given test series
05, 15, 20, etc.	- Size of gaps between pipe segments in mm rounded to the nearest 5 mm
FO	- Indicates tests on fibre-optic instrumented rebar

Double shear tests on 22M (#7) Grade 400 (Grade 60) rebar were conducted first. Five tests on non-instrumented rebar were conducted with various shear plane apertures from 5 mm to 40 mm. The load vs average displacement plots are shown in Figure 3.15. The load per shear plane was plotted on the vertical axis and is exactly one half of the true applied load. As discussed previously, this is approximately the amount of load acting on each shear plane. The average shear plane displacement was calculated by averaging the displacements measured by the two LVDTs.

The results of the double shear tests on 25M (#8) Grade 400 (Grade 60) rebar are plotted in Figure 3.16. Once again, it is important to note the load per shear plane in this figure is one half of the true applied load. A total of 12 double shear tests were conducted using this rebar type, two of which were instrumented with fibre-optic instrumentation in a three-groove configuration. The shear plane apertures ranged from 2 mm to 40 mm. All tests were completed successfully, however the LVDTs reached their stroke limit during test DS-8R-240. As a result, displacement data beyond 30 mm is unavailable for this test.

Five double shear tests were conducted on 22M (#7) Grade 500 (Grade 75) dywidag threadbar. Three of these tests were performed on rebar instrumented with fibre-optics in the three-groove

configuration. The load vs displacement plot of these tests can be found in Figure 3.17, where the load per shear plane is, again, half the applied load and the shear displacement is the average of the two LVDT measurements.

Figure 3.18 shows the samples from tests DS-7D-120-FO and DS-7D-140-FO after testing. These two tests failed at very low loads. Visual inspection of the samples did not reveal any specific reasons for the anomalous behaviour. The cause of the premature failure is likely related to the fibre-optic instrumentation since this reduces the cross-sectional area of the rebar. The ultimate load and displacement results for these two tests were discarded for being erroneous.

All tests for all rebar types exhibit a similar behaviour: an initially stiff load-displacement relation that transitions into a less stiff behaviour at relatively low displacement. This transition is where the rebar steel yields and the strain becomes plastic.

The yield point for each test was estimated and these points are shown in Figure 3.15, Figure 3.16, and Figure 3.17. The behaviour of the samples is roughly linear on either side of this yield point. In tests with a smaller gap aperture, such as test DS-7R-105, the transition from linear elastic to plastic behaviour appears gradual and is much harder to distinguish. The behaviour of small aperture tests is more “curved” instead of bilinear like tests with larger shear plane apertures.

Each test reached some ultimate load after which the load quickly decreased and the rebar failed. The ultimate load each test reached is marked in Figure 3.15, Figure 3.16, and Figure 3.17. All tests failed on one shear plane with the exception of tests DS-7R-105, DS-8R-102, DS-8R-205, and DS-8R-140 which failed on both shear planes.

Generally, the ultimate load of double shear tests on fibre-optic instrumented samples were noticeably lower than tests on un-instrumented samples. This was likely due to the reduced cross-sectional area caused by the fibre-optic instrumentation. Double shear tests DS-8R-305-FO, DS-8R-320-FO, and DS-7D-105-FO had ultimate loads reasonably close to those of un-instrumented samples and were considered a valid result for the rebar ultimate shear loads. Double shear tests DS-7D-120-FO and DS-7D-140-FO had ultimate loads that were significantly lower than other

double shear tests on 22M (#7) Grade 500 (Grade 60) dywidags. These two tests appeared to have failed prematurely and the ultimate shear loads were considered erroneous.

The load per shear plane and corresponding shear displacement of each test at its yield load and ultimate load are listed in Table 3.2. These values correspond to the yield and ultimate points indicated in Figure 3.15, Figure 3.16, and Figure 3.17.

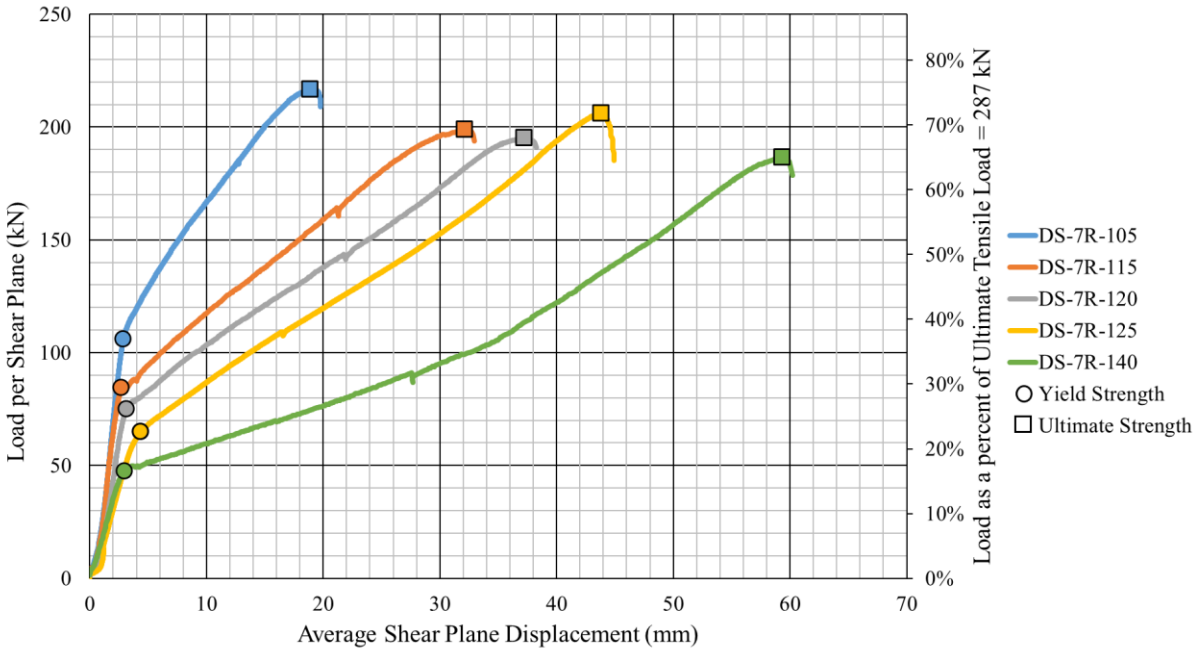

Figure 3.15. Applied load per shear plane vs average shear plane displacement from LVDTs for doubled shear tests on 22M Grade 400 rebar.

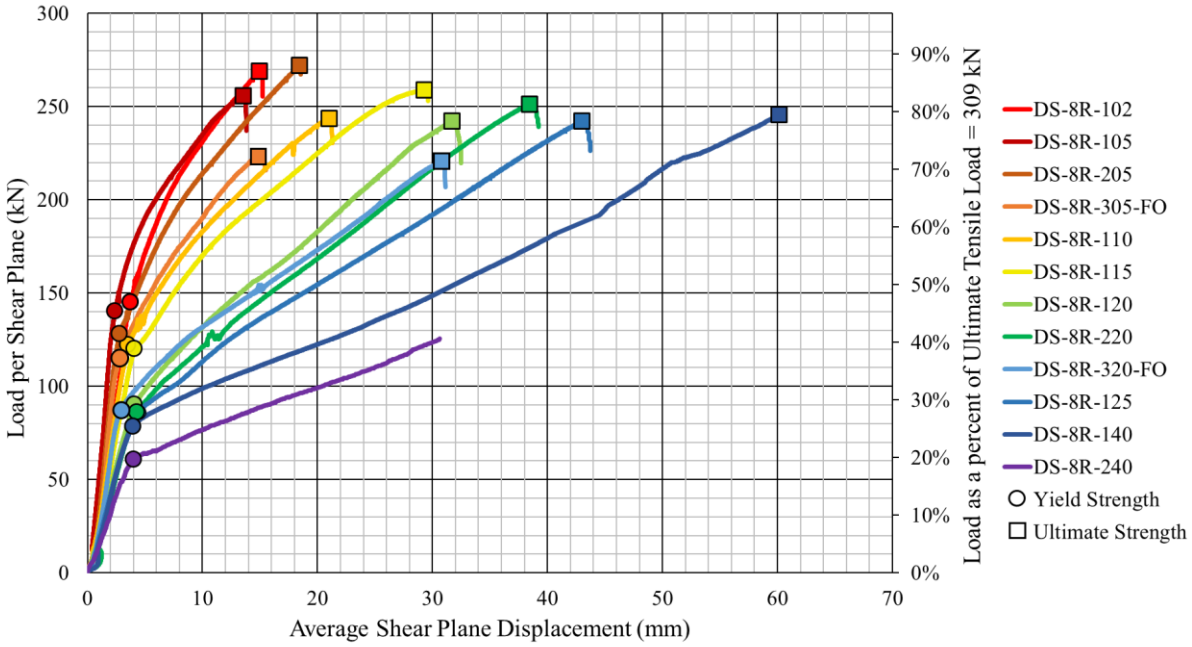

Figure 3.16. Applied load per shear plane vs average shear plane displacement from LVDTs for doubled shear tests on 25M Grade 400 rebar.

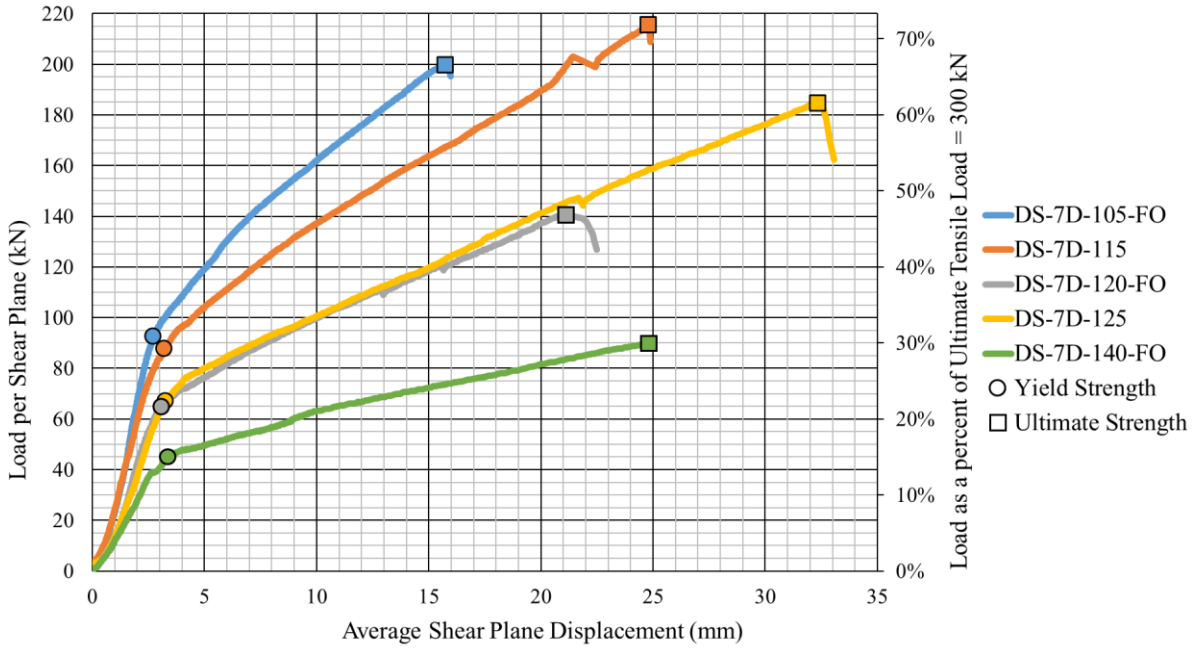

Figure 3.17. Applied load per shear plane vs average shear plane displacement from LVDTs for double shear tests on 22M Grade 500 dywidag.

Figure 3.18. Sample DS-7D-140-FO (top) after testing showing shear displacement of centre pipe segment relative to outer segments and one half of sample DS-7D-120-FO (bottom) after testing and cut longitudinally.

Table 3.2. Summary of yield and ultimate points of double shear tests.

Rebar Type	Sample	Fibre-optic Instrumented? three-groove configuration	Average Shear Plane Aperture (mm)	Yield Load per shear plane (kN)	Average Shear Displacement at Yield Load (mm)	Ultimate Load per shear plane (kN)	Average Shear Displacement at Ultimate Load (mm)
22M (#7) Grade 400 (60) Rebar	DS-7R-105	No	5.5	106	2.9	217	18.9
	DS-7R-115	No	16.4	84	2.7	199	32.1
	DS-7R-120	No	20.3	75	3.1	195	37.2
	DS-7R-125	No	25.1	65	4.4	206	43.8
	DS-7R-140	No	39.7	48	3.0	186	59.4
25M (#8) Grade 400 (60) Rebar	DS-8R-102	No	2.2	145	3.8	269	15.0
	DS-8R-105	No	5.5	140	2.4	255	13.6
	DS-8R-205	No	4.8	128	2.8	272	18.5
	DS-8R-305-FO	Yes	5.0	115	2.8	223	14.9
	DS-8R-110	No	10.7	122	3.6	243	21.1
	DS-8R-115	No	15.7	120	4.1	259	29.3
	DS-8R-120	No	20.0	90	4.1	242	31.7
	DS-8R-220	No	21.2	86	4.3	251	38.5
	DS-8R-320-FO	Yes	20.0	88	3.0	221	30.9
	DS-8R-125	No	25.3	86	4.5	242	43.1
	DS-8R-140	No	40.0	78	4.0	246	60.2
	DS-8R-240	No	40.7	61	4.0	237	-
22M (#7) Grade 500 (75) Dywidag	DS-7D-105-FO	Yes	4.8	93	2.7	199	15.8
	DS-7R-115	No	14.7	88	3.2	215	24.8
	DS-7D-120-FO	Yes	20.2	65	3.1	141	21.1
	DS-7D-125	No	24.9	67	3.3	184	32.4
	DS-7D-140-FO	Yes	40.8	45	3.4	90	24.7

Figure 3.19, Figure 3.20, and Figure 3.21 show the yield load and ultimate load for all specimens plotted against their average shear plane aperture. The test results for 22M Grade 400 rebar, 25M Grade 400 rebar, and 22M Grade 500 dywidag are plotted in the figures, respectively. Linear trendlines were generated for all data sets using the least squares method and the equation for these best-fit lines, as well as their R^2 values, are shown. The linear trendlines were generated for the ultimate loads and yield loads for each rebar type tested.

The fibre-optic instrumented sample results for 25M Grade 400 rebar were noticeably different than results for un-instrumented samples so the fibre-optic instrumented results were not used in generating the linear trendlines in Figure 3.20. However, due to the limited data for 22M Grade 500 dywidag, some results from fibre-optic instrumented samples were used to generate the linear trendlines in Figure 3.21.

The load at which each sample yields is inversely related to the size of the gap between the pipes. The ultimate load also has a negative correlation with the aperture size, but to a much lesser extent. These relations can be seen for all rebar types.

The average shear displacements are plotted against the average shear plane aperture for double shear tests on 22M Grade 400 rebar in Figure 3.22, 25M Grade 400 rebar in Figure 3.23, and 22M Grade 500 dywidag in Figure 3.24. Once again linear trendlines are shown on the three plots along with their equations and R^2 values.

The linear trendlines were generated without the data from fibre-optic instrumented samples for double shear tests on 25M Grade 400 rebar in Figure 3.23 since tests failed at noticeably lower loads. Linear trendlines were generated using non-erroneous test results from fibre-optic instrumented 22M Grade 500 dywidags in Figure 3.24. The fibre-optic data points were used in generating the linear trendlines simply because of the limited data for double shear tests on 22M Grade 500 dywidag.

The displacement at which yield occurs appears independent of the shear plane aperture. The rebar appears to yield at very low displacements for all shear plane apertures and rebar types. The

displacement at ultimate load increases drastically with an increase in shear plane aperture. The shear plane aperture has a large effect on the ultimate shear displacement that a rebar rock bolt can withstand before failing.

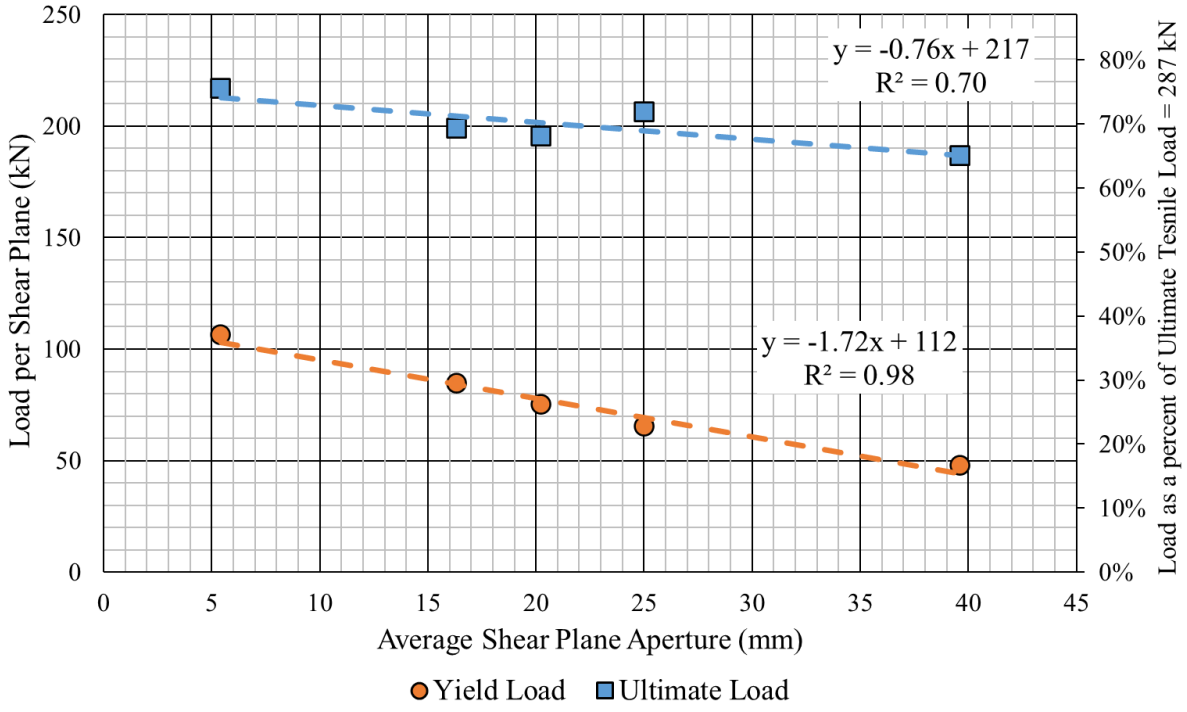

Figure 3.19. Load per shear plane vs average shear plane aperture at yield point and ultimate load for double shear tests on 22M Grade 400 rebar.

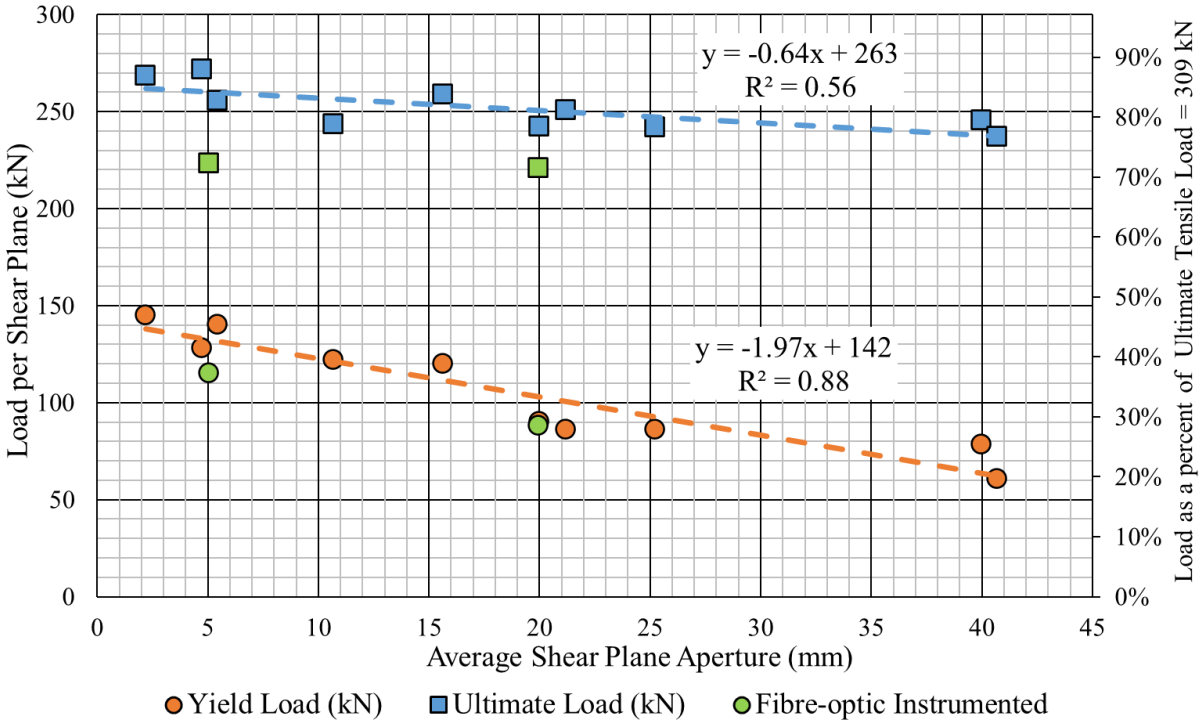

Figure 3.20. Load per shear plane vs average shear plane aperture at yield point and ultimate load for double shear tests on 25M Grade 400 rebar.

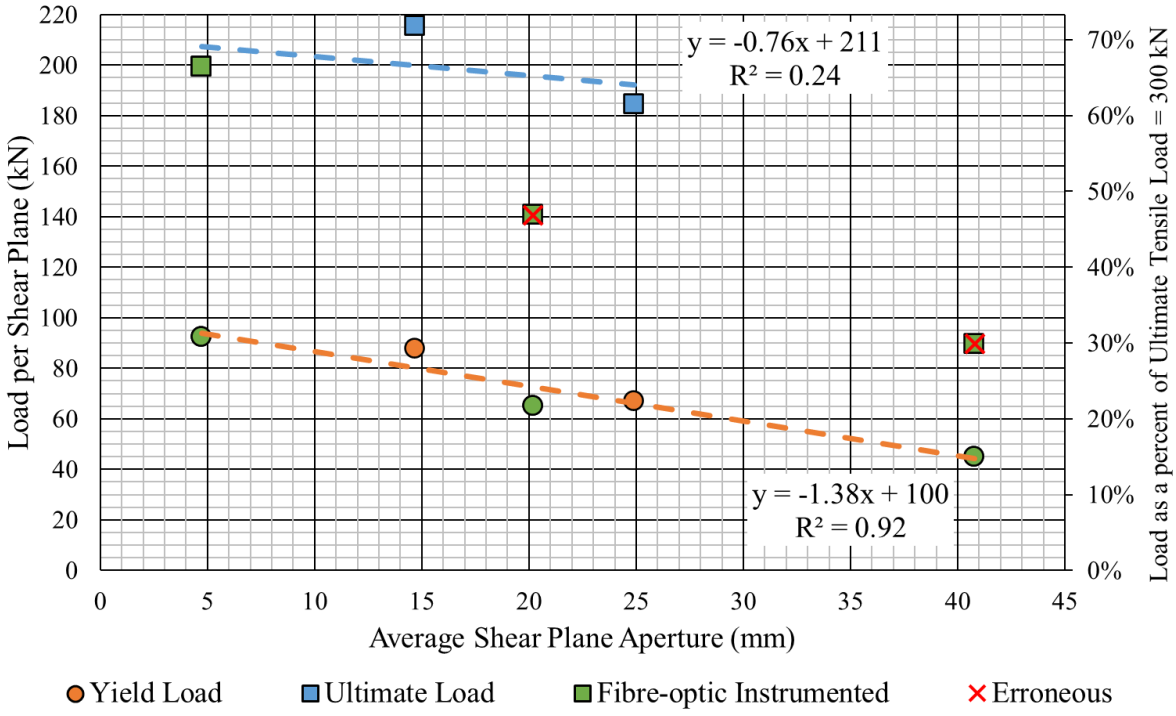

Figure 3.21. Load per shear plane vs average shear plane aperture at yield point and ultimate load for double shear tests on 22M Grade 500 dywidag.

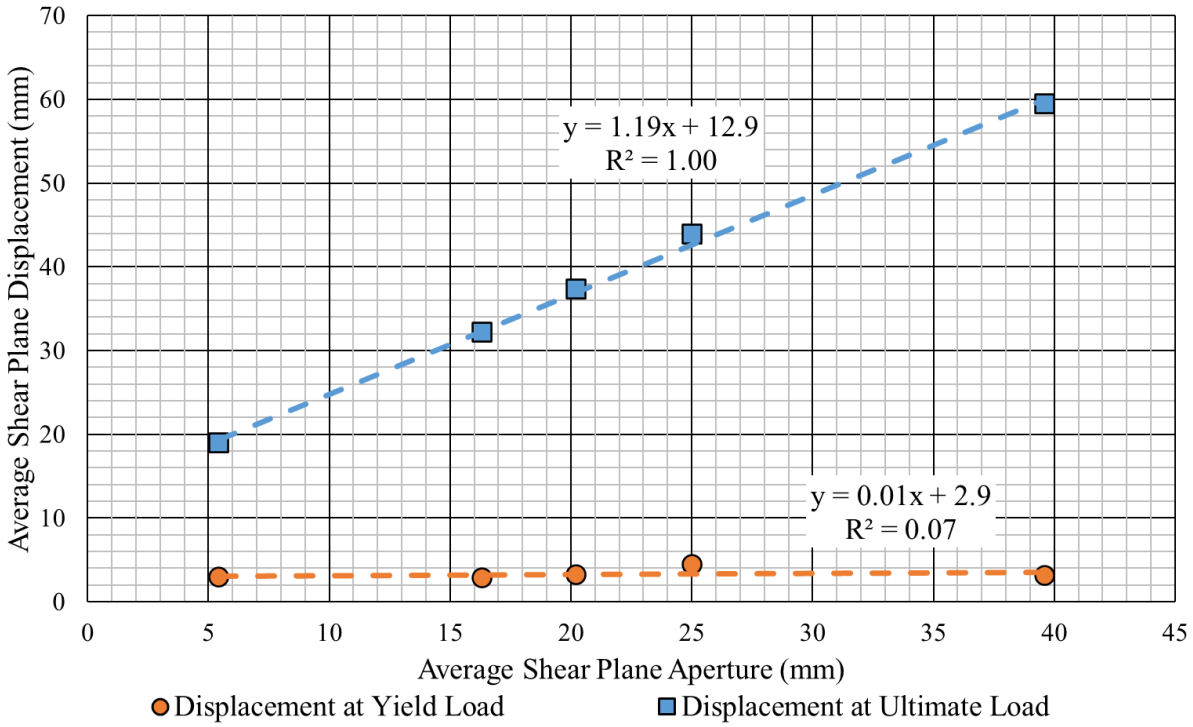

Figure 3.22. Average displacement vs average shear plane aperture at yield point and ultimate load for double shear tests on 22M Grade 400 rebar.

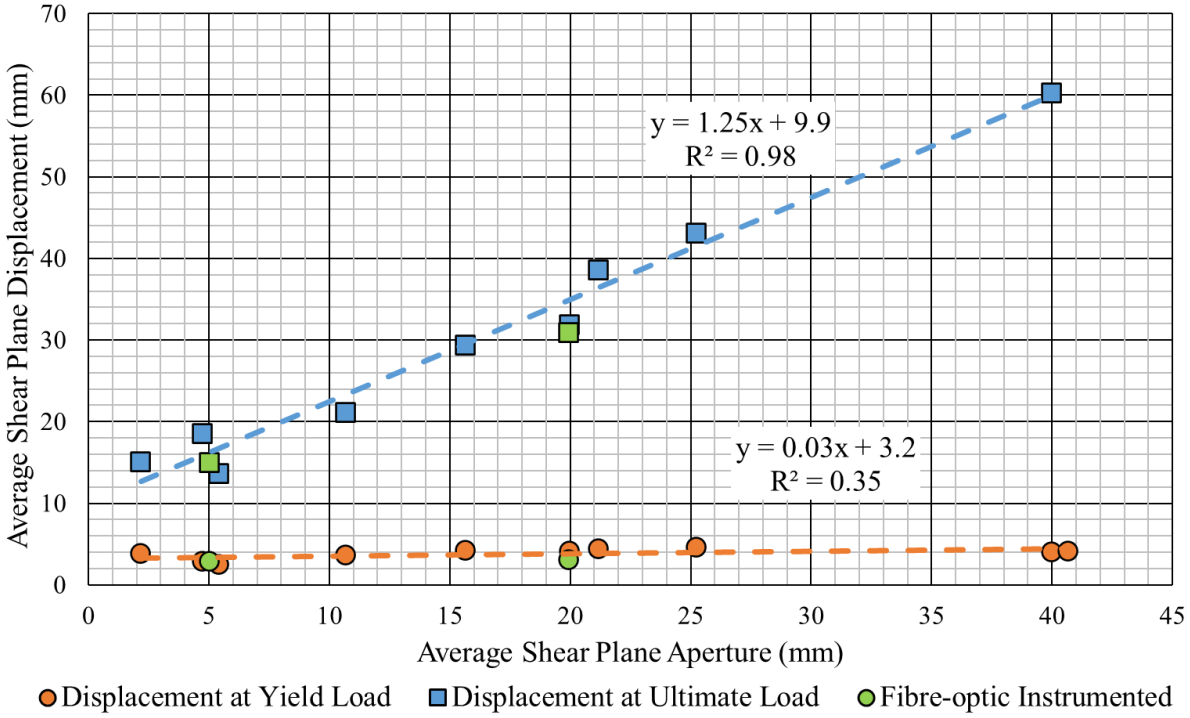

Figure 3.23. Average displacement vs average shear plane aperture at yield point and ultimate load for double shear tests on 25M Grade 400 rebar.

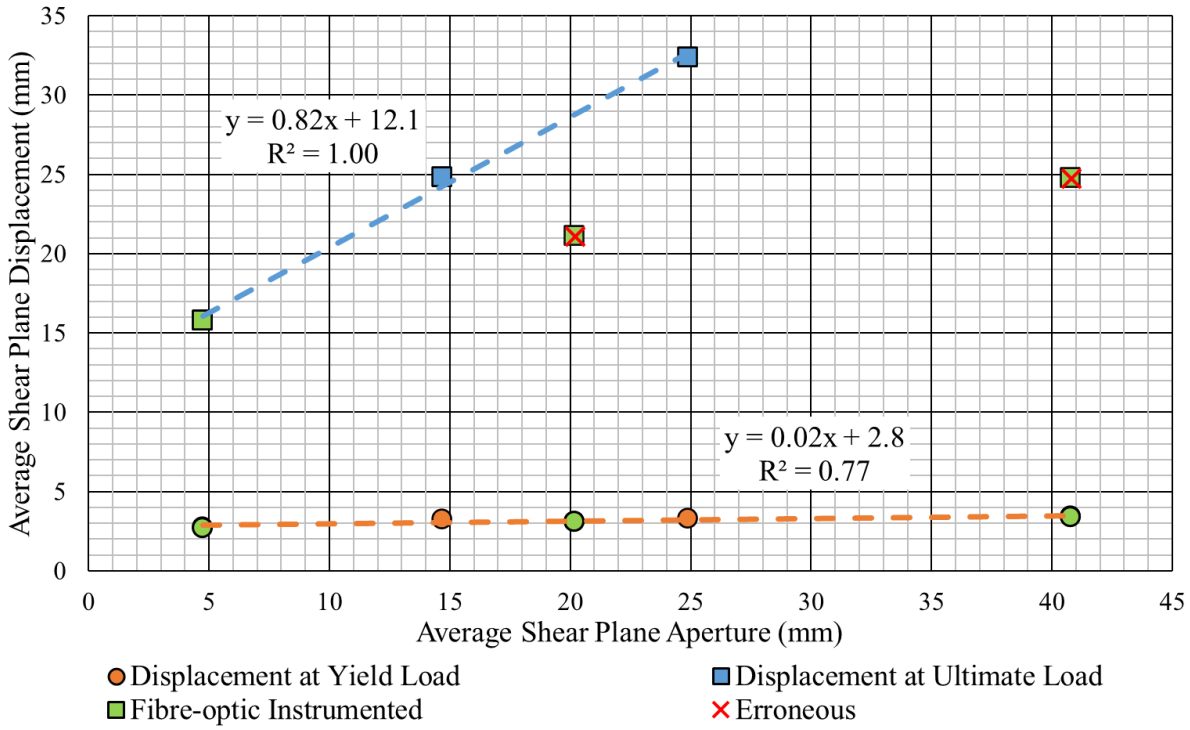

Figure 3.24. Average displacement vs average shear plane aperture at yield point and ultimate load for double shear tests on 22M Grade 500 dywidag.

3.2.3 Analysis Methods of Fibre-Optic Instrumented Rebar

Five double shear tests were conducted on fibre-optic instrumented samples with a three-groove configuration. Analysis of the fibre-optic strain data in the double shear tests was similar to the analysis on beam bending tests described in Sections 3.1.3 and 3.1.4. Many equations used for analyzing the strain data are listed in these sections, however, a more extensive theoretical derivation can be found in Appendix D and Appendix E.

Once again, Equations 3.3 to 3.9 were used to analyse the fibre-optic instrumentation data. These equations assume the strain will vary linearly within the cross-sectional area at any given position along the length of the rebar. The analysis also ignores any occurrence of shear strain and torsion. The equations assume the fibre-optic strands in the three-groove configuration are all oriented exactly 120 degrees apart around the rebar and are an equivalent distance from the rebar central

axis. Finally, the equations ignore any effect of the rib deformations on the surface of the rebar and, instead, assume the rebar is a solid cylindrical rod.

As with the fibre-optic instrumented beam bending tests, the fibre-optic instrumentation provides strain readings along the rebar length. From these readings, the direction of bending relative to the fibre-optic strands and the maximum and minimum strain along the rebar length can be calculated. These values give qualitative and quantitative insights into the behaviour of the rebar during the double shear tests.

The strain distribution can also be used to calculate the internal bending moment within the rebar using Equation 3.8. In turn, the internal bending moment can be used to determine the shear forces within the rebar and compared against the measured lateral load. The ability to determine the lateral load being applied to rebar using only the fibre-optic instrumentation is valuable in field applications where loads being applied to rebar cannot be easily measured. The accuracy of calculating the applied lateral load was investigated using the double shear test data.

The hypothetical internal bending moment and internal shear force in the double shear tests are shown in Figure 3.25 for illustrative purposes. Once again, the internal shear force is assumed to be the slope, or derivative, of the bending moment diagram with respect to the distance along the rebar. This relation is shown mathematically in Equation 3.9.

The load being applied to the centre pipe segment, P, can be calculated from the internal bending moment by summation of the slopes of the internal bending moments at each gap between pipe segments. This is similar to the technique used for the beam bending tests but concerns much smaller lengths of the rebar (5 mm to 40 mm). The calculated load can then be compared against the measured load to determine the accuracy of calculating the applied load in this manner.
Finally, the position of the rebar's centroidal axis can also be calculated using the fibre-optic instrumentation as was done previously for the instrumented beam bending tests. The two-dimensional position of the centroidal axis is determined based on the fibre-optic strain readings at each strain measurement increment (0.65 mm). A full explanation of this analysis is derived and presented in Appendix E.

The beam bending test accurately recorded the deflection of the midspan of the beam. Similarly, the position of the rebar's centroidal axis can be used to estimate the deflection of the midspan in double shear tests. In the following section, the measured deflection will be compared against the calculated deflection to evaluate how accurate these calculations are for double shear tests.

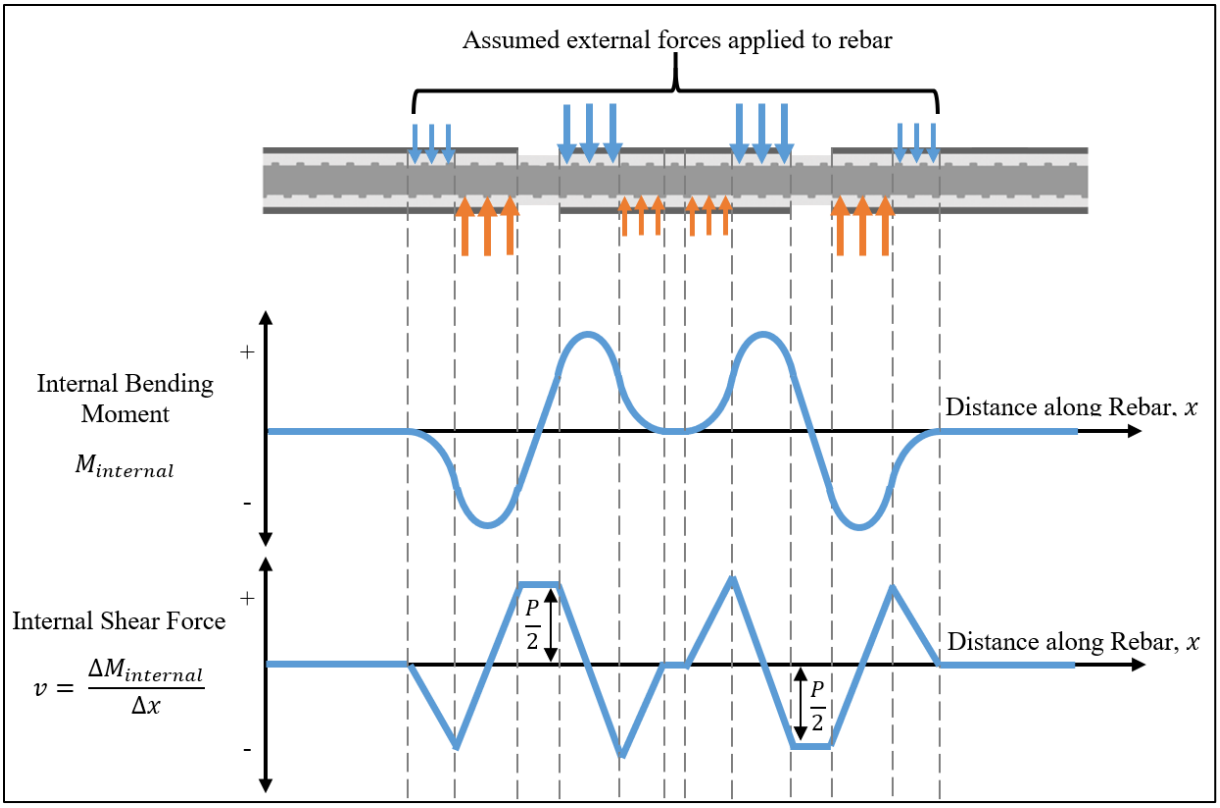

Figure 3.25. Assumed distribution of external forces, internal bending moments, and internal shear forces for rebar during a double shear test.

3.2.4 Results of Fibre-Optic Instrumented Rebar

In total, five double shear tests were conducted on rebar instrumented with fibre-optic in a three-groove configuration. Two of the instrumented rebar were 25M (#8) Grade 400 (60) rebar and three of the instrumented rebar were 22M (#7) Grade 500 (75) dywidag threadbar. As discussed previously, two of the tests on 22M Grade 500 dywidag failed at very low loads and displacement and their ultimate load and displacements are considered erroneous. The reason for this premature failure is not clear but may be due to the instrumentation process.

The strain readings near the beginning of double shear test DS-8R-320-FO are shown in Figure 3.26. At this point in the test, there was 1.5 kN being applied to the centre of the test sample and 0 mm of displacement had been measured. Similar initial strain readings were recorded in all fibre-optic instrumented double shear tests. The strain distributions suggests there is a bending moment within the rebar before the double shear tests began. This is an important observation as it suggests the clamping system is causing some bending moments that could affect the results of the tests.

Figure 3.27 shows the strain readings of the three fibre-optic strands (labelled Strand 1, 2, and 3) for DS-8R-320-FO at 330 seconds into the test. There was a total of 148 kN being applied to the sample and an average of 2.3 mm of displacement had been measured at this stage of the test. The figure shows large magnitudes of strain (both compressive and tensile) in rebar within the outer pipes (0.55 m and 1.1 m) and the inner pipe (0.65 m and 1.0 m). The large magnitude strains occur in Strand 2 and Strand 3 while Strand 1 did not measure significant strain. This is because Strand 1 is located closer to the neutral bending axis and Strand 2 and Strand 3 are located further away from the neutral bending axis.

Similar strain distributions were measured in all fibre-optic instrumented double shear tests. The magnitudes of compressive and tensile strains were found to increase as the applied load increased.

From the strain distributions recorded by the fibre-optic instrumentation, two shear planes can be recognized in each test. In Figure 3.27, the first shear plane is centred on 0.610 m and there is a second shear plane with movement in the opposite direction that is centred on 1.034 m. The increased tensile and compressive strains around 0.55 m in Strand 2 and 3, respectively, indicate sharp bending in the rebar. The polarities are then reversed, i.e. Strand 2 becomes compressive and Strand 3 becomes tensile, around 0.65 m. This reversal indicated sharp bending, but in the opposite direction. The “S” shape that would be created by bending in one direction and then the other is the expected shape for rebar crossing a shear plane, as discussed in Section 1.1.3.

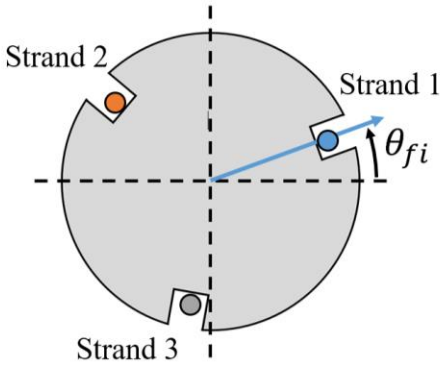

a) Cross-section A-A'

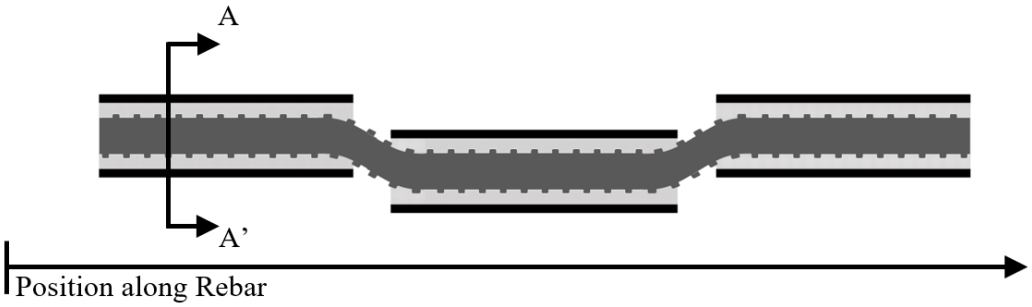

b) Long-section

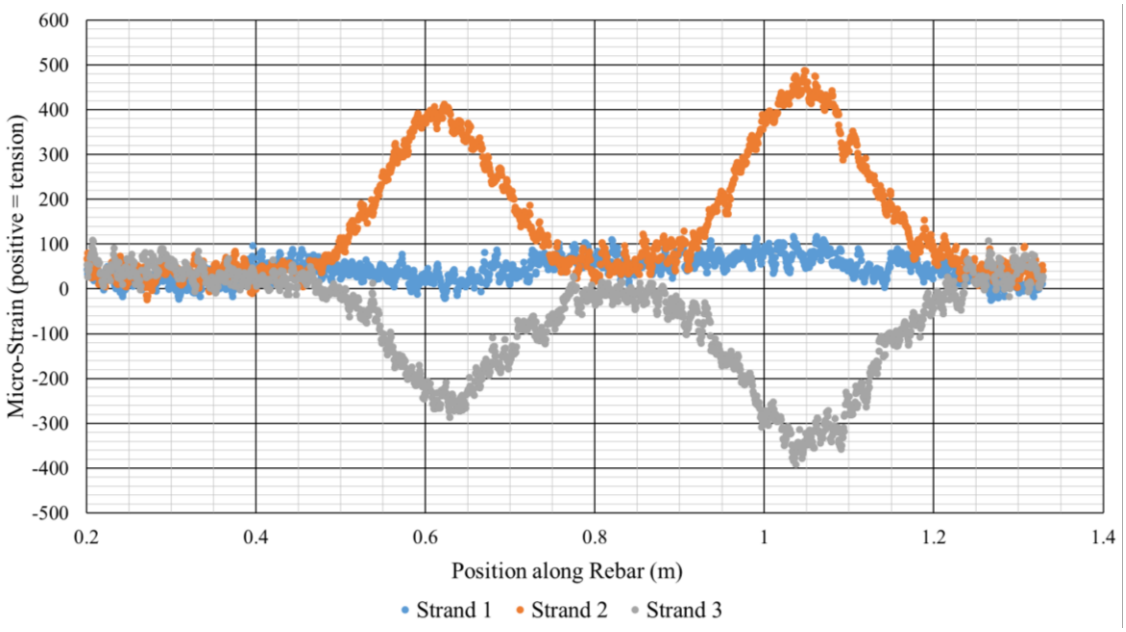

c) Fibre-optic strain readings

Figure 3.26. Double shear test DS-8R-320-FO at 10 seconds with 1.5 kN total applied load. Figure shows a) the cross-section of the rebar with orientation of fibre-optic strands, b) the long-section of the double shear test, and c) the fibre-optic strain measurements.

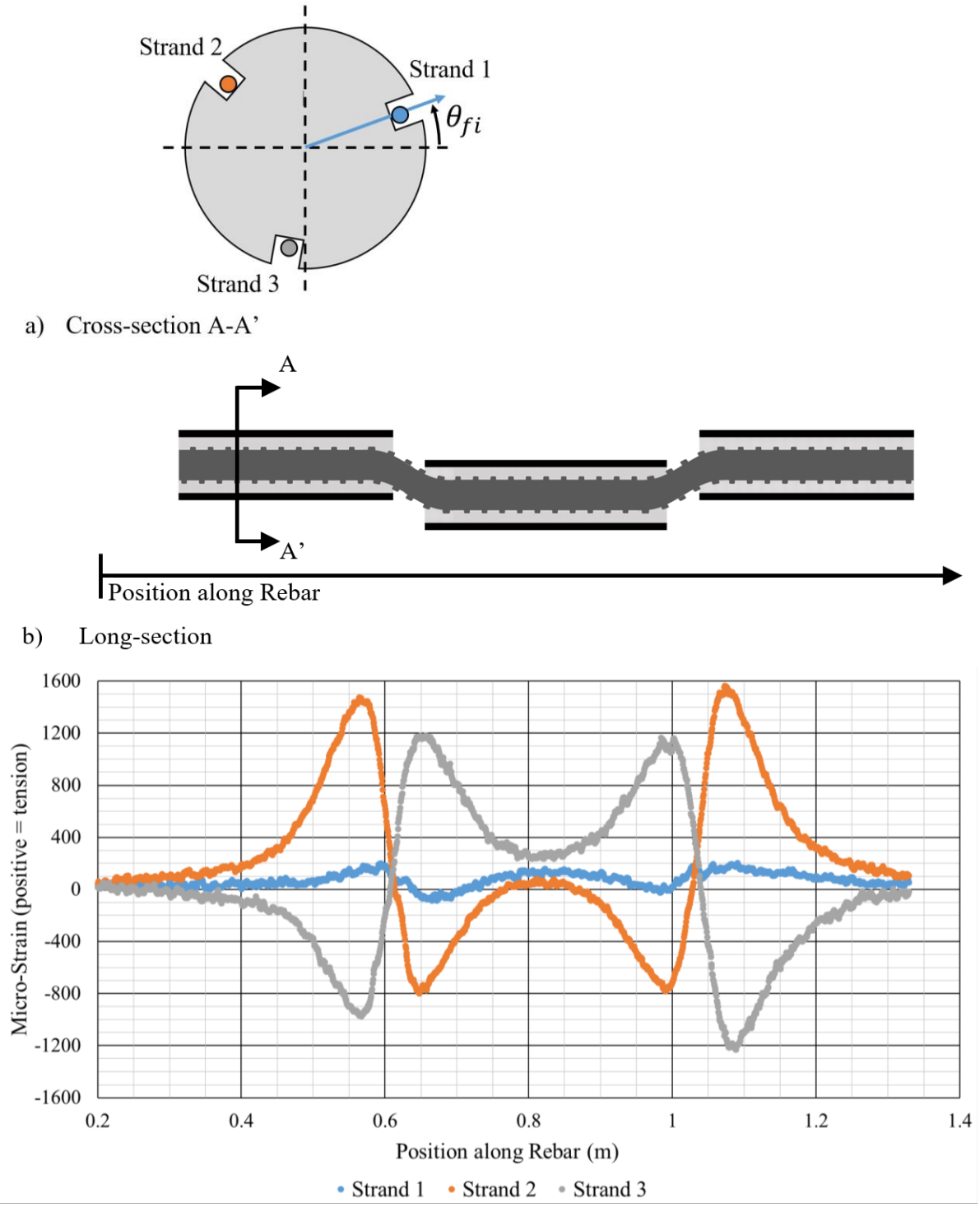

Figure 3.27. Double shear test DS-8R-320-FO at 330 seconds with 148 kN total applied load. Figure shows a) the cross-section of the rebar with orientation of fibre-optic strands, b) the long-section of the double shear test, and c) the fibre-optic strain measurements.

Using the strain measurements from all three fibre-optic strands, the internal bending moments can be calculated, as per the theoretical equations derived in Appendix D. These calculations are only valid for linear elastic behaviour and so were only applied up to the yield point of the tests.

The internal bending moments for DS-8R-320-FO, with a load of 148 kN applied, is shown in Figure 3.28. As was expected from qualitative analysis of the strain readings, the rebar bends in characteristic “S” shapes centred on the shear planes and, therefore, opposite internal bending moments (i.e. positive vs negative) occur on either side of the shear planes.

The rate of change of the internal bending moment, with respect to distance along the rebar, is equal to the shear force within the rebar. At the shear planes, the rebar is not inside the pipe segments and no external lateral forces are exerted on it. To determine an approximate slope for the internal bending moments in this area, a line was fitted, via linear regression, to the internal bending moments at the shear planes. To continue with our example analysis of DS-8R-320-FO with a total applied load of 148 kN, the fitted lines and associated slopes are shown in Figure 3.28.

The sum of the absolute of the shear forces at each shear plane is theoretically equivalent to the applied load. This analysis on fibre-optic instrumented rebar was conducted on all five instrumented samples at every five second interval of each test. The shear loads at each shear plane were calculated and added. This calculated load was then plotted against the measured load in Figure 3.29. Note that all loads refer to the total applied loads, not the load per shear plane. The yield loads of each test are also plotted in Figure 3.29 for reference.

For double shear test DS-8R-320-FO with 148 kN applied, the absolute sum of the shear forces is 33.7 kN. This is substantially lower than the 148 kN of applied load that was measured. In all tests, the load calculated from the fibre-optic instrumentation is far lower than the measured applied load. Recall that the beam bending tests on fibre-optic instrumented rebar found the fibre-optic strain readings could provide a close estimate of the load being applied.

The reason for the discrepancy between the calculated loads and measured loads in the double shear tests is not clear at this time, but likely has to do with the small aperture of the shear plane relative to the rebar diameter. Since the shear plane aperture is small relative to the rebar diameter, compressive forces could be transferred across the shear plane without causing the rebar to bend. Regardless, this issue presents a major limitation to applying this technology in the field, since shear force cannot be determined without some other instrumentation.

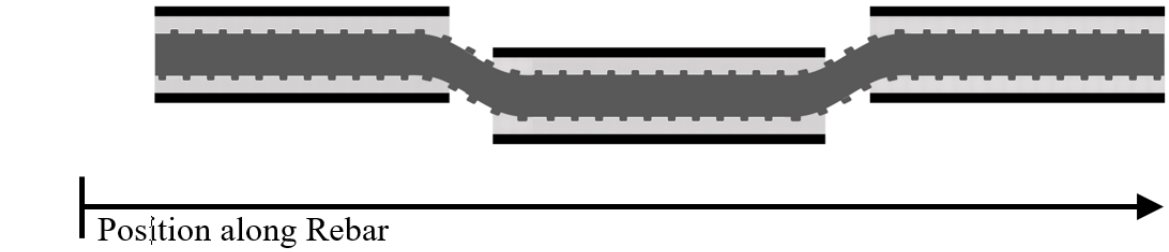

a) Long-section

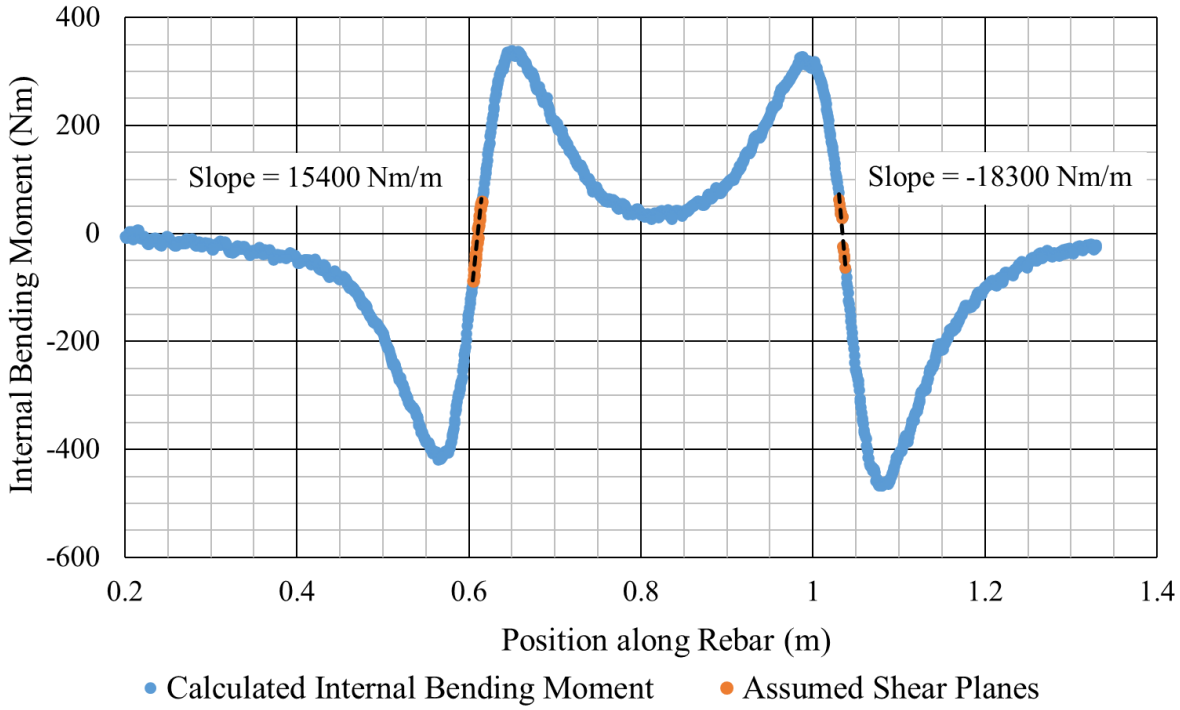

b) Calculated Internal Bending Moments

Figure 3.28. Double shear test DS-8R-320-FO at 330 seconds with 148 kN total applied load. Figure shows a) long-section of the double shear test and b) the internal bending moment calculated from fibre-optic strain measurements.

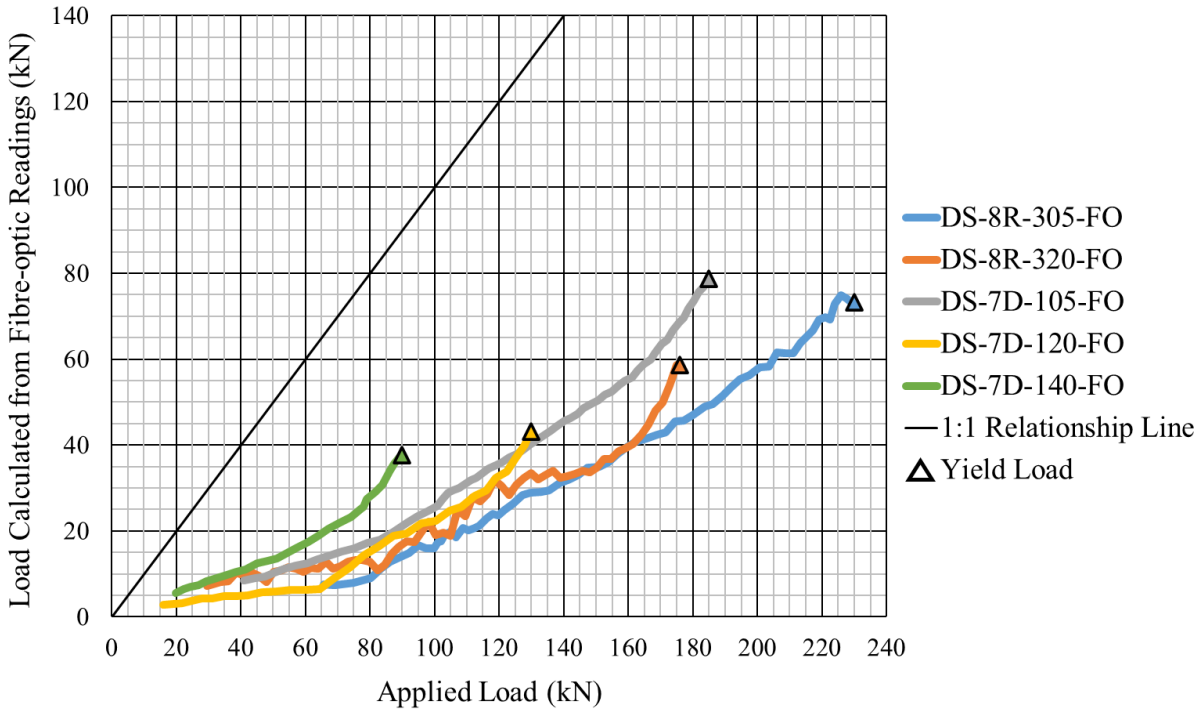

Figure 3.29. Load calculated from fibre-optic instrumentation vs applied load for double shear tests.

The strain readings of the rebar can be used to calculate the theoretical position of the rebar's centroidal axis along its length as per the methods describes in Appendix E. The position of the centroidal axis was then used to approximate the deflection of the rebar midspan relative to the outer pipe segments. To approximate the deflection, the orientation of the rebar had to be assumed. An example of the method used to calculate the deflection from the centroidal position is shown in Figure 3.30

The deflection of the midspan of the rebar relative to the outer segments was calculated for every instrumented test at every five second interval. The calculated displacements are plotted against the average displacement measured by the LVDTs in Figure 3.31.

In all tests, the deflection was calculated from the position plot. The calculated deflection varies from the average measured deflection by up to 1.1 mm for all measurements. Any error seen could be a result of the datums chosen for the displacement estimation. As was previously discussed, relating the centroidal axis of the rebar calculated from the fibre-optic instrumentation to its position and orientation in 3-dimensional space is highly subjective without external instrumentation.

To investigate these tests further, sample DS-7D-140-FO was cut perpendicular to its longitudinal axis at multiple location along the sample after testing. It was found that the rebar was not perfectly centred in the pipes at some locations along the length. One area also had a small cavity in the resin. These issues could affect sample strengths and displacements in double shear tests.

Another issue identified from cutting DS-7D-140-FO is the position of the three fibre-optic instrumentation grooves cut down the rebar length were not oriented 120 degrees around the rebar. In the analysis used here, the grooves were assumed to be oriented perfectly 120 degrees apart from each other for all instrumented samples. Figure 3.32 shows an example of the cross-section of sample DS-7D-140-FO. The angles between instrumentation grooves were estimated and are illustrated in Figure 3.32 and deviated significantly from the ideal 120 degrees.

The analysis and equations used to analyze the fibre-optic strain data can account for fibre-optic instrumentation that is not orientated 120 degrees around the rebar. However, the actual orientations of the fibre-optic notches are somewhat difficult to measure and a method of measuring the angular positions of the fibre-optics would need to be implemented in future testing.

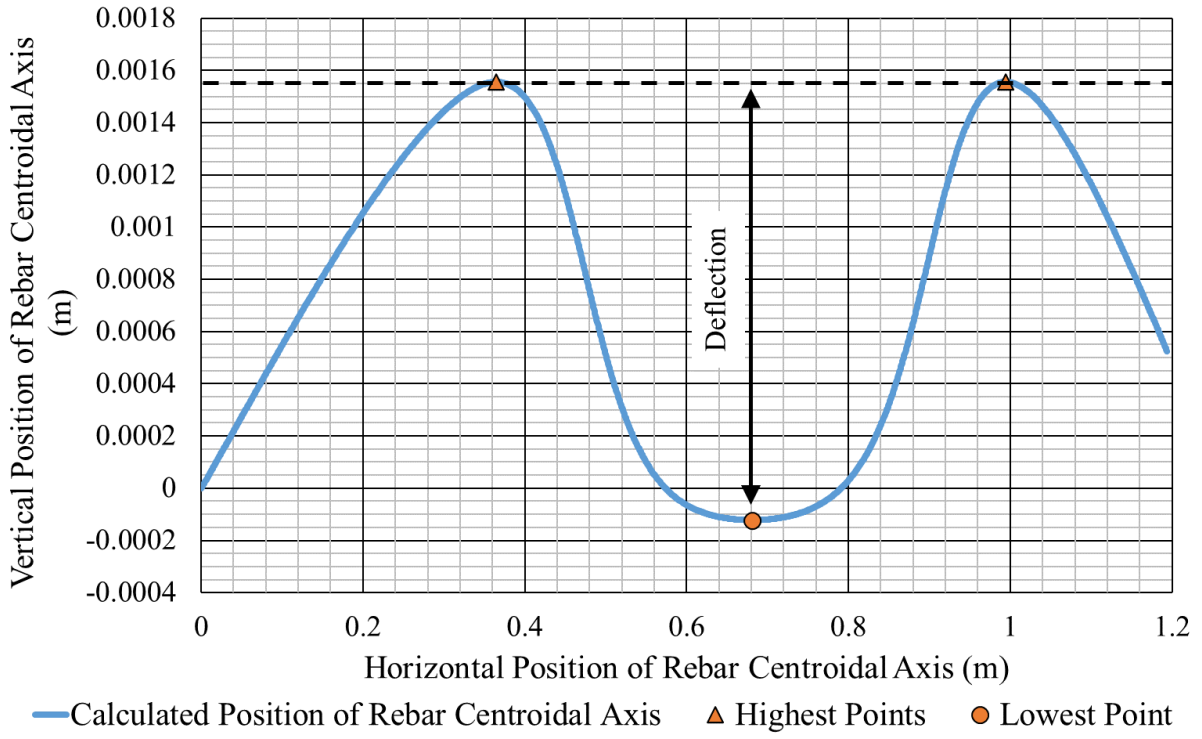

Figure 3.30. Calculated position of the rebar centroidal axis in double shear test DS-8R-320-FO at 330 seconds with 148 kN total applied load.

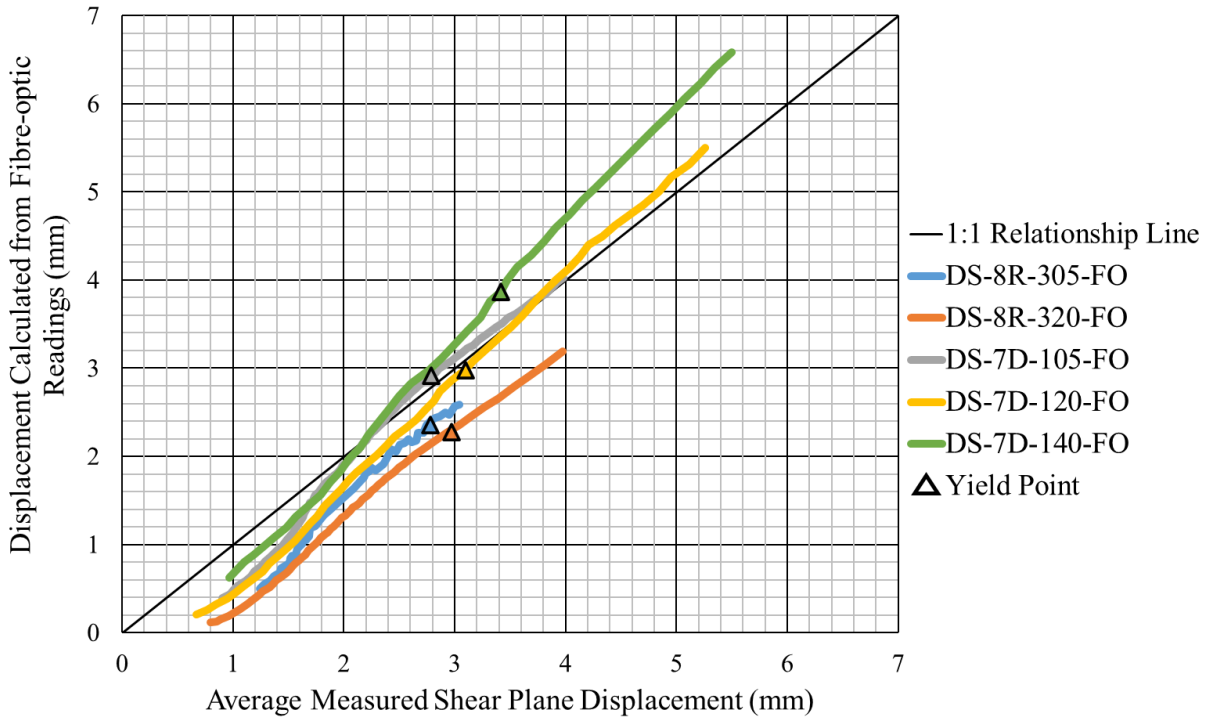

Figure 3.31. Deflection of rebar calculated from fibre-optic instrumentation vs average measured LVDT displacement for double shear tests.

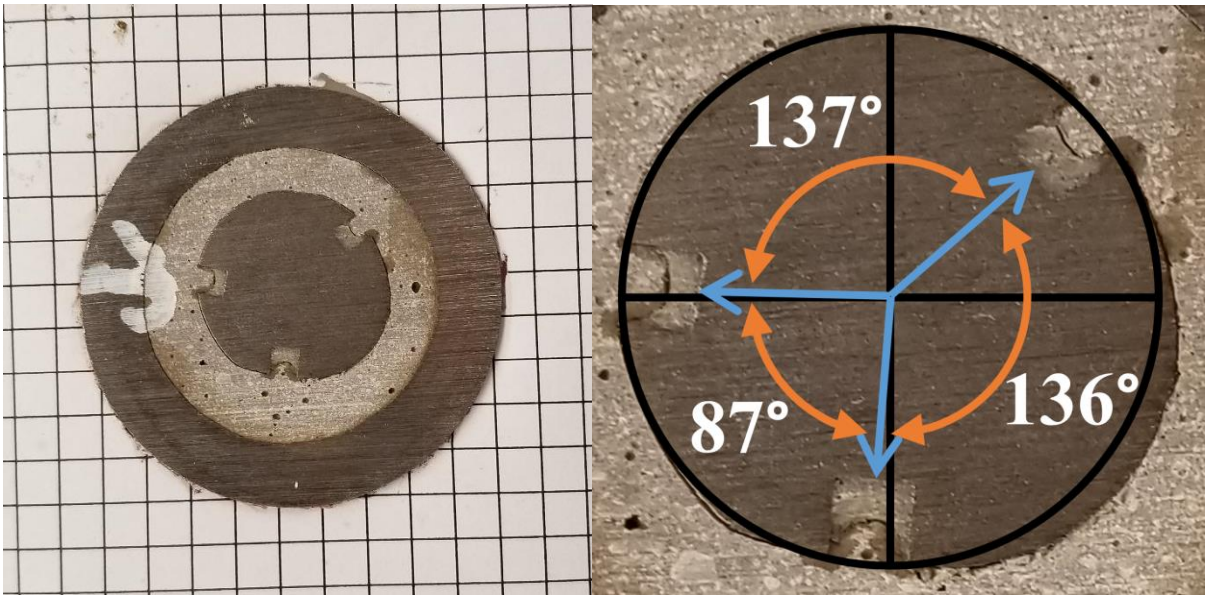

Figure 3.32. Sample DS-7D-140-FO cross-section cut against a 5mm grid (left) and showing approximate angles between fibre-optic instrumentation notches (right).

3.3 Conclusions

Beam bending tests and double shear tests have been summarized in this section. Beam bending tests showed that the difference between the theoretically and experimentally determined area moment of inertia was minimal for both un-instrumented and fibre-optic instrumented rebar. The fibre-optic instrumentation reduced the area moment of inertia by up to 18% relative to the un-instrumented rebar.

Fibre-optic strain measurements from beam bending tests on fibre-optic instrumented rebar were analyzed using the equations derived in Appendix D and Appendix E. The strain measured by the fibre-optic instrumentation provided the expected theoretical strain distributions within the rebar. The load applied to the rebar and the axial position of the rebar were calculated using the fibre-optic instrumentation. Both the calculated load and the calculated displacement were within 20% of the measured values.

The double shear tests include some important observations concerning the behaviour of rebar crossing a shear plane:

- The shear plane displacement required to yield the rebar is very low and is independent of the shear plane apertures considered.
- The ultimate rebar load is not significantly affected by the shear plane apertures.
- The ultimate shear displacement prior to rebar failure is very dependent on the shear plane aperture.

The final point above is an important observation, as it shows the aperture of a shear plane must be considered when estimating the effect of measured shear plane offset on rebar rock bolt support.

The double shear tests suggested the fibre-optic instrumentation is limited in its ability to determine the shear force within rebar rock bolts that cross shear planes. The reason for this is possibly due to the small aperture of the shear plane, especially when compared to the acceptable performance in the beam bending tests. The fibre-optic instrumentation does, however, appear to provide an adequate estimation of the rebar's centroidal axis position and the shear plane displacements in the double shear tests. The displacements calculated from the fibre-optic instrumentation are within roughly 20% of the measured values.

4 LATERAL PULL TESTING

A novel Lateral Pull Test method was developed to measure the shear behaviour of rebar in the field. Field testing was considered important in evaluating the behaviour of rebar in shear because the variables present in an underground mine, such as the in situ rock behaviour and rebar installation conditions, are very difficult to recreate in a laboratory setting. The setup applies a lateral load to installed rebar to simulate one side of the rebar shear scenario. The behaviour of different types of rebar were investigated, with and without fibre-optic instrumentation.

The theory and apparatus design are discussed in Section 4.1. Detailed apparatus drawings and the procedure to install the lateral pull testing apparatus are presented in Appendix F.

4.1 Apparatus Design and Theory

Shear movement in rock typically occurs across a discrete shear plane. The rock mass on one side of the shear plane moves laterally relative to the other side. If all conditions and behaviour are equal on each side of the shear plane, as most researchers have assumed (Pellet and Egger, 1996), then the behaviour of the rebar will have a point of symmetry in the middle of the shear plane (Figure 4.1). Bending in rebar is the result of internal bending moments within the rebar and the bending changes direction at the point of symmetry. The point of symmetry is an inflection point where the internal bending moment is zero. Assuming all conditions are the same on either side of the shear plane, this inflection point will always remain at the midpoint of the shear plane.

The lateral pull testing is designed to recreate one half of the shear behaviour. Since there is no bending moment at the inflection point, the influence of one half of the shear plane on the other can be broken down into a resultant force applied to the rebar at the inflection point. The resultant force can be defined by two components: an axial force parallel to the rebar axis and a shear force perpendicular to the rebar axis (Figure 4.2). Alternatively, the resultant force can be defined as a normal force and a lateral force applied at the inflection point where the normal force acts normal to the shear plane and the lateral force acts parallel to the shear plane.

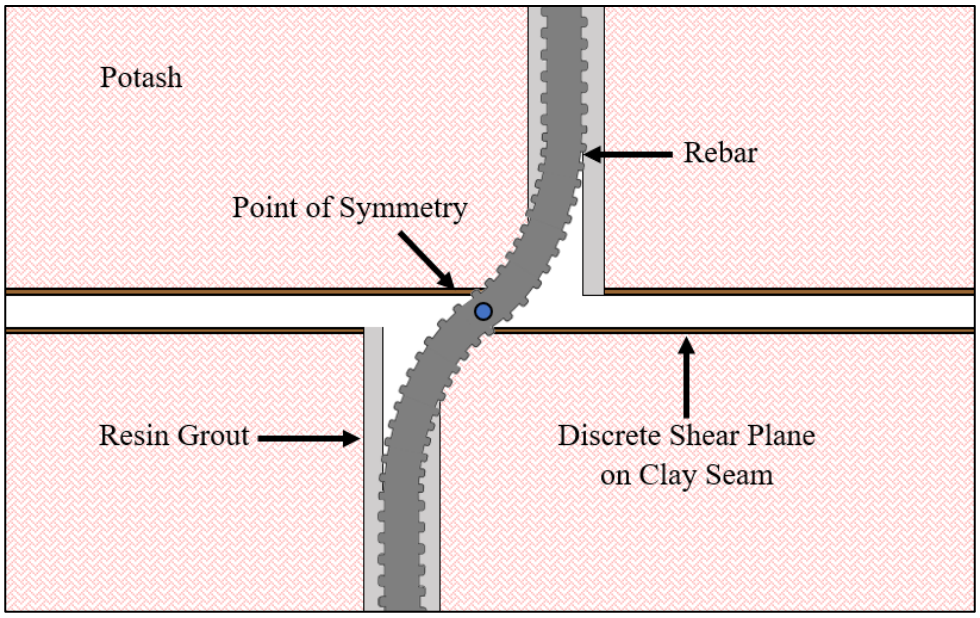

Figure 4.1. Point symmetry of rebar crossing a shear plane.

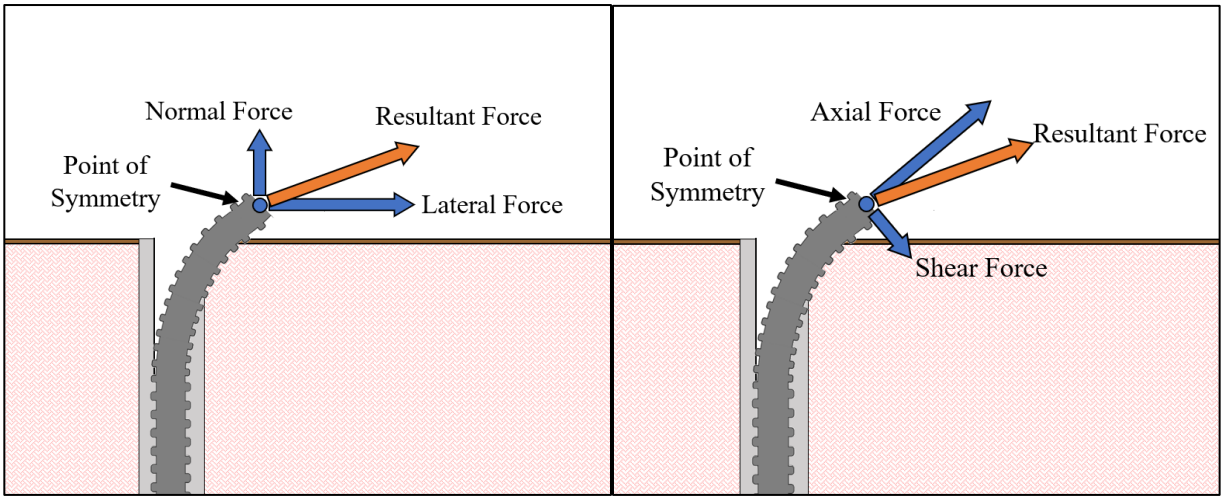

Figure 4.2. Internal forces in the rebar at the inflection point.

A testing apparatus was constructed from off-the-shelf components and specially designed parts machined by USask Machine Shops. SolidWorks was used to design the apparatus parts. The loads the apparatus would be subjected to were not known so SolidWorks was also used to numerically verify that they could withstand 400 kN of force at a factor of safety of 1.5. A Young's modulus of 200 GPa and a yield stress of 400 MPa were assumed for all steel components.

Figure 4.3 and Figure 4.4 show the testing apparatus that was designed. The apparatus was designed to apply an increasing lateral load to the rebar installed into a potash surface until the rebar failed. The apparatus was designed to apply the forces shown in Figure 4.2 and to avoid applying any bending moments at the point of load application to simulate one half of a shear plane as closely as possible. The apparatus prevents vertical displacement of the point of lateral load application while allowing horizontal displacement and rotation about this point.

The chassis of the apparatus is anchored to the rebar by a 63.5mm diameter threaded insert. The threaded insert was intended to allow for easily testing different sizes and styles of rebar as well as to allow for testing fibre-optic instrumented rebar. Vertical displacement was prevented by having the chassis slide along two smooth steel skid plates. The skid plates were attached to the potash surface using a Hilti drill and 0.32 m long HMS-22MX mining screws. As lateral load is applied to the chassis through two 25 mm diameter master links, the chassis slides along the skid plates. Since the master links and skid plates transfer forces through the cylindrical arms of the chassis, the rebar can rotate as it bends and the only moments that should be applied due to the lateral loads would be from friction. All parts were made out of Grade 400 steel.

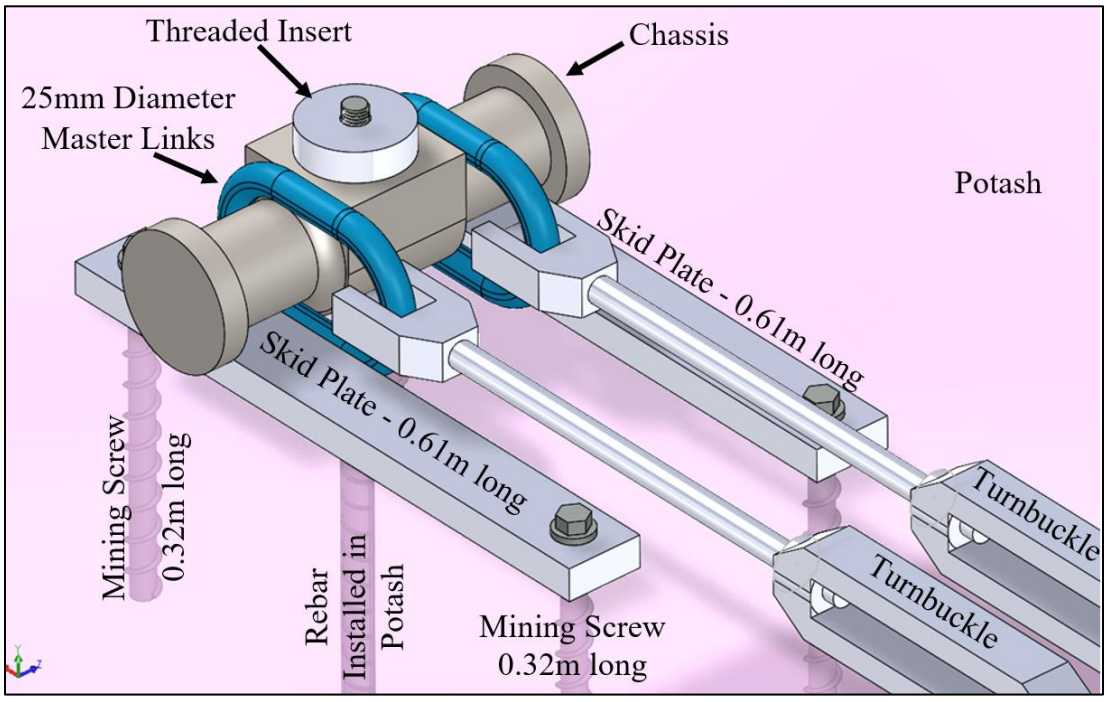

Figure 4.3. Chassis slides along skid plates and applies forces without imparting a moment

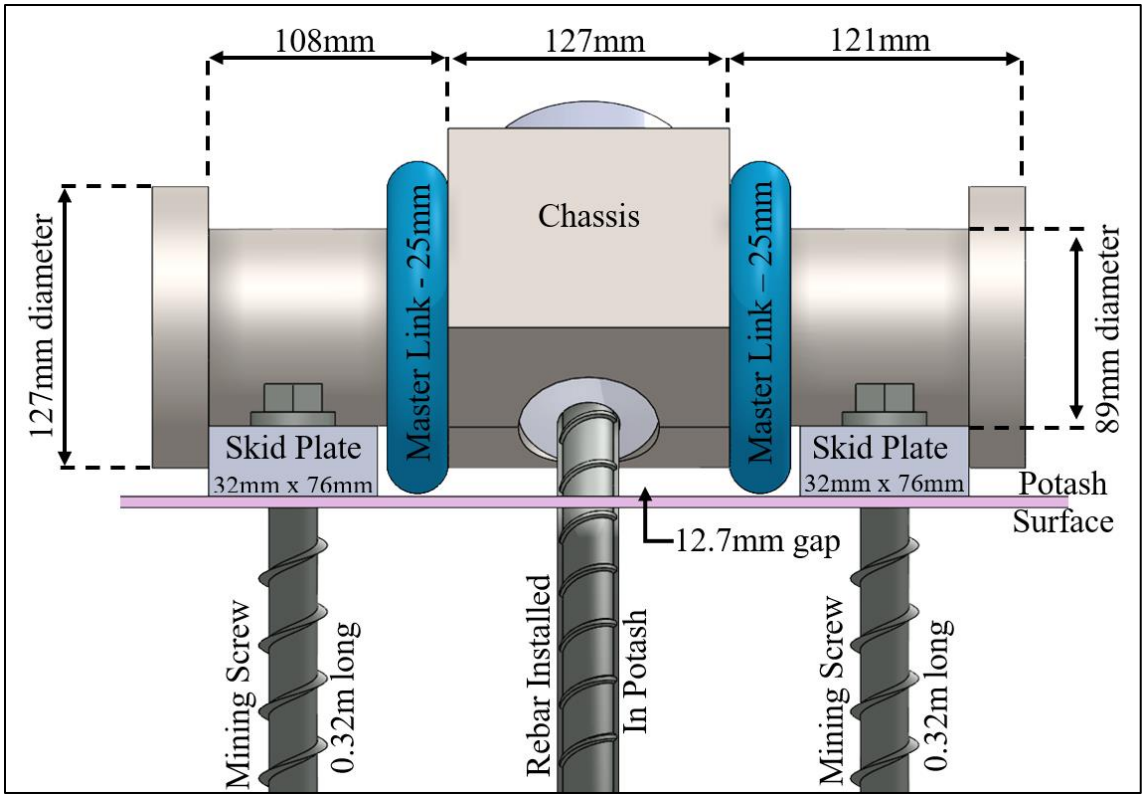

Figure 4.4. Rear view of chassis resting on skid plates as the rebar is being bent

Figure 4.5 shows the threaded insert that anchors the chassis to the rebar. This insert tightens the chassis against the skid plates. By changing out the threaded insert for different thread sizes, three different types of rebar could be tested using the same apparatus. A detailed drawing of the chassis and threaded inserts are included in Appendix F.

There are two important points in the rebar, labelled point O and point C in Figure 4.6. Point C represents the centre of rotation of the chassis and threaded insert as well as the centre of load application. Point O is the point at which the rebar enters the threaded insert. The rebar bends and shears as a result of the lateral load below point O. The threaded insert and chassis was observed to prevent any significant bending from occurring between point O and point C.

Ideally, point O and point C would coincide in the lateral pull tests. This coincidence would mean the point of zero internal bending moment, the centre point of rotation, and the centre point of load application occur at the same point along the rebar. Under in situ shearing, point O and point C

would coincide. Unfortunately, there was no practical way to ensure the two points coincided due to the loads exceeding 200kN being applied and, therefore, the high strength required of the testing apparatus.

The lateral load is applied with an Enerpac RCH 306 hollow-core hydraulic cylinder with a 156 mm stroke length and 320 kN capacity. The hydraulic cylinder is mounted horizontally on a low carbon steel L-bracket (Figure 4.7). A detailed drawing of the L-bracket can be found in Appendix F. The L-bracket was mounted to the rock surface with six 0.32 m long HMS-22MX Hilti mining screws with ultimate tensile loads of 185 kN each.

The load was transferred from the hydraulic cylinder to a 32 mm diameter Grade 500 steel rod and then to a specially machined steel spreader block (Figure 4.8). The spreader block spreads the force from the steel rod to the two master links which are aligned with the master links on the chassis. Two turnbuckles transfer load from the master links on the spreader block to the master links on the chassis. A detailed drawing of the spreader block is shown in Appendix F. The turnbuckles are 25 mm diameter Grade 400 steel turnbuckles and the master links are 25 mm diameter forged oblong master links.

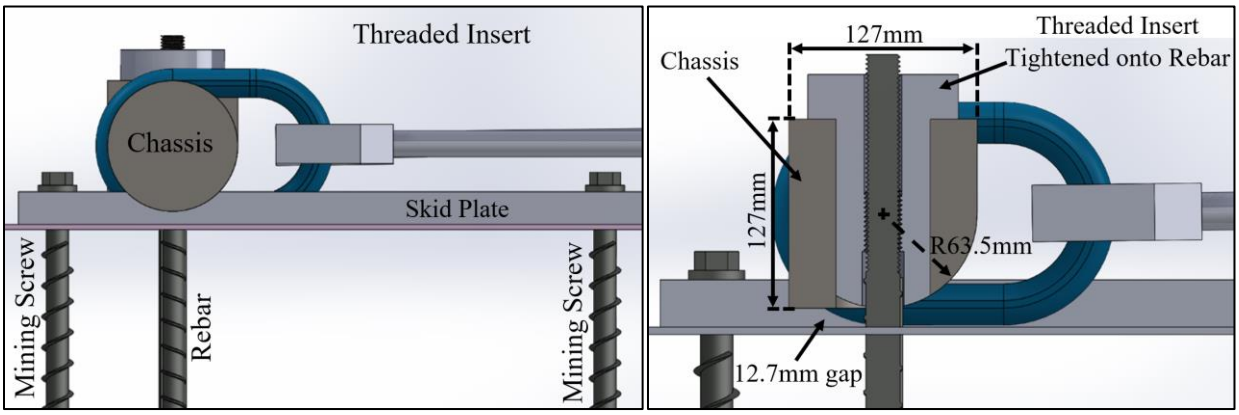

Figure 4.5. Cross-sectional view of chassis and threaded insert tightened onto rebar

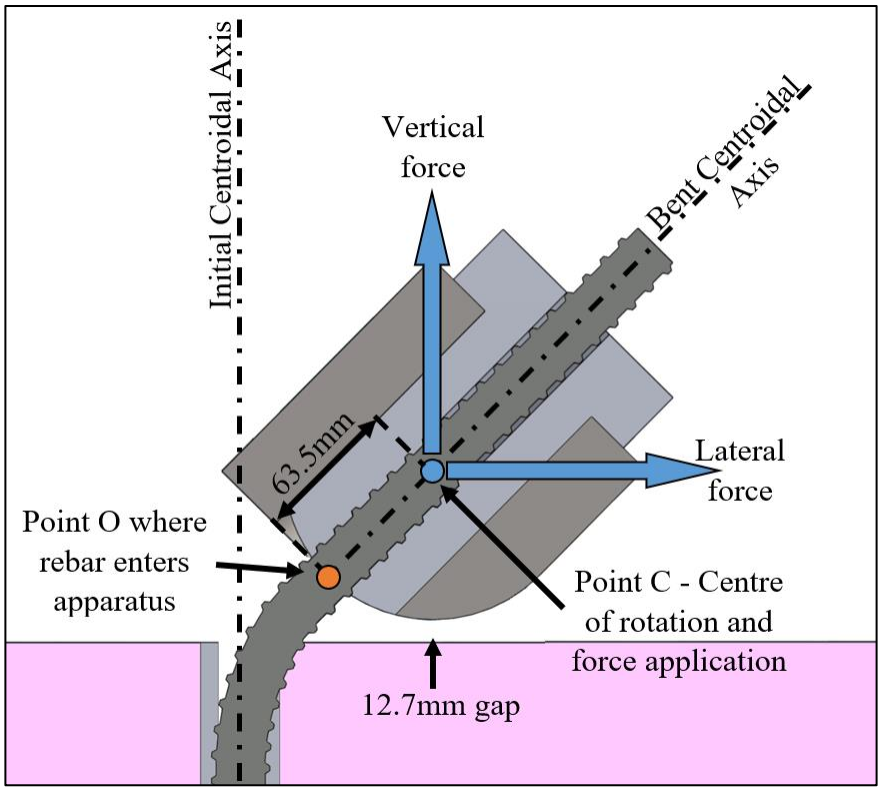

Figure 4.6. Important points of rebar and apparatus in lateral pull tests

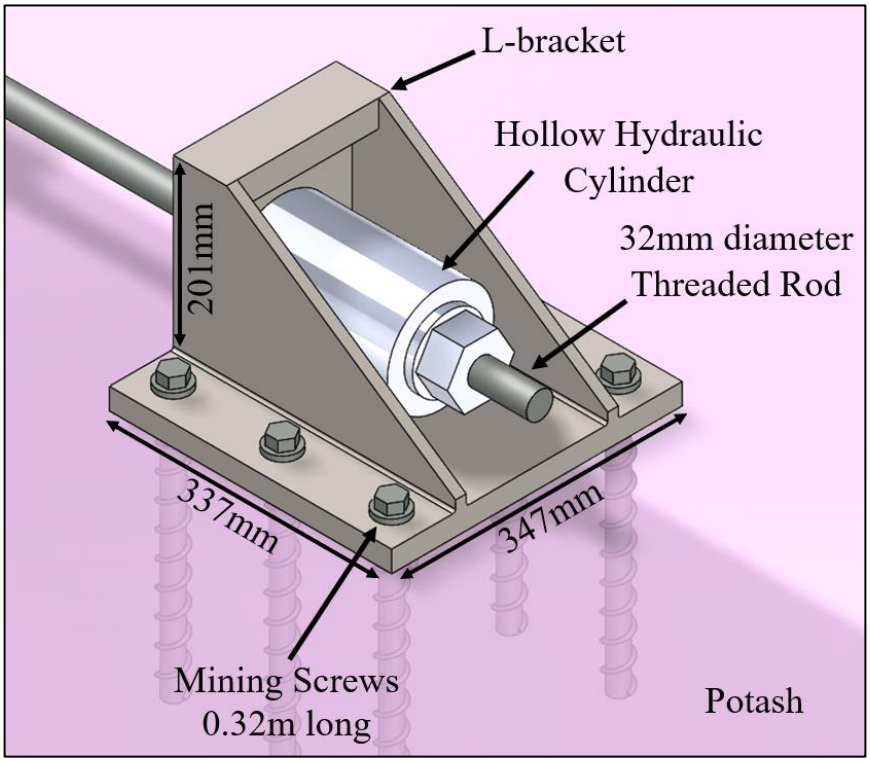

Figure 4.7. Lateral load applied using a hollow-core hydraulic cylinder mounted with an L-bracket

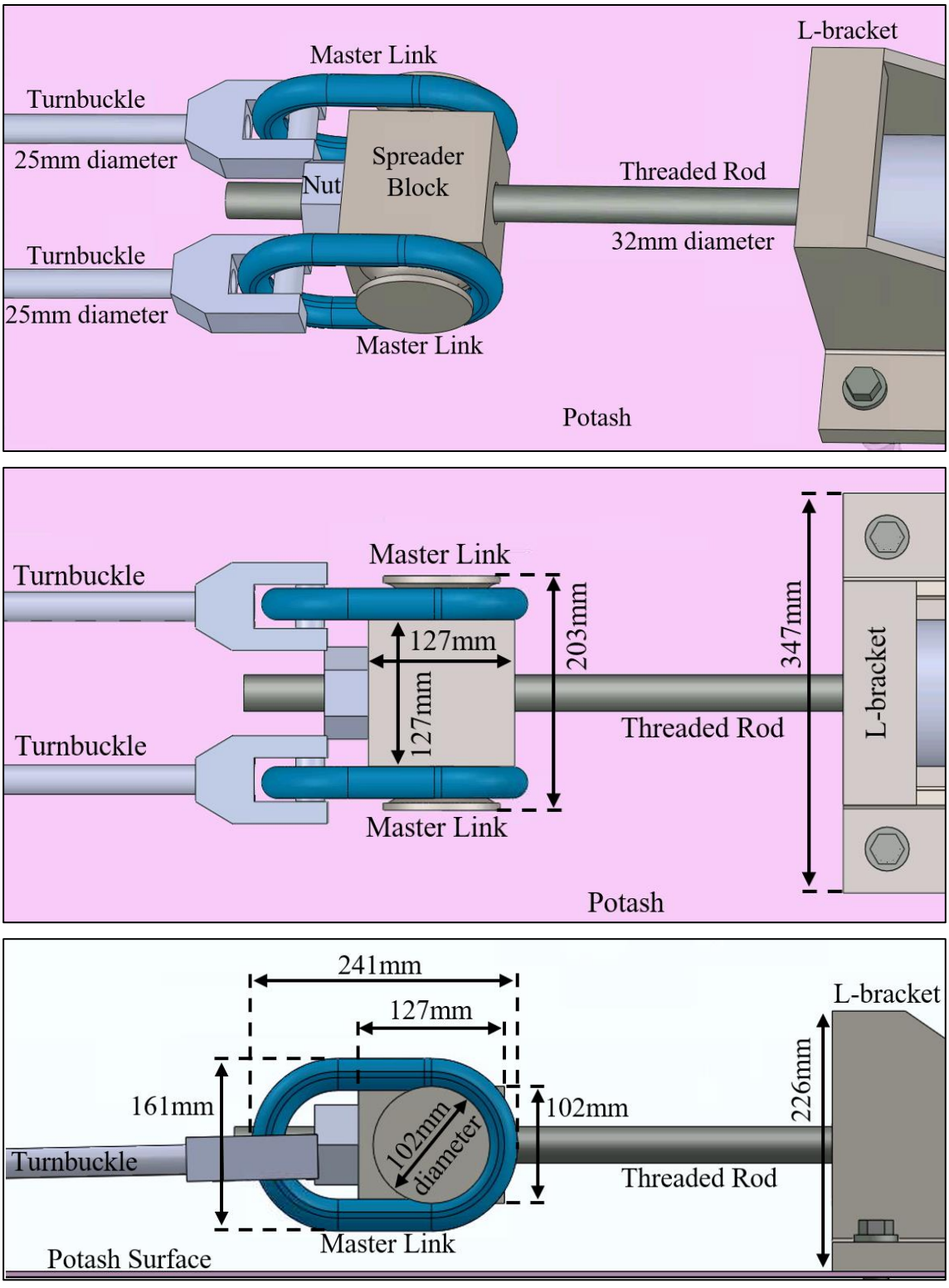

Figure 4.8: Diagrams showing the spreader block for transferring force from threaded rod to turnbuckles. Shown from isometric view (top), plan view (middle), and side view (bottom)

Figure 4.9 shows an isometric rendering of the test setup. The full test setup is roughly between 2.4 m and 3.0 m long, as shown in Figure 4.10. Once the lateral pull test apparatus is setup, the hydraulic cylinder is slowly pressurized with a hand pump. The increasing lateral load on the rebar will cause the rebar to shear and bend. Figure 4.11 shows the movement of the apparatus and rebar bending as lateral load is applied.

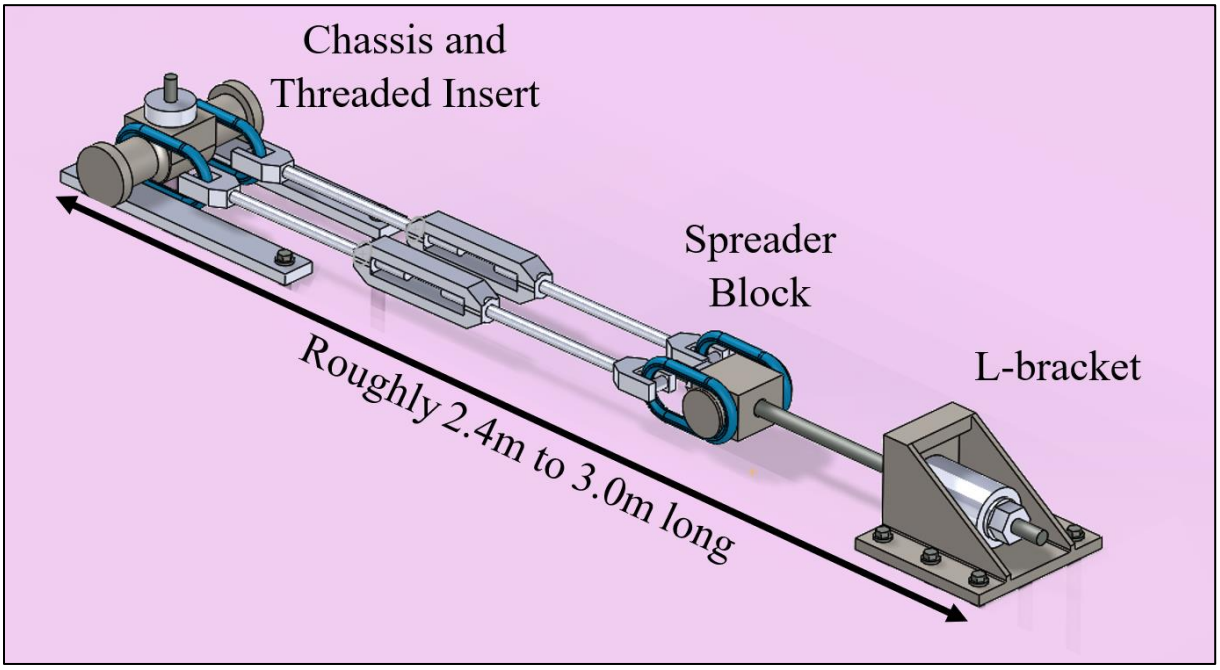

Figure 4.9. Isometric view of the lateral pull test setup

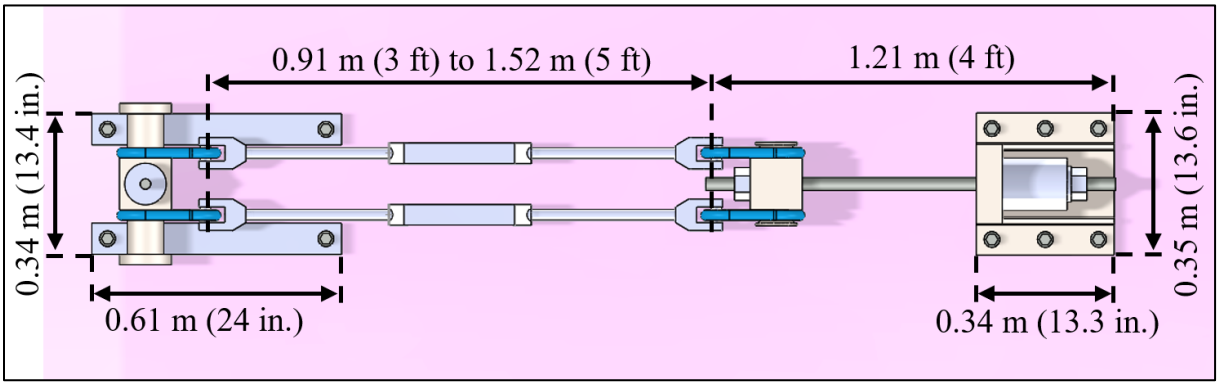

Figure 4.10. Plan view of the lateral pull test setup

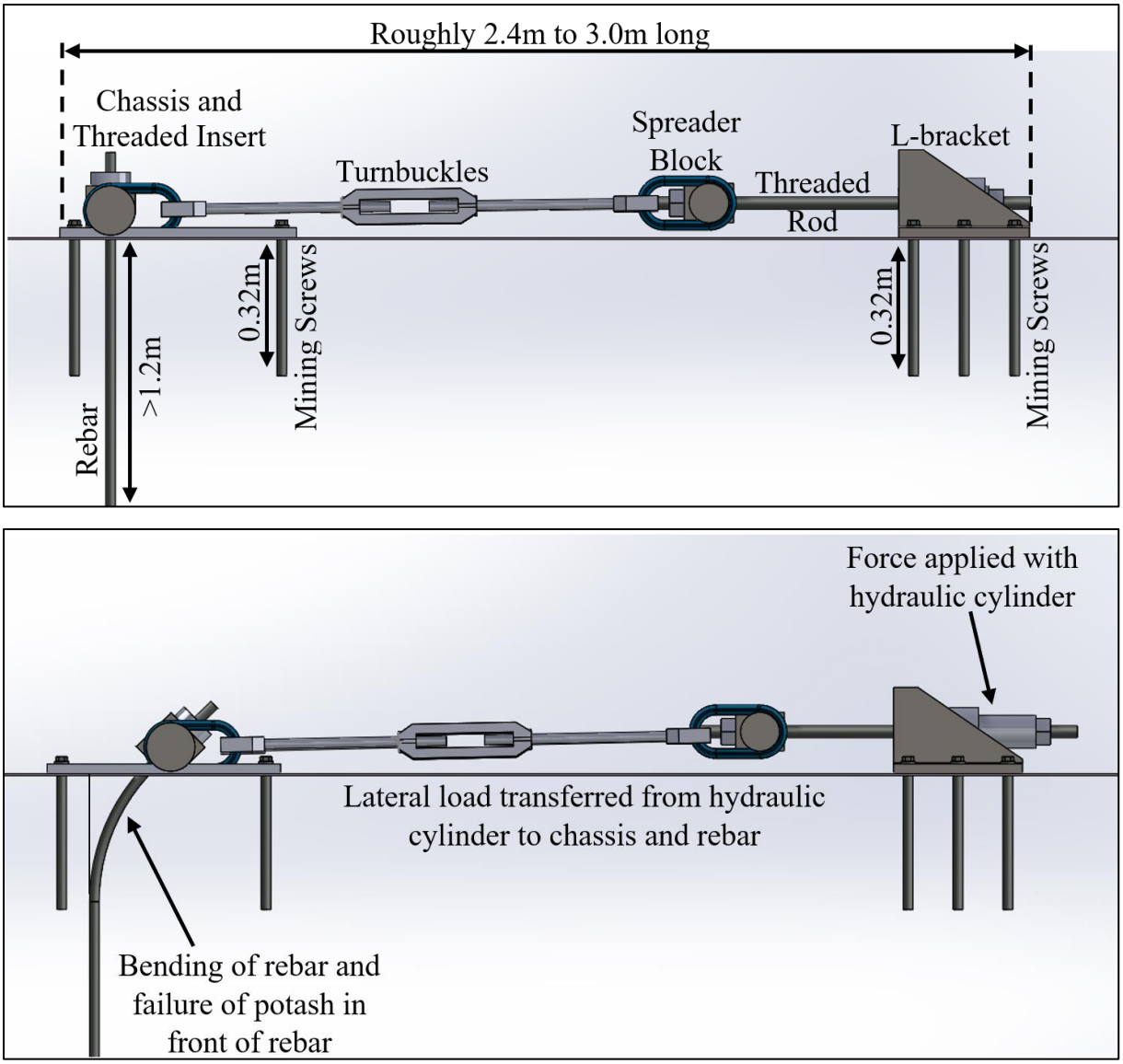

Figure 4.11. Side view of experiment setup before (top) and after (bottom) applying a lateral load

As shown in Figure 4.12, there are two major sources of friction that could not be eliminated during the apparatus design. Friction between the master link and the chassis may apply a moment to the chassis that reduces rotation. Friction between the chassis and the skid plates act against the laterally applied load and may apply a moment to the chassis that increases rotation. A large amount of fresh grease was applied to these areas before every test to reduce the friction as much as possible, however it likely caused some amount of error.

The chassis was attached to the rebar by tightening the threaded insert onto threads cut into the rebar. The threaded insert was tightened until the chassis rested firmly on the skid plates. The 22M (#7) Grade 500 (75) dywidag has course threads incorporated into the rebar as deformations on the rebar surface. The threads on the 22M (#7) and 25M (#8) Grade 400 (60) rebar are 9 TPI UNC and 8 TPI UNC threads, respectively, and have to be machined into the rebar..

Machining threads into rebar removed material, reduced the cross-sectional area of the rebar, and weakened the rebar. To counter this weakening effect, the threaded inserts were designed to counter-sink the rebar further into the threaded insert. This counter-sinking was intended to offset the weak threads further into the threaded insert and chassis to reduce the likelihood of failure in the weak threads. Figure 4.13 (left) shows how the threaded insert for the Grade 400 rebar has threads counter-sunk about 37 mm into the insert. Figure 4.13 (right) shows the threaded insert for the Grade 500 dywidag.

A combination of un-instrumented rebar and fibre-optic instrumented rebar were tested using the LPT apparatus. The process of instrumenting the rebar with fibre-optic strain gauges also requires machining grooves into the rebar and removing material. Generally, the instrumentation process reduces the cross-sectional area of the rebar by less than 8%. However, the instrumentation is composed on a single fibre-optic strand epoxied down the length of the rebar in multiple passes and requires the groove to turnaround at each end of the rebar. This turnaround point removes a significant amount of steel and can reduce the cross-section area of the rebar by up to 20%. As shown in Figure 4.14, the turnaround point for the 22M (#7) and 25M (#8) Grade 400 (60) rebar had to be placed below the threads. The turnaround point for the 22M (#7) Grade 500 (75) dywidag was able to be placed at the end of the rebar and above the threaded insert.

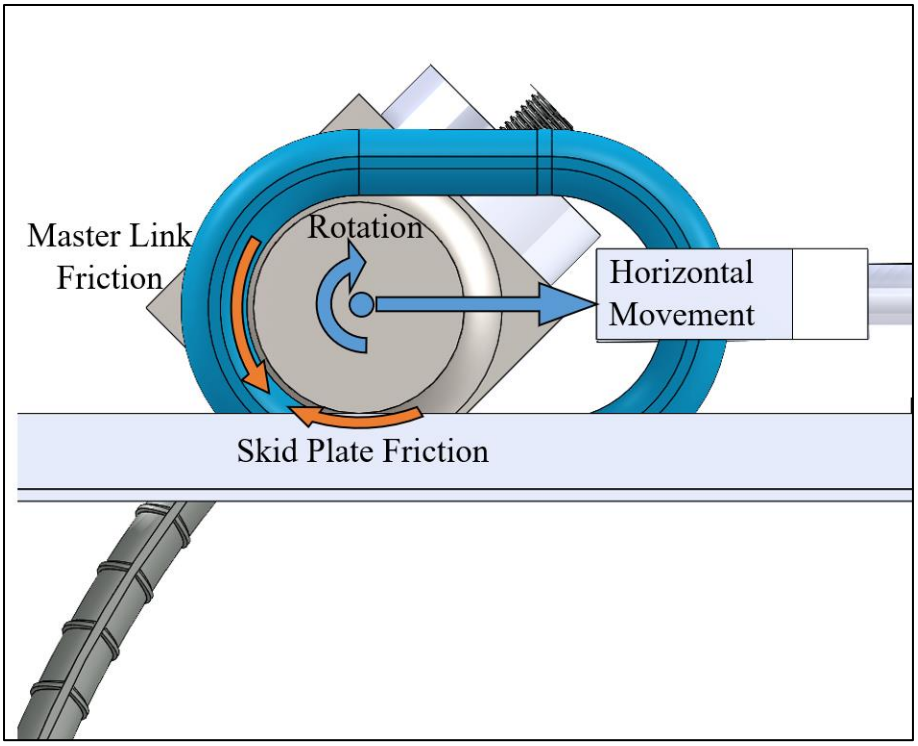

Figure 4.12. Friction sources in the lateral pull test

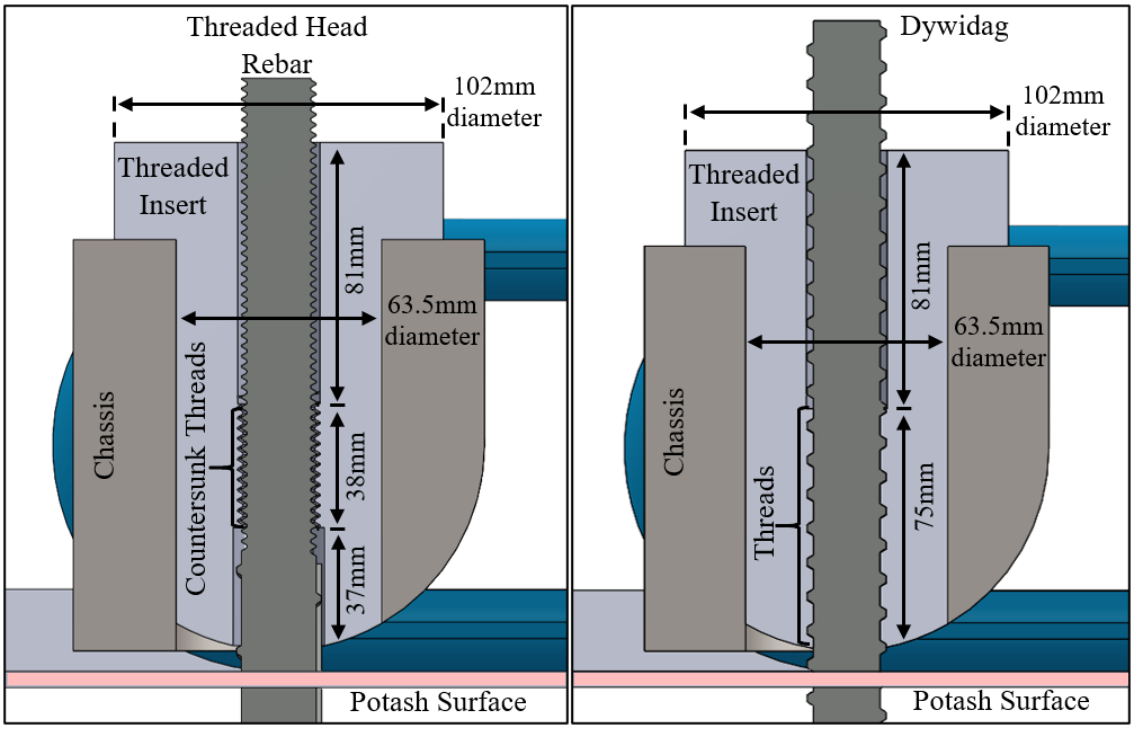

Figure 4.13. Threaded insert for 25M (#8) rebar on the left and 22M (#7) dywidag threadbar on the right

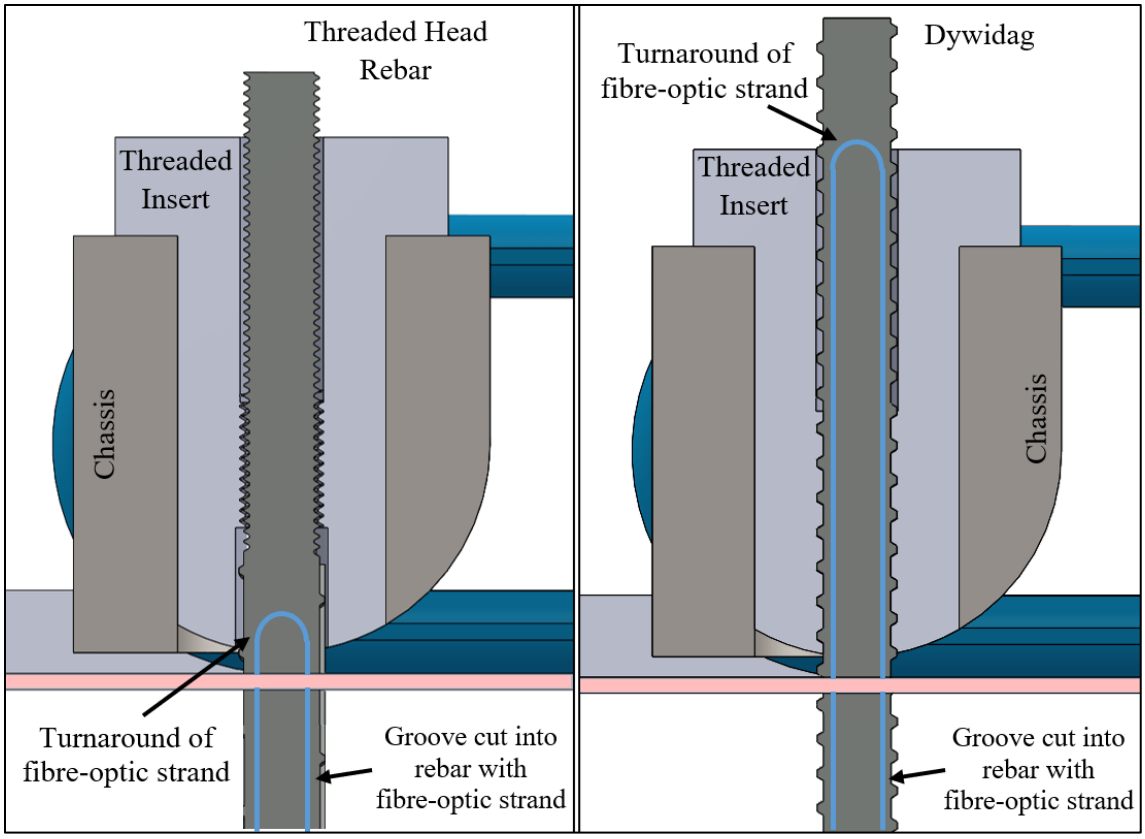

Figure 4.14. Fibre-optic instrumentation for 25M (#8) rebar on the left and 22M (#7) dywidag threadbar on the right

The tests were instrumented with two string potentiometers (string pots) and a pressure transducer. The string pots were TE Connectivity SPD-6 6-inch stroke cable actuated string potentiometers with an accuracy of 0.25%. The string pots were attached to the chassis as shown in Figure 4.15 and allowed for determination of the displacement and rotation of the chassis as the rebar deformed. The pressure transducer was from YieldPoint Inc. and was used to calculate force exerted by the hydraulic cylinder, knowing the effective area of the cylinder of 40.9 cm^2 (6.34 $in.^2$). The readings from the string pots and pressure transducer were recorded using YieldPoint Inc.'s Pulltest software at a sampling rate of 2 Hz.

The displacement and rotation of the lateral pull testing apparatus at any point during the tests can be calculated from the two string pot readings. The horizontal displacement of the testing apparatus, which is the same as the displacement of point C, is shown in Figure 4.16. This

displacement can be calculated by Equation 4.1. The geometric derivation of this equation is presented in Appendix G.

$$d_C = +h(\cos\theta_{Rotation} - \sin\theta_{Rotation}) - L_i - h + \sqrt{(L_i + \Delta L_T)^2 - (h(\sin\theta_{Rotation} + \cos\theta_{Rotation}) - h)^2}$$

Equation 4.1

Where d_C = horizontal displacement of the testing apparatus

h = chassis radius of 63.5 mm (2.5 in.)

$\theta_{Rotation}$ = rotation of testing apparatus

L_i = initial distance from chassis to string pots

ΔL_T = change in length of top string pot

The rotation of the testing apparatus is also shown in Figure 4.16. Due to the relatively rigid behaviour of the threaded insert and the chassis, the rotation of testing apparatus is assumed to be equivalent to the rotation of both point C and point O. The rotation can be calculated from Equation 4.2. Once again, the geometric derivation of this equation is shown in Appendix G. The displacement and rotation of the apparatus could not be easily isolated using Equation 4.1 and Equation 4.2. Instead, a short program was written in excel to iteratively solve for them.

$$\theta_{Rotation} = \frac{d_C - \Delta L_B}{h}$$

Equation 4.2

Where ΔL_B = change in length of bottom string pot

Last, the horizontal displacement of point O, where the rebar enters the threaded insert, can be calculated knowing the rotation and displacement of the testing apparatus. The displacement of point O can be calculated from Equation 4.3 and was derived by basic trigonometry.

$$d_O = d_c - h\sin\theta_{Rotation}$$

Equation 4.3

Where d_O = horizontal displacement of point O

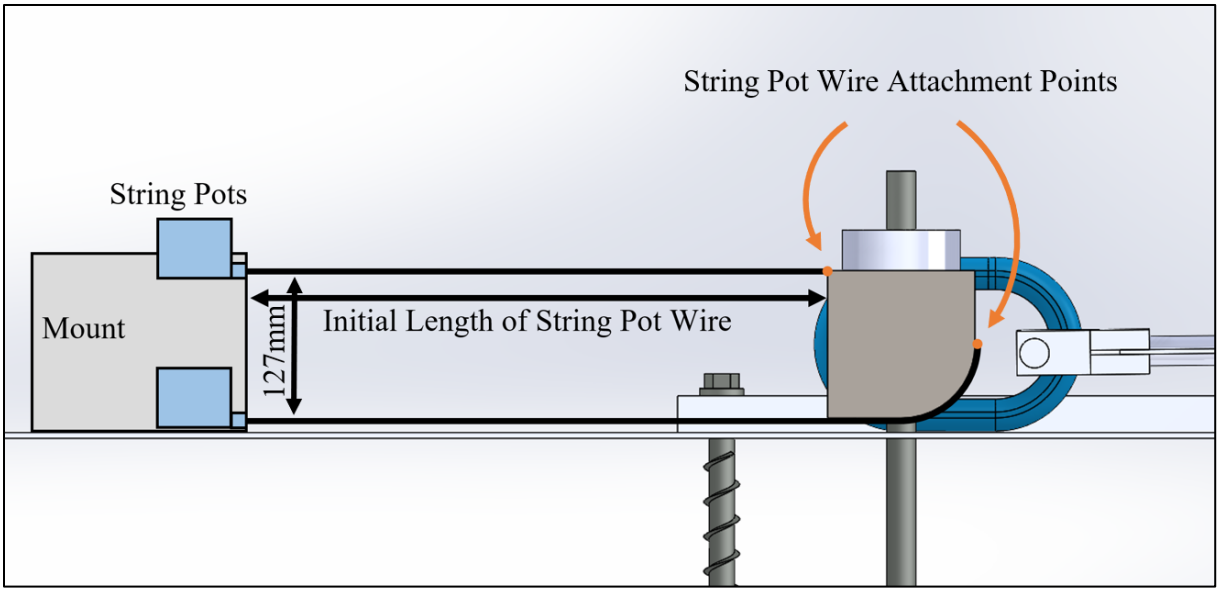

Figure 4.15. String potentiometer (string pot) setup for determining the displacement and rotation of the chassis during lateral pull testing

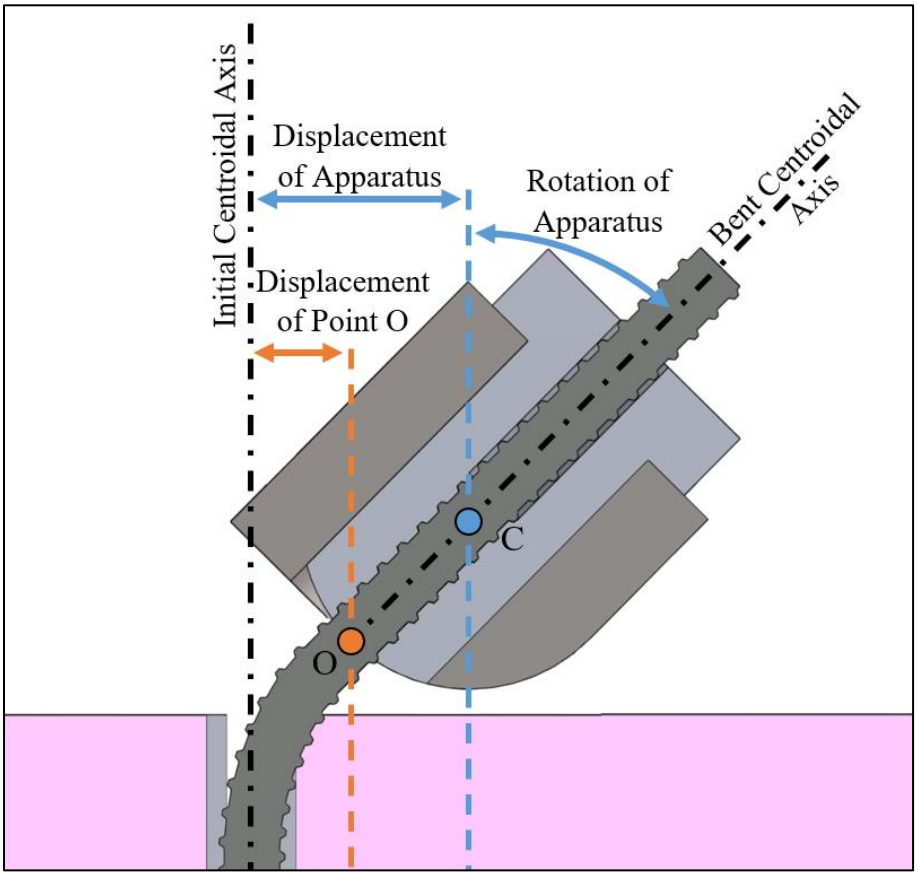

Figure 4.16. Displacement and rotation of point O and C in lateral pull tests

4.2 Nutrien Cory

All lateral pull testing took place at the Nutrien Cory mine during July and August 2017. The mine produces potash from the Upper Patience Lake Member. All tests were conducted in the floor of a production level drift. The geology in this area appeared representative of the general mineralogy for the Upper Patience Lake Member.

Nutrien Cory provided on site employment and training for this research project. The mine provided access to the generators, compressors, pluggers, and drill steel required to conduct this testing. The generators and air compressors were required to run the drills needed. Drills were used for drilling the rebar holes and spinning the rebar into the resin filled holes. Drills were also required to drill holes for the Hilti Screw Anchors that secured the lateral pull testing apparatus to the potash surface. Assistance from summer students and advice from other mine personnel was also provided by Nutrien Cory.

Careful consideration was put into determining a testing site. As this site would have rebar fragments left in the floor, the site had to be in an area that would not be re-mined in the future. However, the area needed to be maintained and stable for the period of testing and be relatively distant from any current mining activity. The floor also had to be in good condition without heavy fracturing or heaving. The separations in the floor had to be minimal as this could provide a cavity for resin to flow into. Last, attention had to be given to fire alarm access and to ensure adequate airflow in the area for drilling and resin grouting. Testing on the drift back was not considered due to safety concerns with handling and securing the heavy testing equipment.

An appropriate testing site was found at Nutrien Cory. Brattice was hung to redirect some ventilation and provide 0.95 m/s of air flow. The area was checked regularly to verify a competent back. A roughly 10 mm separation could be identified 0.76 m (2.5 ft) into the floor in some parts of the testing area, but no tests were conducted in these areas. Fire alarms were already installed within ear and eye shot of the testing area.

4.3 Lateral Pull Test Results

The lateral pull tests were completed underground at the Nutrien Cory potash mine. The testing area at the mine provided adequate ventilation and the resources, such as tools and electricity, were available to successfully complete all tests.

In total, 21 lateral pull tests were conducted. The results of these tests are presented and explained in this section. The tests were labelled using the following system:

Ex. LPT-8R-281-FO

LPT - Indicates a lateral pull test

7 or 8 - Indicates the rebar size in imperial nomenclature: 22M (#7) or 25M (#8)

R or D - Grade 400 (60) rebar or Grade 500 (75) dywidag threadbar

281 - Arbitrary number differentiating tests (generated based on testing date)

FO - Indicates tests on fibre-optic instrumented rebar

An important issue encountered during the lateral pull tests is that all tests on threaded rebar, in other words all 22M (#7) and 25M (#8) Grade 400 (60) rebar, resulted in the rebar failing along the bottom thread. The failure point is shown in Figure 4.17. This observation means that the threads cut into the rebar steel are the weakest point in the sample and the samples are failing prematurely.

Figure 4.17 also shows how the rebar penetrates into the resin and potash at the hole collar before failing. All rebar samples were observed to fail after penetrating into the resin and potash between 25 mm (1 inch) and 35 mm (1.4 inches) at the potash surface.

Another issue observed with the lateral pull tests is that, after failure, the samples appear to have a slight reverse curvature where the rebar enters the threaded insert on the lateral pull testing apparatus. This reverse curvature is shown in Figure 4.18. Figures prior to this show the generally expected behaviour of the rebar and do not depict this reverse curvature. The curvature could be due to friction forces imparting a moment on the apparatus or some other unanticipated issue with the testing apparatus.

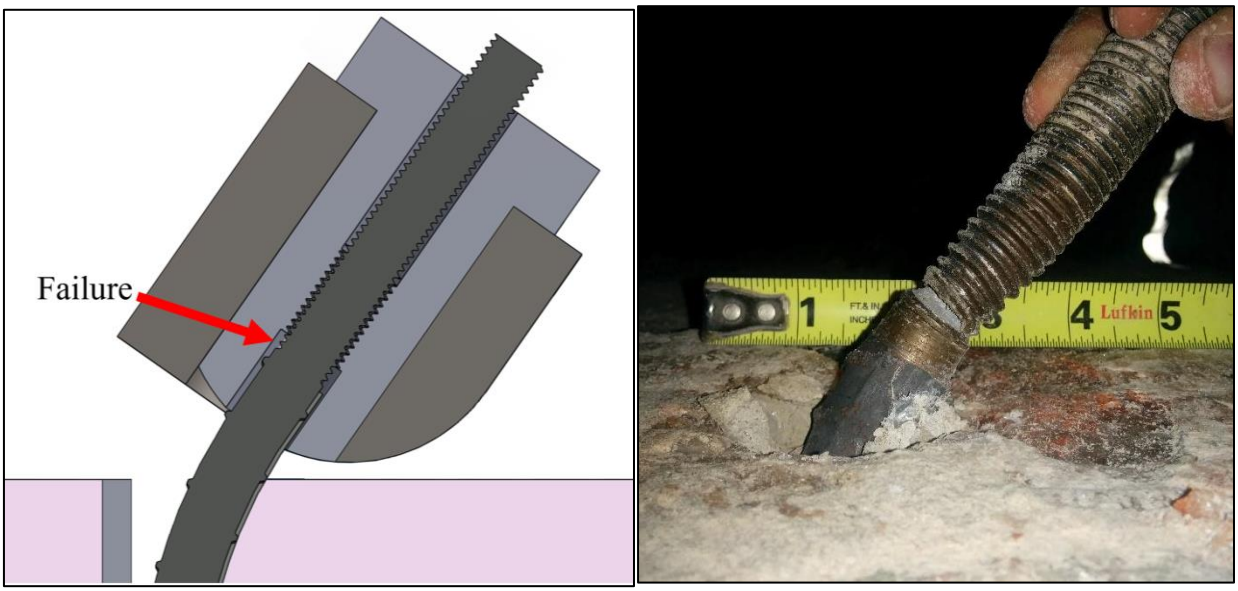

Figure 4.17. Cross-section diagram of failure point on all threaded-head rebar samples in lateral pull tests (left) and photo of failed sample LPT-7R-023 (right)

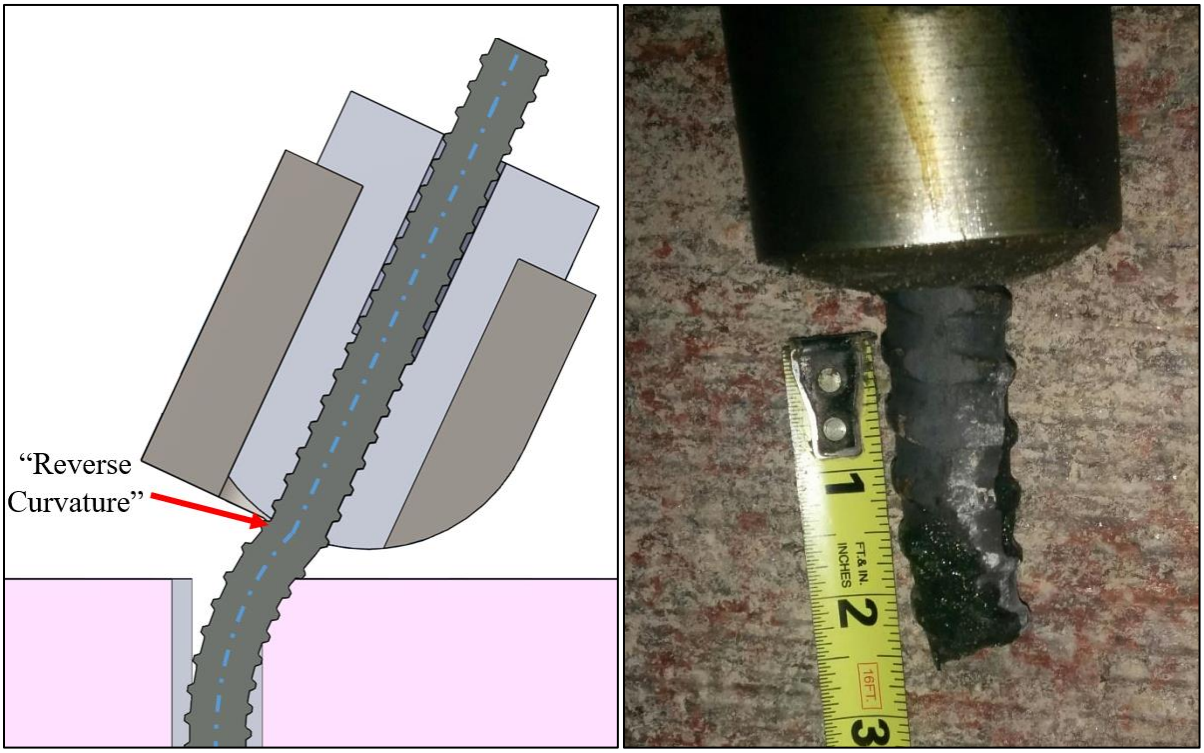

Figure 4.18. Cross-section diagram of rebar with centreline showing unexpected curvature after failure of most samples in lateral pull tests (left) and photo of failed sample LPT-7D-091 showing subtle reverse curvature (right)

Eight lateral pull tests were conducted on 22M (#7) Grade 400 (60) rebar. Two of these rebar samples were instrumented with fibre-optics in a three-groove configuration. The displacement and rotation of the tests on 22M (#7) Grade 400 (60) rebar were calculated from the string potentiometers. The applied load was plotted against the apparatus displacement in Figure 4.19. It should be noted that the measured applied load did not account for friction between the apparatus chassis and the skid plates. This applied load should be considered an overestimate and the true horizontal load is less.

As can be seen in Figure 4.19, the lateral load increased rapidly up to between 10 kN and 15 kN with little displacement. After reaching these loads, tests showed very little increase in lateral load corresponding to displacements of 15 mm to 40 mm. After this varying amount of displacement, the load then began to increase significantly once again until an ultimate load was reached. The load decreased after reaching the ultimate load and the rebar failed after roughly 5 mm of further displacement. The ultimate displacement of most samples was between 55 mm and 77 mm.

Some characteristics of the lateral pull tests on 22M (#7) Grade 400 (60) rebar are summarized in Table 4.1. The initial plateau of the lateral loads has been assumed to correlate to rebar yield. The ultimate load was taken to be the highest magnitude load recorded in the lateral pull tests and the corresponding displacement is also included in Table 4.1.

The samples all reached similar ultimate loads and failed along the lowest thread cut into the rebar, except for the fibre-optic instrumented rebar which failed along the fibre-optic groove. The threads of the rebar had a reduced cross-sectional area and provided the weakest point in the rebar for failure to occur. The fibre-optic instrumented samples failed at much lower loads than rebar without instrumentation. This premature failure is believed to be caused by the grooves cut into the rebar to accommodate the fibre-optic instrumentation and the turnaround point which reduces the cross-sectional area by up to 20%.

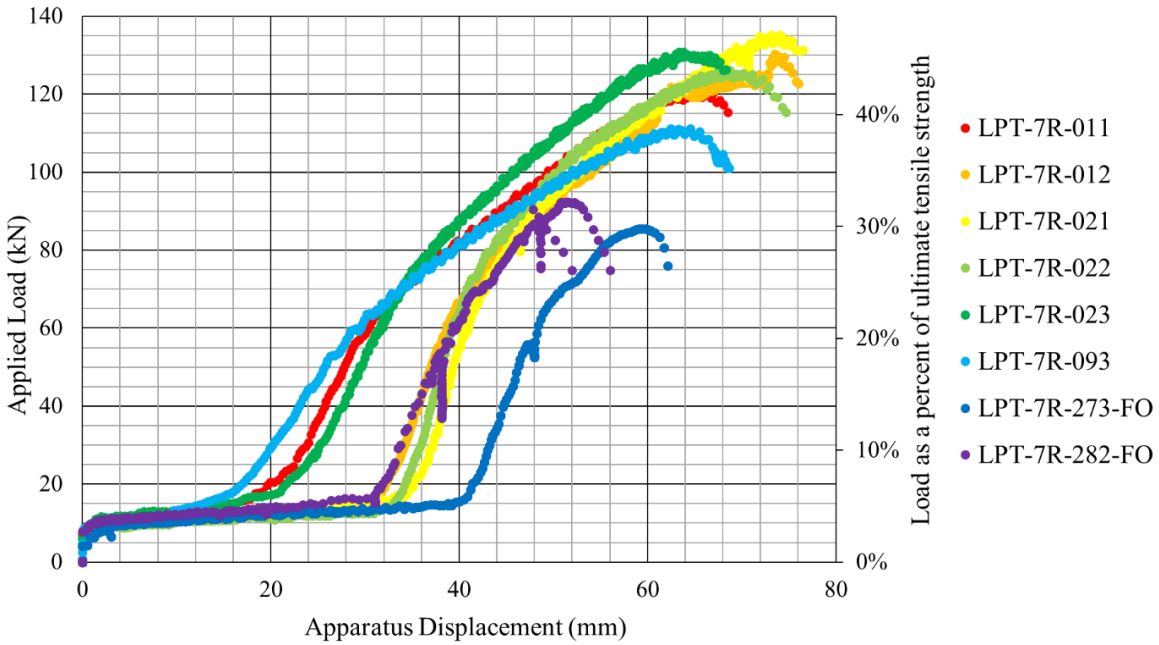

Figure 4.19. Applied load vs displacement for lateral pull tests on 22M Grade 400 rebar

Table 4.1. Summary of characteristics of lateral pull tests on 22M Grade 400 rebar

Test Number	Yield Load kN [tonnes]	Ultimate Load kN [tonnes]	Apparatus Displacement at Ultimate Load mm	Apparatus Rotation at Ultimate Load degrees	Displacement of Point O at Ultimate Load mm
LPT-7R-011	11 [1.1]	121 [12.3]	64.6	31.4	31.5
LPT-7R-012	11 [1.1]	130 [13.3]	73.5	34.5	37.5
LPT-7R-021	10 [1.1]	135 [13.8]	73.1	32.5	39.0
LPT-7R-022	9 [0.9]	126 [12.9]	67.5	28.8	36.9
LPT-7R-023	12 [1.2]	131 [13.3]	63.4	29.9	31.7
LPT-7R-093	10 [1.0]	111 [11.3]	64.5	31.1	31.7
LPT-7R-273-FO	9 [1.0]	86 [8.7]	59.3	31.8	25.8
LPT-7R-282-FO	11 [1.1]	92 [9.4]	51.5	28.8	20.9
Mean*	10 [1.0]	126 [12.8]	67.8	31.4	34.7

*Excluding fibre-optic instrumented samples

A total of five lateral pull tests were conducted on 25M (#8) Grade 400 (60) rebar. One of these tests were conducted on rebar instrumented with fibre-optic in a three-groove configuration. The applied loads are plotted against the calculated apparatus displacements in Figure 4.20 and important characteristics of the tests are summarized in Table 4.2. It should be noted that the measured applied load did not account for friction between the apparatus chassis and the skid plates. This applied load should be considered an overestimate and the true horizontal load is less.

The lateral load of each test once again appears to plateau between 10 kN and 20 kN. The load then begins to increase again at displacements varying between 10 mm and 40 mm. The samples all reached ultimate lateral load of 150 kN to 200 kN and failed at a range of displacements from 65 mm to 85 mm.

The tests reached a load of 160 kN to 200 kN before the samples failed, with the exception of the fibre-optic instrumented rebar which had an ultimate load of approximately 150 kN. Once again, the un-instrumented rebar samples failed at the lowest thread due to the reduced cross-sectional area of the threads. Similarly, the fibre-optic instrumented sample failed along the groove at the turnaround point for the fibre-optic instrumentation since it reduces the cross-section area of the rebar by up to 20%.

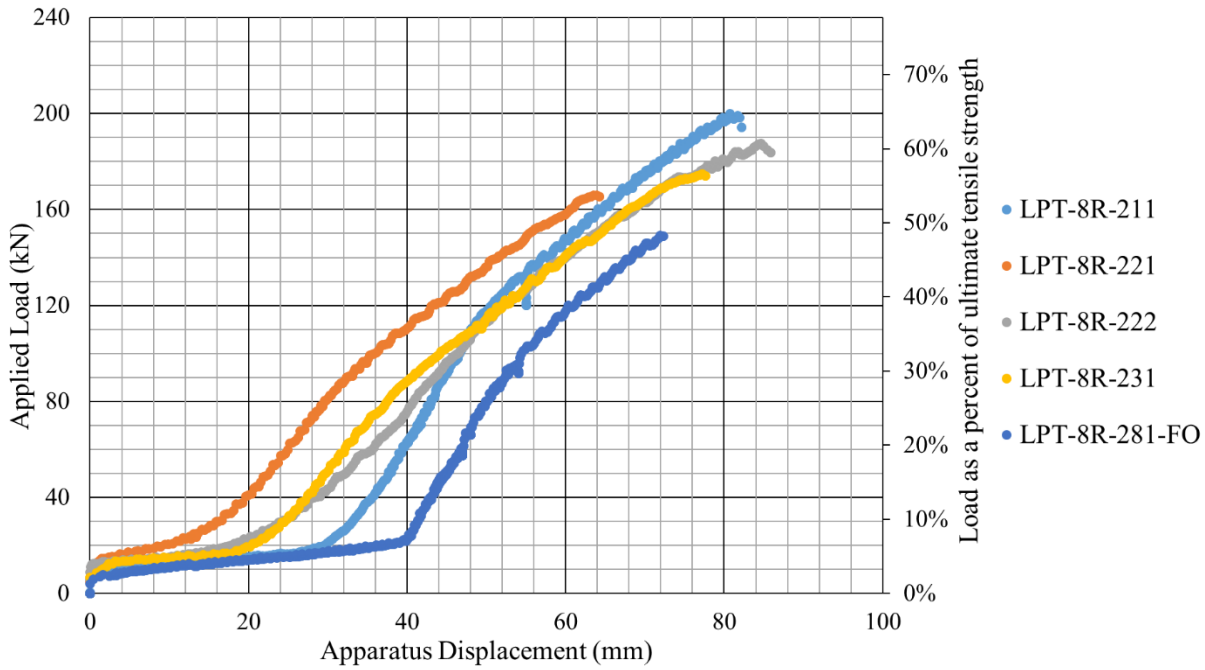

Figure 4.20. Applied load vs displacement for lateral pull tests on 25M Grade 400 rebar

Table 4.2. Summary of characteristics of lateral pull tests on 25M Grade 400 rebar

Test Number	**Yield Load kN [tonnes]**	**Ultimate Load kN [tonnes]**	**Apparatus Displacement at Ultimate Load mm**	**Apparatus Rotation at Ultimate Load degrees**	**Displacement of Point O at Ultimate Load mm**
LPT-8R-211	13 [1.3]	200 [20.4]	80.7	31.0	48.0
LPT-8R-221	15 [1.5]	166 [16.9]	63.5	27.8	33.9
LPT-8R-222	13 [1.3]	188 [19.1]	84.6	29.9	52.9
LPT-8R-231	14 [1.4]	175 [17.8]	77.2	31.7	43.8
LPT-8R-281-FO	8 [0.8]	149 [15.2]	71.9	30.0	40.2
Mean*	14 [1.4]	182 [18.6]	76.5	30.1	44.7

*Excluding fibre-optic instrumented samples

A total of eight lateral pull tests were conducted on 22M (#7) Grade 500 (75) dywidag threadbar. Two tests were conducted on fibre-optic instrumented samples. As discussed previously, the lateral pull tests on dywidag threadbar did not have the drawbacks that the threaded-head rebar tests did. Specifically, the rebar ribs acted as the threads as opposed to having threads cut into the rebar and the fibre-optic instrumentation extended well into the threaded insert of the apparatus rather than having the turnaround point below the insert. The dywidag samples did not suffer these drawbacks and did not fail prematurely during the lateral pull tests.

Qualitatively, the dywidag samples all failed below the potash surface, as opposed to failing where the sample entered the threaded insert of the testing apparatus which was the case for all tests on Grade 400 (60) rebar. The samples all failed roughly 3 cm below the potash surface.

The load versus displacement plots of all lateral pull tests on dywidags are shown in Figure 4.21 and important behaviour characteristics are summarized in Table 4.3. It should be noted that the measured applied load did not account for friction between the apparatus chassis and the skid plates. This applied load should be considered an overestimate and the true horizontal load is less.

As with the previous tests, the tests on 22M Grade 500 dywidags exhibited the same load plateau at between 10 kN and 20 kN applied load. After between 10 mm and 40 mm of displacement, the load then increased substantially until the samples ultimately failed.

A noticeable difference in these tests is that the ultimate load for most tests is higher than previously seen. Viewed as a percent of the ultimate tensile load of the rebar type, the applied load is considerably higher than lateral pull tests on Grade 400 (60) rebar likely because the dywidag did not have threads cut into the rebar. The fibre-optic instrumented samples once again, had a reduction in strength. However, the reduction in strength does not appear as substantial as for the 22M (#7) and 25M (#8) Grade 400 (60) rebar samples likely due to the geometry of the fibre-optic instrumentation grooves.

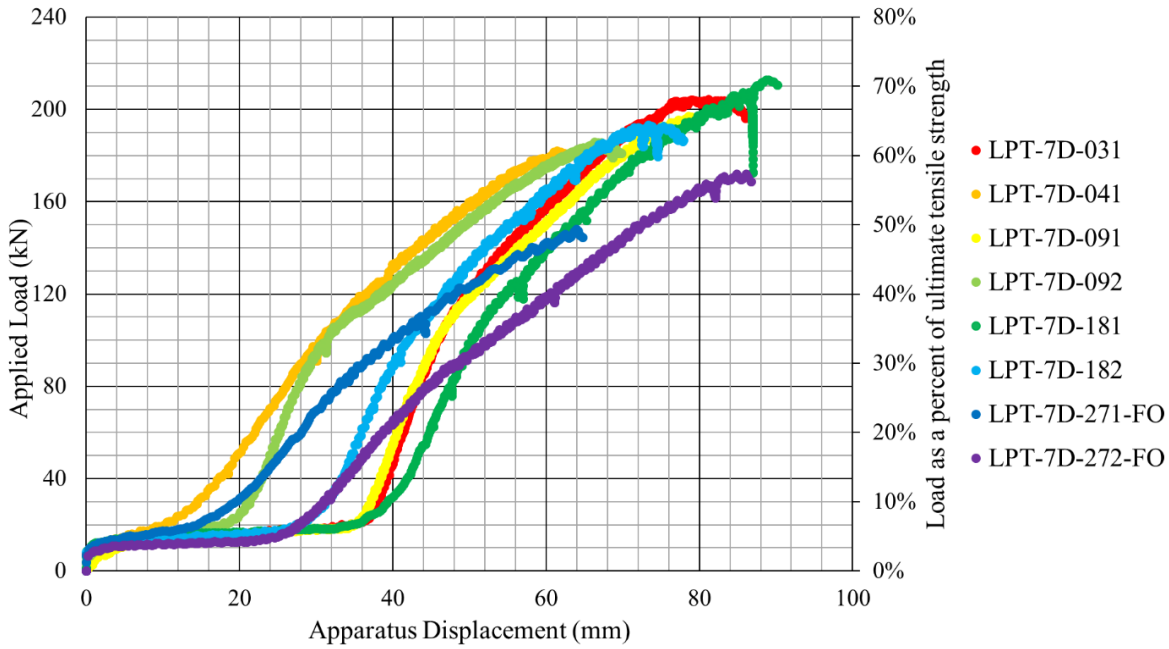

Figure 4.21. Applied Load vs displacement for lateral pull tests on 22M Grade 500 dywidag

Table 4.3. Summary of characteristics of lateral pull tests on 22M Grade 500 rebar

Test Number	**Yield Load kN [tonnes]**	**Ultimate Load kN [tonnes]**	**Displacement at Ultimate Load mm**	**Rotation at Ultimate Load degrees**	**Displacement of Point O at Ultimate Load mm**
LPT-7D-031	13 [1.3]	204 [20.8]	81.2	33.5	46.2
LPT-7D-041	11 [1.1]	182 [18.6]	61.4	27.6	32.0
LPT-7D-091	12 [1.2]	197 [20.1]	78.5	32.5	44.4
LPT-7D-092	12 [1.2]	186 [18.9]	66.3	28.0	36.5
LPT-7D-181	14 [1.5]	213 [21.7]	89.0	34.8	52.8
LPT-7D-182	12 [1.2]	193 [19.7]	73.3	31.5	40.1
LPT-7D-271-FO	12 [1.2]	148 [15.1]	63.9	29.3	32.8
LPT-7D-272-FO	10.4 [1.1]	172 [17.5]	84.8	32.6	50.6
Mean*	12.3 [1.3]	196 [20.0]	75.0	31.3	42.0

*excluding fibre-optic instrumented samples

All lateral pull tests exhibited plateaus where the displacement and rotation increased without a significant increase in lateral load. The plateaus were not expected and could suggest an issue with the lateral pull testing apparatus. Furthermore, the widely varying amount of displacement and rotation that occurs during these load plateaus between tests on similar rebar suggests the cause is not controlled or constant between the tests.

A possible explanation for the load plateaus and their varying amount of displacement and rotation is shown in Figure 4.22. In this figure, the apparatus chassis was not in full contact with the skid plates at the start of the lateral pull test. A lack of firm contact between these two pieces would allow for additional movement of the chassis with only a slight increase in load on the rebar. An effort was made during apparatus installation to ensure the chassis was properly seated on the skid plates, but some misalignment was inevitable due to the design of the testing apparatus. Future iterations of the apparatus design should allow for fine adjustment of the skid plates after anchoring them. This would allow the operator to ensure the apparatus and skid plates are aligned and in full contact.

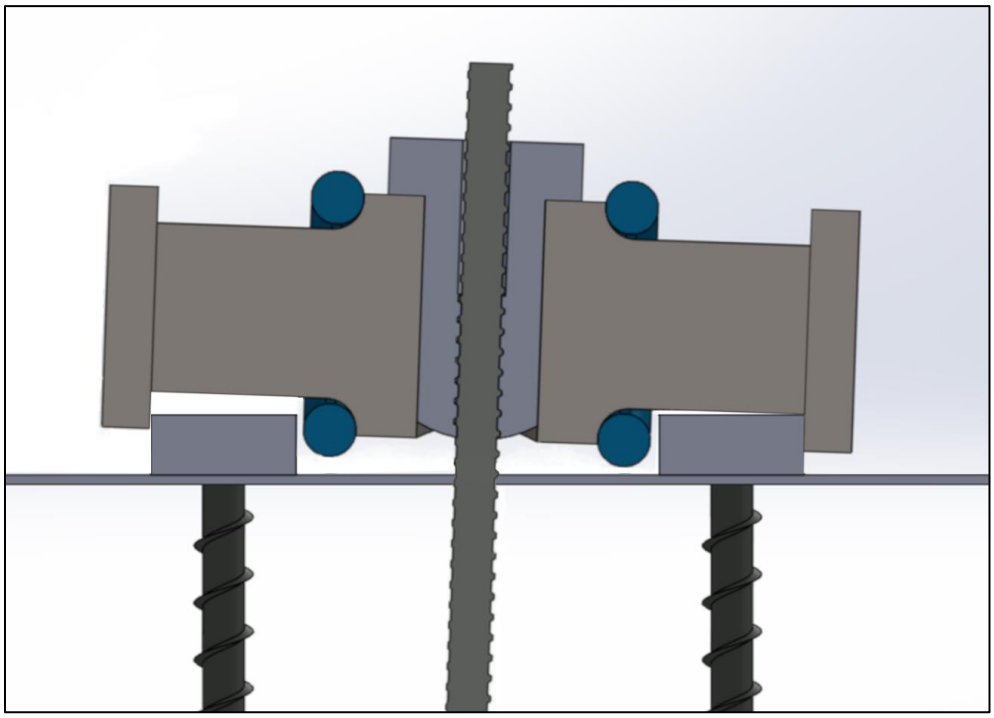

Figure 4.22. Lateral pull testing chassis not properly seated on the skid plates is a possible reason for the plateaus in load-displacement behaviour

4.4 Analysis Methods of Fibre-optic Instrumented Rebar

Five of the lateral pull tests previously discussed were performed on fibre-optic instrumented samples. All fibre-optic instrumented rebar were instrumented in a three-groove configuration. The strain readings from these tests were analyzed in a similar manner as the double shear tests on the instrumented rebar samples. Some of the basic equations used in the analysis are presented in Section 3.1.3 where they were first used and an extensive derivation is included in Appendix D and E.

Equations 3.5 to 3.9 were used to analyse the fibre-optic strain readings and determine the distribution and magnitude of strain within the rebar throughout each test. First, the strain readings provided by the fibre-optic instrumentation were used to determine the direction of bending relative to the fibre-optic strands. The direction of bending then allowed for the calculation of the minimum, maximum, and axial strain within the rebar at every 0.65 mm increment along the rebar length.

The lateral pull tests were developed for this project and the fibre-optic instrumentation provided further insight into how well the tests are performing. The strain readings from the fibre-optic instrumentation were used to estimate the internal bending moment within the rebar. The expected internal bending moment distribution within the rebar are shown in Figure 4.23.

The internal bending moment can be used to calculate the shear force within the rebar. The internal shear force in the small length of rebar between the lateral pull testing apparatus and the potash surface should be equivalent to the lateral force being applied to the rebar. This force is calculated for lateral pull tests on fibre-optic instrumented rebar and compared to the measured lateral load.

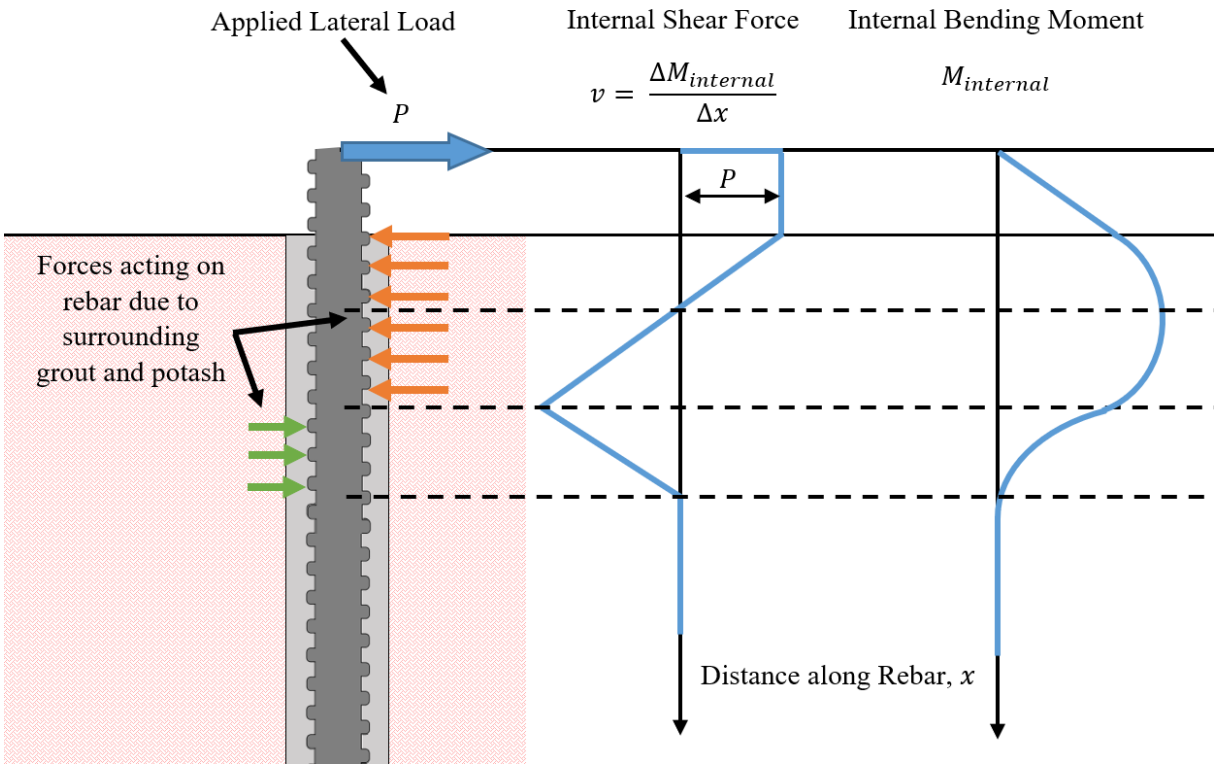

Figure 4.23. Forces acting on rebar and the resulting internal shear forces and internal bending moments within rebar during lateral pull tests

4.5 Results of Fibre-optic Instrumented Rebar

In total, five lateral pull tests were conducted on fibre-optic instrumented rebar. Results from the fibre-optic instrumentation are presented in this section and additional test results can be found in Appendix K. Two tests were conducted on the fibre-optic instrumented 22M (#7) Grade 400 (Grade 60) rebar. One test was conducted on the fibre-optic instrumented 25M (#7) Grade 400 (Grade 60) rebar. Two tests were conducted on the fibre-optic instrumented 22M (#7) Grade 500 (Grade 75) dywidag threadbar.

Due to the threaded end for attaching the lateral pull testing apparatus, the fibre-optic instrumentation needed to have a turnaround point below these threads for instrumented Grade 400 samples. The turnaround point causes additional material to be removed immediately below the threaded length and, as a result, the rebar all failed lateral loads roughly 25% lower than rebar

without fibre-optic instrumentation. Additionally, the fibre-optic instrumentation only extended roughly 1 cm out of the potash surface and did not provide significantly useful results. The fibre-optic strain readings were not analyzed for any tests on Grade 400 (Grade 60) rebar.

The instrumented 22M (#7) Grade 500 (Grade 75) dywidag threadbar, on the other hand, provided unique insight into the behaviour of the rebar during the lateral pull test. Because the dywidag threadbar uses large course deformations as threads, the fibre-optic instrumentation was able to be run along the entire length of the dywidag starting within the testing apparatus. Only the fibre-optic strain readings from 22M (#7) Grade 500 (Grade 75) dywidag threadbar were analyzed.

The strain was measured using the fibre-optic instrumentation throughout each test at a rate of 10 Hz. Unfortunately, the fibre-optic instrumentation is only operable up to roughly 1% strain which was surpassed at roughly 25 kN of lateral load in each test. The fibre-optic instrumentation provided 0.65 mm resolution strain readings at a rate of 10 Hz prior to this limit.

The strain readings at the beginning of test LPT-7D-271-FO are shown in Figure 4.24. For simplicity, only the upper 0.6 m of the strain readings are shown in this figure. As can be seen, the rebar has significant strain near the collar of the hole before any load is applied with the hydraulic cylinder. This strain is due to tightening the turnbuckles between the hydraulic cylinder and the chassis which imparted some initial lateral load to the rebar despite 0 kN being recorded. Future iterations of the lateral pull test should attempt to reduce this initial load.

The strain readings shown in Figure 4.25 are for test LPT-7D-271-FO with 10 kN of lateral load applied. At this load, the test was beginning to enter the plateau region of the load-displacement relation seen in Section 4.3. At this point in the test, it can be clearly seen that all strains are localized near the collar of the hole. There is no significant strain exhibited more than roughly 15 cm into the potash surface.

The strain readings from the fibre-optic instrumentation were used to calculate the strain throughout the rebar. Figure 4.26 shows the calculated strains of test LPT-7D-271-FO with 10 kN of applied lateral load. At this point in the test, the strain at the front edge and back edge of the

rebar is passing -2000 micro-strain (compressive) and 2000 micro-strain (tensile), respectively. The strain values are approximately the strain at which the rebar yields. This suggests the rebar is beginning to yield when it enters the initial plateau discussed in Section 4.3. Similar results were found for test LPT-7D-272-FO.

The internal bending moments along the rebar were calculated from the fibre-optic strain readings and are displayed in Figure 4.27. Only the internal bending moments for the upper 0.2 m are shown since the bending moments below this point were insignificant. As can be seen, the distribution of internal bending moment is very similar to what was expected and displayed in Figure 4.23.

A linear trendline was fitted to the bending moments shown in Figure 4.27 between 0.01 m and 0.02 m along the rebar length. In this area, the rebar is expected to have a constant internal shear force equal to lateral force being applied to the rebar. The slope of the moment, with respect to the distance along the rebar, theoretically equals the internal shear force and the applied lateral load.

The shear force calculated from the fibre-optic instrumentation is plotted against the applied lateral force for tests LPT-7D-271-FO and LPT-7D-272-FO in Figure 4.28. As can be seen, the fibre-optic instrumentation provided a reasonable estimate for the applied load. It should be noted that data with zero applied load was excluded from the plot due to the initial lateral load that wasn't accurately measured. Data beyond 13 kN of applied lateral load was also excluded from this plot since the calculated strains suggest the rebar has yielded beyond this point and the material behaviour can no longer be considered linear elastic.

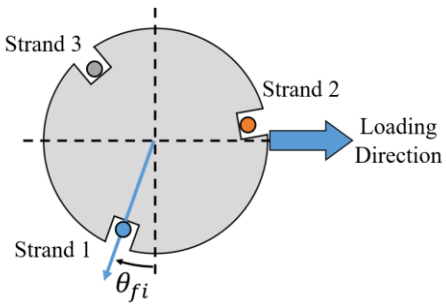

a) Cross-section A-A'

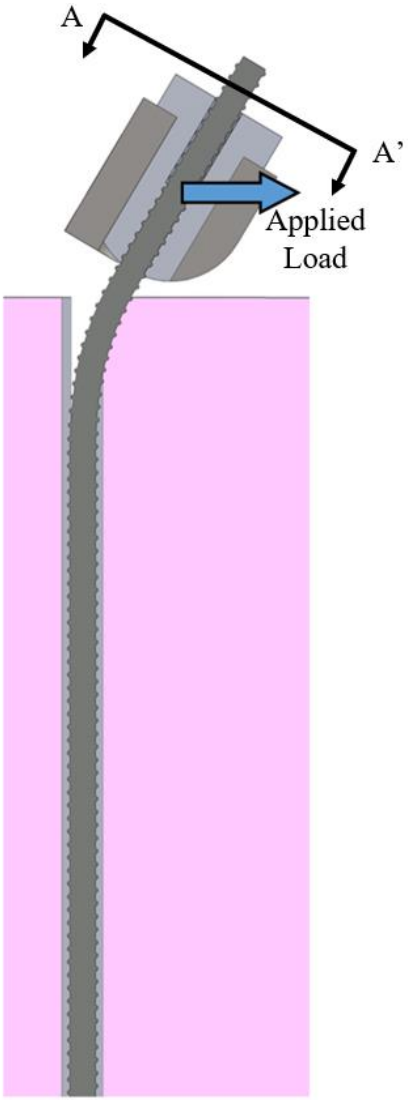

b) Long-section

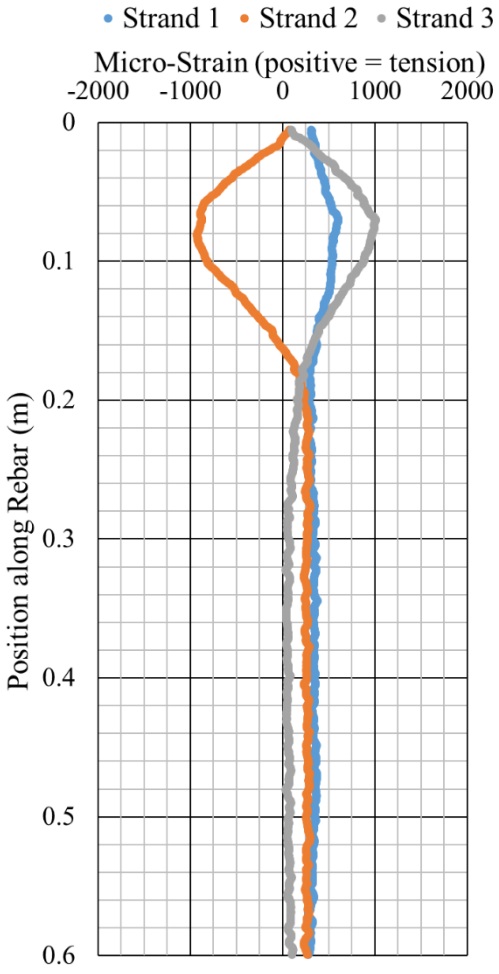

c) Fibre-optic strain readings

Figure 4.24. Fibre-optic instrumented rebar at the beginning of test LPT-7D-271-FO with 0 kN applied lateral load. Figure shows a) the cross-section of instrumented rebar, b) the long-section view of the lateral pull test, and c) the strain readings from the fibre-optic instrumentation.

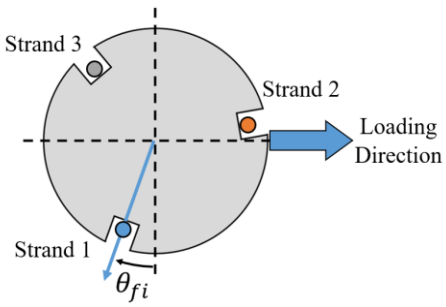

a) Cross-section A-A'

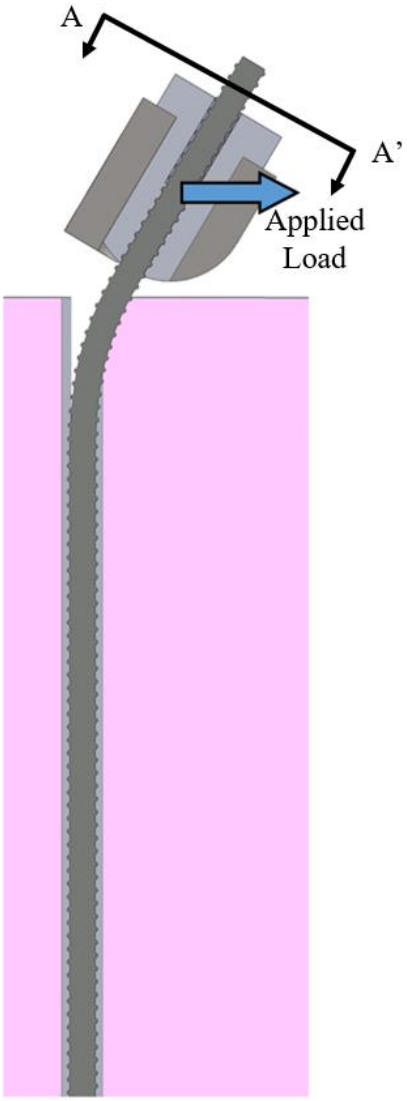

b) Long-section

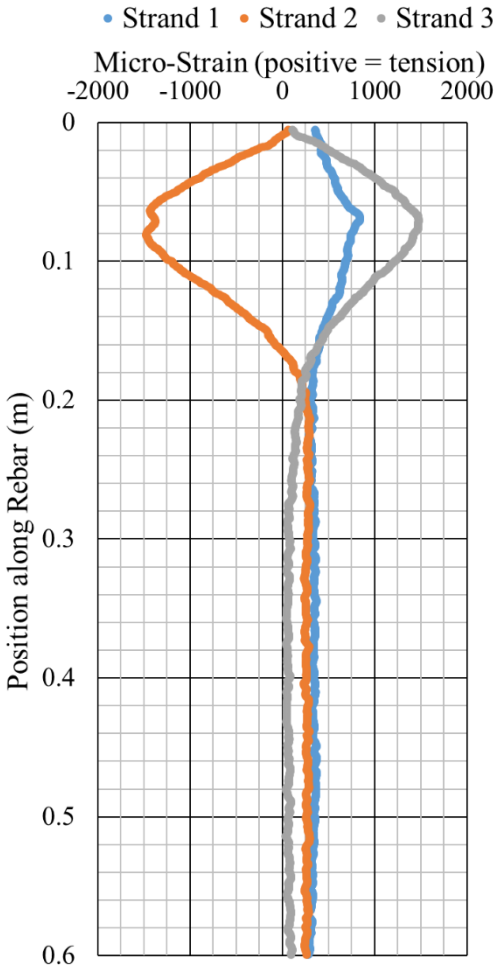

c) Fibre-optic strain readings

Figure 4.25. Fibre-optic instrumented rebar in test LPT-7D-271-FO with 10 kN applied lateral load. Figure shows a) the cross-section of instrumented rebar, b) the long-section view of the lateral pull test, and c) the strain readings from the fibre-optic instrumentation.

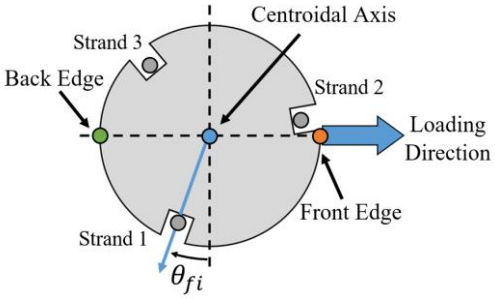

a) Cross-section A-A'

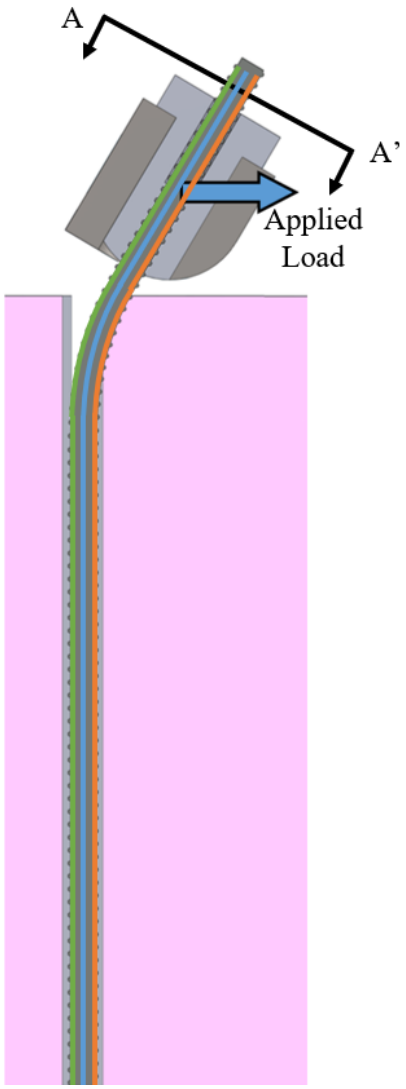

b) Long-section

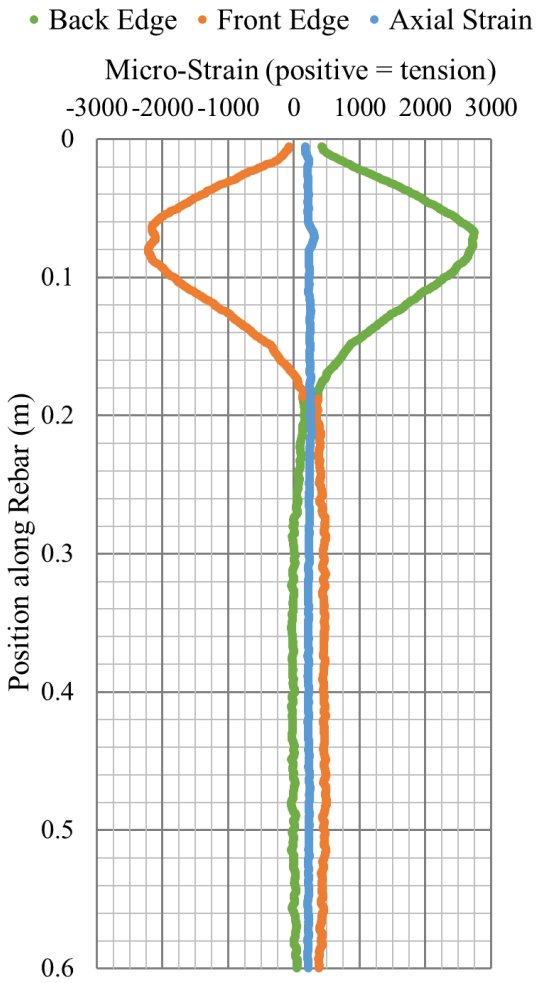

c) Calculated strains

Figure 4.26. Fibre-optic instrumented rebar in test LPT-7D-271-FO with 10 kN applied lateral load. Figure shows a) the cross-section of instrumented rebar, b) the long-section view of the lateral pull test, and c) the calculated strain from the fibre-optic instrumentation.

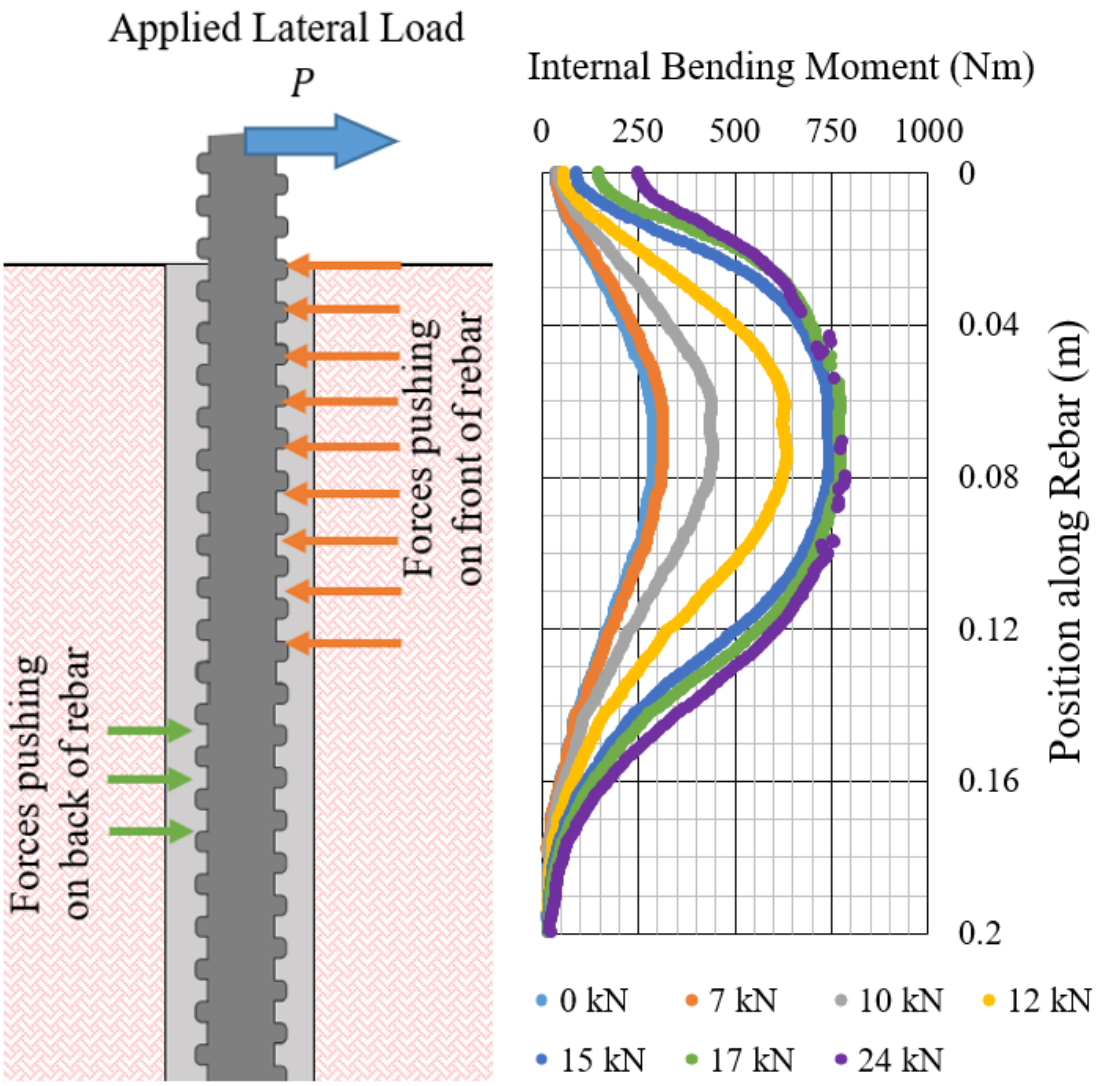

Figure 4.27. Internal bending moments calculated from fibre-optic instrumentation for test LPT-7D-271-FO at various applied lateral loads. Only bending moments near the upper end of the bolt are shown here.

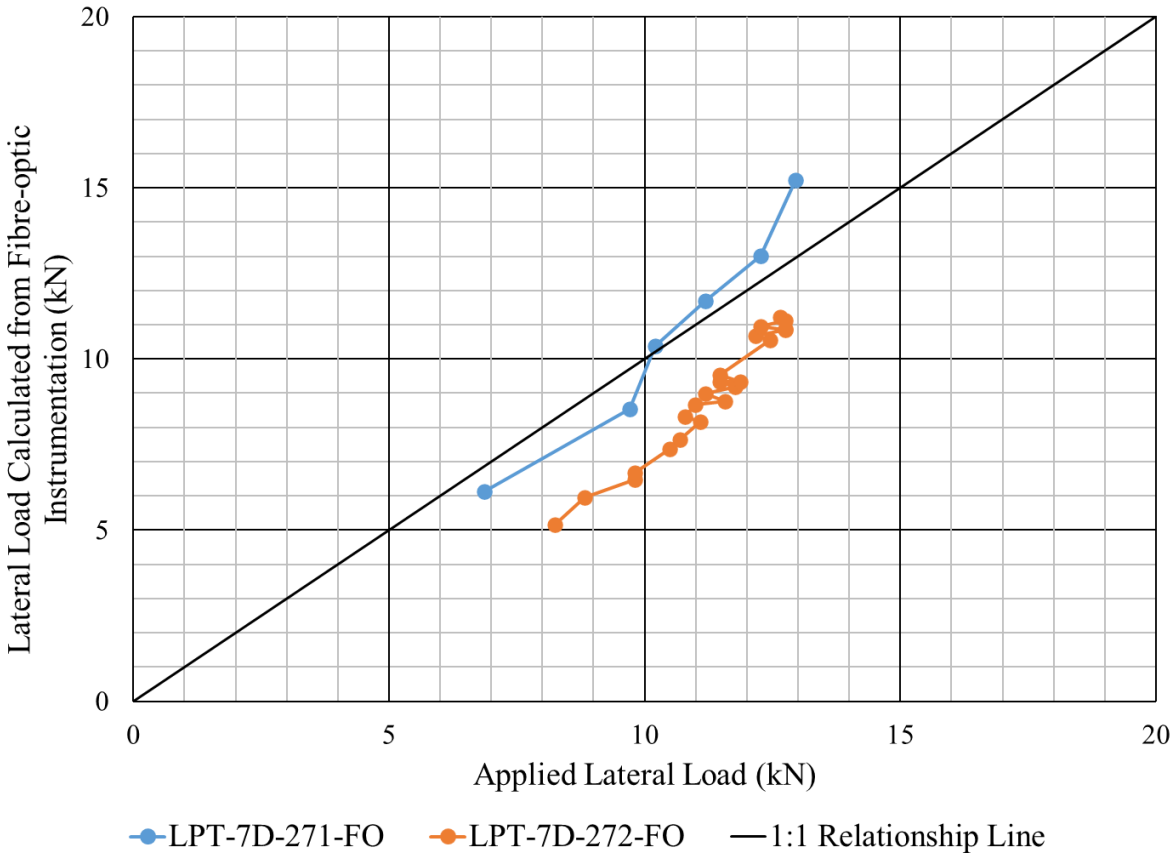

Figure 4.28. Calculated lateral load from fibre-optic instrumentation plotted against measured lateral load for tests LPT-7D-271-FO and LPT-7D-272-FO with less than 13 kN applied lateral load.

4.6 Conclusions

In conclusion, the lateral pull tests have a few issues that need to be addressed in future iterations of the testing apparatus. There were possible issues with friction imparting some bending moment on the testing apparatus. Also, there is some evidence the apparatus chassis was not initially tight against the skid plates which seems to have altered the behaviour of the rebar. It is not clear how these factors affected the test results.

The lateral pull tests resulted in rebar yielding at very low loads and displacements. The ultimate lateral loads of the 22M (#7) Grade 500 (Grade 75) dywidag threadbars tested were between 60%

and 70% of their ultimate tensile load. The corresponding displacements of the testing apparatus were between 61 mm and 89 mm.

The fibre-optic instrumentation used in the lateral pull tests was only useable for a short period at the start of the lateral pull tests. The rebar strain goes beyond the instrumentation limits at very low loads and displacement. The fibre-optic instrumentation did allow for identification of the applied load and lateral displacement at which the rebar yielded. The instrumentation has also suggested the initial plateau of the load-displacement behaviour exhibited by the rebar is caused by yielding of the rebar.

The distribution of the internal bending moment could be calculated from the fibre-optic instrumentation and suggested all rebar bending occurs in the upper 0.2 m of the rebar during the initial stages of the test. The internal bending moments were able to be used to approximate the lateral load being applied to the rebar to within roughly 40% of the measured value.

Future iterations of the lateral pull testing apparatus design should attempt to make three improvements. Roller bearings should be incorporated into the apparatus design. Specifically, bearings should be used to reduce the friction between the chassis and the skid plates, as well as between the chassis and the master links. Future designs should also incorporate a method to finely adjust and align the testing apparatus. Last, future designs should attempt to reduce the distance between point O and point C as much as possible. This means trying to get the centre of rotation, the centre of load application, and the point at which the rebar exits the testing apparatus to coincide.

5 IN SITU FIBRE-OPTIC INSTRUMENTED REBAR

For this monitoring program, the deformation was measured for standard installation and in situ shear loading conditions, but the loads applied to the rebar could not be measured. The in situ instrumentation measured the shear deformation behaviour of rebar crossing a shear plane in a potash mine, which helped determine if the lab and field tests have been reasonably successful at approximating field conditions.

Rebar rock bolts were instrumented with fibre-optics in a three-groove configuration and were installed in the three Saskatoon area mines described in Section 1.2. The goal of this instrumentation was to observe the in situ behaviour of fully-grouted rebar rock bolts in shear. Areas of various mines that exhibited shear movement were evaluated based on expected access to area, non-anomalous geology, and timing relative to project deadlines. Three installation sites were then chosen at the Mosaic Colonsay, Nutrien Vanscoy, and Nutrien Allan potash mines. The rock bolts were installed using the same procedure that mining operations currently use and in areas of the mines exhibiting shear movement.

At each installation site, two instrumented rebar rock bolts were installed in the same area. This is not a statistically significant sample size but was meant to serve as preliminary testing to investigate how the instrumented rebar performed with in situ conditions. One rebar was a 25M (#8) Grade 400 (Grade 60) forged-head rebar and the other was a 22M (#7) Grade 500 (Grade 75) dywidag threadbar to provide results for two of the most widely used rebar in mining.

The rebar was supplied by DSI and then instrumented by YieldPoint Inc. All rebar was 2.44 m long to increase the likelihood of the rebar intersecting shear planes and achieving an adequate bond strength on either side of the shear planes. YieldPoint Inc. made low-profile fibre-optic readout connections at the rock bolt heads to fit into all bolter chucks during installation. Figure 5.1 shows the low-profile connector for a forged-head rebar.

The fibre-optic readings were analyzed using the theory derived in Appendix D and E, and first described in Section 3.1.3. This analysis involved first plotting the strain readings from the fibre-

optic strands. Then the minimum, maximum, and axial strain of the rebar could be calculated using Equations 3.5 to 3.9. These strain values give an indication of the behaviour of the rebar under these in situ conditions as well as the time at which the rebar begins yielding. The results of the fibre-optic analysis are presented throughout this section. Additional test results can be found in Appendix L.

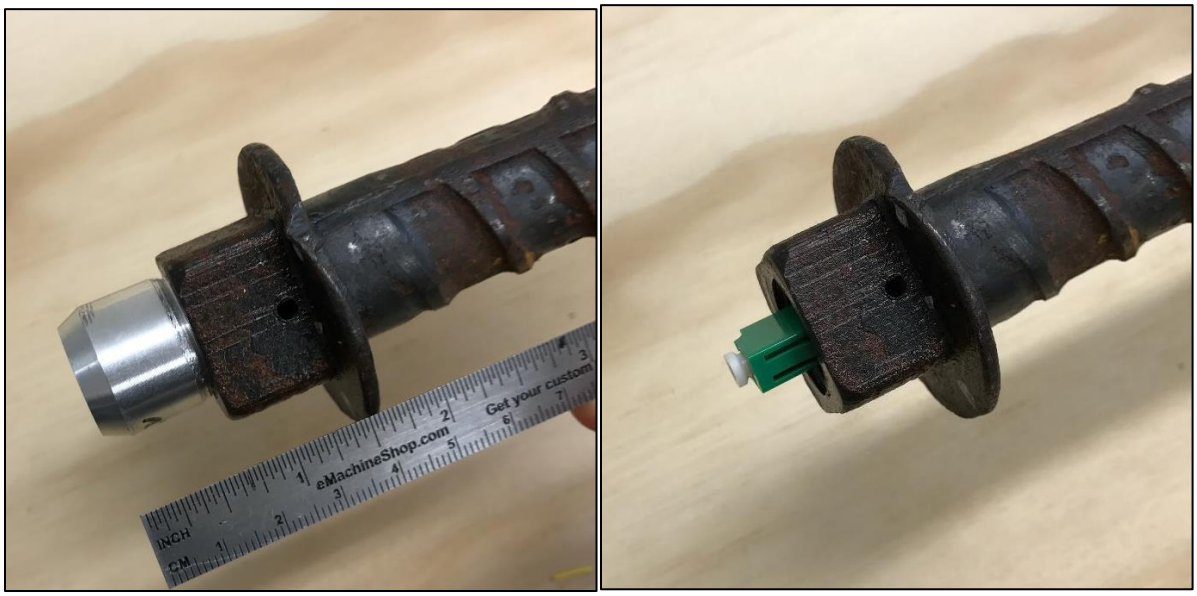

Figure 5.1. Low-profile fibre-optic connector on forged-head rebar with/without protector cap

Figure 5.2. Fibre-optic connector on dywidag with protector cap

5.1 Mosaic Colonsay Potash Mine

The first fibre-optic instrumentation installation occurred at the Mosaic Colonsay mine on March 9, 2017. The mine had a drift subjected to significant stress in the back. The decision was made by mine site personnel to slot cut the back to prevent buckling of the immediate roof beam. The slot cut provided a cavity for the potash layers to shear into, as was discussed in Section 1.1.2. The mineralogy of the potash in the area appeared to be typical of the Upper Patience Lake Member, as described in Section 1.1.1. The area was also in a main travel-way, so long-term safe access would be maintained.

The rebar were installed with a bolting machine and bolting crew, as shown in Figure 5.3. Rock bolt holes were drilled with a 35 mm diameter rotary drill bit to a length of approximately 2.3 m. The holes were slightly shorter than the rebar but it was the longest available drill rod. After drilling the holes, seven 28 mm diameter by 305 mm long two-part FasLoc resin cartridges were put into each hole. The rebar were then inserted into the holes with the bolting machine. The rebar were spun as they were inserted and then spun for approximately five seconds, as per the manufacturer instructions.

Figure 5.4 and Figure 5.5 show the position of the rebar relative to the slot cut in plan view and cross-sectional view of the drift, respectively. The slot-cut was cut about 1.6 m deep and 0.3 m wide. Both instrumented rebar were installed approximately 0.36 m from the edge of the slot cut and roughly 4m apart.

The approximate orientations of the fibre-optic instrumented rebar are shown in Figure 5.6. The orientation of the fibre-optic strands relative to the direction of shearing should be reflected in the strain readings gathered.

Figure 5.3. Bolting machine installing instrumented rebar at Mosaic Colonsay

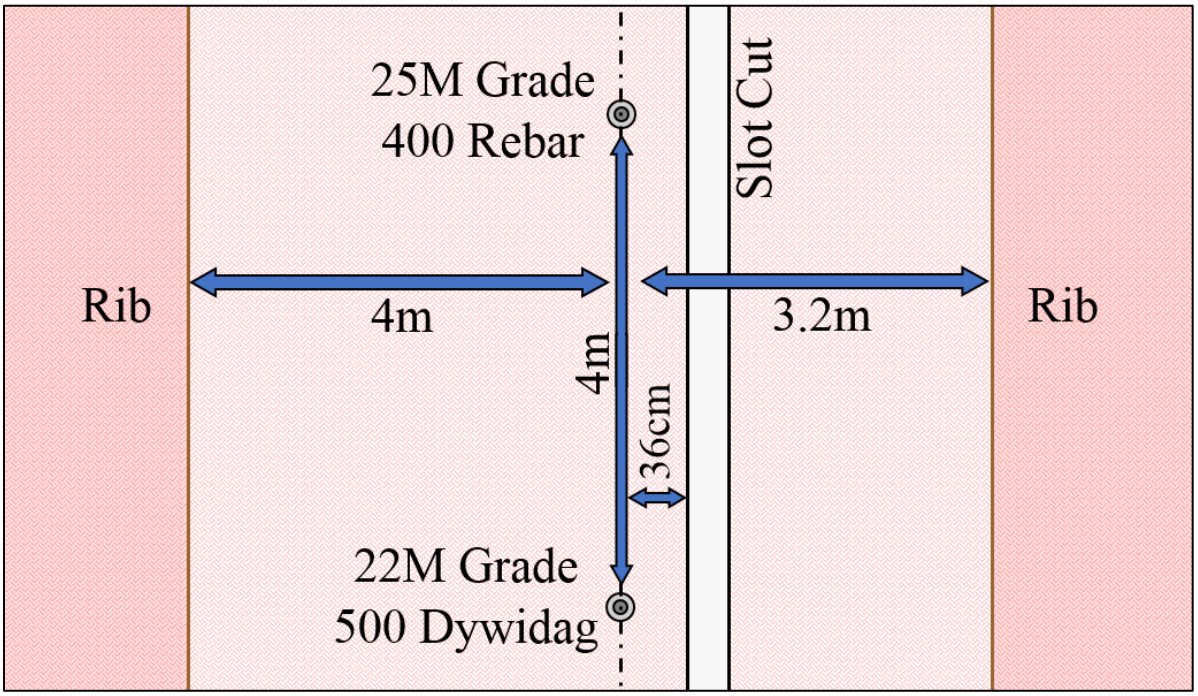

Figure 5.4. Plan view of the installation of instrumented rebar at Mosaic Colonsay

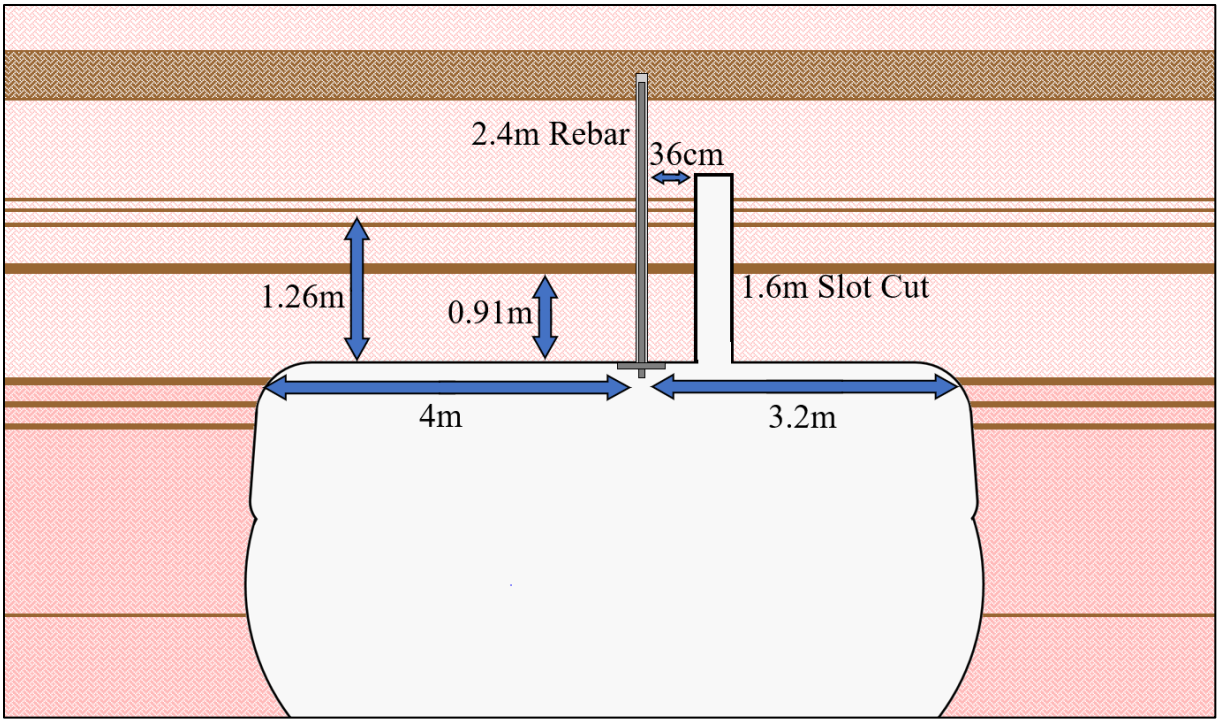

Figure 5.5. Cross-sectional view of the drift where instrumented rebar was installed at Mosaic Colonsay

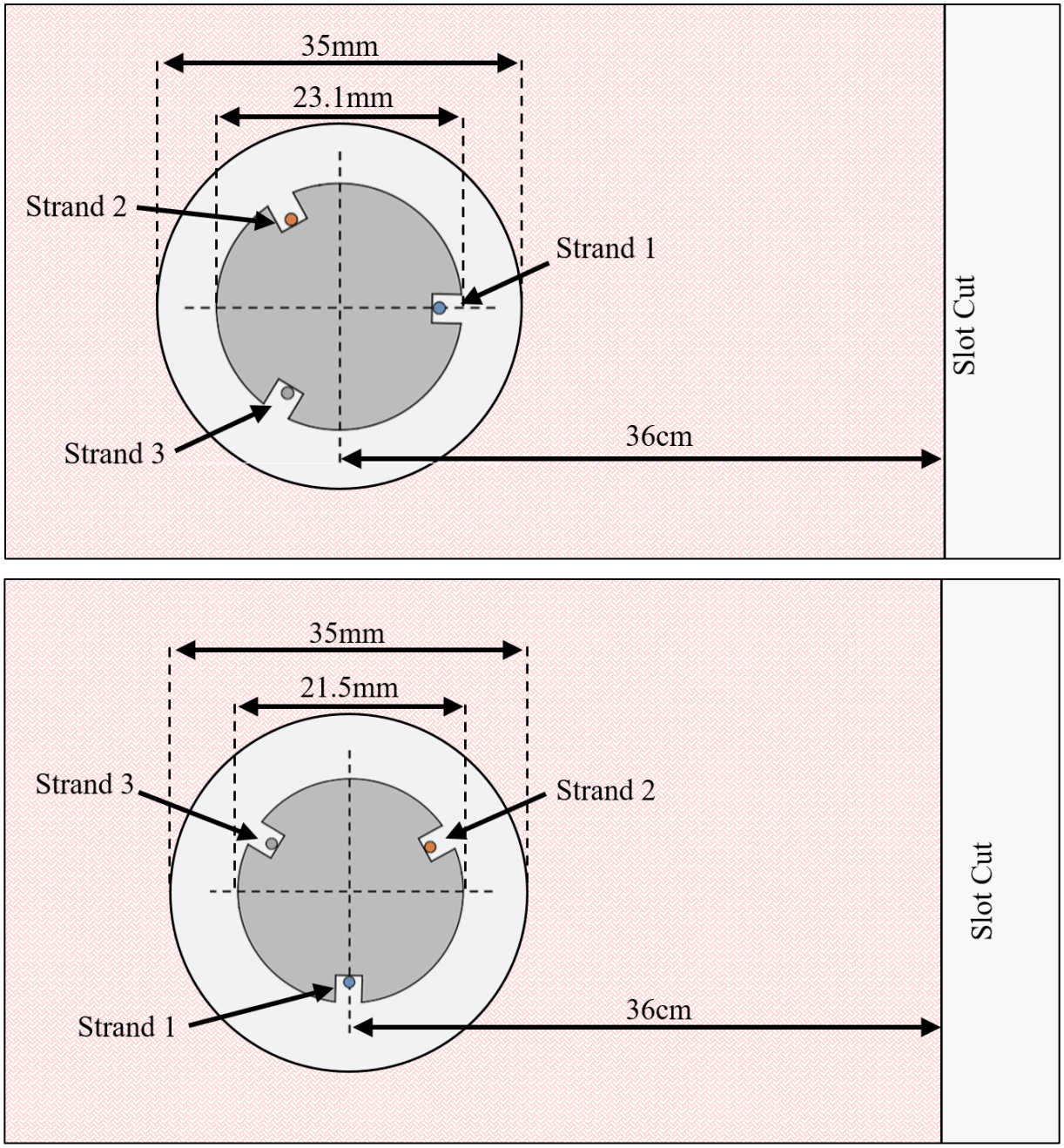

Figure 5.6. Plan view orientation of fibre-optic strands on instrumented 25M Grade 400 rebar (top) and 22M Grade 500 dywidag (bottom) relative to the slot cut in plan view (not to scale)

5.1.1 Results of Fibre-optic Instrumented Rebar

The two instrumented rebar were installed at Mosaic Colonsay on March 9, 2017. Five subsequent instrumentation readings were made based on the availability of the researcher and mining staff. The dates and relative timing of these readings are summarized in Table 5.1.

Table 5.1. Time frame of instrumentation program at Mosaic Colonsay

	Installation	Reading 1	Reading 2	Reading 3	Reading 4	Reading 5
Date	March 9, 2017	March 30, 2017	April 25, 2017	May 24, 2017	June 20, 2017	October 17, 2017
Time since installation	0 days	21 days	47 days	76 days	103 days	222 days

The results from the six instrument readings for 25M (#8) Grade 400 (Grade 60) rebar, including at installation, are displayed in Figure 5.7. These are the micro-strain readings from the fibre-optic instrumentation after filtering out erroneous values and averaging the remaining strain values. As can be seen, there are large differential strains (up to ~300 micro-strain) between 1.1 m and 1.8 m along the rebar as time progresses.

The readings in Figure 5.7 were used to calculate the maximum, minimum, and axial strain at each 0.65 mm increment along the rebar. The maximum and minimum strains are assumed to occur on the extreme outer edges of the rebar, according to the theory and calculations summarized in Section 3.1.3 and developed in Appendix E. The calculated strains for select readings are presented in Figure 5.8 and all calculated strains can be found in Appendix L. The extreme edges of the rebar have been arbitrarily named Side 1 and Side 2 in Figure 5.8 for convenience**.** A rough interpretation of the strain results and the resulting rebar shapes has also been included in this figure.

At 21 days after installation, a shear plane developed at 1.65 m along the rebar. This is identifiable by large magnitude strains in the arbitrarily named Side 1 and Side 2 that are roughly equal but opposite polarity (compressive vs tensile). The magnitudes of strain switch polarity on either side of the shear plane.

Tensile testing included in Appendix B measured the 25M Grade 400 rebar yield strain to be approximately 2000 micro-strain. At 47 days after installation, the rebar began to yield on either side of the initial upper shear plane. This is identifiable by the strain readings exceeding +/-2000 micro-strain in Figure 5.8. The upper shear plane at this time could be observed to have roughly a few millimeters of shear displacement based on a nearby monitoring hole.

A second shear plane also began to develop at around 1.25 m along the rebar at 47 days. Although this shear plane developed later, the magnitude of strain on either side of the shear plane is greater than the initial shear plane at 222 days after installation. At 76 days after installation, the rebar has begun to yield at 1.35 m, where the strain exceeds +/-2000 micro-strain (Figure 5.8).

An interesting result seen in Figure 5.8 is the distribution of bending strain between the bolt collar and 1.25 m along the rebar. There is significant compressive (negative) and tensile (positive) strain in this length of the rebar. The strain is distributed along the rebar a significant distance from the lower shear plane.

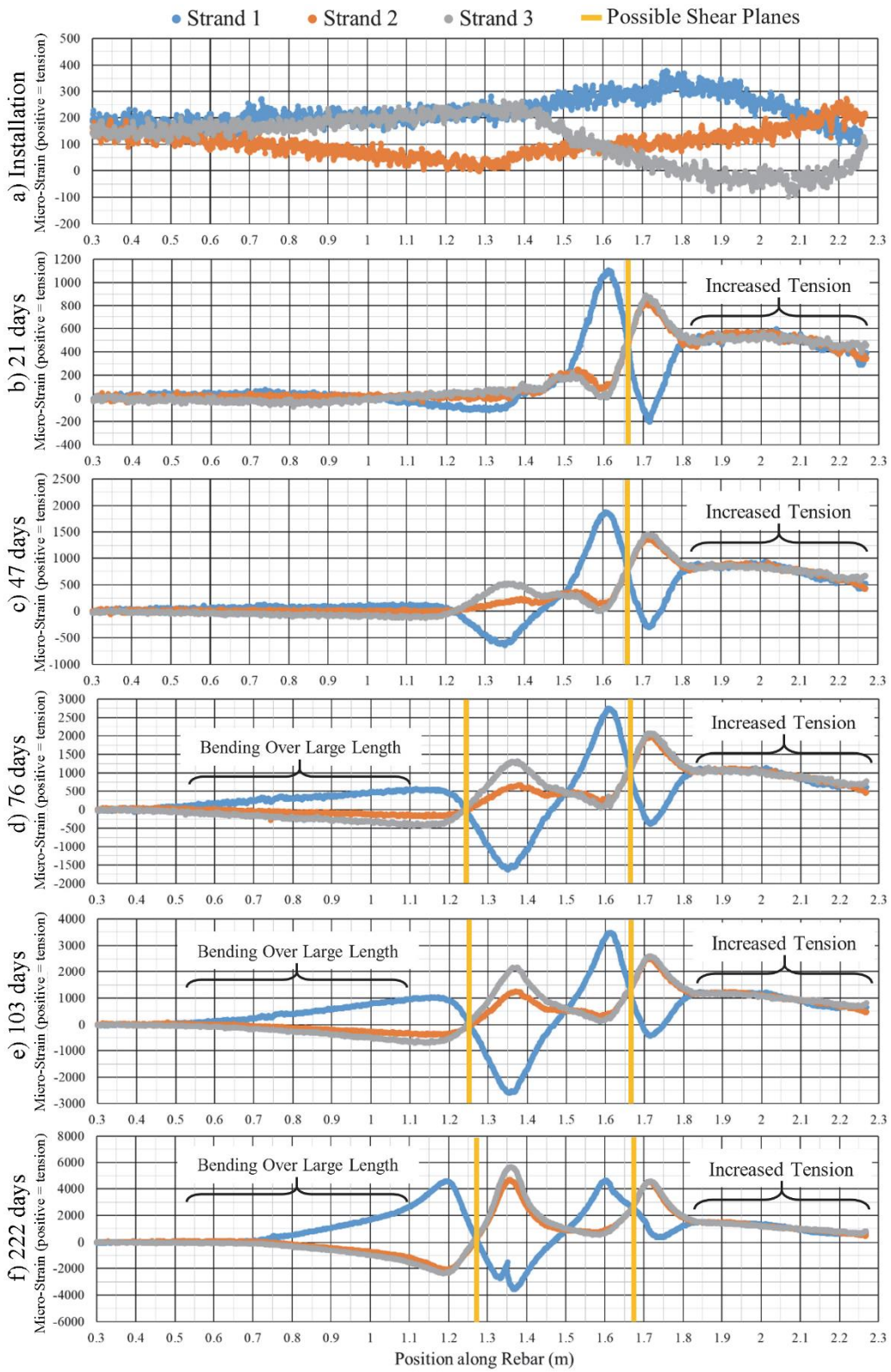

Figure 5.7. Strain readings from fibre-optic instrumentation in 25M Grade 400 rebar at Mosaic Colonsay at a) installation, b) 21 days, c) 47 days, d) 76 days, e)103 days, and f) 222 days.

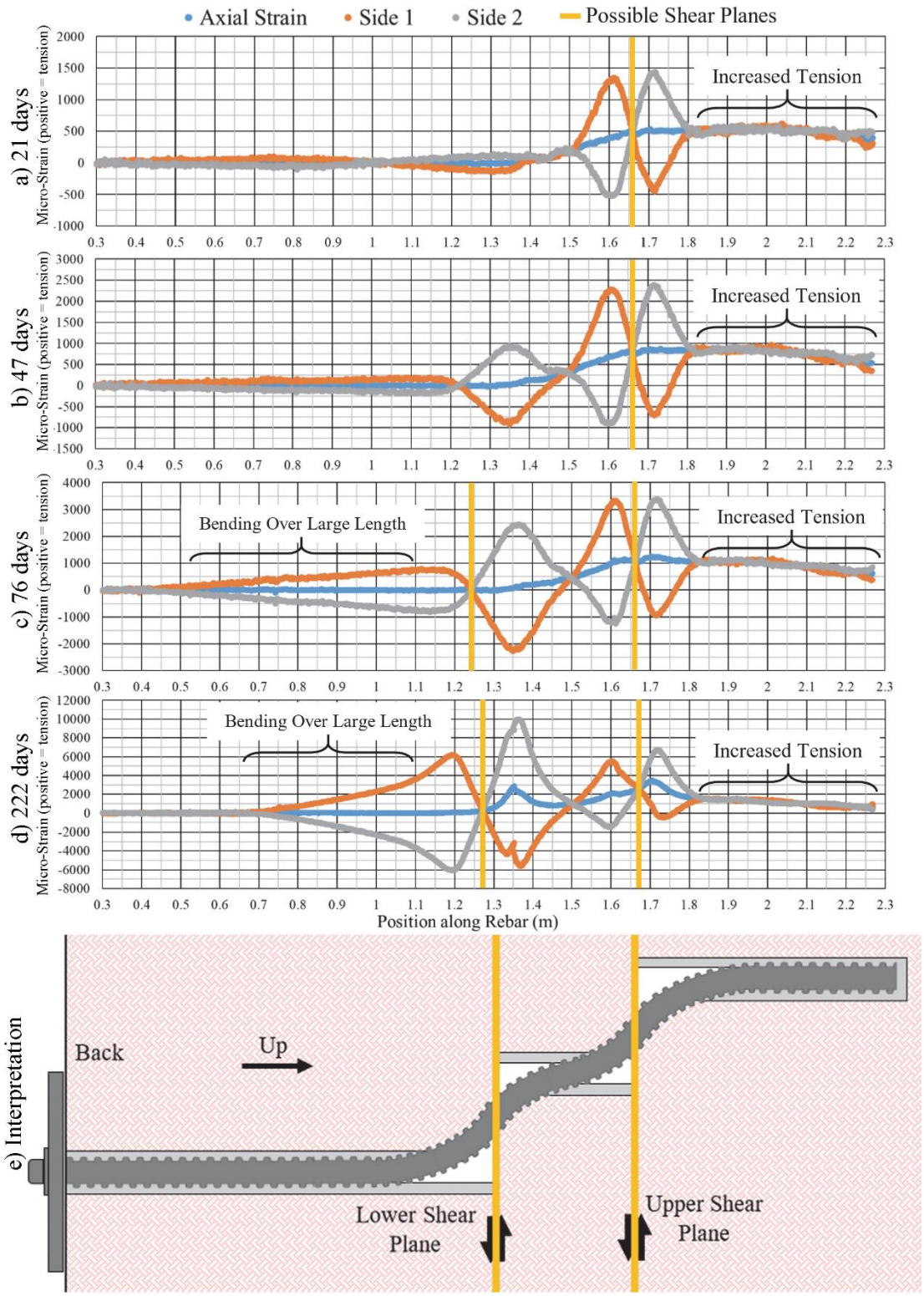

Figure 5.8. Strain along centroidal axis and extreme edges of rebar calculated from fibre-optic instrumentation in 25M Grade 400 rebar at Mosaic Colonsay at a) 21 days, b) 47 days, c) 76 days, and d) 222 days. e) shows an approximate interpretation of the rebar shape (not to scale).

The results from the six readings for 22M (#7) Grade 500 (Grade 75) instrumented dywidag are displayed in Figure 5.9. Once again, the areas with high tensile and compressive strains occur between 1.1 m and 1.8 m along the dywidag. Unlike the 25M (#8) Grade 400 (Grade 60) rebar, two shear planes are formed at the same time. The two shear planes immediately began deforming the dywidag at approximately 1.30 m and 1.62 m along the dywidag.

The strains along the centroidal axis and at the extreme edges of the rebar were calculated from the fibre-optic strain readings and select reading results are displayed in Figure 5.10. Calculated results for all readings can be found in Appendix L. A rough interpretation of the strain readings and resulting dywidag shape is also included in Figure 5.10.

At 21 days after installation, the dywidag began to yield on either side of the lower shear plane (1.30 m) and was close to yielding on either side of the upper shear plane (1.62 m). Yielding occurs at roughly 2500 micro-strain in the Grade 500 (Grade 75) dywidag, as seen in the testing included in Appendix B. At this time, the shear displacement of the shear planes could be observed to be roughly a few millimeters in a nearby monitoring hole.

There is a noticeable increase in axial strain in the area around the shear planes, but this axial strain decreases away from the shear planes. The bending strains also decrease quickly away from the shear planes. The quickly decreasing strains are due to the dywidag transferring internal forces through the epoxy grout and into the surrounding potash. This suggests the dywidag has an adequate bond strength along its length that is capable of transferring loads generated by shear planes.

As was observed in the 25M (#8) Grade 400 (Grade 60) rebar, the 22M (#7) Grade 500 (Grade 75) instrumented dywidag shows a gradually increasing magnitude of compressive and tensile strains on either side of the two shear planes as time progresses. This is due to the time dependant shear displacement of the shear planes and corresponding bending of the rebar and dywidag.

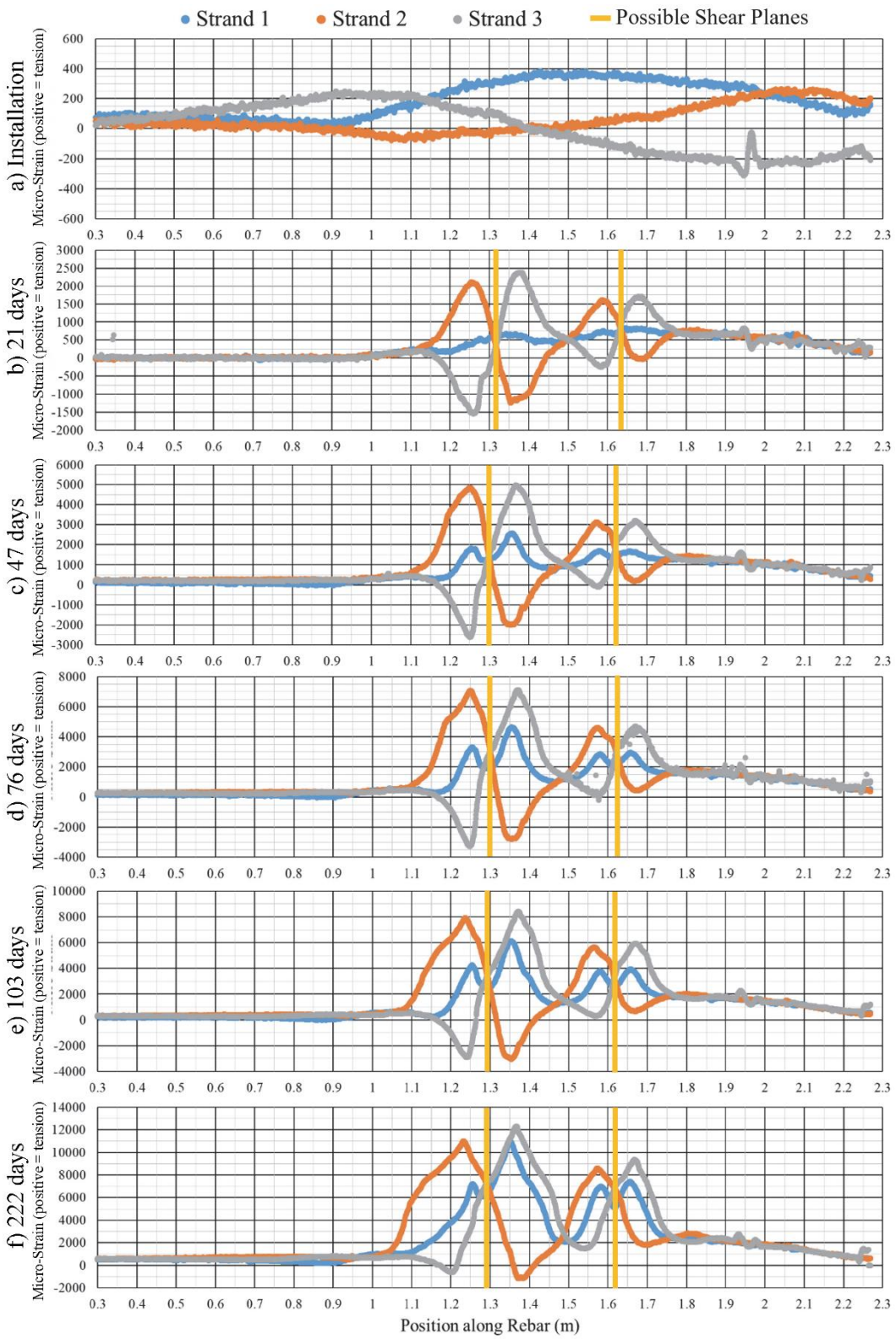

Figure 5.9. Strain readings from fibre-optic instrumentation in 22M Grade 500 dywidag at Mosaic Colonsay at a) installation, b) 21 days, c) 47 days, d) 76 days, e)103 days, and f) 222 days.

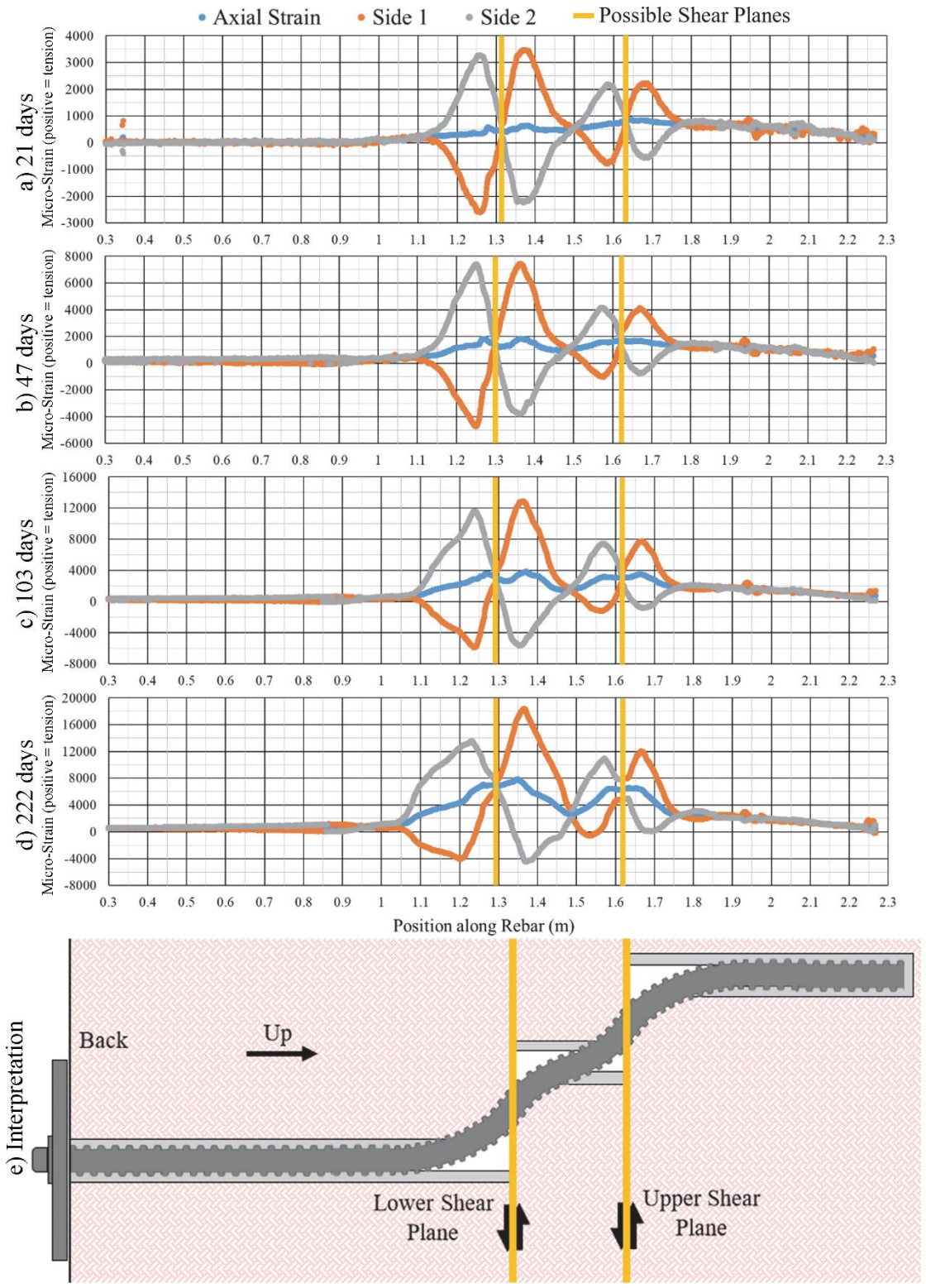

Figure 5.10. Strain along centroidal axis and extreme edges of rebar calculated from fibre-optic instrumentation in 22M Grade 500 dywidag at Mosaic Colonsay at a) 21 days, b) 47 days, c)103 days, and f) 222 days. e) shows an approximate interpretation of the rebar shape (not to scale).

5.2 Nutrien Vanscoy Potash Mine

The second installation occurred at the Nutrien Vanscoy mine. The mine had developed dipping shear planes in the back of a high stress drift. The mineralogy once again appeared to be typical of the Upper Patience Lake Member. The area was in a production drift nearing the end of its life so long-term safe access could not be guaranteed. Fortunately, access was available for the duration of the study before being closed off to personnel.

A mine bolting crew installed the instrumented rebar with a bolting machine. The installation is shown in Figure 5.11. Both holes were drilled with a 34.9 mm diameter rotary drill bit to a length of 2.45 m. At installation, several separations could also be identified with a tape measure. The separations could provide a cavity for resin to flow into and also suggests there could be multiple shearing planes.

Two 762 mm long and one 610 mm long resin cartridges were put into each hole after drilling. All cartridges were 28 mm diameter FasLoc resin cartridges available from DSI. The rebar was then inserted into the holes with the bolting machine. The rebar were spun as they were inserted, and continued to be spun five seconds after placement.

Figure 5.12 shows a plan view of the installation site at Nutrien Vanscoy. A series of shear planes had developed in the area, so crib supports were constructed to support the back. It was anticipated that the shear planes would continue to exhibit shear displacement despite the crib supports. The shear planes had a strike roughly parallel to the cribs but the depth and dip could not be determined.

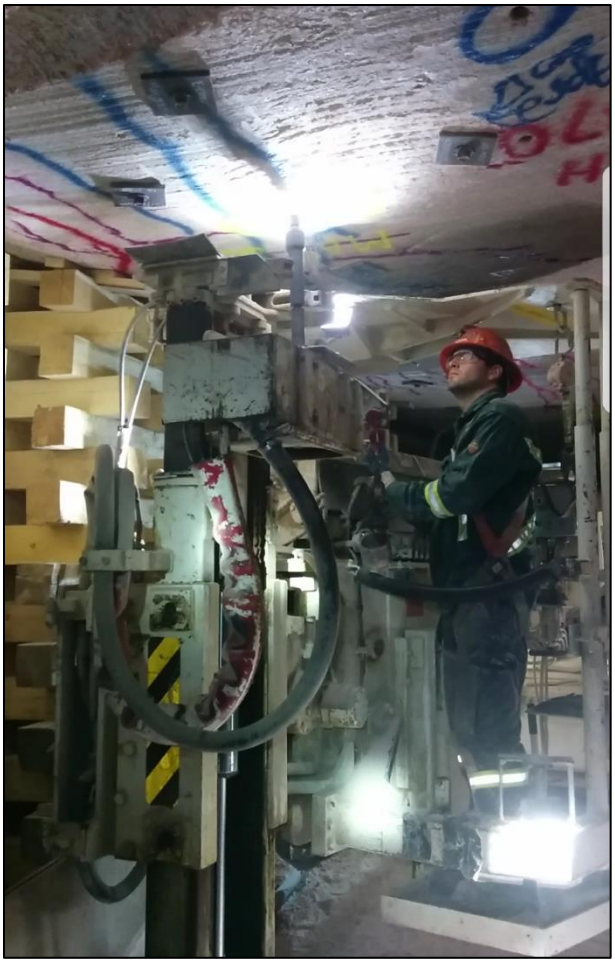

Figure 5.11. Instrumented rebar installation at Nutrien Vanscoy

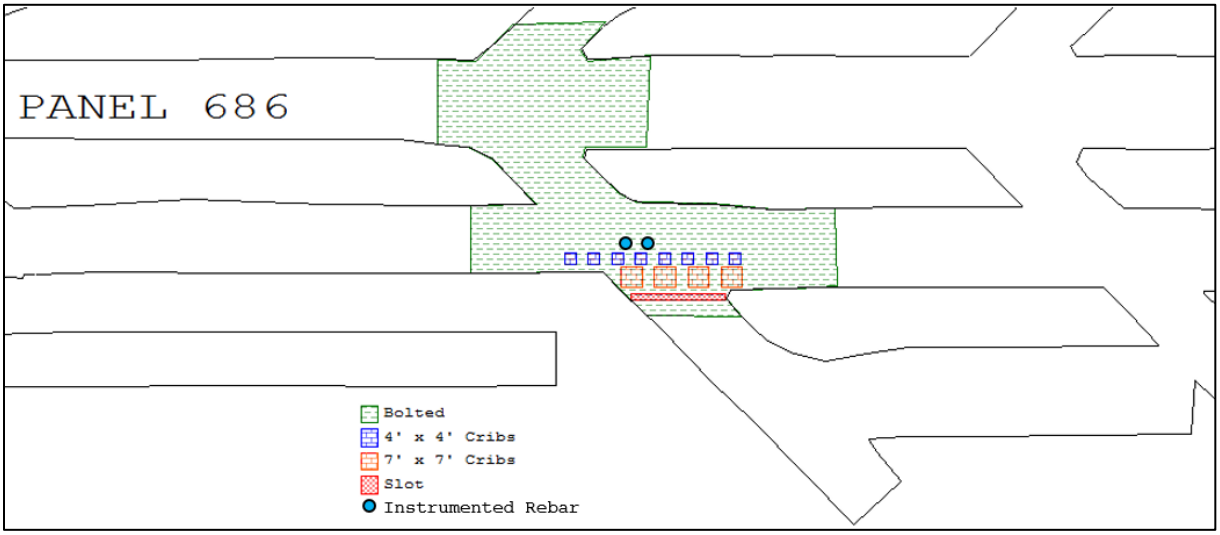

Figure 5.12. Nutrien Vanscoy installation site

5.2.1 Results of Fibre-optic Instrumented Rebar

The instrumented rebar at Nutrien Vanscoy were installed on June 28, 2017. Only two subsequent instrumentation readings were able to be made before ground in the area degraded too extensively and the fibre-optics were strained beyond their usable limits (roughly 10000 micro-strain). Table 5.2 summarizes the dates and relative times of these instrument readings.

Table 5.2. Time frame of instrumentation program at Nutrien Vanscoy

	Installation	Reading 1	Reading 2
Date	June 28, 2017	July 26, 2017	October 18, 2017
Time since installation	0 days	28 days	112 days

Figure 5.13 shows the three sets of strain readings from the instrumented 25M Grade 400 rebar installed at Nutrien Vanscoy. The strain readings were processed according to the equations in Appendix D and Appendix E. The strains at either extreme edge of the rebar and the axial strain were calculated and are shown in Figure 5.14. Rough interpretations of the strain results and the resulting rebar shapes are also included in Figure 5.14.

At 28 days, the strain readings indicate shear planes had developed at roughly 1.57 m and 2.10 m along the instrumented rebar. Furthermore, the polarity of the strain readings indicates the shear planes are shearing in opposite directions. This is shown by the reversal of tensile and compressive strain on either side of the rebar as it crosses the shear plane.

At 112 days after installation, an even more complex deformation distribution developed. A new shear plane appears at roughly 1.36 m along the rebar and the shear planes at 1.57 m and 2.1 m are no longer clear in the fibre-optic strain readings. Although the shear displacement at 1.36 m appears to be along a relatively discrete shear plane, the rebar above this is not likely being loaded by typical discrete shear planes. Interpreting conditions for this rebar is not feasible without further information or data.

The strain readings from the instrumented 22M (#7) Grade 500 (Grade 75) dywidag are shown in Figure 5.15. The strain readings at 28 days were used to calculate the strain along the centroidal axis of the rebar and the strain at the extreme edges of the instrumented rebar, as per Appendix E. The calculated strains are shown in Figure 5.16 along with a rough interpretation of the rebar shape.

It should be noted the reading at 112 days after installation could not measure the strain past the first pass of the fibre-optic. This lack of measurement is likely due to damage to the fibre-optic by excessive strain. As a result, the strain along the centroidal axis of the rebar and at the extreme edges could not be calculated.

The strain readings for the instrumented dywidag show a lower shear plane develop at 1.88 m along the rebar at 28 days. The increased compressive and tensile strains at the end of the dywidag is also evidence of an upper shear plane at 2.3 m. However, the dywidag ends roughly at this shear plane so the effect could not be measured.

There is significant tensile strain along the centroidal axis, roughly 1000 micro-strain, in the dywidag from 0 m (the collar) to 1.9 m (the lower shear plane). This tensile strain appears relatively constant along much of the dywidag. This suggests the dywidag has a relatively poor bond along this length otherwise the tensile stress would be transferred into the surrounding potash.

Although the strain readings for Strand 2 and Strand 3 are not available at 112 days after installation, Strand 1 provides partial evidence of the deformation along the rebar. There is increased strain near the lower shear plane already identified which suggests continued shear displacement. Additionally, there are other areas of increased strain near 1 m and 1.5 m. However, a proper interpretation is not possible without the strain data for Strand 2 and Strand 3 of the fibre-optic instrumentation.

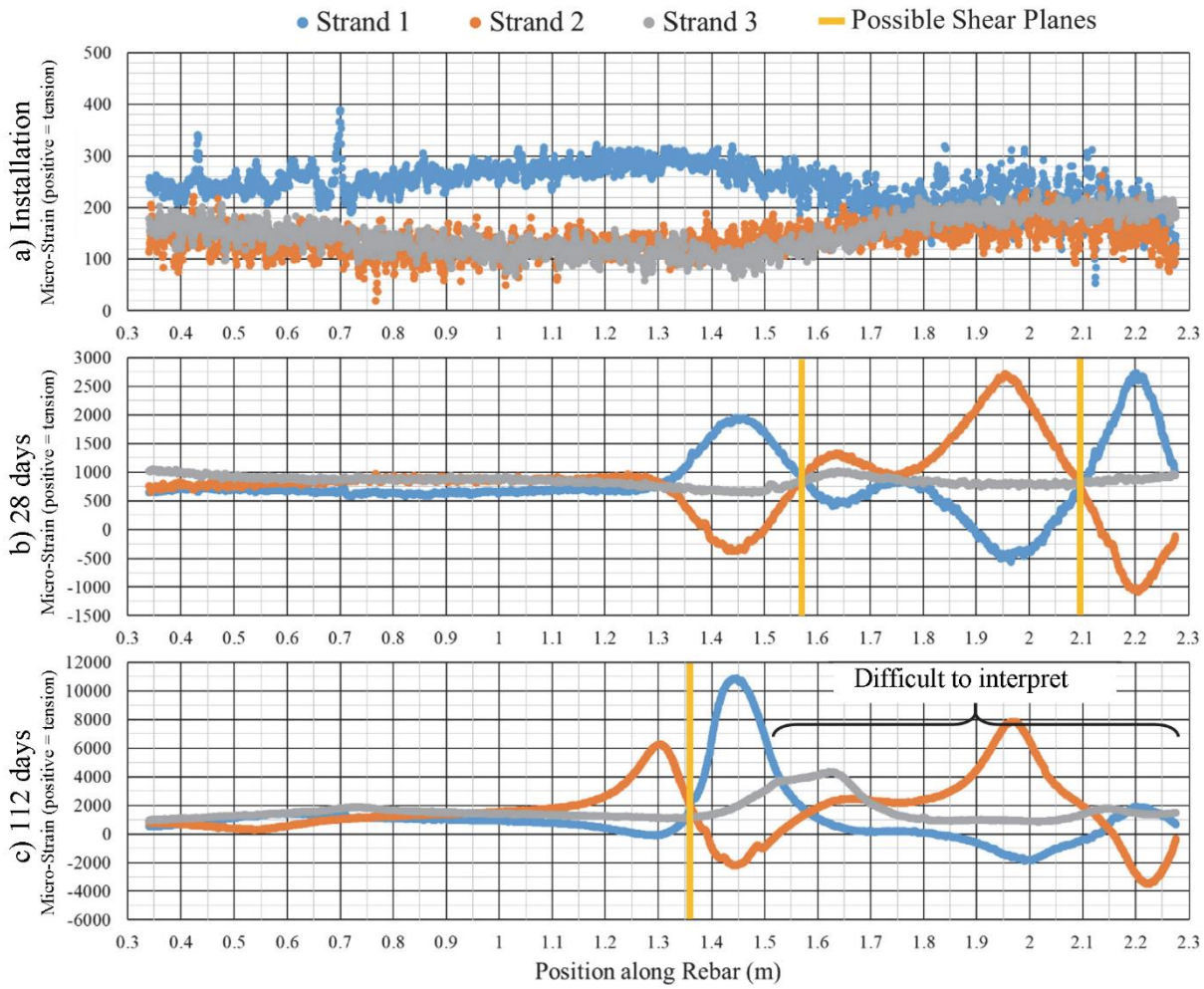

Figure 5.13. Strain readings from fibre-optic instrumentation in 25M Grade 400 rebar at Nutrien Vanscoy at a) installation, b) 28 days, and c) 112 days.

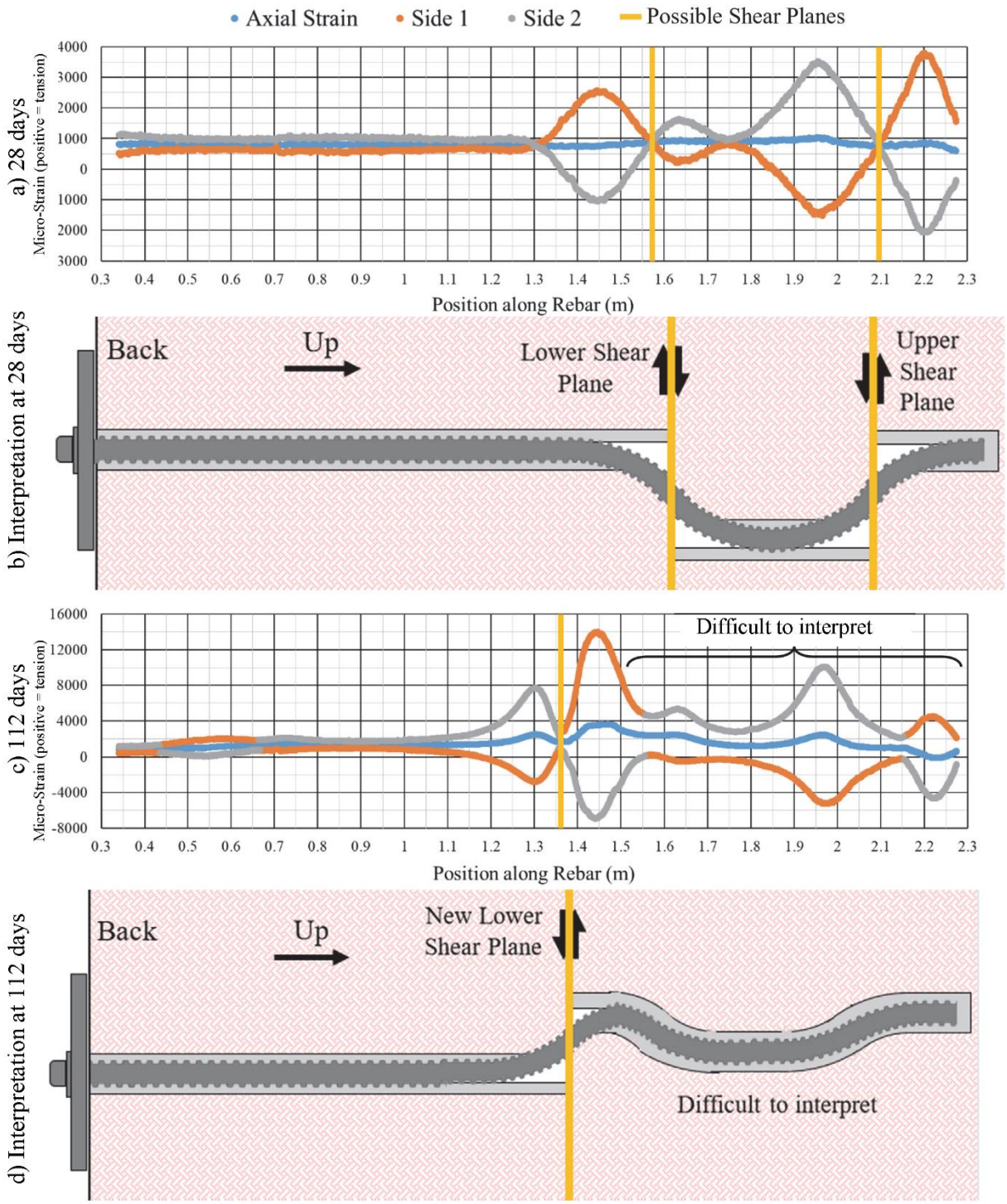

Figure 5.14. Strain along centroidal axis and extreme edges of rebar calculated from fibre-optic instrumentation in 25M Grade 400 rebar at Nutrien Vanscoy at a) 28 days and c) 112 days. An approximate interpretation of the rebar shape (not to scale) is also shown at b) 28 days and d) 112 days.

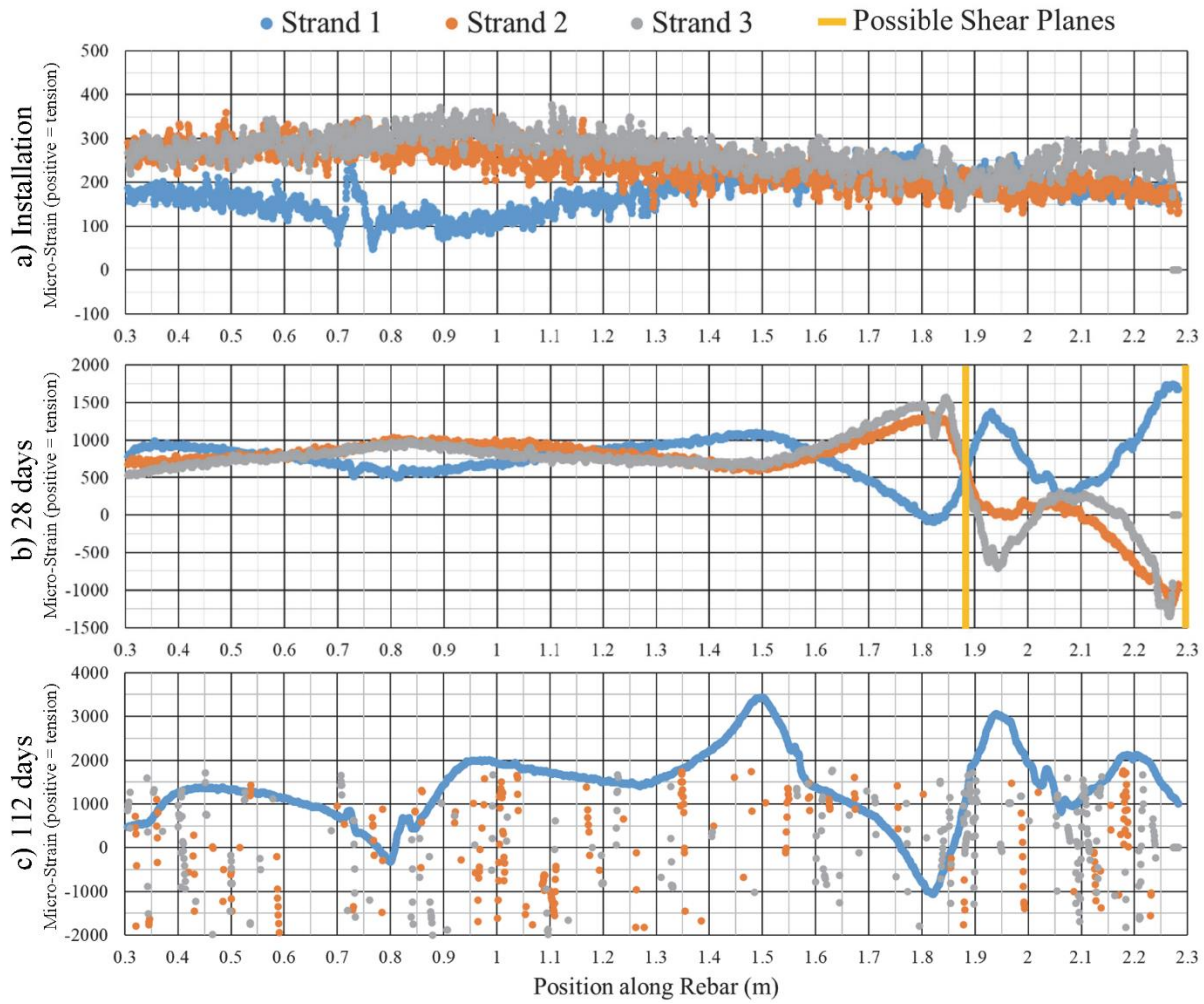

Figure 5.15. Strain readings from fibre-optic instrumentation in 22M Grade 500 dywidag at Nutrien Vanscoy at a) installation, b) 28 days, and c) 112 days.

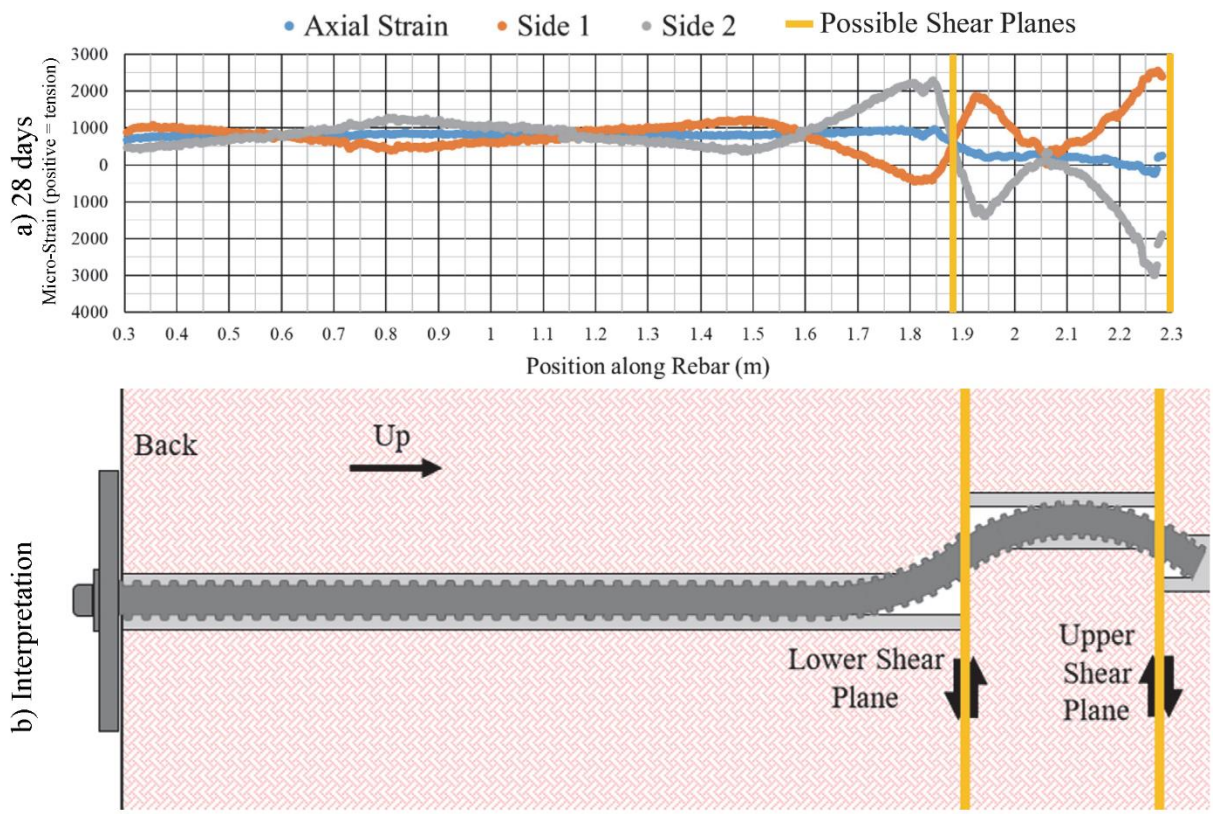

Figure 5.16. Strain along centroidal axis and extreme edges of rebar calculated from fibre-optic instrumentation in 22M Grade 500 dywidag at Nutrien Vanscoy at a) 28 days and b) an approximate interpretation of the rebar shape (not to scale).

5.3 Nutrien Allan Potash Mine

The third installation occurred at the Nutrien Allan mine. The mine has observed yielding of potash in a ramp down to the bottom of an ore bin. This ramp developed wedge instabilities in the back. The back was recently rehabilitated but wedges were beginning to develop again. The instrumented rebar were installed 75 cm from a newly mined brow on this ramp as seen in Figure 5.17. As this area was vital to mine production, long-term safe access was expected.

Since this was a ramp, the installation did not occur in the production level of the Upper Patience Lake Member. Instead, the back where the bolts were installed is approximately 2.2 m stratigraphically below the back of a typical drift. The mineralogy in this area is likely different than the other two installation sites of Sections 5.1.1 and 5.2.1 but appeared similar based on visual

inspection. It should also be noted that some carnallite concentrations have been found nearby. This mineralogy is likely to have different geomechanical properties than typical Upper Patience Lake potash. However, none of these small concentrations were observed immediately near the installation.

A stoper operator installed the instrumented 22M (#7) dywidag using a stoper. Stopers are pneumatically driven percussive drills that can drill into potash and spin rebar bolts into resin. The hole was drilled using a 35 mm diameter percussion drill bit and the hole was measured to be 2.39 m long. Using a tape measure, a separation was identified at 2.36 m into the hole and shear planes could be identified at 0.89 m and 2.36 m in an older hole nearby. After drilling the hole, two 914 mm long x 28 mm diameter resin FasLoc resin cartridges were put into the hole. The 22M dywidag was then pushed into the hole with the stoper. The dywidag was spun at 75 rpm and percussed as it was inserted, then was spun and percussed another five seconds once inserted all the way.

The instrumented 25M (#8) rebar was installed with a bolting machine in a hole that was 2.39 m long. No separations were felt using a tape measure but the shear planes at 0.89 m and 2.36 m were still identifiable nearby. Two 914 mm long by 28 mm diameter FasLoc resin cartridges were put into the hole and the 25M (#8) rebar was pushed into the hole with the bolter. The rebar was spun at roughly 100 rpm as it was inserted. Unfortunately, there was an issue inserting the bolt all the way in and the resin began to set up before it could be fully inserted and spun. The rebar was left sticking out of the hole approximately 18 cm (7 in.) as seen in Figure 5.18.

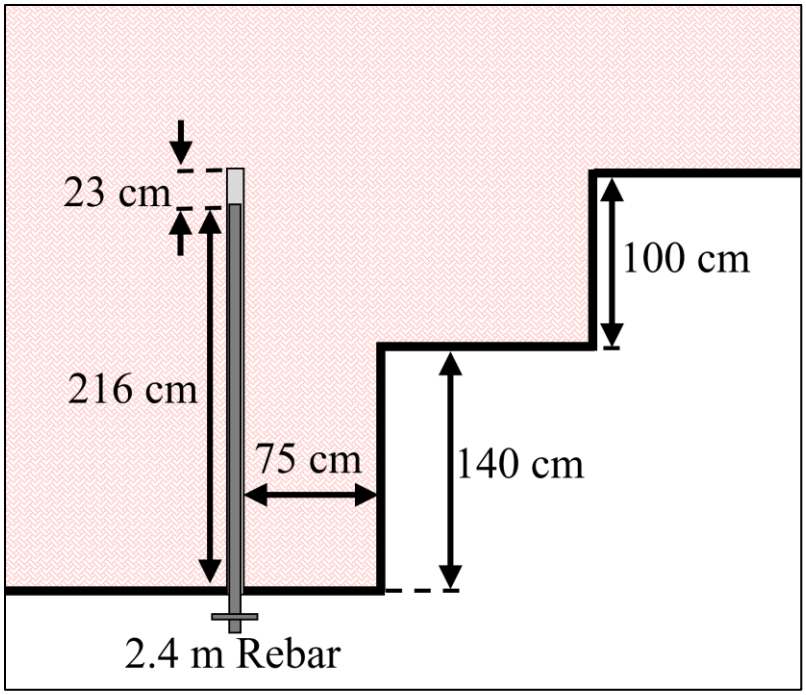

Figure 5.17. Position of instrumented 25M rebar in ramp brow at Nutrien Allan

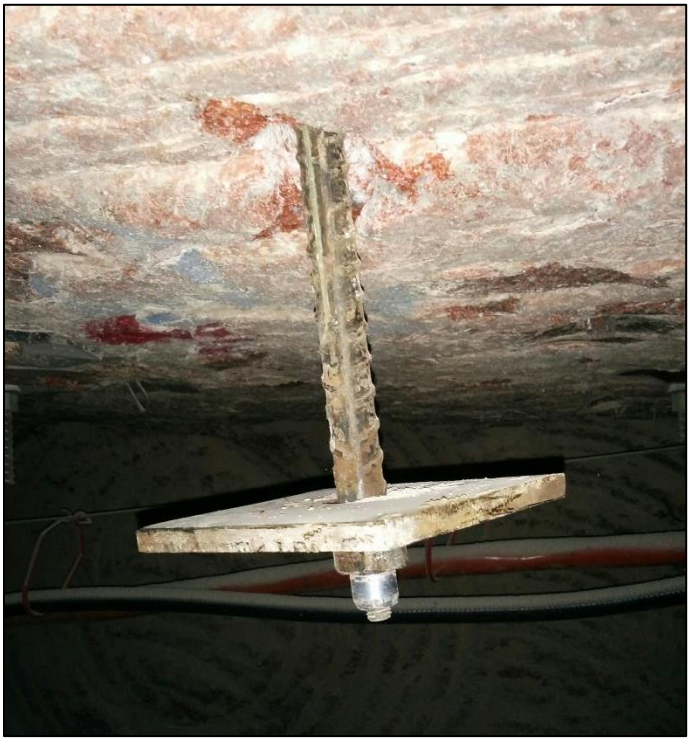

Figure 5.18. Installed instrumented rebar at Nutrien Allan

5.3.1 Results of Fibre-optic Instrumented Rebar

The fibre-optic instrumented 22M Grade 500 dywidag was installed using a stoper. Unfortunately, the percussive action of the stoper damaged the instrumented dywidag during installation. The plastic connectors used by the 1.25 mm LC fibre-optics are made of a brittle plastic. Although these connections are protected from direct impact, the heavy vibrations of the stoper were enough to shatter the connectors. This issue was not known to the experimental team or to YieldPoint Inc. and identifying this limitation was an important step in further developing this relatively new technology.

Issues with ground rehabilitation delayed the instrumentation installation at Nutrien Allan until September 21, 2017. Afterwards, two readings were taken from the 25M Grade 400 rebar before the conclusion of the project. The timeline for these readings is summarized in Table 5.3.

Table 5.3. Time frame of instrumentation program at Nutrien Allan

	Installation	Reading 1	Reading 2
Date	September 21, 2017	November 28, 2017	April 24, 2018
Time since installation	0 days	68 days	215 days

The strain readings from the 25M Grade 400 rebar are shown in Figure 5.19. These strain readings were used to calculate the strain along the extreme edges of the rebar and along the centroidal axis of the rebar. The calculated strains are shown in Figure 5.20 along with a rough interpretation of the corresponding rebar shape.

There are three possible shear planes identifiable from the strain readings. These occur at roughly 1.23 m, 1.37 m, and 2.05 m along the rebar. The shear planes at 1.23 m and 1.37 m along the rebar appear to be shearing in opposite directions based on the strain readings. This is an interesting result due to the close vicinity of the two shear plane and suggests the conditions are more complex in this area than assumed.

There is also an area of high tensile strain in the centroidal axis between 1.5 m and 2 m. Tensile strains would be expected to decrease away from shear planes and tensile separations as tensile stress is transferred from the rebar into the surrounding ground. Since the higher tensile strains do not decrease away from the shear planes, there could be a poor bond/encapsulation in this area.

At 215 days after installation, the rebar strains have begun to reach the yield strain of the steel rebar (roughly 2000 micro-strain). This suggests the shear plane displacement is slower that the shear planes studied at the previous two sites.

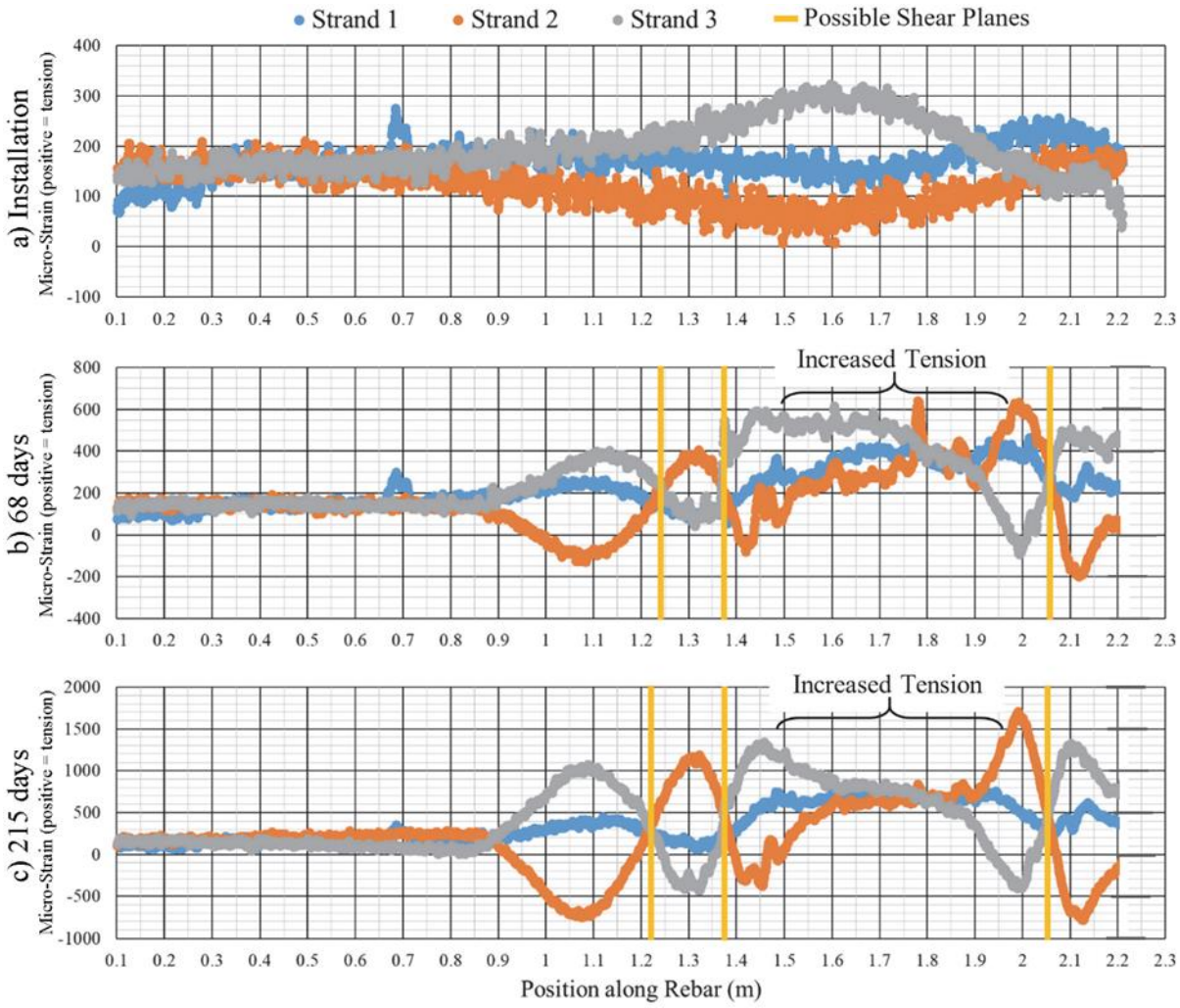

Figure 5.19. Strain readings from fibre-optic instrumentation in 25M Grade 400 rebar at Nutrien Allan at a) installation, b) 68 days, and c) 215 days.

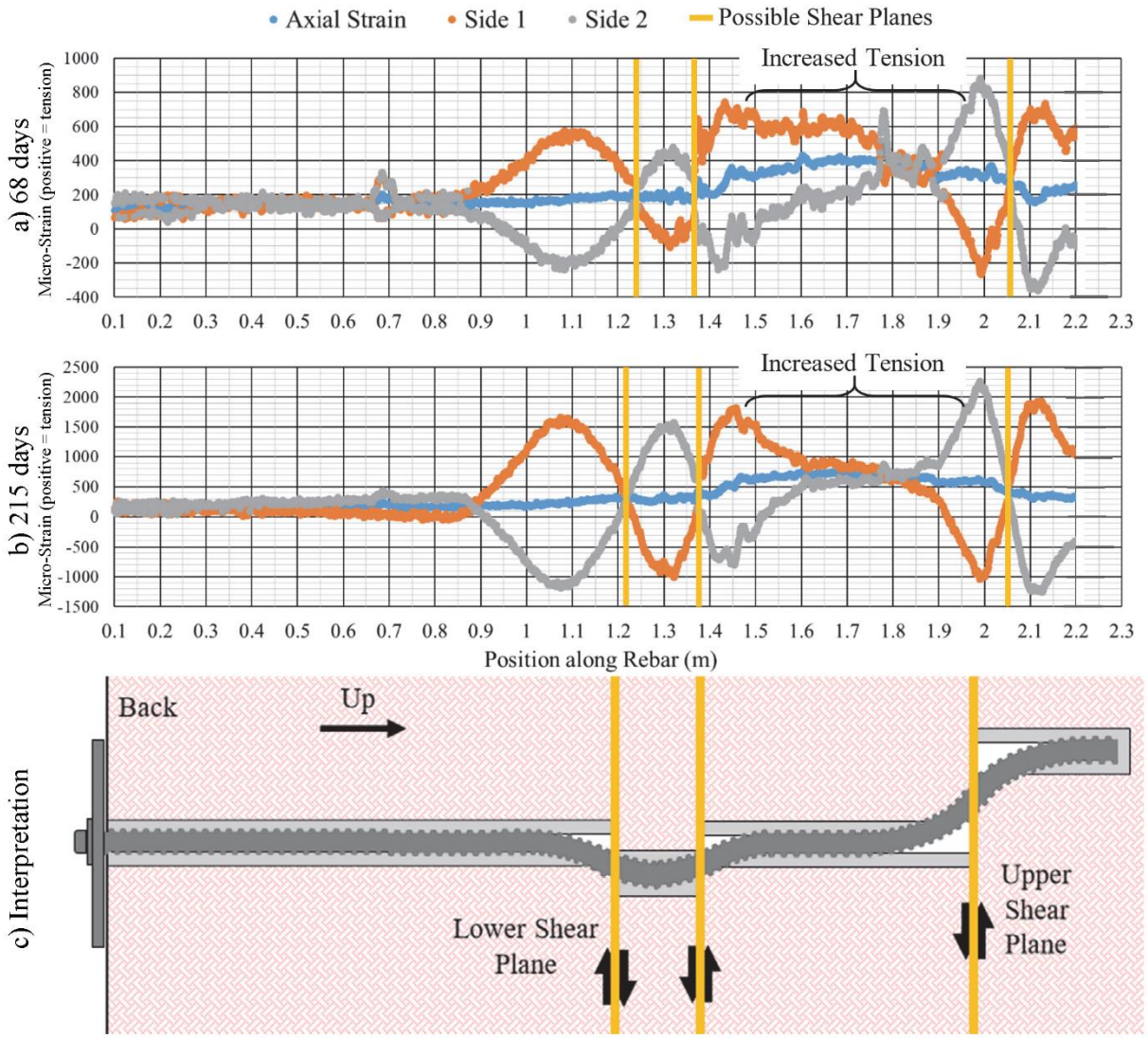

Figure 5.20. Strain along centroidal axis and extreme edges of rebar calculated from fibre-optic instrumentation in 25M Grade 400 rebar at Nutrien Allan at a) 68 days and b) 215 days, and c) an approximate interpretation of the rebar shape (not to scale).

5.4 Conclusions

A total of six fibre-optic instrumented rebar were installed in three different potash mines exhibiting shear movement. The instrumented rebar were installed with either a bolter machine or a stoper in drifts exhibiting shear movement in the back. Both an instrumented 25M (#8) Grade 400 (60) rebar and an instrumented 22M (#7) Grade 500 (75) dywidag were installed at each of the three sites.

Instrumented rebar were installed adjacent to a slot cut at Mosaic's Colonsay potash mine. Two shear planes progressively displaced in shear and the instrumentation appeared to accurately measure the corresponding deformation of the rebar. The distance into the back of the two shear planes roughly corresponded to the location of two known clay seams. The rebar were estimated to have begun yielding at shear displacements of roughly a few millimeters.

Fibre-optic instrumented rebar were installed with a bolter machine in a drift at Nutrien's Vanscoy potash mine identified as having shear planes in the back. The fibre-optic instrumentation revealed the initial development of two possible shear planes deforming each of the rebar. Unfortunately, interpretation of the rebar behaviour was made difficult due to questionable bond strengths between rebar and the surrounding potash, shear movement along multiple closely spaced shear planes, and "bulk" shear deformation of the potash instead of shear deformation along discrete shear planes.

It should be noted that in situ instrumentation introduces uncontrollable variables such as:

- Full encapsulation of the instrumented rebar by grout cannot be guaranteed or measured.
- The rate of shear movement is not reliable or consistent.
- The shear movement of the potash commonly occurs in combination with tensile separation.

Fibre-optic instrumented rebar were installed at Nutrien's Allan potash mine in a ramp brow that was expected to develop shear movement. One instrumented dywidag was installed with a stoper that has a percussive impact as it spins. The heavy vibrations of the stoper's percussions caused the connector of the fibre-optic instrumentation to shatter and rendered the instrumented rebar useless.

The second instrumented rebar installed at Allan provided strain measurements but revealed a similar situation as found in the Vanscoy mine; the rebar behaviour was difficult to interpret due to complex ground behaviour.

The strain measurements of the fibre-optic instrumented rebar provided excellent insight into rebar behaviour when installed in the field and subjected to relatively simple shearing scenarios. However, the behaviour of instrumented rebar under in situ shear displacement of potash becomes very difficult to interpret when the rock mass behaves in a complex manner or unanticipated variables are introduced.

6 DISCUSSION AND IMPLEMENTATION OF RESULTS

This section interprets and combines the results of laboratory and field tests conducted as part of this research to create a useful design chart for mining operations. Since the behaviour of fully-encapsulated rebar crossing a shear plane is complex, the experiments were designed to investigate variables pertinent to a mining environment and were expected to influence the rebar behaviour.

6.1 Shear Displacement as an Indicator of Support Performance

One of the primary goals of this research was to correlate shear displacement of rebar rock bolts in Saskatchewan potash mines with the failure of the rebar. Achieving this goal would allow mine engineers to use estimated shear displacement and shear plane aperture of shearing potash in the field and estimate if the existing ground support is acceptable. Double shear tests and the lateral pull tests are combined and presented in this section to reach this goal.

The lateral pull tests discussed in Section 4 were interpreted as shown in Figure 6.1. As was discussed in Section 4, the equivalent shear displacement of a shear plane is double the displacement of where the rebar begins threading into the lateral pull testing apparatus, labelled point O. This is due to the point of symmetry in the test setup discussed in Section 4.1. Similarly, the shear plane aperture is taken as double the distance to the bottom of the lateral pull testing apparatus. The threaded insert for the lateral pull testing apparatus could not be placed closer than about 12.7 mm above the potash floor so all lateral pull tests had shear plane apertures of approximately 25.4 mm. An accurate measurement of the apertures could not be taken so this had to be assumed based on the geometry of the testing apparatus

To further explain the point of symmetry shown as point O in Figure 6.1, consider a vertical rebar bolt installed across a horizontal shearing plane. Both ends of the rebar will remain vertical as shearing occurs and point O is the point of symmetry for the two sides of the shearing plane. In the lateral pull test, one end remains vertical while the other end is free to bend. Point O is the base of the threaded insert in the lateral pull test and the portion of the rebar below point O represents

half of an in situ shear configuration. Between point O and the potash surface represents one half of the aperture for an equivalent in situ shear plane.

The double shear tests discussed in Section 3.2 were interpreted as shown in Figure 6.2. The ultimate shear displacement of each test was taken as the average measured shear displacement of both shear planes at the ultimate applied load. A variety of shear plane apertures were tested and each aperture was measured prior to testing the samples.

Figure 6.3 shows the displacement at ultimate load for the double shear tests and lateral pull tests plotted against the shear plane apertures. The lateral pull tests exhibit more shear displacement than the double shear tests of similar shear plane aperture. The rebar rock bolts in the lateral pull tests were grouted into potash while the rebar rock bolts in the double shear tests were grouted into steel pipes. The weaker and more deformable potash should allow for greater shear displacement prior to the rebar failing compared to the stronger steel pipes so the difference in shear displacement visible in Figure 6.3 is not surprising.

It should also be noted that there is not a clear difference in behaviour between the rebar types tested in either the double shear tests or the lateral pull tests. The rebar diameters and strengths were relatively similar and any slight differences in behaviour are indistinguishable. For this reason, separate plots have not been generated for each rebar type.

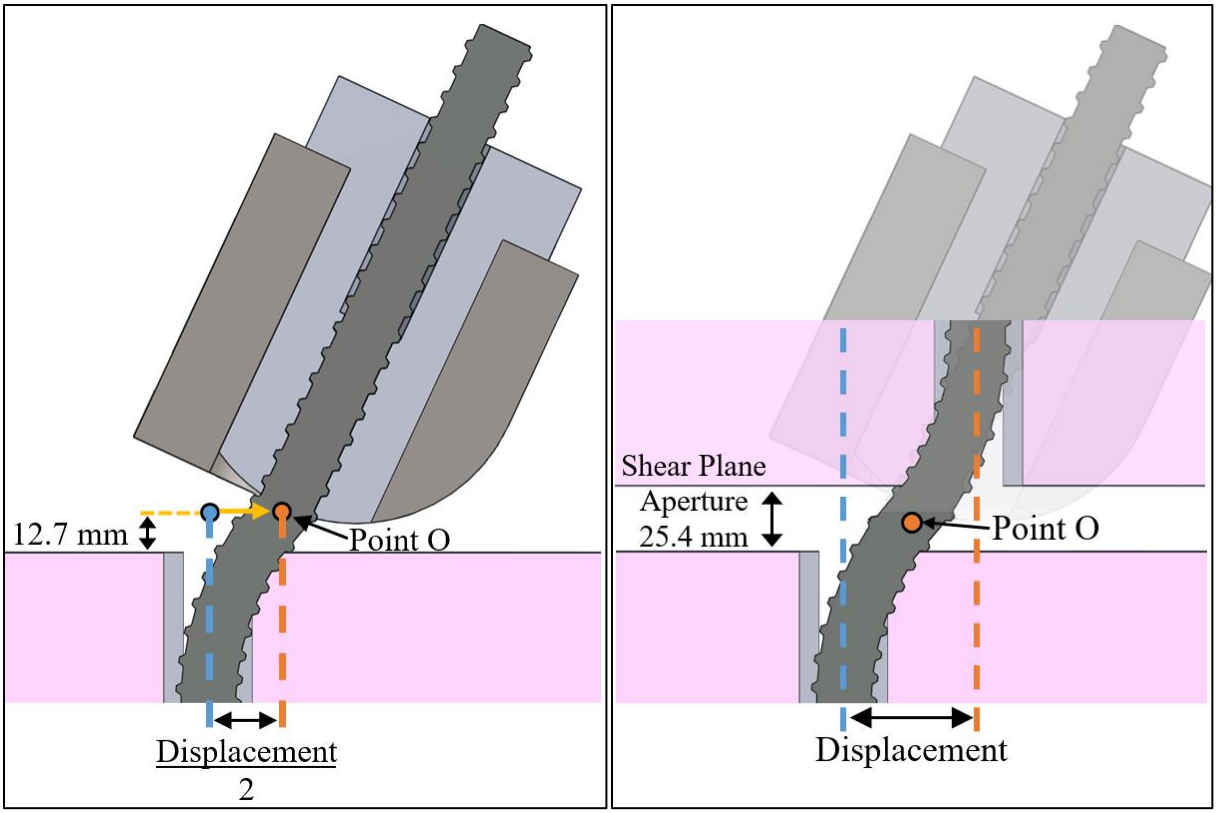

Figure 6.1. Interpretation of the lateral pull tests showing a cross-section of the apparatus (left) and the equivalent shear plane (right)

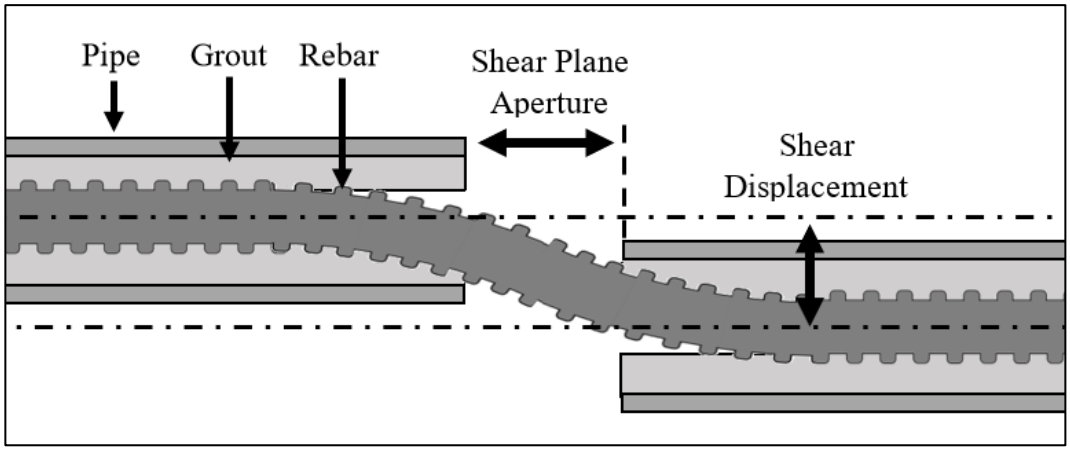

Figure 6.2. Interpretation of the double shear tests showing a cross-section of one shear plane

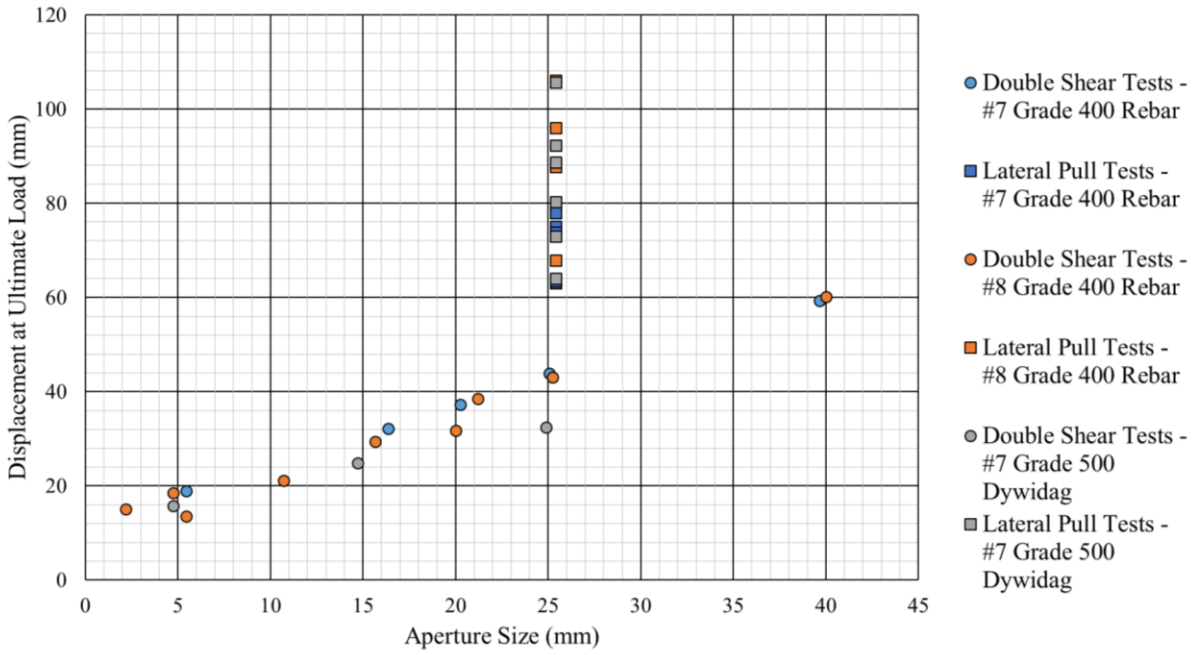

Figure 6.3. Displacement at the ultimate load of the double shear tests and lateral pull tests plotted against the shear plane aperture

6.2 Implementation of Results into Mining Practices

The results of this research project can be implemented into ground support guidelines to ensure additional rock bolts are installed along side existing sheared rock bolts at an appropriate time. To achieve this objective, the results and interpretation presented in Figure 6.3 were used.

A chart showing various linear relationships between shear displacement and shear plane aperture is presented in Figure 6.4. This chart includes the ultimate shear displacements for all three rebar types from both the double shear tests and the lateral pull tests.

To create Figure 6.4, a linear trendline through the double shear tests was generated from the test results by linear regression. The slope from the double shear test trendline was then used to generate two linear trendlines for the lateral pull tests. These trendlines were constructed for the lateral pull tests by assuming a similar displacement-aperture relationship (i.e. line trendline slope) applies to the lateral pull test data as what was determined using the double shear tests. The two

trendline intersections were adjusted in order to intersect the lowest and the mean displacement of the lateral pull tests at the ultimate load.

Generating the trendlines in this way assumes the same relationship/slope between ultimate shear displacement and shear plane aperture from double shear testing will apply to shearing rebar installed in potash. It is worth noting that, after the rebar failed in lateral pull tests, the rebar was observed to have penetrated into the resin and potash between 25 mm (1 inch) and 35 mm (1.4 inches) at the surface. Although this penetration distance varied, it was seen in all samples and rebar types. Conversely, the rebar was not able to penetrate the steel pipes in any double shear tests. This penetration of the rebar into the potash provides another means of justification for the offset of the linear trendline lines for lateral pull tests from the double shear tests in Figure 6.4.

The final design chart presented in Figure 6.5 has been generated from the trendlines of Figure 6.4. This final design chart is intended to help mine engineers in Saskatchewan potash mines apply the testing results. When fully-grouted rebar are installed, a monitoring hole is often drilled nearby allowing the shear plane aperture and shear plane movement to be measured. When shear movement is identified in an area with fully-grouted rebar rock bolts, then the shear displacement should be monitored from the monitoring hole.

The design chart is intended to be used as illustrated in Figure 6.6. In this hypothetical example, a shear plane aperture is initially measured when rock bolts are installed. This aperture determines the x-axis position on the design chart. Periodically, the shear plane displacement is estimated from a nearby monitoring hole. The shear displacement is monitored and the y-axis position can be plotted on the design chart. Once shear displacement reaches the area labelled “Possible Rebar Failure”, then mine engineers should communicate this to other mine personnel and plan to rebolt the area.

It should be noted that Section 2.4 discusses potash behaviour and the large role that creep plays in potash strength and deformation. The lateral pull tests were conducted in under five minutes while actual shear displacement of a shear plane will often occur over several weeks or months. This slow rate of movement will likely cause the potash to be weak and deformable which will

allow fully-grouted rebar to undergo more shear displacement before failing than is suggested in Figure 6.5.

A significant limitation of the recommended design chart is that it does not consider the effect of a change in the shear plane aperture after support has been installed. Additional aperture dilation would increase the axial stress in the rebar and reduce the shear displacement at failure. The combined effect of shear plane aperture and shear plane dilation is unknown and is a possible topic of future research. To properly apply the design chart in Figure 6.5, mine engineers must be conscious of this limitation regarding shear plane dilation.

Previous researchers also found that rebar installed at an angle towards the direction of shear movement will behave stiffer (Section 2.1.2). This research project assumed all fully-grouted rebar was installed perpendicular to the shear plane. Rebar is generally installed perpendicular to the shear planes in Saskatchewan potash mines since the shear planes typically form along the sub-horizontal clay seams and the rebar is installed vertically into the back. Once again, mine engineers should be aware of this condition in order to properly employ these results.

Last, implementing the research findings is limited by mine personnel's ability to measure shear plane apertures and displacements. These measurements are typically made from nearby monitoring holes using direct observation and a tape measure. These measurement methods are highly subjective. Unfortunately, no other practical method for measurement has been developed that can realistically be employed in the many areas of potash mines that must be monitored.

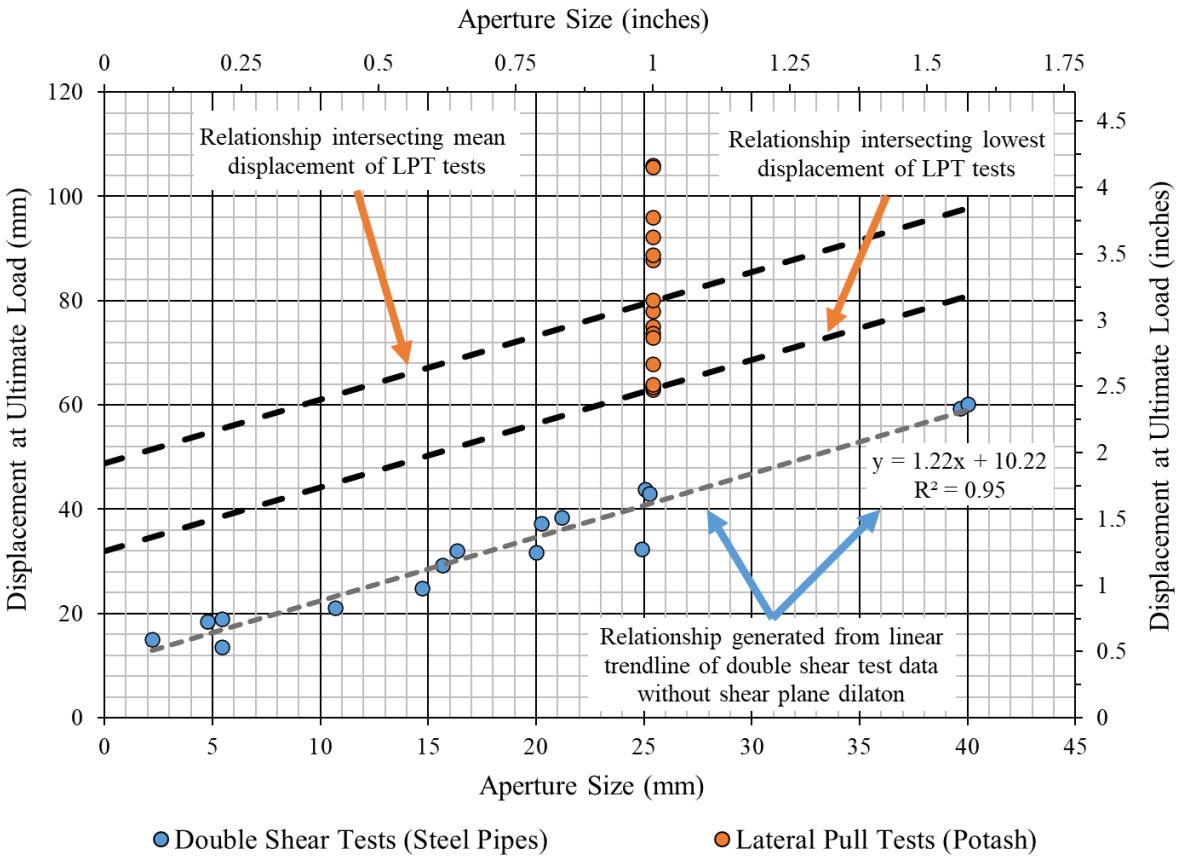

Figure 6.4. Generation of shear displacement vs aperture size relationship from double shear test data and its application to lateral pull test data

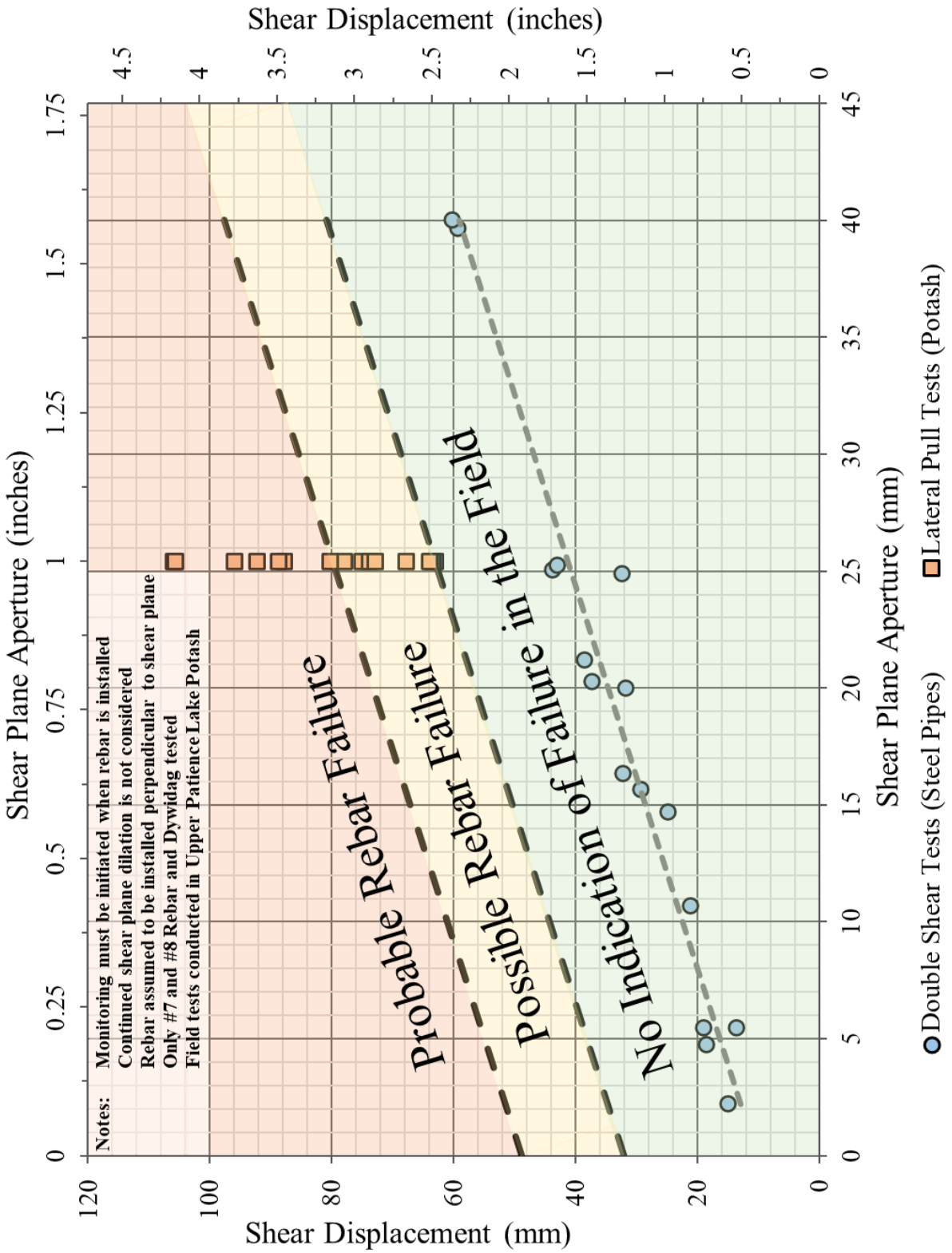

Figure 6.5. Shear performance criteria for fully-encapsulated resin grouted rebar in Upper Patience Lake potash mines

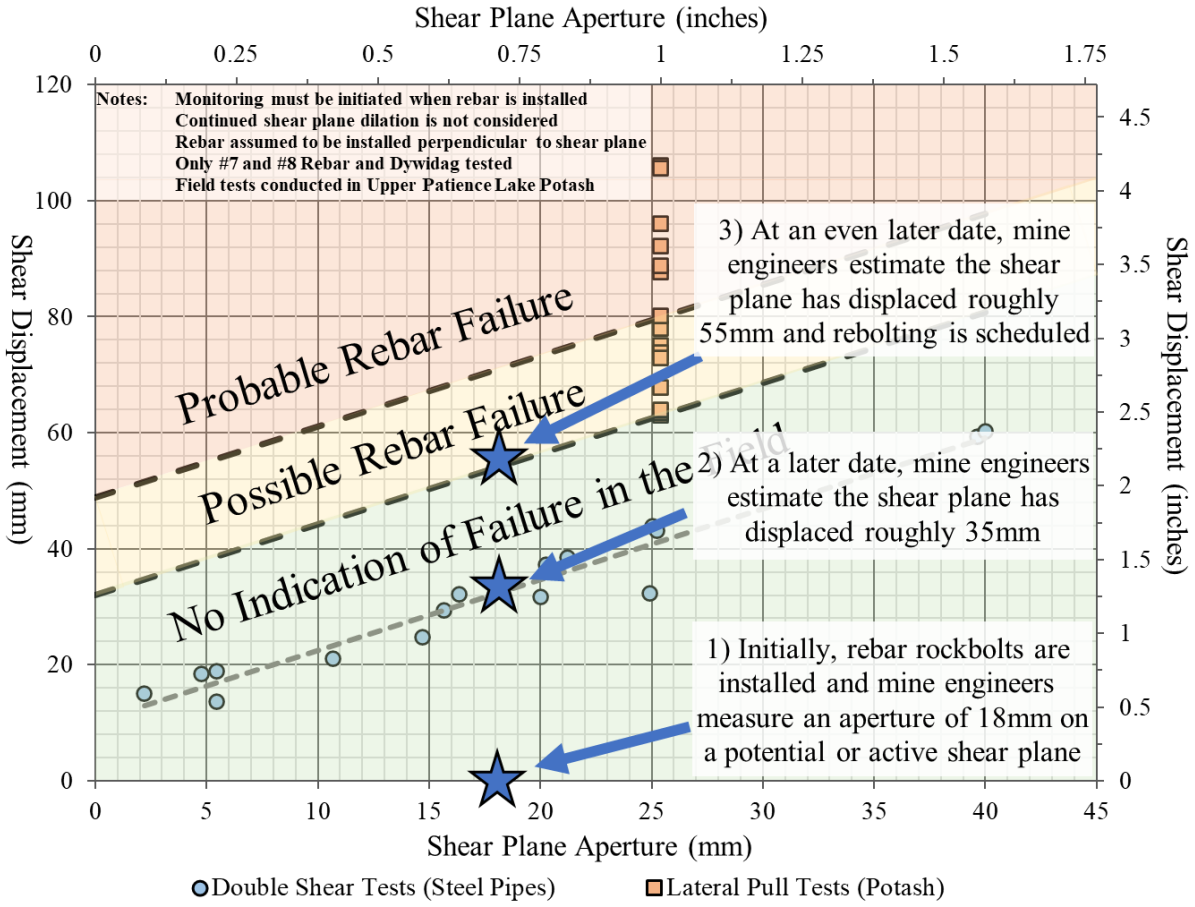

Figure 6.6. Proposed use of the design chart in practice

6.3 Comparison of Results with Previous Models

As was discussed in Section 2.2.6, many models have been presented by previous researchers to describe the behaviour of fully-encapsulated rebar rock bolts crossing a shear plane. Two models, Spang and Egger (1990) and Pellet and Egger (1996), have shown good correlation with their experimental data and are simple to apply.

Unfortunately, there are no analytical models that considered the effect of a shear plane aperture and these two models do not either. The models were still solved and compared against the results presented in the previous section despite only describing the behaviour of a tight shear plane.

Equation 2.1 presented by Spang and Egger (1990) was solved using the parameters shown in Table 6.1. The variables shown were determined from laboratory testing presented in Appendix A and Appendix B.

The equations presented by Pellet and Egger (1996) were solved using the parameters shown in Table 6.2. These parameters were also determined from laboratory testing presented in Appendix A and Appendix B, except for the Young's Modulus of the rebar which was assumed to be 200 GPa. In these equations, the angle of inclination, which describes the angle between the shear plane and the rebar axis, was set to 89.9 degrees instead of 90 degrees. This was simply done to avoid the mathematical issues of calculating the tangent of 90 degrees and had a negligible effect on the result.

Table 6.1. Input parameters for solving the model from Spang and Egger (1990)

	Ultimate Tensile Load (kN)	**Rebar Diameter (mm)**	**Angle of Inclination, β (degrees)**
22M Grade 400 Rebar	287	21.1	90
25M Grade 400 Rebar	309	23.1	90
22M Grade 500 Dywidag	300	21.0	90

Table 6.2. Input parameters for solving the model from Pellet and Egger (1996)

	Young's Modulus (GPa)	**Yield Stress of Rebar (MPa)**	**Ultimate Stress of Rebar (MPa)**	**Ultimate Strain of Rebar**	**Rebar Diameter (mm)**	**Angle of Inclination, β (degrees)**
22M Grade 400 Rebar	200	415	686	0.103	21.1	89.9*
25M Grade 400 Rebar	200	403	625	0.114	23.1	89.9*
22M Grade 500 Dywidag	200	495	717	0.125	21.0	89.9*

*89.9 degrees used instead of 90 degrees due to tan (β) in the model equations

The two models were solved at four different uniaxial compressive strengths (UCS). The calculated ultimate shear displacements are shown in Figure 6.7 for all three rebar types using both models. Also shown are the various strengths for potash and epoxy that were determined from laboratory testing in Appendix A.

In situ shear of rebar is not dependent on a single surrounding medium but is instead dependent on a combination of the resin and potash surrounding the rebar. Potash (17 MPa – 25 MPa) was shown to be weaker than epoxy (29 MPa – 31 MPa) as seen from their relative strengths in Figure 6.7.

The ultimate shear displacements were calculated using the mean strength of the UCS tests on epoxy (31 MPa). This strength was chosen since it is the highest strength determined and will provide a conservative calculation of ultimate shear plane displacement. The ultimate shear displacements for all three rebar types using both models are compared against the lateral pull tests and double shear tests in Figure 6.8. These model results for no shear plane aperture compare remarkably well with the design chart created and suggest the results and proposed implementation are acceptable.

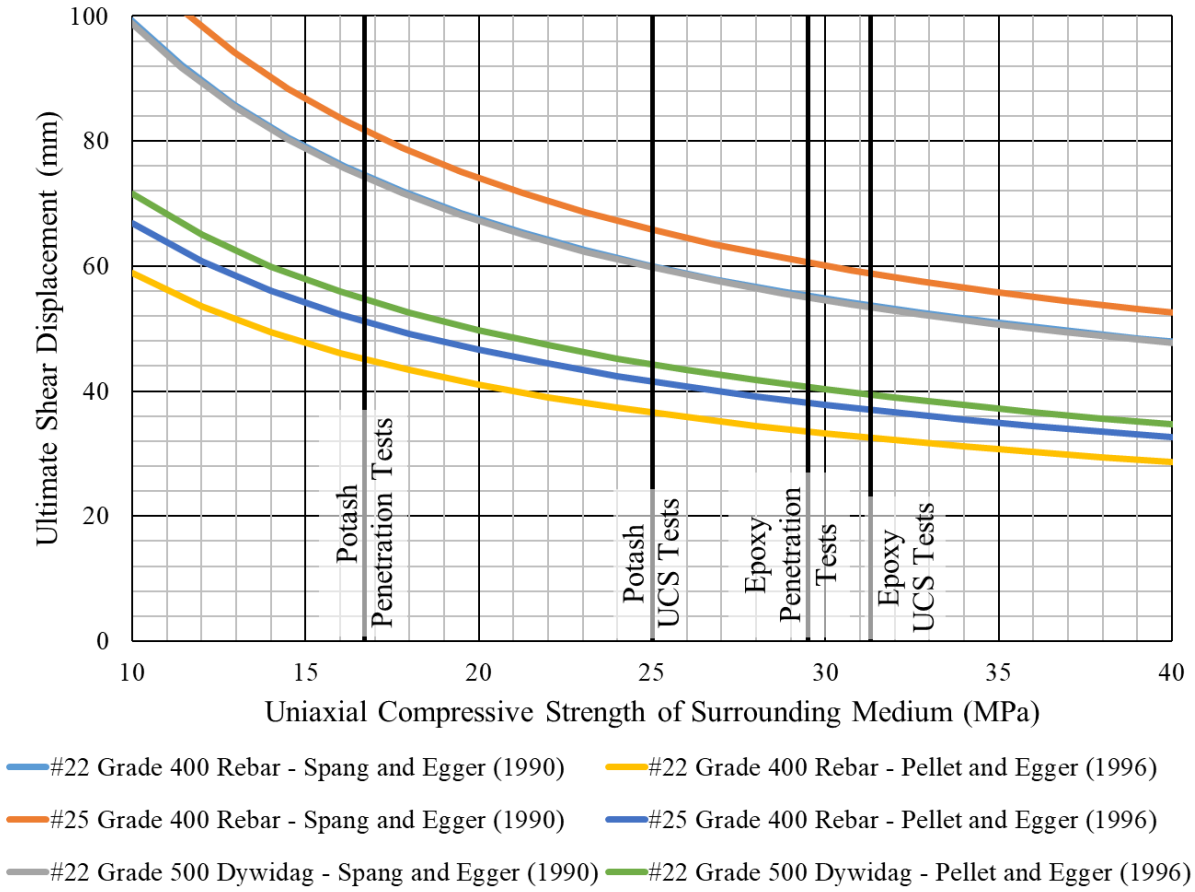

Figure 6.7. Ultimate shear displacement for three rebar types predicted by Spang and Egger (1990) and Pellet and Egger (1996) at various potash and epoxy strengths

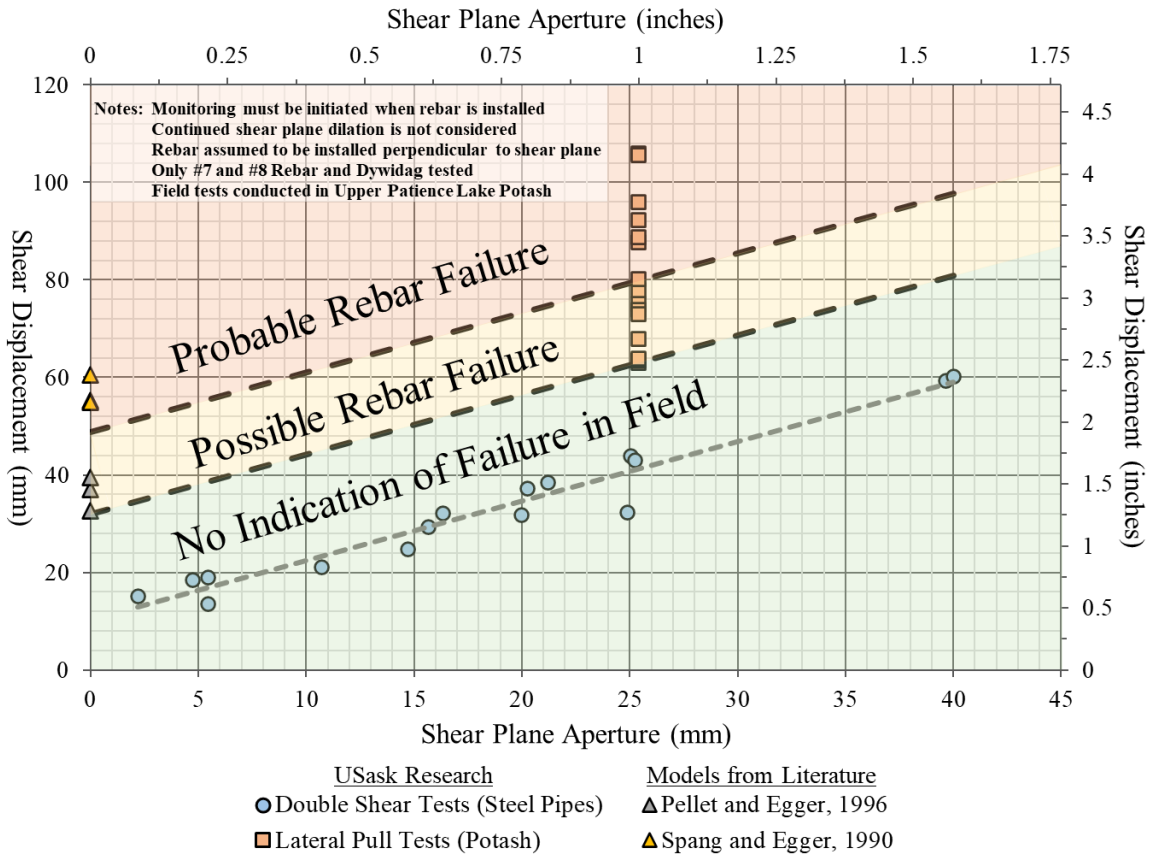

Figure 6.8. Comparison of final design chart with models from Spang and Egger (1990) and Pellet and Egger (1996) using epoxy UCS results

7 CONCLUSIONS AND RECOMMENDATIONS

The maximum shear displacement for a fully-grouted rebar prior to failure is an important factor in determining when additional rebar must be installed to maintain ground stability in underground potash mines. In this study, shear displacements were correlated with the failure of rebar using double shear tests in the laboratory and lateral pull tests in the field. A design chart (Figure 6.5) was generated using the results of these tests and provides a guideline for mine engineers to determine if additional bolting is required.

The double shear tests showed that shear plane aperture significantly affect the amount of shear displacement a fully-grouted rebar rock bolt can undergo before failing. Since varied shear plane apertures occur in potash mines, this parameter was incorporated into the design chart. Testing showed that the shear plane aperture did not have a significant effect on the ultimate lateral load before rebar failure.

There has been significant research into the behaviour of rock bolts crossing shear planes by previous researchers. Unfortunately, few researchers considered the presence of a shear plane aperture. Two models were evaluated and compared against the results found in this research. The models were only applicable to tight shear planes with no aperture and have limited applicability for the conditions investigated in this research project. Regardless, the models exhibited good correlation with the design chart generated.

The relatively new distributed optical sensing system from Luna Inc. was used and mathematical methods for analyzing the strain data were developed. The fibre-optic strain sensing instrumentation was used in the laboratory and the field. The strain measurement provided by the fibre-optic instrumentation appeared accurate and provided unique insight into the behaviour of rebar rock bolts subjected to shear deformation.

Field installations of instrumented rebar were generally successful, but interpretation of results was difficult due to complex potash deformations. Fibre-optic instrumented rebar installed at Mosaic's Colonsay mine provided excellent results. Two discrete shear planes developed

progressively and deformed the rebar rock bolts. The deformation and resulting strain measurements were as expected, showing high localised bending moments on either side of a discrete shear plane.

The behaviour of rebar rock bolts subjected to shear is a complex subject that has not been well understood in potash mine applications. New field tests and laboratory tests have been coupled with analysis techniques to improve our understanding of the rebar, epoxy, and potash behaviour. This research has provided the mine with guidelines to link shear plane aperture and shear plane offset to approaching support failure. These guidelines are easily applied and are based on laboratory testing methods, field testing equipment and tests, as well as data interpretation conducted for this research project.

7.1 Recommendations for Future Work

Future work should include modifications to the laboratory double shear test, due to the development of minor bending moments during testing. It is recommended that the rebar-pipe samples should be mounted in a manner that better prevents the generation of bending moments at the shear planes prior to loading the samples. Additional testing should be done to verify the expected minimal influence of these bending moments.

Revisions to the field based lateral pull testing apparatus should be made prior to future testing. Although the initial testing apparatus performed adequately, future iterations should include developing a more compact design that can shear the rebar closer to the potash surface. Also, reducing the friction by incorporating roller bearings into the design could help provide more reliable results. Last, a method for finely adjusting the apparatus and alignment should be devised to gather more consistent results.

The in situ instrumented rebar performed adequately at Mosaic Colonsay, but the results were difficult to interpret at Nutrien Vanscoy and Nutrien Allan. The difficulty in interpretation can be attributed to complex ground movements and a lack of secondary instrumentation to help

understand these ground movements. Measuring ground movements separately in future research projects would assist in interpretation. Alternatively, future installations are recommended to be conducted in simple shear conditions, as was observed at Mosaic's Colonsay mine.

REFERENCES

ASTM International (2008). *D5731 - 08 Standard Test Method for Determination of the Point Load Strength Index of Rock and Application to Rock Strength Classifications.* ASTM International.

ASTM International (2013). *F432 -13 Standard Specification for Roof and Rock Bolts and Accessories.* ASTM International.

ASTM International (2014a). *D5873 - 14 Standard Test Method for Determination of Rock Hardness by Rebound Hammer Method.* ASTM International.

ASTM International (2014b). *D7012 - 14 Standard Test Methods for Compressive Strength and Elastic Moduli of Intact Rock Core Specimens under Varying States of Stress and Temperatures.* ASTM International.

Aziz, N., Hossein, J., & Hadi, M. (2005). The Effect of Resin Thickness on Bolt-Grout-Concrete Interaction in Shear. *2005 Coal Operators' Conference (3-9_.* Brisbane, Australia: University of Wollongong & the Australasian Institute of Mining and Metallurgy.

Aziz, N., Pratt, D., & Williams, R. (2003). Double Shear Testing of Bolts. *2003 Coal Operators' Conference (154-161).* University of Wollongong & the Australasian Institute of Mining and Metallurgy.

Bjurstrom, S. (1974). Shear Strength of Hard Rock Joints Reinforced by Grouted Untensioned Bolts. *3rd International Congress of the ISRM (1194-1199).* Denver: International Society for Rock Mechanics and Rock Engineering.

Chen, R. (1993). *In situ and laboratory studies of potash deformation.* Winnipeg, Canada: Ph.D. Thesis, University of Manitoba.

Chen, Y. (2014). Action of Fully Grouted Rock Bolts with Pull-and-Shear Loading. *48th US Rock Mechanics / Geomechanics Symposium.* Minneapolis, MN, USA: American Rock Mechanics Association.

Chen, Y., & Li, C. (2015). Performance of fully encapsulated rebar bolts and D-Bolts under combined pull-and-shear loading. *Tunnelling and Underground Space Technology*, 99-106.

Cook, R. (1993). Behaviour of Chemically Bonded Anchors. *ASCE Journal of Structural Engineering*, 2744-2762.

CSA (2007). *CAN/CSA-G30.18-M92 Billet-Steel Bars for Concrete Reinforcement (Renewed 2007).* Canadian Standards Association.

CSA (2011). *CAN/CSA-M430-90 Roof and Rock Bolts, and Accessories (Renewed 2011).* Canadian Standards Association.

Davis, M. (2015). *Distributed Fibre Optic Strain Sensing to Monitor Deterioration in Reinforced Concrete.* Kingston, Canada: M.Sc. Thesis, Queen's University.

Deere, D., & Miller, R. (1966). *Engineering Classification and Index Properties for Intact Rock.* Air Force Weapons Laboratory - Research and Technology Division.

Dight, P. (1982). *Improvements to the Stability of Rock Walls in Open Pit Mines.* Melbourne, Australia: Ph.D. Thesis, Monash University.

Dube, S. (1995). *A Laboratory Study on the Behaviour of Cable Bolts Subjected to Combined Tensile and Shear Loads.* Kingston, Canada: M.Sc. Thesis, Queen's University.

Duncan, E. S. (1990). *Deformation and Strength of Saskatchewan Potash Rock.* Winnipeg, Canada: Ph.D. Thesis, University of Manitoba.

Duncan, E. S., & Lajtai, E. Z. (1993). The creep of potash salt rocks from Saskatchewan. *Geotechnical and Geological Engineering*, 159-184.

Dywidag Systems International. (2015). *Mining and Tunneling Products Catalogue.* www.dsiunderground.com.

Feldman, L., & Bartlett, F. M. (2007). Bond Stresses Along Plain Steel Reinforcing Bars in PUllout Specimens. *ACI Structural Journal*, Vol. 104, 685-692.

Ferrero, A. (1995). The Shear Strength of Reinforced Rock Joints. *International Journal of Rock Mechanics and Mining Sciences & Geomechanics*, 595-605.

Goodman, R. E. (1989). *Introduction to Rock Mechanics.* John Wiley and Sons.

Grasselli, G., Kharchafi, M., & Egger, P. (1999). Experimental and numerical comparison between fully grouted and frictional bolts. *Proceedings of International Congress on rock mechanics (903-907).* Paris, France.

Haas, C. J. (1976). Shear Resistance of Rock Bolts. *Transactions of the Society of Mining Engineers, American Institute of Mining, Metallurgy, and Petroleum Engineers*, Vol. 260, 32-41.

Hoek, E. (2006). Shear strength of discontinuities. In E. Hoek, *Practical Rock Engineering.* RocScience Inc.

Hyett, A., Forbes, B., & Spearing, S. (2013). Enlightening Bolts: Using Distributed Optical Sensing to Measure the Strain Profile along Fully Grouted Rock Bolts. *32nd International Conference on Ground Control in Mining (107-112).* Morgantown, USA: Society for Mining, Metallurgy & Exploration.

International Society for Rock Mechanics Commission on Standardisation of Laboratory and Field Tests. (1978). Suggested methods for the quantitative description of discontinuities in rock masses. *International Journal of Rock Mechanics and Mining Sciences & Geomechanics*, 319-368.

Jalalifar, H., Aziz, N., & Hadi, M. (2006). The effect of surface profile, rock strength and pretension load on bending behaviour of fully grouted bolts. *Geotechnical and Geologcial Engineering*, 1203-1227.

Li, X., Nemcik, J., Mirzaghorbanali, A., Aziz, N., & Rasekh, H. (2015). Analytical model of shear behaviour of a fully grouted cable bolt subjected to shearing. *International Journal of Rock Mechanics & Mining Sciences*, Vol. 80, 31-39.

Luna Inc. (2016). *ODISI-B User's Guide Ver. 4.4.1.* Retrieved from Luna Inc. Resource Library: https://lunainc.com/resource-library

Neely, D. (2014). *Failure Mechanism of Resin Anchored Rebar in Potash.* Saskatoon, Canada: M.Sc. Thesis, University of Saskatchewan.

Pellet, F., & Egger, P. (1996). Analytical Model for the Mechanical Behaviour of Bolted Rock Joints Subjected to Shearing. *Rock Mechanics and Rock Engineering*, 73-97.

Regier, R. (2013). *Application of Fibre Optics on Reinforced Concrete Structures to Develop a Structural Health Monitoring Technique.* Kingston, Canada: M.Sc. Thesis, Queen's University.

Samiec, D. (2012). Distributed fibre-optic temperature and strain measurement with extremely high spatial resolution. *Optical Metrology Photonik International*, 10-13.

Schubert, P. (1984). *Das Tragvermogen des mortelversetrzten Ankers unter aufgezwungener Kluftverschiebung.* Leoben Austria: Montan-Universitat.

Spang, K., & Egger, P. (1990). Action of Fully-Grouted Bolts in Jointed Rock and Factors of Influence. *Rock Mechanics and Rock Engineering*, 201-229.

Stillborg, B. (1984). *Experimental investigation of steel cables for rock reinforcement in hard rock.* Lulea, Sweden: Ph.D. Thesis, Lulea University of Technology.

Stimpson, B. (1987). An analytical method for determining shear stiffness of an inclined grouted bolt installed across an open discontinuity. *International Journal of Mining and Geological Engineering*, 299-305.

Stimpson, B. (1994). Rock Bolting and Reinforcement - An Overview. *Workshop on Rock Mechanics and Ground Control in the Soft Rock and Coal Industries.* Saskatoon, Canada: Canadian Institute of Mining, Metallurgy and Petroleum.

Worsley, N., & Fuzesy, A. (1979). The Potash-bearing Members of the Devonian Prairie Evaporite of Southeastern Saskatchewan, South of the Mining Area. *Economic Geology*, Vol. 74, 377-388.

APPENDICES

The Appendices include the following sections:

A: Strength Tests on Potash and Resin

B: Tensile Tests on Rebar Rock Bolts

C: Distributed optical sensing technology

D: Theoretical derivation of the area moment of inertia for a slotted rod

E: Derivations and methods for analyzing fibre-optic strain gauge data

F: Lateral pull testing apparatus drawings and installation procedure

G: Theoretical derivation of equations for analyzing the lateral pull test data

H: Rebar Geometries

I: Additional data, plots, and discussion of beam bending test results

J: Additional data, plots, and discussion of double shear test results

K: Additional data, plots, and discussion of lateral pull tests

L: Additional data, plots, and discussion of in situ instrumentation

Appendix A – Strength Tests on Potash and Resin

This testing was conducted to obtain strengths for the potash and resin associated with rebar testing. A variety of tests have been developed and standardized to quantify the strength of rock so four methods were used in this research. This chapter summarizes the testing methods and the results of these tests.

The potash samples were collected using a pneumatic rotary drill from the back of the production level drifts at Nutrien's Cory mine. These samples were 75 mm diameter cores of various lengths. The samples were sealed in plastic prior to being brought to surface in order to minimize the effect of air moisture on their strength.

The resin cylinders tested were cast in 75 mm PVC pipe coated with form oil. This resin is a two-component pourable "Ground Lok" polyester resin supplied by Dywidag Systems International (DSI). The resin begins hardening after 24 minutes at room temperature. DSI advertises the pourable resin has a UCS of 83 MPa (12,000 psi) (DSI, 2015).

It should be noted, that this pourable resin is not the same resin used to install rebar rock bolts in the potash mines. In the underground environment, two-component resin cartridges are used and will fully harden within 2 minutes of mixing. Creating resin cylinders and other test specimens from this quick hardening resin was not practical, so only the pourable resin was used and tested in the laboratory. Without a practical method to test the strength of the resin cartridges, it has to be assumed that the pourable resin and the resin cartridges are of similar strength.

A.1 UCS Tests

Uniaxial compression strength (UCS) tests are one of the simplest and most common tests used to quantify the strengths of rocks. UCS tests were conducted on potash and resin samples according to ASTM D7012 – 14, unless otherwise stated. The potash and resin samples were loaded at a rate of 334 N/s, using a Tinius Olsen Loading Frame (Figure A.1). This loading rate was chosen to fail the sample within 5 to 15 minutes, as specified in the standards.

Three UCS tests were conducted on potash samples and three were conducted on resin samples. Although this is a very small sample size, the tests were simply intended to verify the strengths reported by previous researchers and advertised by DSI.

Figure A.1. Tinius Olsen loading frame used for UCS testing

A.2 Leeb and Schmidt Tests

Potash and resin samples were also tested with a Leeb Digital Hardness Tester from Wilson and a Schmidt Hammer from Proceq (Figure A.2). These tests are very easy to perform and are non-destructive. Testing for the Schmidt was done according to Standard ASTM D5873 – 14 and the instructions in the user manual were followed for the Leeb Tester

The Schmidt hammer impacts the samples with spherical tip of radius 25 mm while the Leeb hardness tester impacts with a sphere of radius 1.5 mm. The impact area suggests that the Leeb hardness tester will measure the hardness of samples at a smaller scale and, likely, is more representative of potash crystal hardness. The Schmidt hammer measures hardness on a larger scale and should be representative of hardness on the order of two crystal grains.

All tests were conducted in a downward direction. Ten tests were conducted at a random position on each sample with each instrument and the results were averaged. Three samples of potash were tested and three samples of resin were tested. The results of the Schmidt hammer tests were then converted to UCS values using the table originally presented in Deere and Miller (1966) and more recently in ISRM (1978) and Hoek (2006).

Figure A.2. Schmidt Hammer (left) and Leeb Hardness tester (right)

A.3 Penetration Tests

The penetration tests were developed by Schubert (1984) while investigating the behaviour of fully-encapsulated rock bolts crossing a joint surface. The tests provide the penetration modulus on which Spang and Eggers (1990) empirical model is based. The penetration modulus can be compared to UCS using Equation 2.1 presented by Spang and Egger (1990).

The penetration tests are performed by pressing a 20 mm diameter ball bearing into a rock sample with an increasing force normal to the rock surface (Figure A.3). An adequately large rock sample, especially in the case of a weak rock like potash, must be used so that premature splitting similar to a point load test (ASTM Standard D5731-08) is avoided. The load on the ball bearing was increased at a rate of 222 N/s using the Tinius Olsen machine in Figure A.1. The load was applied to the ball bearing via a 150mm square AR-400 steel plate.

Displacements were based on the average of the two Linear Variable Differential Transformers (LVDT's) positioned between the loading platform and AR-400 plate. Given the hardness of the ball bearing and loading platen as well as the relative weakness of the samples being tested, the system was assumed to be perfectly rigid. This procedure does not account for any mode of failure of the samples, it only considers the penetration of the ball bearing with applied load.

The penetration modulus, EM, was determined from the load vs displacement plots of the penetration tests. The steepest and most linear section of the plot near the middle of the test was visually identified. A least-sum-of-squares method is then used to fit a line to this section of data and the slope of that line is taken to be the penetration modulus.

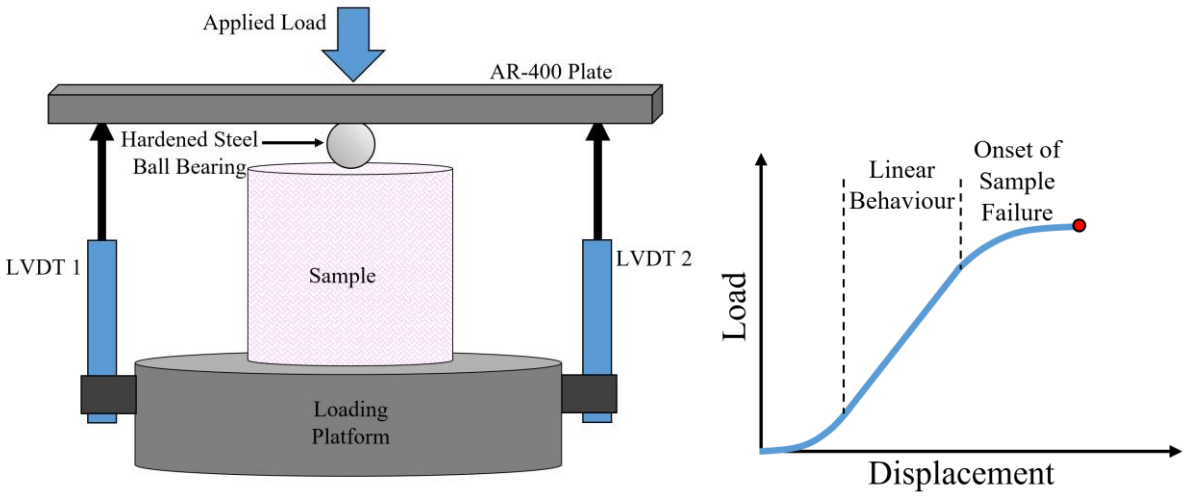

Figure A.3. Penetration test set-up (left) and typical test curve (right)

A.4 Results from Tests on Potash

This section describes the results of all strength tests conducted on potash and resin samples. The raw results of each testing suite are presented followed by a comparison of across all testing methods.

The UCS tests on potash are summarized in Table A.1. The sample geometries are also listed. Figure A.4 shows the three samples prior to testing. It should be noted that the length to diameter ratio for sample POT-UCS-1 was slightly below the recommended ratio proposed in ASTM D7012−14. Despite this, the tests were still conducted as these were the longest core samples that could be drilled without fractures.

Figure A.5 shows the three potash UCS samples after testing. Although the samples did not fail along a single discrete failure plane, the failure methods appear to be valid. The UCS values have a coefficient of variation of 16%, which suggests significant variability but was deemed acceptable given the nature of geological materials. The mean UCS value is in close agreement with the findings of previous researchers (Section 2.4).

Table A.1. UCS test results on potash core

Test Number	Sample Length mm [in.]	Sample Diameter mm [in.]	Length/Diameter Ratio	Maximum Load kN [kips]	UCS MPa [ksi]
POT-UCS-1	178.6 [7.03]	92.7 [3.65]	1.93	187 [42.0]	27.7 [4.02]
POT-UCS-2	226.7 [8.93]	92.8 [3.65]	2.44	190 [42.6]	28.0 [4.06]
POT-UCS-3	232.0 [9.13]	92.8 [3.65]	2.50	131 [29.5]	19.4 [2.82]
Mean					25.0 [3.63]
Standard Deviation					4.0 [0.58]
Coefficient of Variation					16%

Figure A.4. Potash UCS samples prior to testing: POT-UCS-1 (left), POT-UCS-2 (middle), and POT-UCS-3 (right)

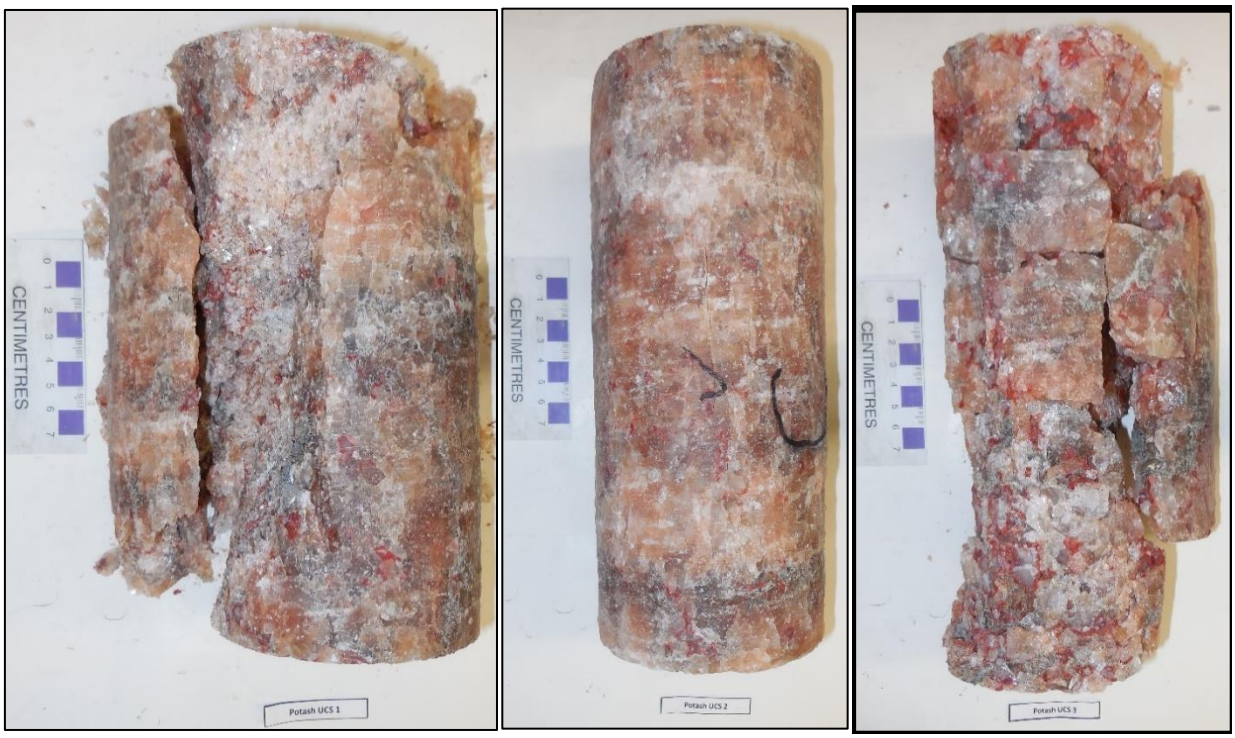

Figure A.5. Potash UCS samples after testing: POT-UCS-1 (left), POT-UCS-2 (middle), and POT-UCS-3 (right)

Schmidt hammer and Leeb rebound hardness tests were also conducted on three separate potash samples. The results of these tests are shown in

. The tests provide index values to help understand the general strength of the potash rock relative to other rock types. Relatively speaking, the potash rock is quite weak. One should also note the Schmidt Hammer test results were converted to UCS values using the table from Hoek (2006).

Table A.2. Potash Leeb and Schmidt Hammer test results

Sample Number	Leeb Rebound Hardness (average of 10 tests)	Schmidt Hammer (average of 10 tests)	Unit Weight kN/m3 [lb/ft3]	UCS Calculated from Schmidt Hammer MPa [ksi]
POT-RBND-1	295	18.0	20.7 [133]	22 [3.2]
POT-RBND-2	316	17.0	21.1 [136]	21 [3.0]
POT-RBND-3	300	13.7	20.5 [132]	18 [2.6]
Mean	303	16.2	20.8 [134]	20 [2.9]
Standard Deviation	9.1	1.8	0.2 [1.3]	1.6 [0.23]
Coefficient of Variation	3%	11%	1%	8%

Four penetration tests were conducted on potash core samples. The potash core samples are shown in Figure A.6 and their geometries are summarized in Table A.3. The samples were short relative to UCS tests, but there are no standards defining the sample size for penetration tests.

All samples were loaded until failure. The samples failed through the entire sample similar to a point load test. The failed samples are shown in Figure A.7. The load-penetration plots of the tests are shown in Figure A.8 along with the linear sections of the plots that were used to estimate the penetration modulus.

Another interesting relation visible in the plots in Figure A.8 is the lower “stiffness” at the start and end of each test. The lower stiffness at the start of the test is attributed to seating the loading platens and ball bearing on the surface of the potash. The lower stiffness at the end of the test can be attributed to the gradual plastic failure of the sample as a whole. The linear behaviour in the middle of the tests is believed to be sufficient for estimating the penetration modulus and thus the samples tested were large enough for a valid test.

The results of the tests are summarized in Table A.3. The penetration moduli estimated from the tests are all relatively close with a mean value of 7.17 kN/mm. These moduli were converted to a rough UCS using the empirical relationship in Spang and Egger (1990). The mean UCS is 16.7 MPa.

Table A.3. Penetration test results for Potash Samples

Test Number	**Sample Length mm [in.]**	**Sample Diameter mm [in.]**	**Penetration Modulus, EM kN/mm [kips/in.]**	**UCS Calculated from Equation 2.1 MPa [ksi]**
POT-PEN-1	89.7 [3.53]	92.6 [3.64]	6.69 [38.2]	15.1 [2.19]
POT-PEN-2	89.1 [3.51]	93.1 [3.67]	8.04]45.9]	19.6 [2.85]
POT-PEN-3	92.6 [3.64]	95.3 [3.75]	6.83 [39.0]	15.5 [2.25]
POT-PEN-4	112.3 [4.42]	94.0 [3.70]	7.13 [40.7]	16.6 [2.40]
Mean			7.17 [41.0]	16.7 [2.42]
Standard Deviation			0.52 [3.0]	1.8 [0.26]
Coefficient of Variation			7%	11%

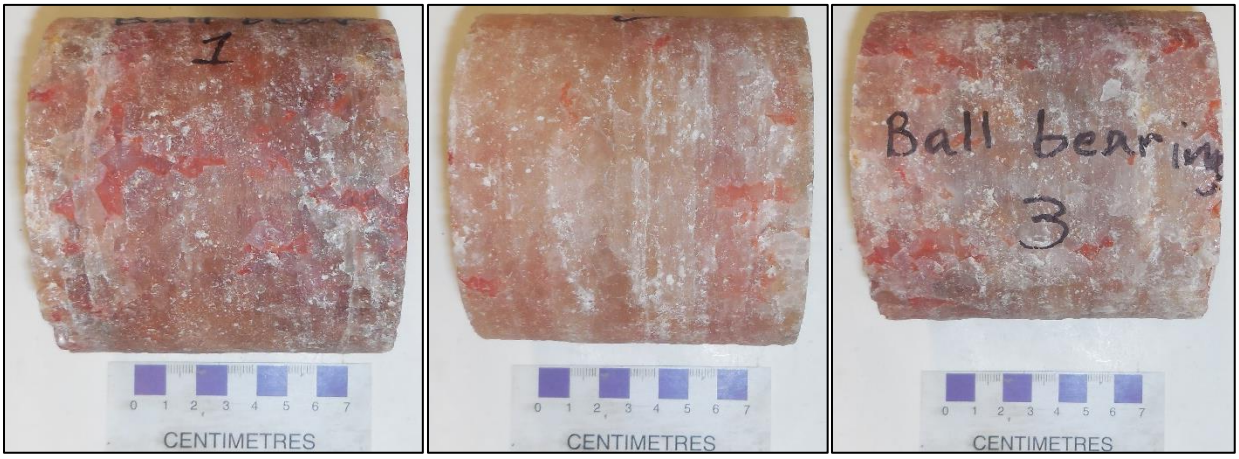

Figure A.6. Potash samples prior to Penetration Testing with POT-PEN-1 (left), POT-PEN-2 (centre), and POT-PEN-3 (right)

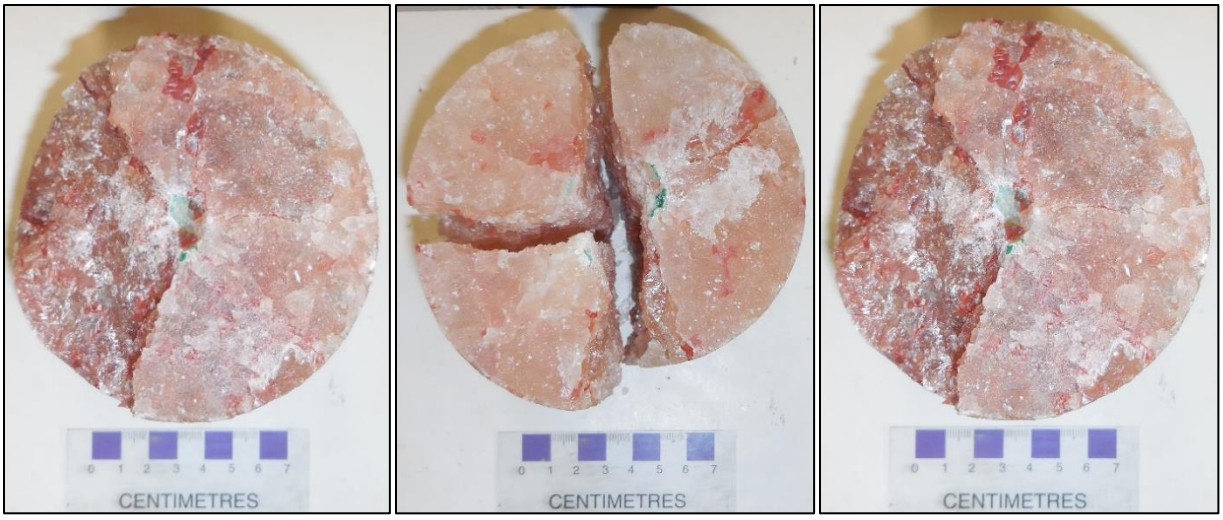

Figure A.7. Potash samples after Penetration Testing with POT-PEN-1 (left), POT-PEN-2 (centre), and POT-PEN-3 (right)

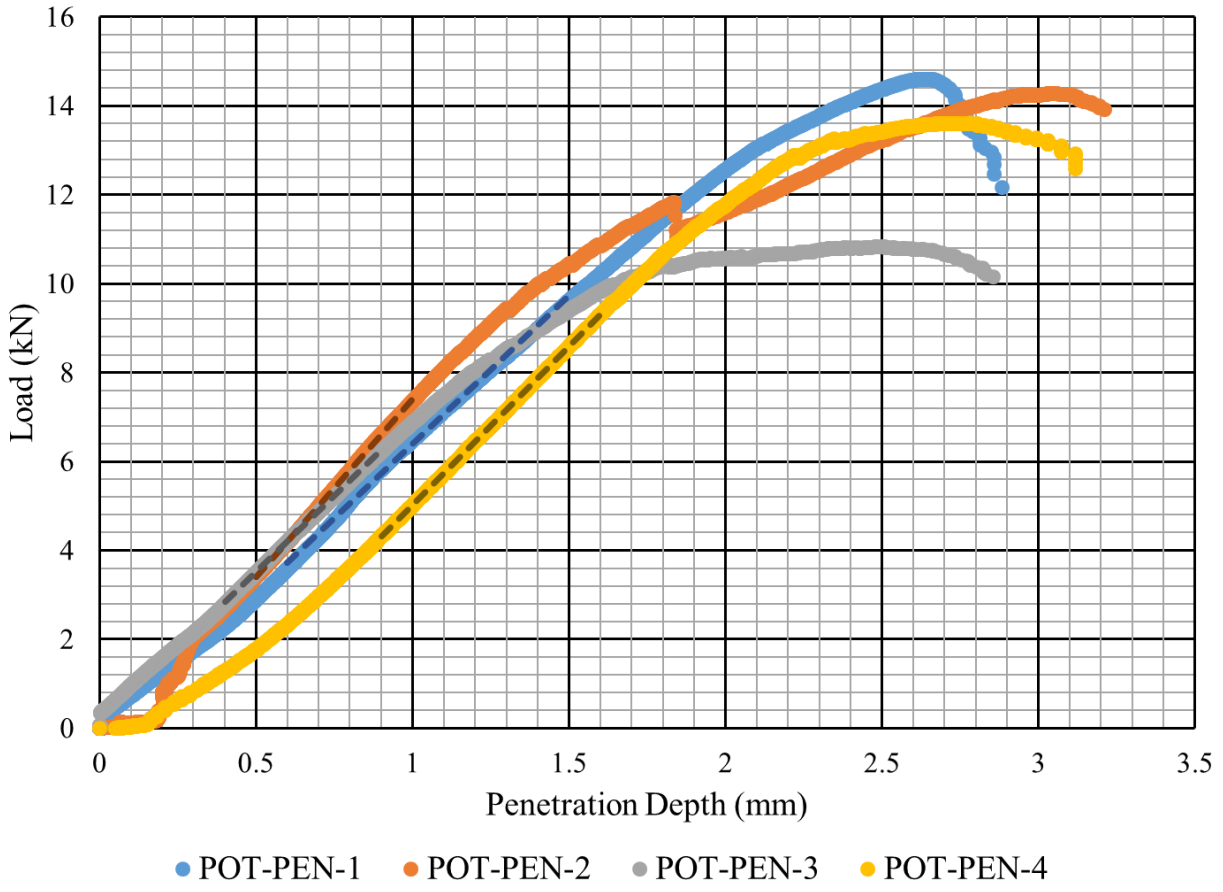

Figure A.8. Load vs Penetration plot of penetration tests on potash samples

The mean value of the UCS tests on potash as well as the converted UCS values from the Schmidt Hammer and penetration tests are compared in Table A.4. The mean potash strength measured directly using UCS tests is in close agreement with the short term strengths found by Neely (2014). The UCS calculated from the penetration tests however, are considerably lower. This is not surprising since the conversion from Spang and Egger (1990) is an empirical conversion.

Table A.4. Summary of potash strength test results

	Uniaxial Compressive Strength tests	**UCS calculated from Schmidt Hammer tests**	**UCS calculated from penetration tests**	**UCS from Neely (2014)**
Mean UCS MPa [ksi]	25.0 [3.63]	20 [2.9]	16.7 [2.42]	25.4 [3.68]

A.5 Results from Tests on Resin

Three UCS tests were conducted on the two-part pourable resin from DSI and the results are summarized in Table A.5. The sample lengths and diameters are also listed. Figure A.9 shows the three samples prior to testing. The length to diameter ratio for both RSN-UCS-2 and RSN-UCS-3 were below the recommended ratio proposed in ASTM D7012−14. The tests were still conducted but it is possible that the UCS values measured are affected by the shorter length.

Qualitatively, the resin samples could be seen to have striations and different colouring throughout the samples. The colouring suggests there was incomplete mixing of the pourable resin, but the samples appeared to be fully hardened regardless. There could be weakness within the samples that cause the samples to fail prematurely in the UCS tests.

Figure A.10 shows the three resin samples after testing. Although the samples did not fail along a single discrete failure plane, the failure methods appear to be valid. All three UCS values measured are significantly lower than the 83 MPa UCS advertised by DSI (2015). This weakness was likely due to poor mixing of the two components causing the colour striations and unhardened resin within the samples.

Table A.5. UCS test results on cast resin cylinders

Test Number	Sample Length mm [in.]	Sample Diameter mm [in.]	Length/Diameter Ratio	Maximum Load kN [kips]	UCS MPa [ksi]
RSN-UCS-1	152.6 [6.01]	76.0 [2.99]	2.01	92.0 [20.7]	20.3 [2.94]
RSN-UCS-2	144.1 [5.67]	75.9 [2.99]	1.90	110 [24.9]	24.5 [3.55]
RSN-UCS-3	146.0 [5.75]	76.2 [3.00]	1.91	224 [50.5]	49.2 [7.13]
Mean					31.3 [4.54]
Standard Deviation					12 [1.8]
Coefficient of Variation					38%

Figure A.9. Resin UCS samples prior to testing: RSN-UCS-1 (left), RSN-UCS-2 (middle), and RSN-UCS-3 (right)

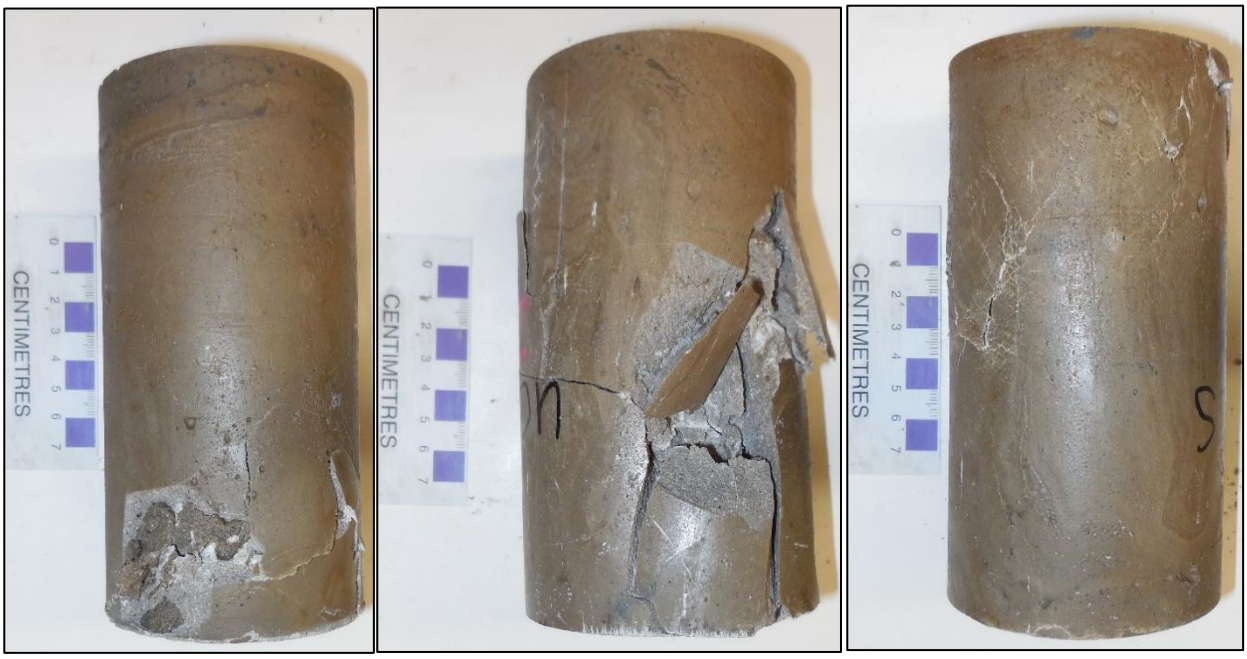

Figure A.10. Resin UCS samples prior to testing: RSN-UCS-1 (left), RSN-UCS-2 (middle), and RSN-UCS-3 (right)

Schmidt hammer and Leeb rebound hardness tests were conducted on the resin casts. A total of ten of each test were conducted on each resin sample and then averaged. The averaged results of these tests are shown in

Table A. A.6. Converting the Schmidt Hammer test results to a UCS using the table from Hoek (2006) provides a much higher UCS value than the UCS previously determined. This value, however, is still significantly lower than the advertised strength from DSI.

Table A.6. Resin Leeb and Schmidt Hammer test results

Sample Number	Leeb Rebound Hardness (average of 10 tests)	Schmidt Hammer (average of 10 tests)	Unit Weight kN/m3 [lb/ft3]	UCS Calculated from Schmidt Hammer MPa [ksi]
RSN-RBND-1	591	42.1	19.5 [125]	56 [8.1]
RSN-RBND-2	620	34.1	19.0 [122]	39 [5.7]
RSN-RBND-3	613	39.3	19.6 [126]	50 [7.3]
Mean	608	38.5	19.4 [125]	48 [7.0]
Standard Deviation	12	3.3	0.3 [1.9]	6.9 [1.0]
Coefficient of Variation	2%	9%	2%	14%

The pourable resin casts are shown in Figure A.11 prior to testing. Once again the samples were short relative to UCS testing. The sample geometries are given in Table A.6. Qualitatively, the samples could be seen to have striations and of darker and lighter resin. Although the entirety of the samples appeared fully hardened, the different colouring suggests incomplete mixing of the resin. The samples could potentially have weak areas within them.

The resin samples failed through the entire sample similar to the potash samples. The failed samples are shown in Figure A.12. The Load-Penetration plots of the three tests are shown in Figure A.13. The linear sections of the plots that were used to estimate the penetration moduli are highlighted.

The load-penetration behaviour of the resin tests in Figure A.13 do not exhibit as much plastic failure as the potash towards the end of the tests. This suggests the resin is more brittle than the potash. Regardless, the tests have sufficient linear behaviour to estimate the penetration modulus for the resin.

The results of the tests are summarized in Table A.7. The penetration moduli estimated from the tests have a mean value of 10.7 kN/mm and a coefficient of variation of 17%. These moduli were converted to a rough UCS and the mean value is 29.7 MPa.

Table A.7. Penetration test results for resin samples

Test Number	**Sample Length mm [in.]**	**Sample Diameter mm [in.]**	**Penetration Modulus, EM kN/mm [kips/in.]**	**UCS Calculated from Equation 2.1 MPa [ksi]**
RSN-PEN-1	86.7 [3.41]	76.1 [3.00]	12.6 [71.8]	37.2 [5.40]
RSN-PEN-2	57.7 [2.27]	75.8 [2.99]	8.31]47.5]	20.6 [2.99]
RSN-PEN-3	72.6 [2.86]	76.4 [3.01]	11.1 [63.6]	31.3 [4.54]
Mean			10.7 [61.0]	29.7 [4.31]
Standard Deviation			1.8 [10]	6.9 [1.0]
Coefficient of Variation			17%	23%

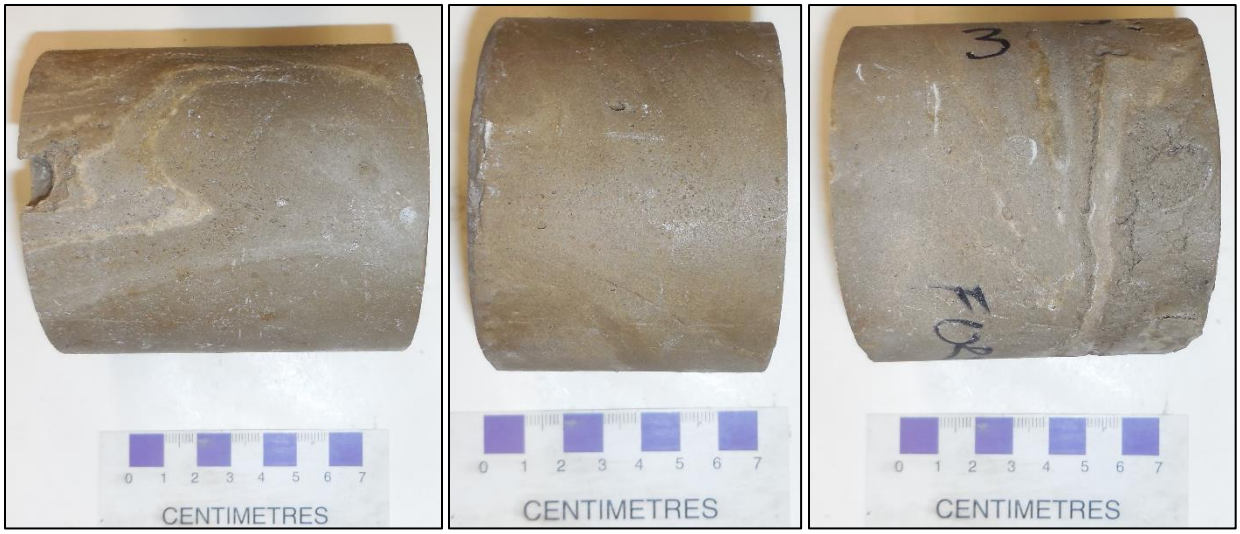

Figure A.11. Resin samples prior to Penetration Testing with RSN-PEN-1 (left), RSN-PEN-2 (centre), and RSN-PEN-3 (right)

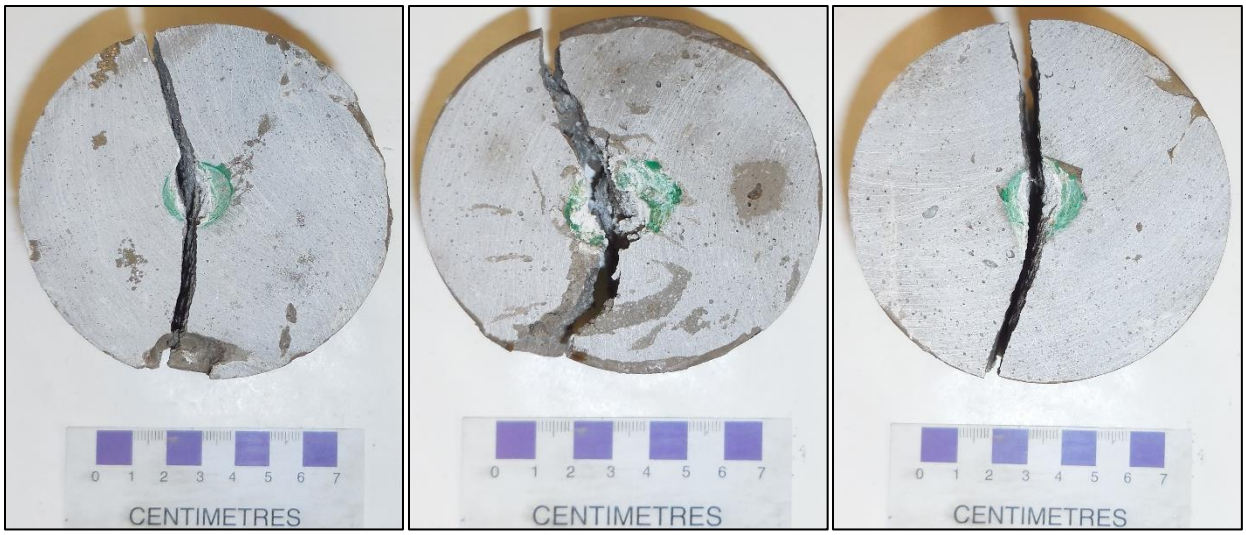

Figure A.12. Resin samples after Penetration Testing with RSN-PEN-1 (left), RSN-PEN-2 (centre), and RSN-PEN-3 (right)

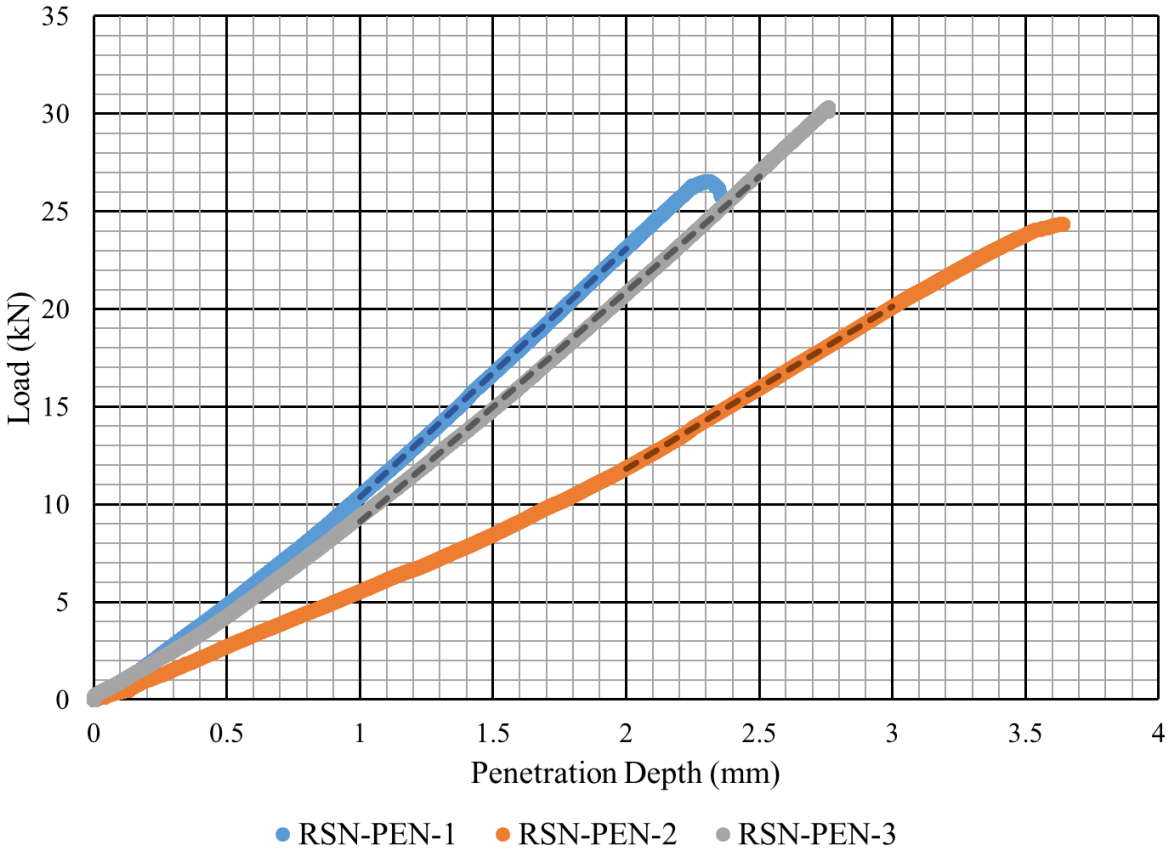

Figure A.13. Load vs Penetration plot of penetration tests on resin samples

The results of the UCS tests, the converted UCS values of the Schmidt Hammer tests, and the converted UCS values of the penetration tests on resin are compared in Table A.8. The mean values of all tests are significantly lower than the advertised strength of the resin from DSI. The reduced strength is attributed to poor mixing of the two-component resin despite closely following the manufacturer's instructions.

Table A.8. Summary of resin strength test results

	Uniaxial Compressive Strength tests	**UCS calculated from Schmidt Hammer tests**	**UCS calculated from penetration tests**	**UCS from DSI (2015)**
Mean UCS MPa [ksi]	31.3 [4.54]	48 [7.0]	29.7 [4.31]	83 12]

Appendix B – Tensile Tests on Rebar Rock Bolts

Tensile tests were conducted to determine the stress-strain behaviour of the rebar being investigated. The stress-strain behaviour is important for categorizing the type of rebar being tested as well as for quantifying at what stress and strain the rebar will yield and fail. The results of the tensile tests are also required for analyzing the fibre-optic instrumented rebar.

B.1 Experimental Design

Tensile tests were conducted to determine the Young's modulus, yield load, yield strain, ultimate load, and ultimate strain from the stress-strain curves of the various types and sizes of rebar used in this study. An ideal rebar stress-strain behaviour is shown in Figure B.1. From this behaviour, the yield point is identified as the transition from elastic to plastic behaviour and is defined by a yield stress, σ_{Yield}, and yield strain, ε_{Yield}. The ultimate stress, σ_{Ult}, is also identified in Figure B.1 along with the corresponding strain, ε_{Ult}.

All tensile tests were conducted on a Satec 600X Loading Frame (Figure B.2). Data collection from the load cells, pressure transducers, and LVDT's was done with LabVIEW. The cross sectional view of the set-up in Figure B.3 shows that the samples were loaded using "friction grips" that "grabbed" the rebar samples. This gripping mechanism is expected to result in some slippage of the rebar especially at lower loads so the two LVDTs were mounted directly to the rebar.

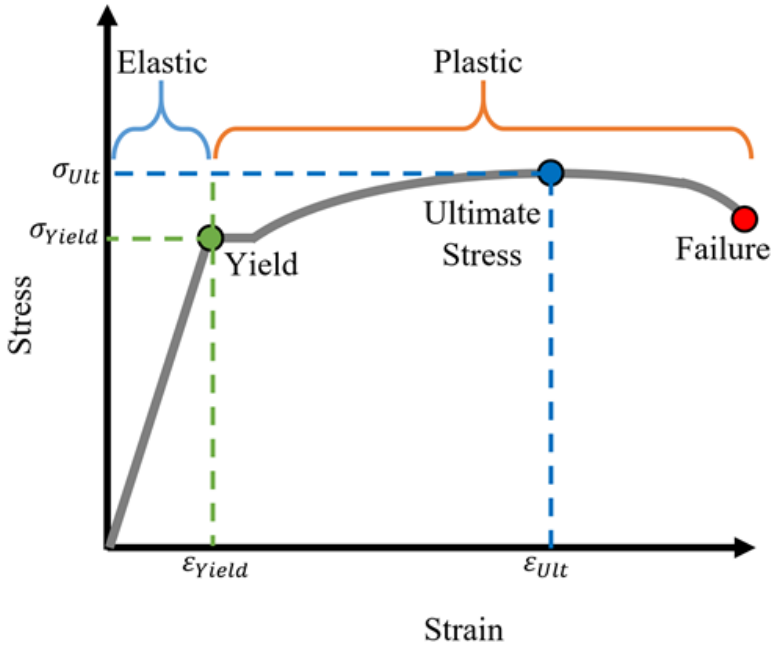

Figure B.1. Expected stress-strain behaviour of rebar showing the yield point and maximum stress

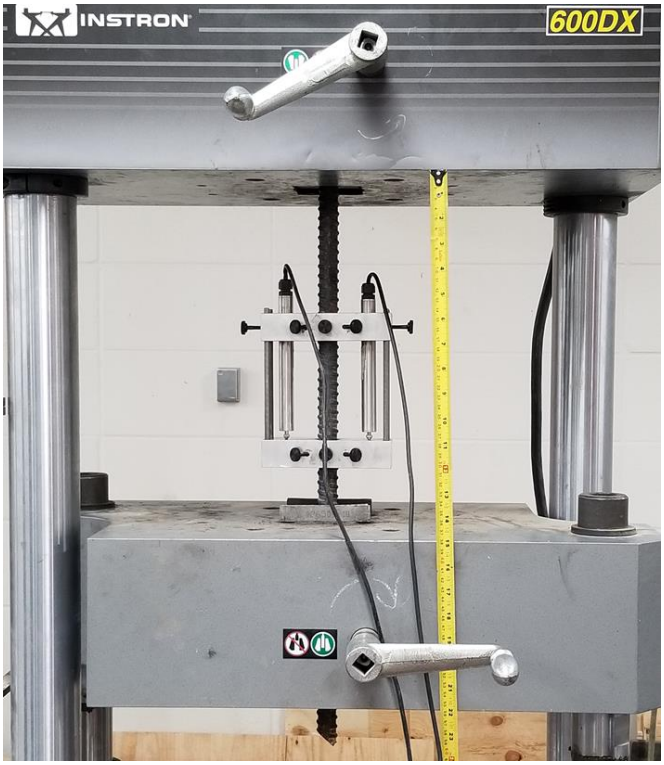

Figure B.2. Tensile testing machine

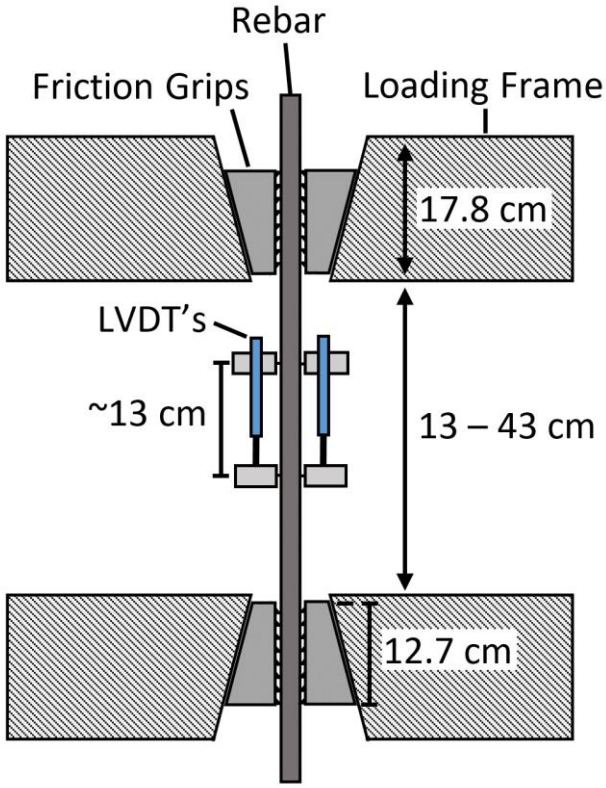

Figure B.3. Cross-sectional view of tensile test setup

In calculating stress from the load data, the cross sectional area of the grooved rebar was assumed to be a perfect circle and the minimum diameter was used. Tensile stress calculations were made according to Equation B.1:

$$\sigma_T = \frac{4\,P}{\pi\, d_{rebar}^2}$$

Equation B.1

Where σ_T = tensile stress within the rebar

P = applied tensile load

d_{rebar}= minimum diameter of the rebar

The measurements from the two LVDTs were used to plot the stress-strain curves for each test. The yield stress, σ_{yield}, was visually estimated as the maximum stress on the initial linear portion of the stress-strain plot. The corresponding strain was then taken as the yield strain, ε_{yield}. The experimentally determined Young's Modulus, E_{exp}, can then be calculated from Equation B.2.

$$E_{exp} = \frac{\sigma_{yield}}{\varepsilon_{yield}}$$

Equation B.2

Where E_{exp} = tensile stress within the rebar

σ_{yield} = applied tensile load

ε_{yield}= minimum diameter of the rebar

The ultimate stress, σ_{ult}, for each test was the maximum stress calculated throughout the test. The corresponding strain at that stress was determined to be the ultimate strain, ε_{ult}. This method disregards any necking behaviour that the rebar exhibits, which can be complex and difficult to measure.

B.2 Results

The tensile tests were completed successfully. Five valid tests were conducted on 22M (#7) Grade 400 (60) rebar. Unfortunately, issues with the LVDT data collection caused erroneous data in all but one of the tests. The applied tensile load is plotted against the axial strain for the one test with available strain data in Figure B.4.

The axial stress within the rebar was calculated from the load and is plotted against strain in Figure B.5. Both of these plots exhibit the key behaviours of medium carbon steel: an initial linear elasticity followed by a large component of plastic deformation.

The defining properties of the rebar are summarized in Table B.1. It should be noted that although the strain measurements for most samples was not available, the yield and ultimate loads and stresses could still be identified.

The average Young's modulus can be calculated from the mean yield stress and mean yield strain. The average Young's modulus of the 22M (#7) Grade 400 (60) rebar was found to be 246 GPa. This is significantly higher than the 200 GPa that is typically assumed for this steel.

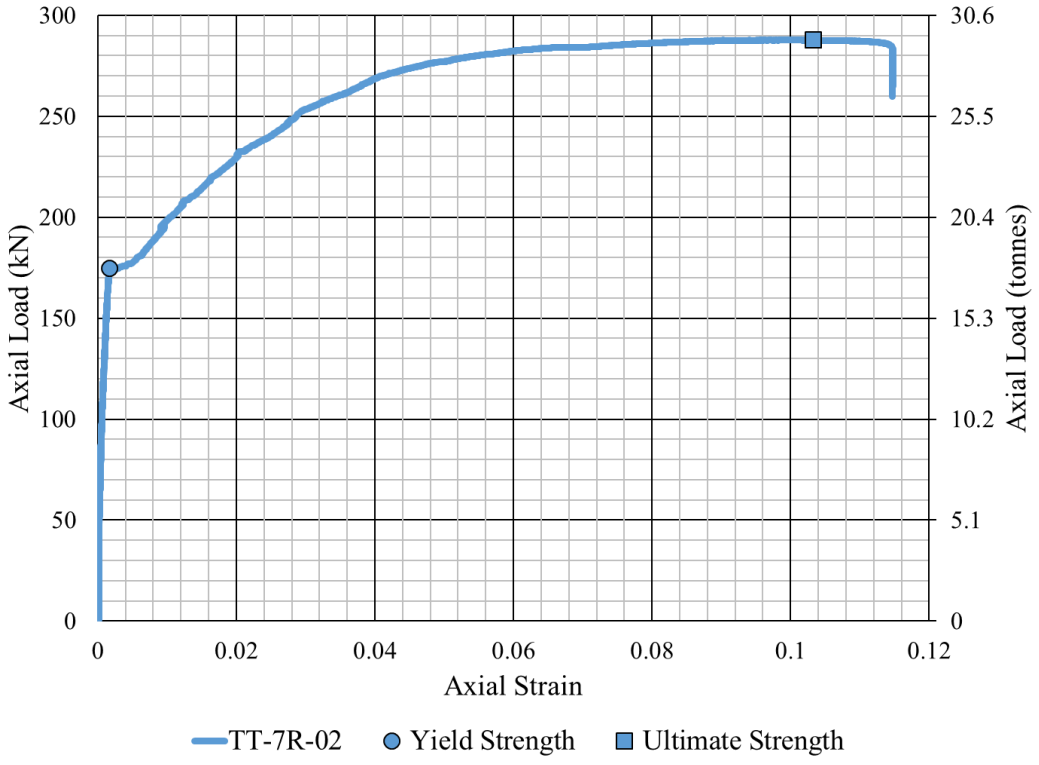

Figure B.4. Load vs Strain plot for tensile tests on 22M Grade 400 rebar

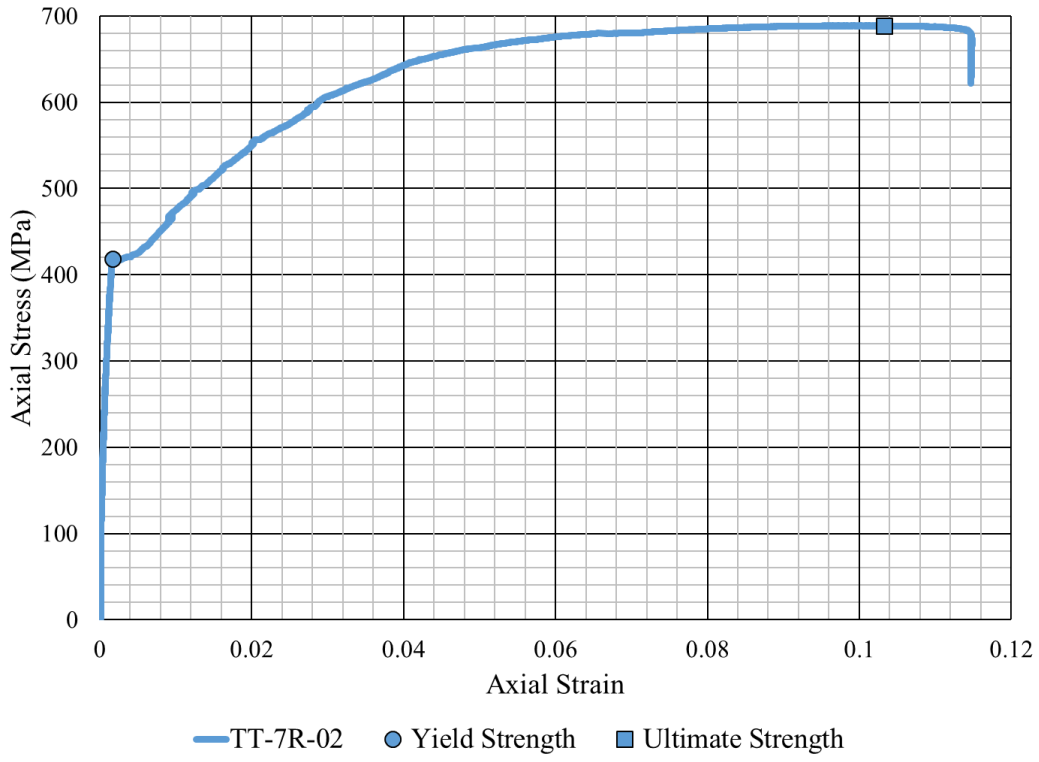

Figure B.5. Stress vs Strain plot for tensile tests on 22M Grade 400 rebar

Table B.1. Summary of results for tensile tests on 22M Grade 400 rebar

Sample	Yield Strength				Ultimate Strength		
	Load kN [tonnes]	**Stress MPa**	**Strain**	**Young's Modulus GPa**	**Load kN [tonnes]**	**Stress MPa**	**Strain**
TT-7R-02	175 [17.8]	418	0.0017	246	288 [29.4]	688	0.103
TT-7R-03	173 [17.6]	415	-	-	286 [29.2]	684	-
TT-7R-04	172 [17.5]	412	-	-	286 [29.2]	685	-
TT-7R-05	184 [18.8]	440	-	-	276 [28.1]	660	-
TT-7R-06	173 [17.6]	415	-	-	286 [29.2]	684	-
Mean	173 [17.6]	415	0.0017	246	287 [29.3]	686	0.103
Standard Deviation	1.1 [0.11]	2.5	-	-	0.87 [0.089]	1.8	-
Coefficient of Variation	0.6%	0.6%	-	-	0.3%	0.3%	

Four valid tests were conducted on 25M (#8) Grade 400 (60) rebar. Again, the applied tensile load was plotted against the axial strain for all tests in Figure B.6. The axial stress is plotted against the axial strain for all tests in Figure B.7. All tests exhibit the typical behaviour for mild steel.

Error! Reference source not found. summarizes the important characteristics of the rebar tests, such as the yield and ultimate load, stress, and strain. All values of load and stress were very similar, however the strain values varied considerably.

The average Young's modulus can again be calculated from the mean yield stress and mean strain at yield. The average Young's modulus of the 25M (#8) Grade 400 (60) rebar was found to be 237 GPa. Similar to the 22M rebar, this value is significantly higher than 200 GPa.

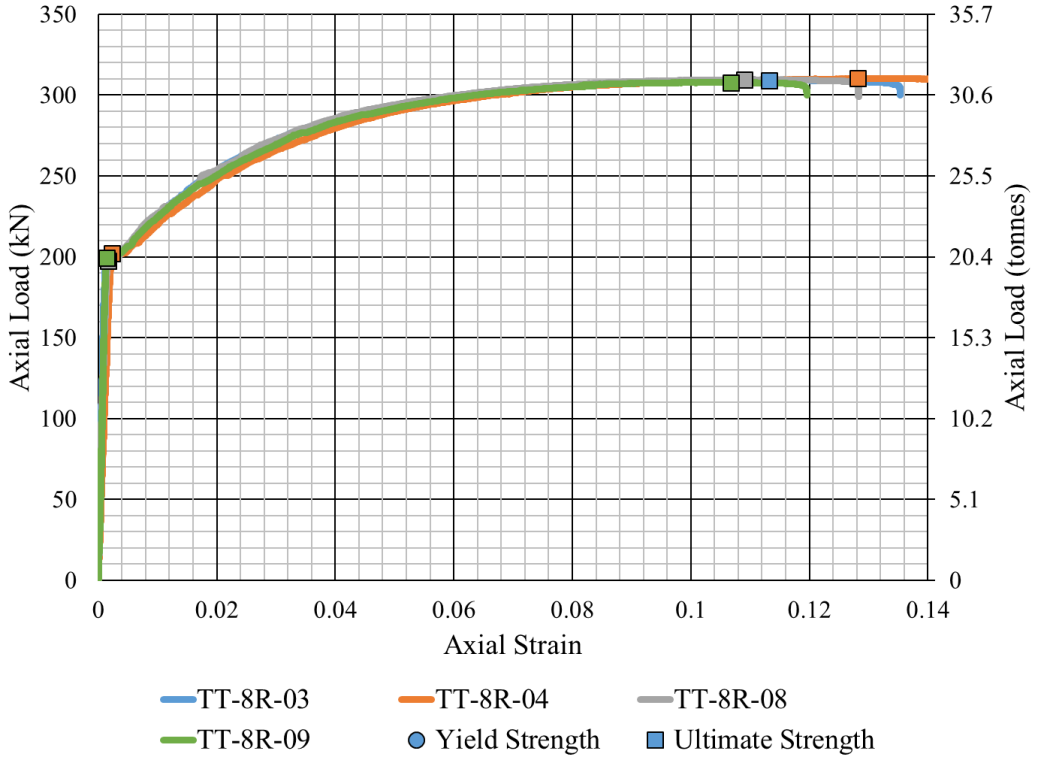

Figure B.6. Load vs Strain plot for tensile tests on 25M Grade 400 rebar

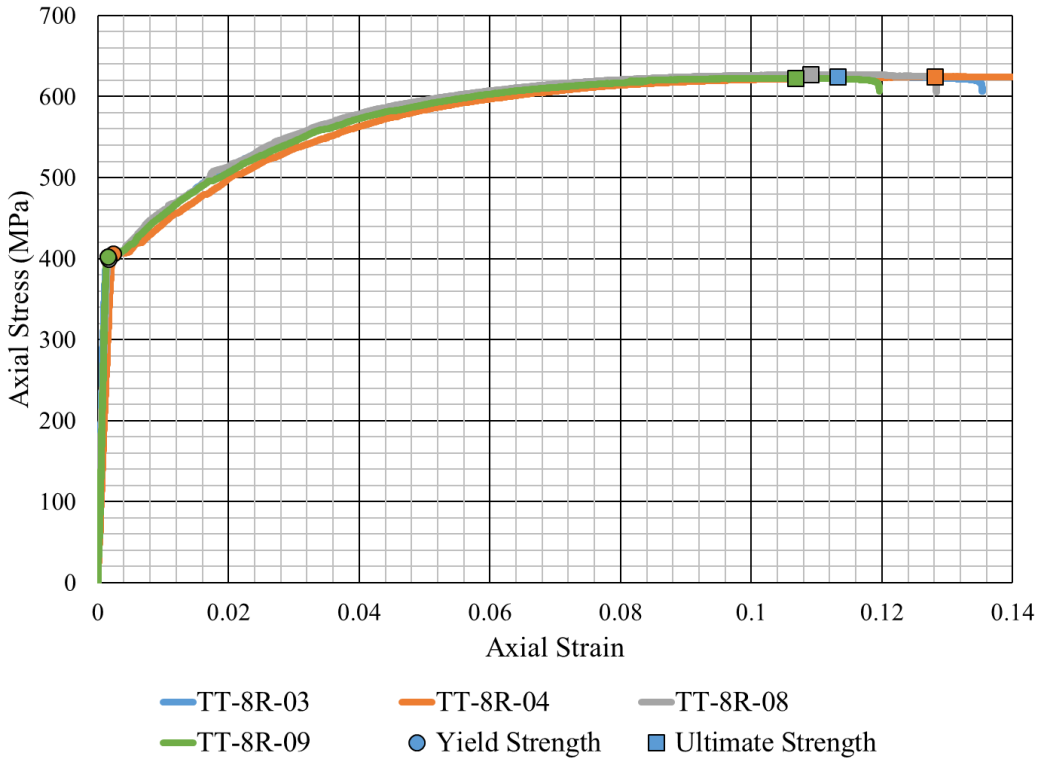

Figure B.7. Stress vs Strain plot for tensile tests on 25M Grade 400 rebar

Table B.2. Summary of results for tensile tests on 25M Grade 400 rebar

Sample	Yield Strength				Ultimate Strength		
	Load kN [tonnes]	Stress MPa	Strain	Young's Modulus GPa	Load kN [tonnes]	Stress MPa	Strain
TT-8R-03	200 [20.4]	402	0.0015	268	309 [31.5]	624	0.113
TT-8R-04	202 [20.6]	406	0.0023	177	310 [31.6]	625	0.128
TT-8R-08	198 [20.2]	400	0.0017	235	310 [31.6]	627	0.109
TT-8R-09	199 [20.3]	402	0.0015	268	308 [31.4]	622	0.107
Mean	200 [20.4]	403	0.0018	237	309 [31.5]	625	0.114
Standard Deviation	1.6 [0.16]	2.3	0.0003	37	0.87 [0.089]	1.7	0.008
Coefficient of Variation	0.8%	0.6%	17%	16%	0.3%	0.3%	7%

Six valid tests were conducted on 22M (#7) Grade 500 (75) dywidag threadbar. The applied tensile load is plotted against the axial strain for three tests in Figure B.8. Issues with the LVDT data collection prevented acquiring displacement and strain data for three of the tests.

The axial stress was calculated from the tensile load and is plotted against the axial strain in Figure B.9. The tests exhibited the typical behaviour as expected for mild steel which suggests the tensile tests were valid.

Table B.3 summarizes the important characteristics of the tests. Once again, despite the strain measurements not being available for some tests, the yield load and ultimate load was still identifiable. Similar to the #8 rebar tests, the yield and ultimate loads and stress were very similar, but the yield and ultimate strains varied considerably.

The average Young's modulus was calculated from the mean yield stress and mean strain at yield. The average Young's modulus of the 22M (#7) Grade 500 (75) dywidag was found to be 138 GPa. This value is significantly lower than the widely assumed Young's modulus of 200 GPa for this steel.

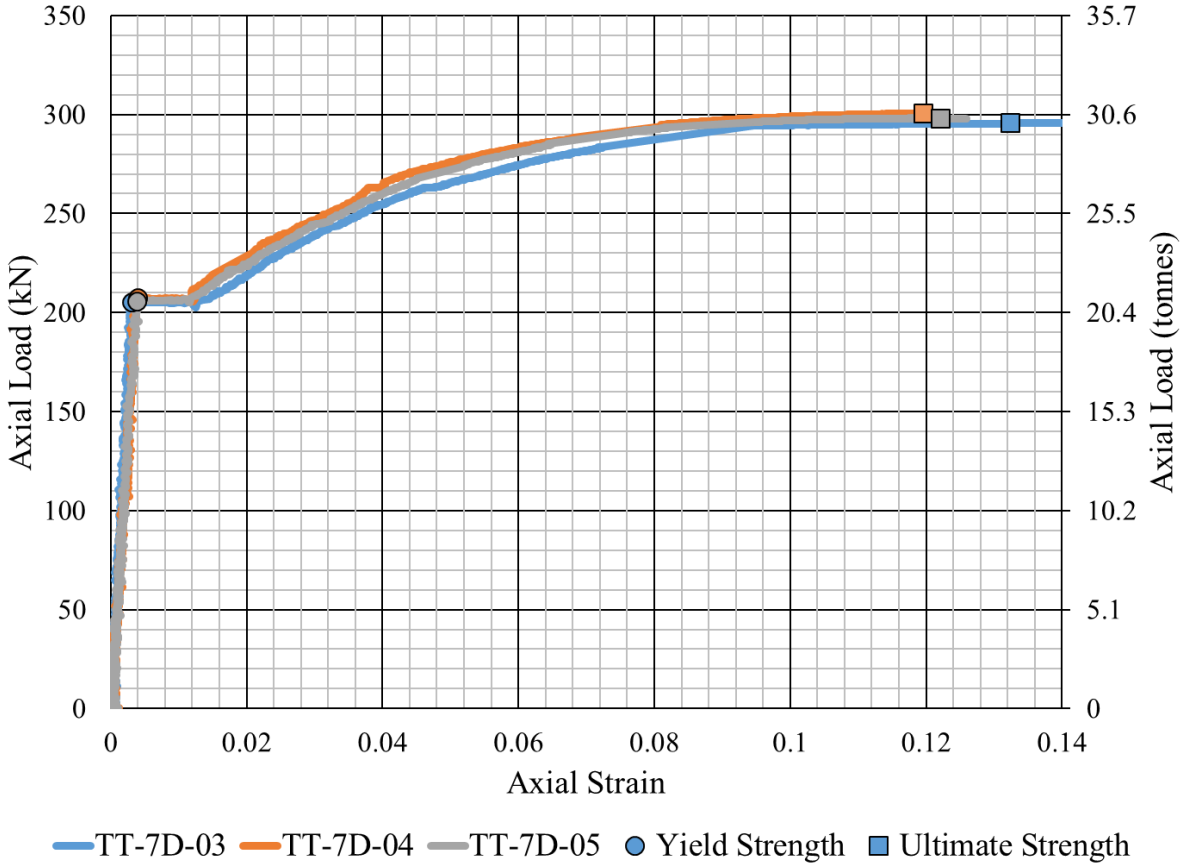

Figure B.8. Load vs Strain plot for tensile tests on 22M Grade 500 dywidag

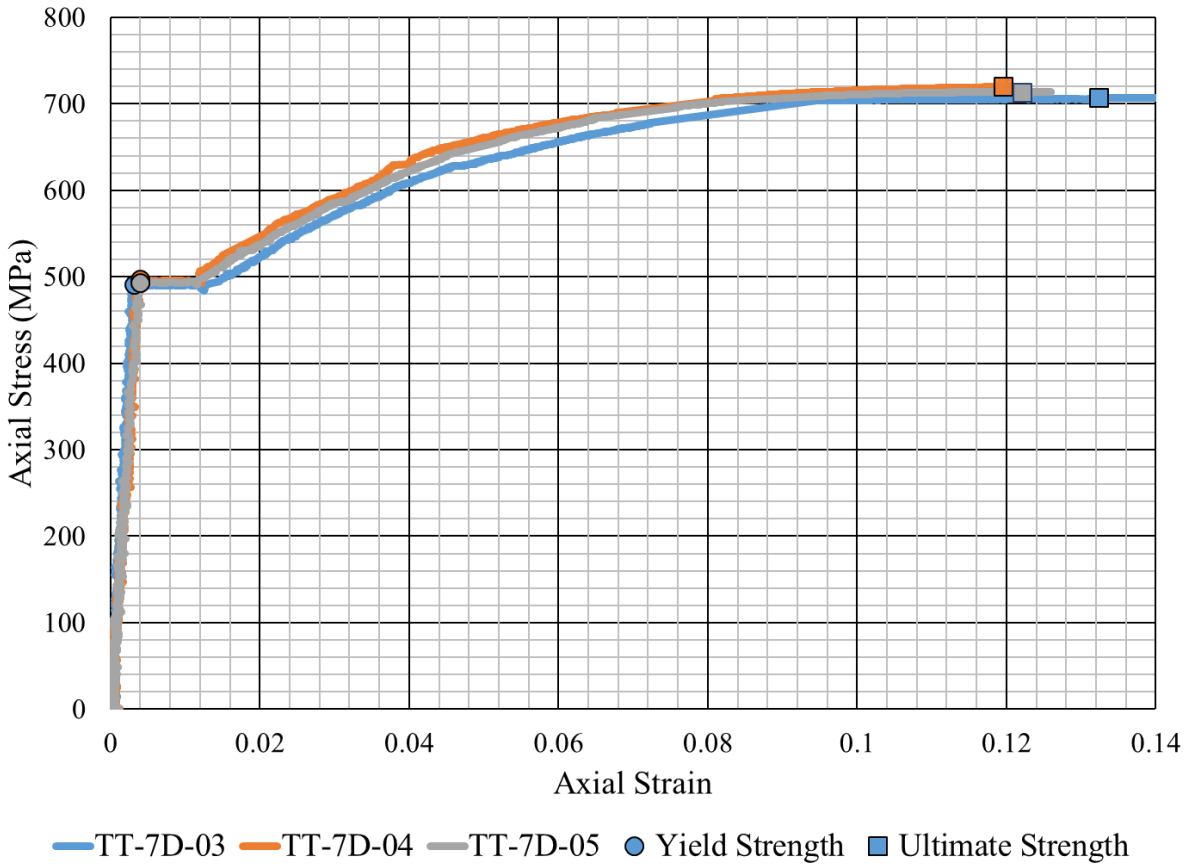

Figure B.9. Stress vs Strain plot for tensile tests on 22M Grade 500 dywidag

Table B.3. Summary of results for tensile tests on 22M Grade 500 dywidag

Sample	Yield Strength				Ultimate Strength		
	Load kN [tonnes]	**Stress MPa**	**Strain**	**Young's Modulus GPa**	**Load kN [tonnes]**	**Stress MPa**	**Strain**
TT-7D-03	205 [20.9]	491	0.0031	158	296 [30.2]	707	0.132
TT-7D-04	208 [21.2]	497	0.0040	124	301 [30.7]	720	0.120
TT-7D-05	206 [21.0]	493	0.0039	126	298 [30.4]	714	0.122
TT-7D-06	208 [21.2]	498	-	-	304 [31.0]	727	-
TT-7D-07	206 [21.2]	492	-	-	298 [30.4]	713	-
TT-7D-08	205 [20.9]	490	-	-	296 [30.2]	708	-
Mean	207 [21.1]	495	0.0036	136	300 [30.6]	717	0.125
Standard Deviation	1.2 [0.12]	3.0	0.0004	16	2.9 [0.29]	7.3	0.005
Coefficient of Variation	0.6%	0.6%	11%	11%	0.9%	1%	4%

The tensile tests appeared to provide valid measurements of the rebars strength. As discussed, issues with the LVDT data in some tests prevented calculation of some strain measurement. Additionally, the LVDT bracket used did not firmly attach to the rebar throughout the tests. The bracket attached to the rebar using set-screws and, as a tensile load was applied to the rebar, Poisson's ratio caused the diameter to decrease slightly. The set screws had to be continually retightened throughout each test. These issues with the LVDT instrumentation are likely the reason for the experimental Young's Moduli differing from the expected value of 200 GPa

Despite the results of these tensile tests, the Young's modulus of all rebar, E_{Rebar}, will be assumed to be 200 GPa in all analysis. This assumption requires calculation of a new ε_{yield} in agreement with σ_{yield} and a Young's modulus of 200 GPa. The various strength properties of each rebar type are summarized in Table B.4.

Table B.4. Summary of tensile strengths for all rebar types assuming a Young's Modulus of 200 GPa

Rebar Type	Yield Strength				Ultimate Strength		
	Load kN [tonnes]	**Stress MPa**	**Strain**	**Young's Modulus GPa**	**Load kN [tonnes]**	**Stress MPa**	**Strain**
22M (#7) Grade 400 (60) Rebar	173 [17.6]	415	0.0021	200	287 [29.3]	686	0.103
25M (#8) Grade 400 (60) Rebar	200 [20.4]	403	0.0020	200	309 [31.5]	625	0.114
22M (#7) Grade 500 (75) Dywidag	207 [21.1]	495	0.0025	200	300 [30.6]	717	0.125

Appendix C – Distributed Optical Sensing Technology

The following appendix section summarizes the distributed optical sensing system used to measure strain in this research project. The discussion has largely been taken from an internal report written for industry professionals with involvement in the project. The report was intended to summarize the practical implementation of the fibre-optic strain measuring technology for any individuals using the system either within the University or within the organizations that were involved in the project.

C.1 Introduction

Between August 2016 and April 2018 Garrett Snell carried out an intensive testing program using fibre-optic instrumented rebar. The fibre-optic instrumentation was purchased from YieldPoint Technologies and was used to measure strain within steel rebar in the laboratory and in Saskatchewan potash mines

The goal of the testing program was to determine the relation between the shear plane offset and the rebar's internal stress. This objective was approached using several different lab and field tests with the fibre-optic instrumented rebar. This report attempts to summarize the basics of the fibre-optic technology, analysis methods used, and various lessons learned throughout the testing program.

In its current state, the system is capable of measuring strain at 0.65mm increments along up to 10m of optical fibre. The technology and software are continuously being revised and improved upon by the manufacturer, Luna Inc. and the supplier, YieldPoint. The current version of this technology and how to use it is described herein.

The fibre-optic technology is being adapted for use in the mining industry by instrumenting rebar rock bolts in order to measure their deformation in various loading scenarios. Instrumented rebar will typically provide up to 10,000 strain measurements per reading and can sustain a measurement frequency up 10 Hz. Further information about the instrumented rebar can be found within this

report. A description of the analysis techniques used for processing the strain data can also be found in this report.

The technology has originally been developed with a controlled laboratory setting in mind. As with many technologies, certain alterations and precautions must be taken to use them in the rugged mining environment. This report summarizes the steps taken to ensure the distributed optical sensing technology survives in an underground potash mine.

C.2 The Optical Strain Sensing System

This section contains a brief description of the parts to the fibre-optic strain sensing system and how they connect to each other.

The strain sensing system is comprised of 4 main components: desktop computer, readout unit, high definition remote module, and the strained fibre. The four components and the way they interact is shown in Figure C.1. The entire package (excluding the instrumented rebar) was purchased from YieldPoint for $91,000 in August 2016. YieldPoint acts as an exclusive distributor in Canada for Luna Technologies. Luna Technologies developed and builds the components.

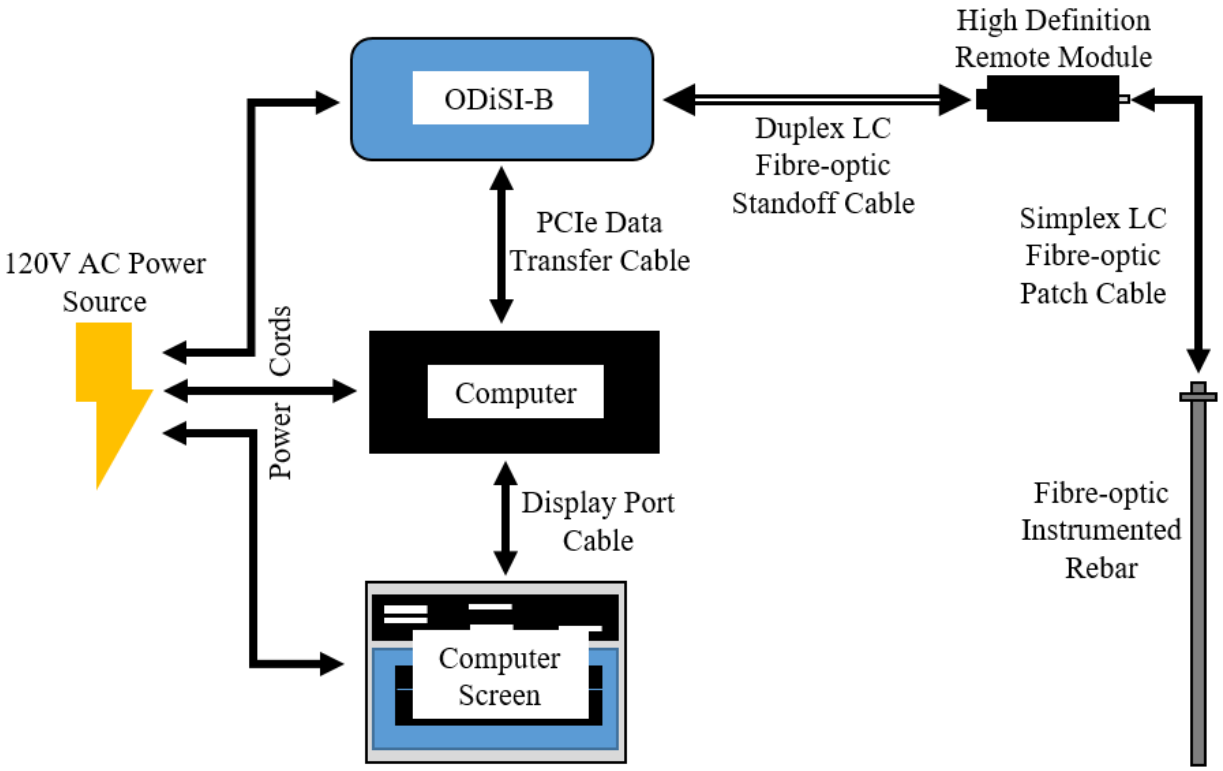

Figure C.1. Fibre-optic strain sensing components and connections

The desktop computer used was supplied by Luna technologies with the purchase of the readout unit and is shown in Figure C.2. It is a generally ordinary computer with a PCIe connection port. This is a high bandwidth port capable of large data throughput. The computer came preloaded with the three software programs used to connect to the readout unit and analyze the data: ODiSI, ODiSI Config, and ODiSI Post-processor.

The desktop computer must be connected to the ODiSI-B readout unit via a PCIe cable. The computer must also be connected to a computer screen with a display port cable and to a 120V AC power source with a power cord. **Please note: the computer must be turned on after the screen and the ODiSI-B readout unit or else the computer will not recognise these other two components.**

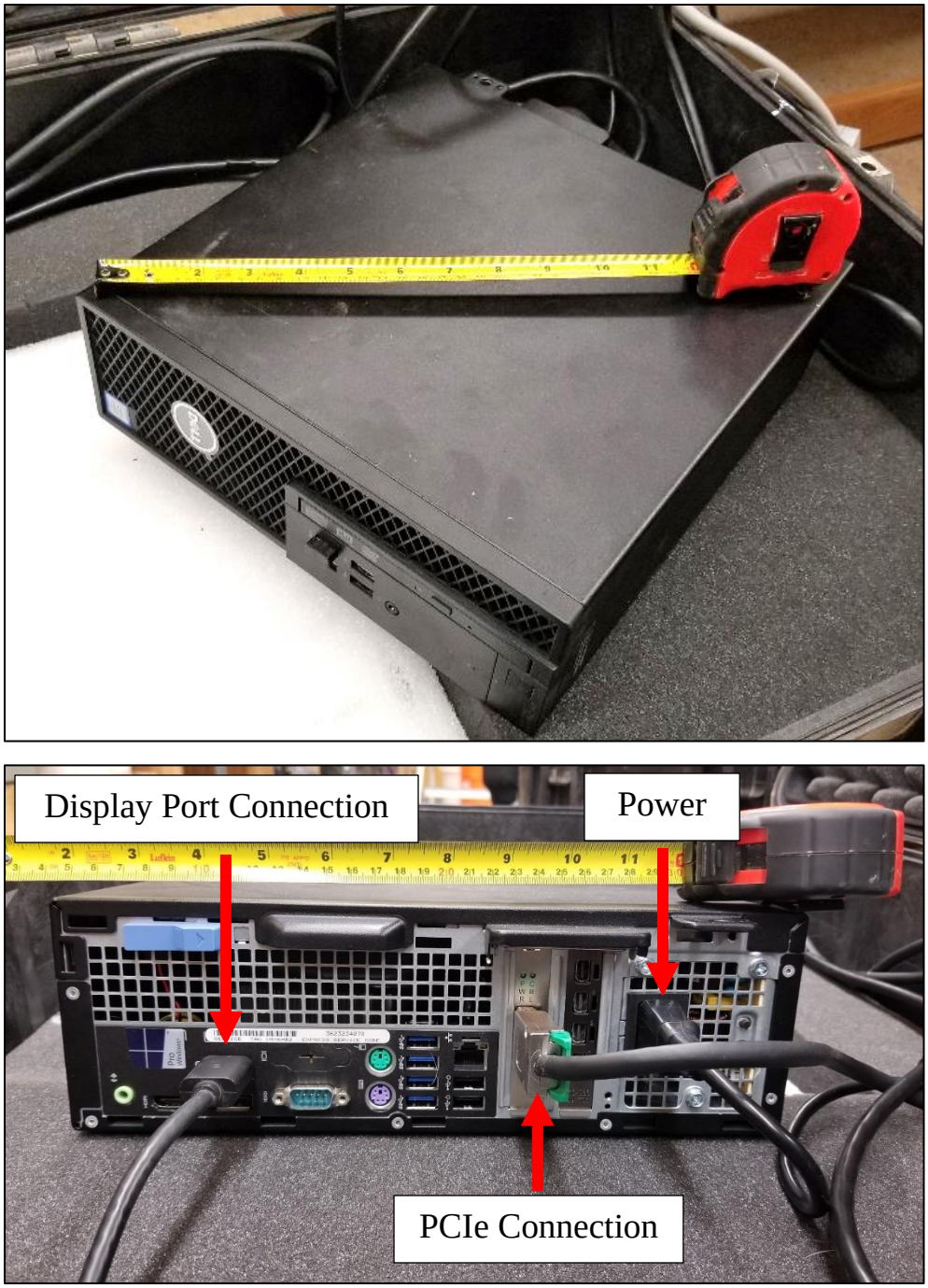

Figure C.2. Desktop computer (top) and the rear of the computer (bottom)

The readout unit is called the ODiSI-B and is shown in Figure C.3. This unit contains the optical source that sends light down the optical fibre. It also measures the reflected light and ultimately calculates the strain along the length of the strained fibre. Because of the large data collection rate

(up to1 million strain readings per second), the readout unit must send the data to the desktop through a PCIe connection.

The ODiSI-B unit must be connected to the desktop computer using a PCIe cable. The unit must also be connected to the high-definition remote module using a Duplex LC 1.25mm fibre-optic standoff cable (Figure C.4). **Please note: the ODiSI-B uses a laser as an optical source and operators should avoid looking directly into the fibre-optic connections.** Lastly, the readout needs to be connected to a 120V AC power source with a power cord.

Whenever connecting fibre-optic cables, the operator needs to repeatedly clean the LC connections. The male Duplex LC connection on the standoff cable needs to be cleaned with the female cleaning tool in Figure C.5. Swipe the small white connectors (called Ferrules) in one direction along the fabric surface of the cleaning tool. Cycle the tool so that only one swipe is made on the same section of fabric.

The female Duplex LC connection on the ODiSI-B unit needs to be cleaned with the male cleaning tool in Figure C.5. Insert the tool into the connection and continue firmly pushing on the blue part of the tool until the tool clicks and stops. The tool will insert a small piece of fabric into the connection and wipe the ferrule inside of the connection.

Please note: when the system is unable to detect the sensor or when there is excessive noise in a reading, the issue is almost always due to dirty connections!

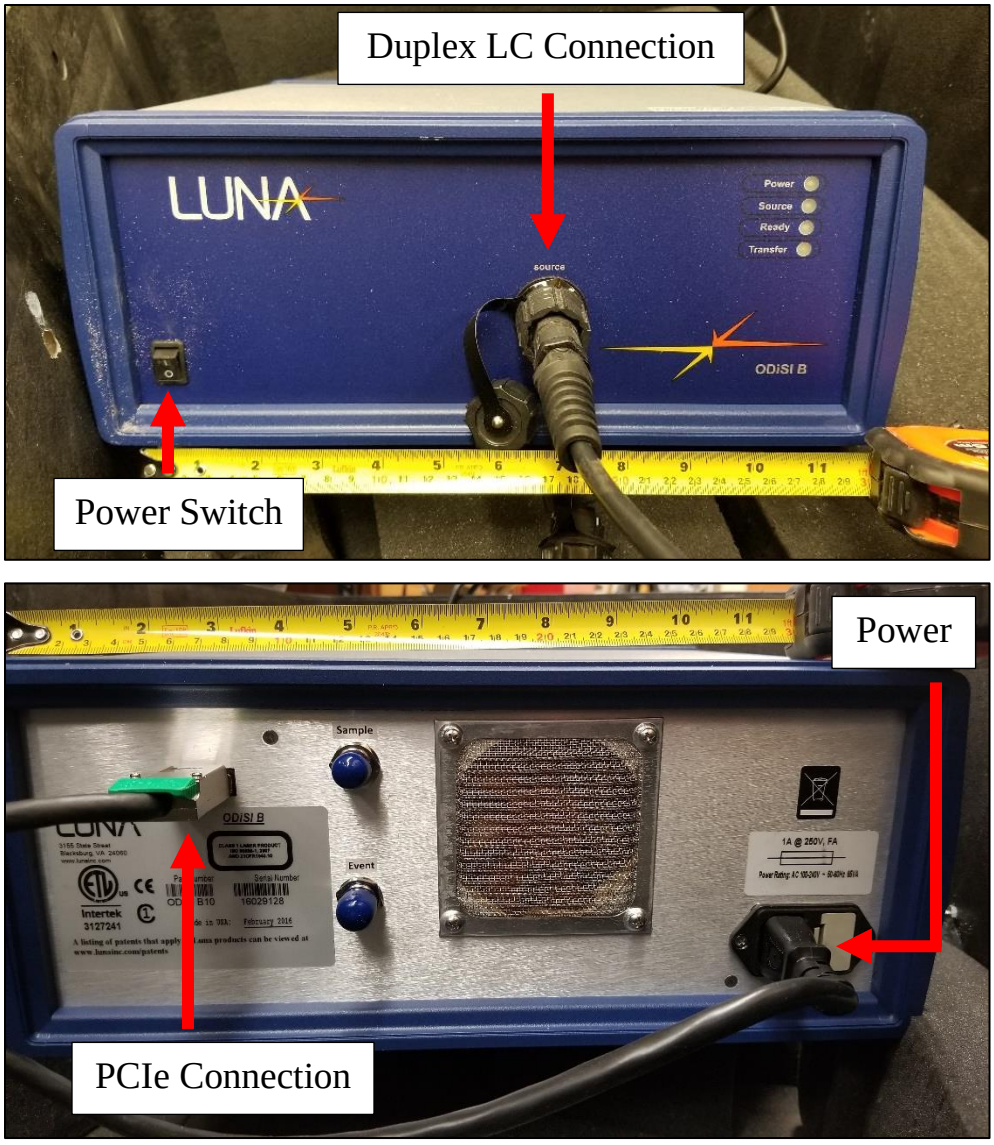

Figure C.3. Front of ODiSI-B readout unit (top) and rear of ODiSI-B (bottom)

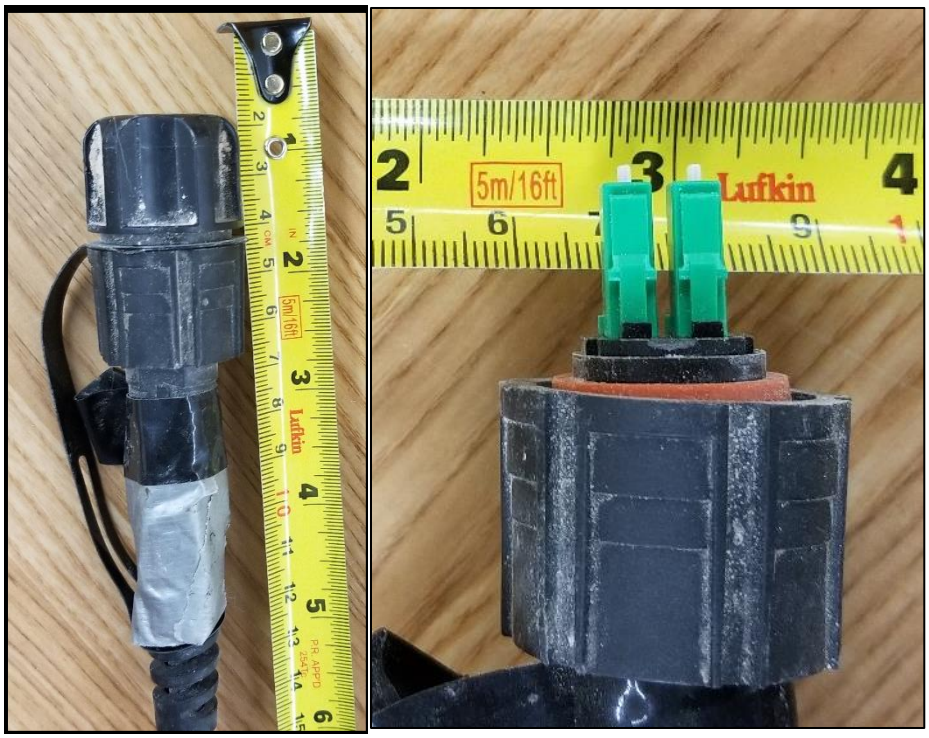

Figure C.4. Rugged Duplex LC fibre-optic connection with protector cap on (left) and unprotected Duplex LC connection (right)

Figure C.5. Cleaning male Duplex LC connection (left) and female Duplex LC connection (right)

The high definition remote module (HDRM) is connected between the readout unit and the strained fibre. The HDRM is shown in Figure C.6. It must sit close (within ~6 feet) to the strained fibre being measured.

It can be connected either directly to the strained fibre, or via a short "patch cable". This connection is a standard Simplex LC 1.25mm fibre-optic connection (Figure C.7). The cable between the high definition box and the readout unit has a standard Duplex LC 1.25mm fibre-optic connection. Before connecting either the patch cable or the standoff cable, the female connections need to be thoroughly cleaned with the male cleaning tool (Figure C.8) and the male connections need to be cleaned with the female cleaning tool. **Please note: when the system is unable to detect the sensor or when there is excessive noise in a reading, the issue is almost always due to dirty connections!**

Figure C.6. High definition remote module (top), Duplex LC connection (left), and Simplex LC connection (right)

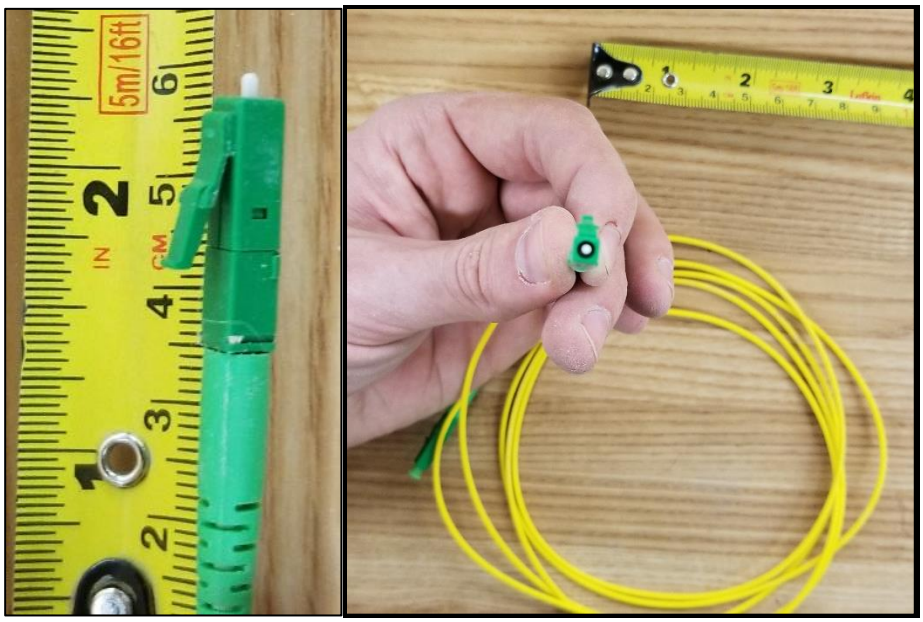

Figure C.7. Simplex LC connection (left) and Simplex LC patch cable (right)

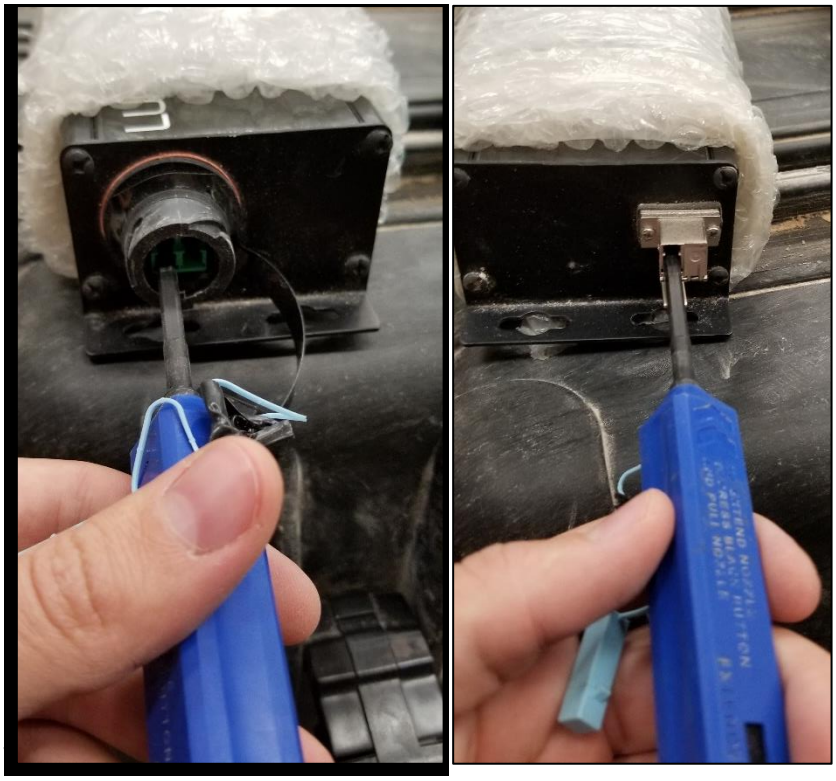

Figure C.8. Cleaning Duplex LC connection (left) and Simplex LC connection (right) on the high definition remote module

C.3 Fibre-optic Instrumented Rebar

This section describes how the rebar is instrumented with the fibre-optic instrumentation as well as the practical issues encountered when using the instrumented rebar.

The optical fibre is bonded to the steel in notches cut down the length of the rebar. These notches are cut approximately 3mm into the rebar and are 3mm wide.

The instrumented rebar supplied by YieldPoint is commonly made in two configurations: two-groove and three-groove instrumented rebar. These configurations are both shown in Figure C.9.

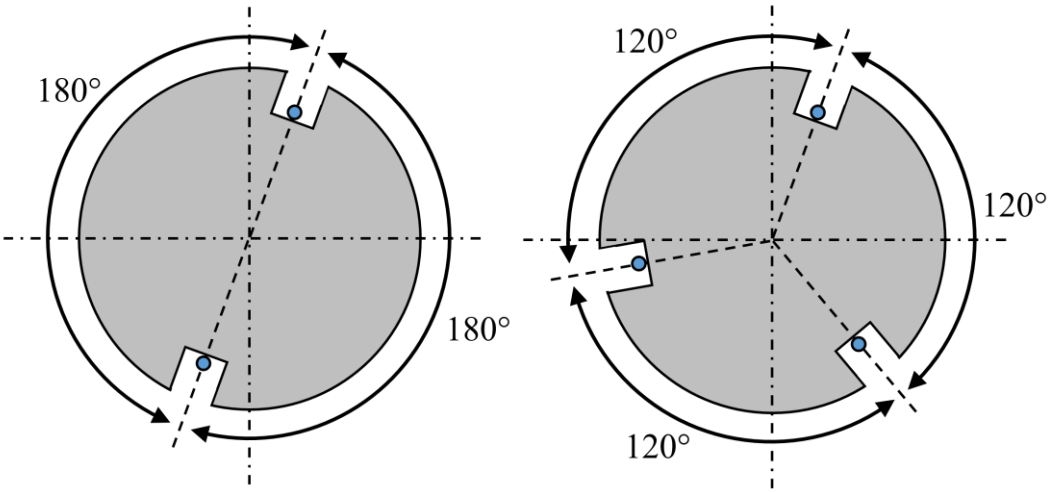

Figure C.9. Two-groove instrumented rebar (left) and three-groove instrumented rebar (right)

The two-groove configuration has two notches cut at approximately 180 degrees from each other. The axial strain within these rebar can be determined. However, in order to calculate the bending component of the strain, the relative direction of bending must be known.

The three-groove configuration has three notches cut at approximately 120 degrees from each other. This configuration has the benefit of being able to determine the axial strain, bending strain, and bending direction everywhere along the bolt. The downside of the three-groove configuration is that the instrumentation process is more difficult, so the cost per bolt is higher.

Three sets of instrumented rebar were ordered from YieldPoint over the course of 12 months. A total of 24 instrumented rebar bolts were ordered.

Dates of the various purchase orders being issued and the delivery dates are summarized in Table 1. YieldPoint needs approximately 3 months to manufacture and deliver an order of instrumented rebar bolts.

Table C.1. Order Summary

Order Number	Number of Rebar Bolts	P.O. Issued	Order Completed and Delivered
1	3	July 26, 2016	Aug. 15, 2017
2	12	Nov. 24, 2016	Mar. 1, 2017
3	8	May 29, 2017	August 15, 2017

YieldPoint is able to instrument a wide range of rebar types and is very accommodating. There are, however, limitations to the instrumentation process.

The notches cut into the rebar are generally not an issue along its length. However, looping the optical fibre back along the rebar can cause some issues. Since the notch does a "u-turn", a large amount of steel has been removed from the bolt at this turn-around point. Care needs to be taken to ensure the position of this reduced area does not affect test results.

The connection for the fibre-optic strand on the instrumented rebar can be large and is fragile. The connection can be protected by an aluminum cap but vibrations from a stoper have broken these connections despite the protection. Additionally, the connections and protection caps can make it difficult to fit the bolt heads in bolter sockets. The connections and protector caps are shown in Figure C.10.

Instrumenting rebar smaller than 18mm in diameter is not recommended. This requires the optical fibre to be curved too tightly when looping it back along the rebar which can cause excessive noise in the strain measurements

Figure C.10. Fibre optic connections for instrumented rebar (left) and instrumented rebar with aluminum protector caps (right)

C.4 Using the System in the Field

Fourteen instrumented rebar rock bolts were installed in underground potash mines. In order to install and measure these bolts, several steps needed to be taken to adapt the fibre-optic system and instrumented rebar for underground use.

C.4.1 Protecting the system for Underground Use

The fibre-optic system consisting of the desktop computer and ODiSI-B measurement unit had to be protected for underground use in Saskatchewan potash mines. The environment in a potash mine has various factors that could easily damage the fibre-optic system so, given how expensive this equipment is, it was mounted in a Pelican case for field use. This section describes the way the system was protected from environmental damage.

The three factors that caused major concerns of damage in the underground environment were:

- Fine airborne salt dust causing corrosion and interfering with internal optics
- Water/brine shorting electronics
- Vibration/impacts damaging electronics and optics

The method for protecting the fibre-optic system was decided to be mounting the system in a foam insulated protective case and ensuring this case didn't need to be opened anytime during operation. A Pelican 1660 Protector Case with 28.20" x 19.66" x 17.63" interior dimensions was ordered from B&E Electronics for $566. This case is shown in Figure C.11.

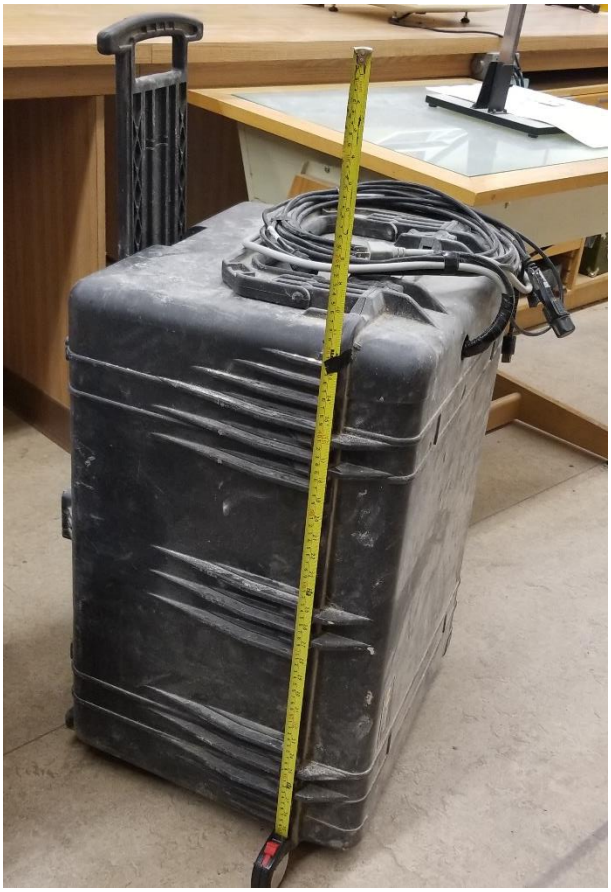

Figure C.11. Pelican case with fibre-optic system mounted inside (with 1m long tape)

The ODiSI-B unit was placed in the Pelican case first and is shown in Figure C.12. The power cord, PCI cable, and the duplex fibre-optic standoff cable is connected to the ODiSI-B unit. Figure C.13 shows the duplex fibre-optic standoff cable attached to the front of the ODiSI-B unit while mounted in the Pelican case.

A small port was installed on the Pelican case, as seen in Figure C.14. Through this port, the rocker switch on the ODiSI-B unit could be toggled to power the unit on and off when operating the system.

Figure C.12. ODiSI-B unit mounted in the Pelican case (with 30 cm long tape)

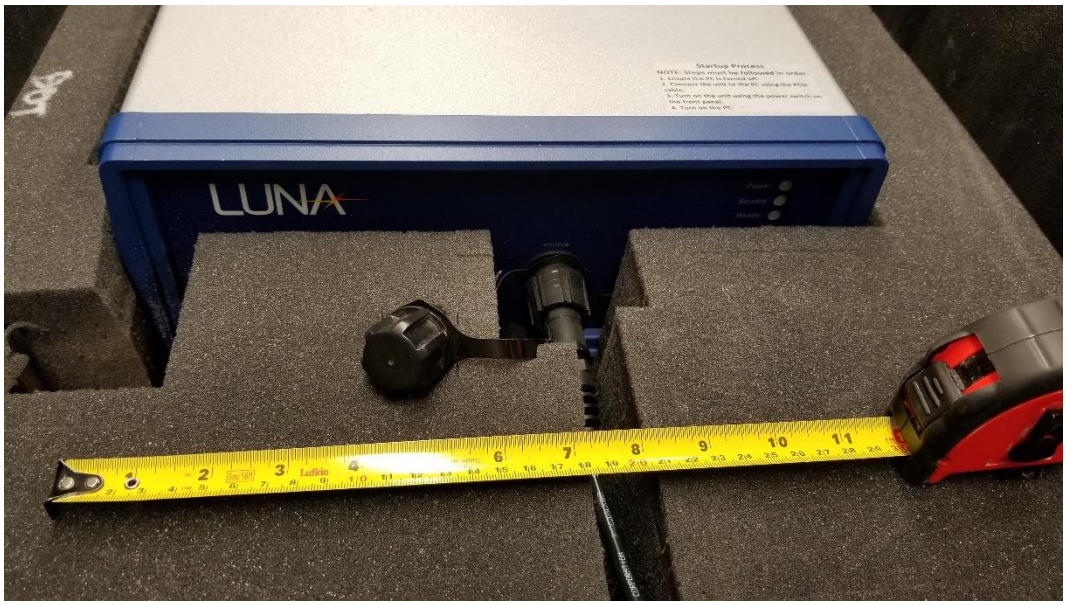

Figure C.13. Front of the ODISI-b unit mounted in the Pelican case with the duplex fibre-optic standoff cable attached (30 cm long tape)

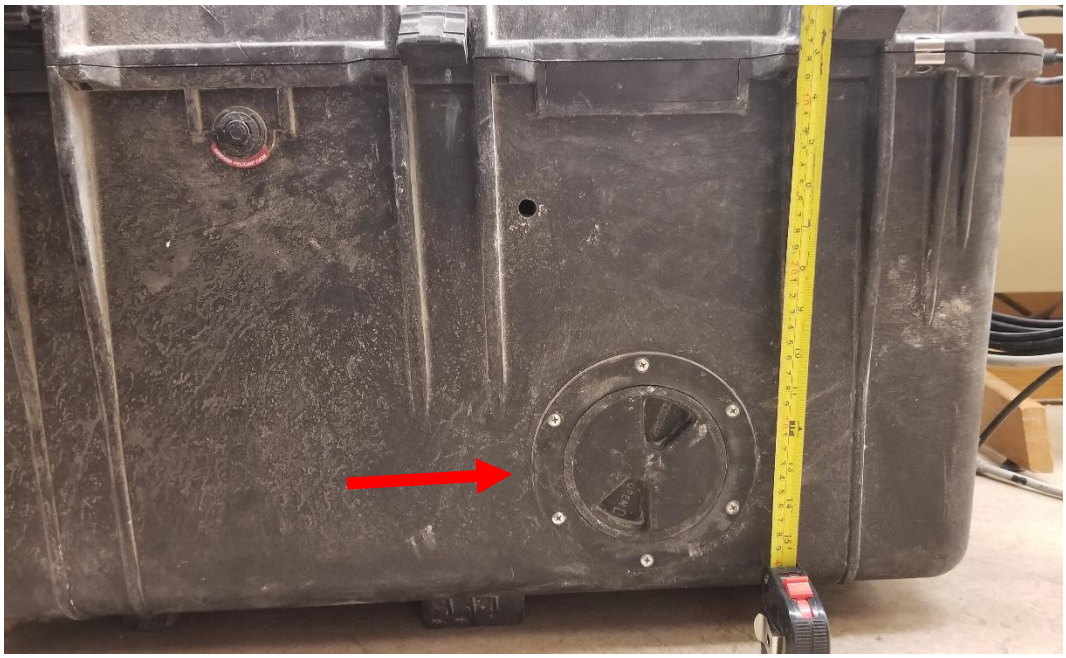

Figure C.14. Access port installed in the Pelican case to power ODiSI-B unit on and off (with 35 cm long tape)

The desktop computer was mounted in the Pelican case on top of the ODiSI-B unit, as seen in Figure C.15 and Figure C.16. The PCI cable, display port cable, and power cord were plugged into the computer. Additionally, a wireless mouse and keyboard "dongle" were plugged into the computer. A small hole was drilled into the Pelican case and a small rubber plug was used to block this hole (Figure C.17). A pen or screw driver could be inserted in the hole to press the power button on the computer to start it.

A power bar with surge protection was placed in the Pelican case and the power cords from the ODiSI-B unit and desktop computer were plugged into it.

Figure C.15. Desktop computer and power bar mounted in Pelican case (with 40 cm long tape)

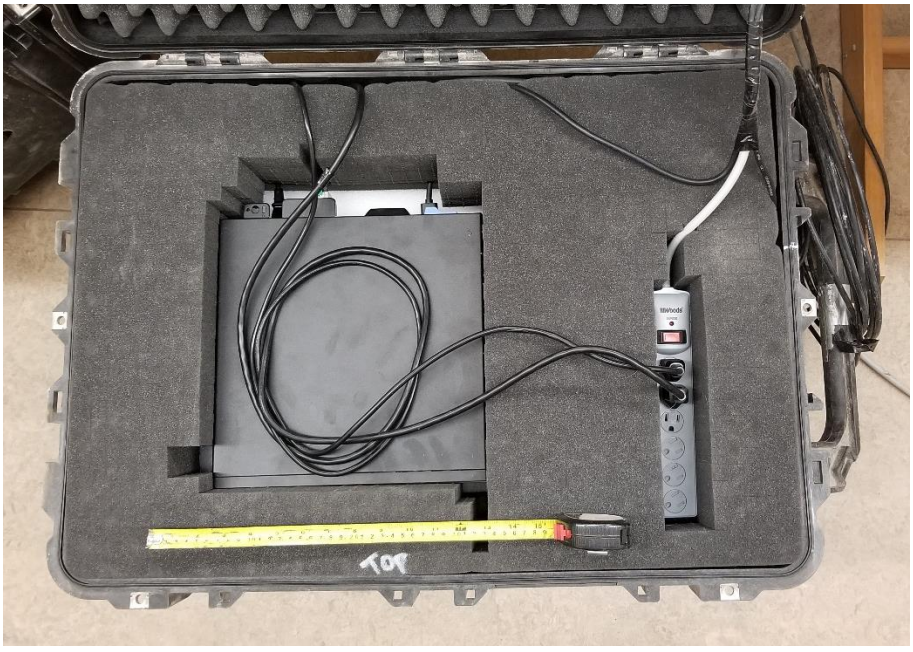

Figure C.16. Top view of desktop computer and power bar mounted in Pelican case (with 40 cm long tape)

Figure C.17. Hole in Pelican case for pressing the power button on the desktop computer (with 35 cm long tape)

The display port cable, power bar cord, and duplex fibre-optic standoff cable exited the Pelican case through a small hole drilled through the top (Figure C.18). The Pelican case could be closed and operated entirely using these three connections and the access port/hole to turn on the equipment.

Figure C.18. Power bar cord, duplex fibre-optic standoff cable, and display port cable exiting the Pelican case

The fibre-optic system requires a 120V power source to run the computer, ODiSI-B unit, and screen. The areas of potash mines where fibre-optic instrumentation was installed would rarely have a power source available. Additionally, the power source needed to be of high enough quality that it did not damage the computer or ODiSI-B unit. A battery and inverter were chosen to power the system in the field.

Figure C.19 shows the inverter and battery used. The inverter was a true sine-wave inverter as opposed to the more common stepped wine-wave inverters. It was unclear if this could damage any of the equipment, but extra caution was used. The power bar cord and the power cord for the screen were plugged into the inverter.

The battery was a marine/RV deep cycle battery. These batteries are better suited to rough transportation and providing long periods of low amperage power.

Figure C.19. True sine-wave inverter (left) and deep cycle marine/RV battery (right) used to power the fibre-optic system in the field (with 30 cm long tape)

The display port cable and the screen power cord were plugged into the screen shown in Figure C.20. After powering everything on and connecting to the remote module and fibre-optic strain sensor, the fibre-optic system was ready to take a measurement in the field.

Figure C.20. Small screen used to take a measurement in the field (with 30 cm long tape)

C.4.2 Installation in Mining Environment

In total, 14 rebar bolts were installed in an underground setting. Six 8ft bolts were installed for in situ deformation measurements. Eight 4 ft bolts were installed for pull testing.

The first issue encountered with installing the bolts is compatibility with bolter and stoper chucks/sockets. Typically, bolts are installed with either a square socket for forged heads or an oval socket for dywidags. However, these do not typically have enough clearance for the fibre-optic connection and aluminum protector. Or else, they put direct pressure on this fragile connection which could damage it.

Sockets were ordered that had a large and deep hole for the protector caps to fit through and that allowed the bolter/stoper to push on the bolt instead of the connection. An example diagram of the clearance necessary is shown in Figure C.21.

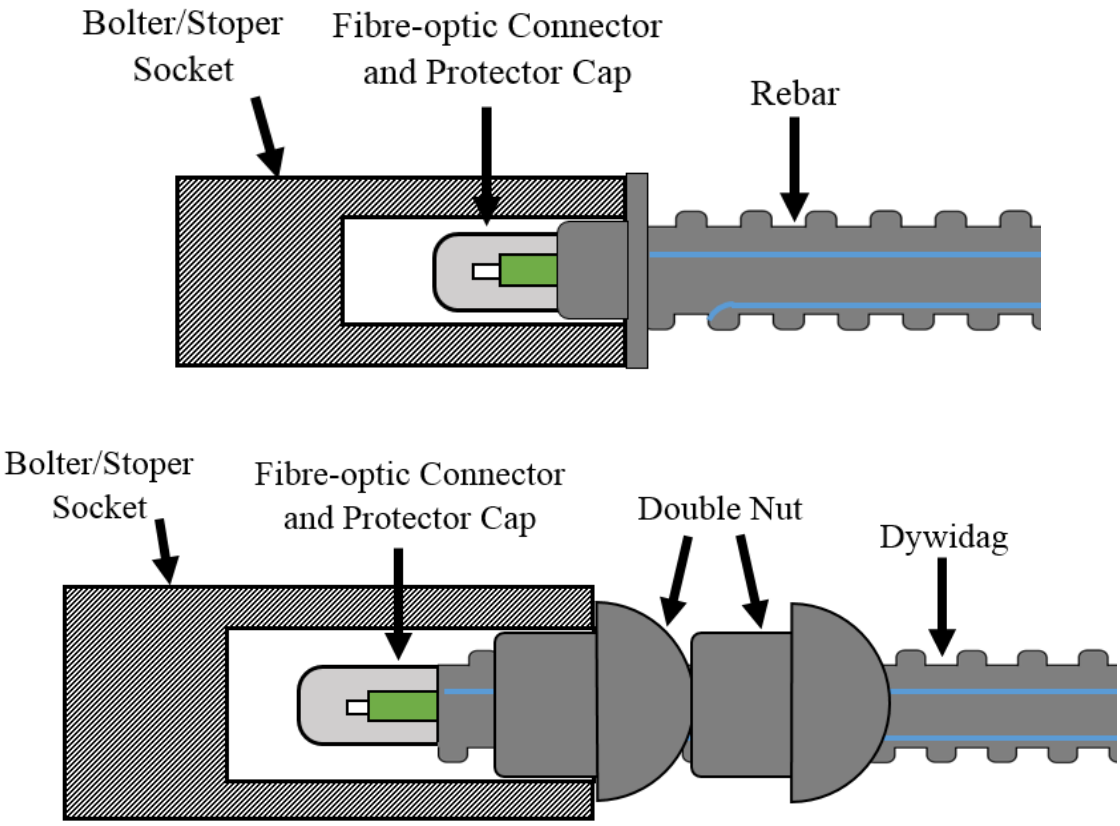

Figure C.21. Deep socket used to install instrumented forged-head rebar (top) and instrumented dywidag (bottom)

Half of the fibre-optic instrumented rebar were installed using a bolter. The other half were installed using a stoper (or plugger). The first bolt installed using a stoper was damaged during installation (Figure C.22). It is thought that the percussive action of the stoper was too intense for the brittle plastic connection.

Figure C.22. Shatter fibre-optic connection due to percussive action of stopper

For the other six rebar, the connector was left loosely hanging out of the rebar (as opposed to being epoxied to the rebar steel) and the protector had some bubble wrap in it. This was meant to decouple the vibration of the steel from the plastic connector. No damage was sustained in these installations.

C.5 Data Processing and Analysis

Some understanding of the rebar behaviour can be gathered from the strain measurements as they are reported by the fibre-optic strain sensing software. However, in order to fully utilize the data, a somewhat complex amount of processing and analysis must be conducted. This section describes the methods developed to process and analyze the fibre-optic strain data for a three-groove instrumented rebar.

C.5.1 Filtering and Averaging of Strain Readings

The fibre optic strain readings are often littered with erroneous readings and errors (recorded as "NaN" values). Figure C.23 below shows an example reading from an instrumented dywidag installed at the Mosaic Colonsay potash mine. This rebar was subjected to shear movement resulting in the strain readings shown.

The raw data has several readings that are clearly inaccurate as well as multiple "gaps" in the strain profile. These errors can cause issues when analyzing the data and rebar behaviour. To resolve these issues it is recommended that the operator takes at least one hundred readings from the fibre optic instrumentation.

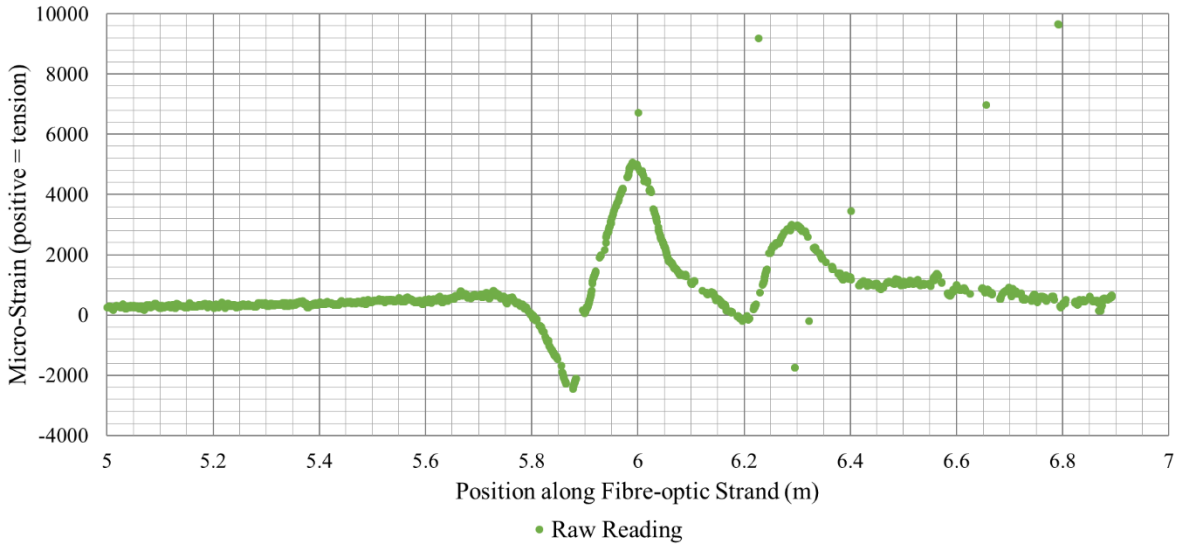

Figure C.23. A single raw reading from an instrumented dywidag

One may be inclined to simply average the hundred or so fibre optic strain measurements. This was done and is shown in Figure C.24. Unfortunately, due to the erroneously large and low strain measurements, the averaged value of roughly one hundred measurements still results in significant noise in the strain profile.

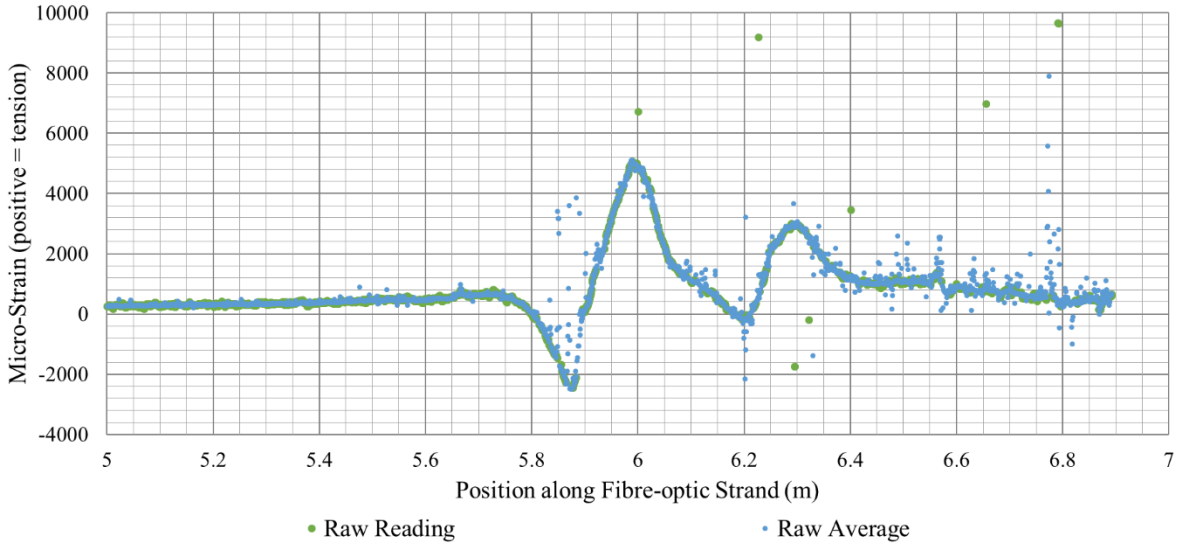

Figure C.24. A single raw strain reading and averaged profile of one hundred readings

Instead of taking a direct average of the strain readings, the erroneous readings must be filtered first. A simple band pass filter can be applied, which will remove strain values that are over or under set strain limits. For a more restrictive filter, multiple linearly varying filters can be applied. The upper and lower limits of a linear varying band pass filter are shown relative to a raw reading in Figure C.25.

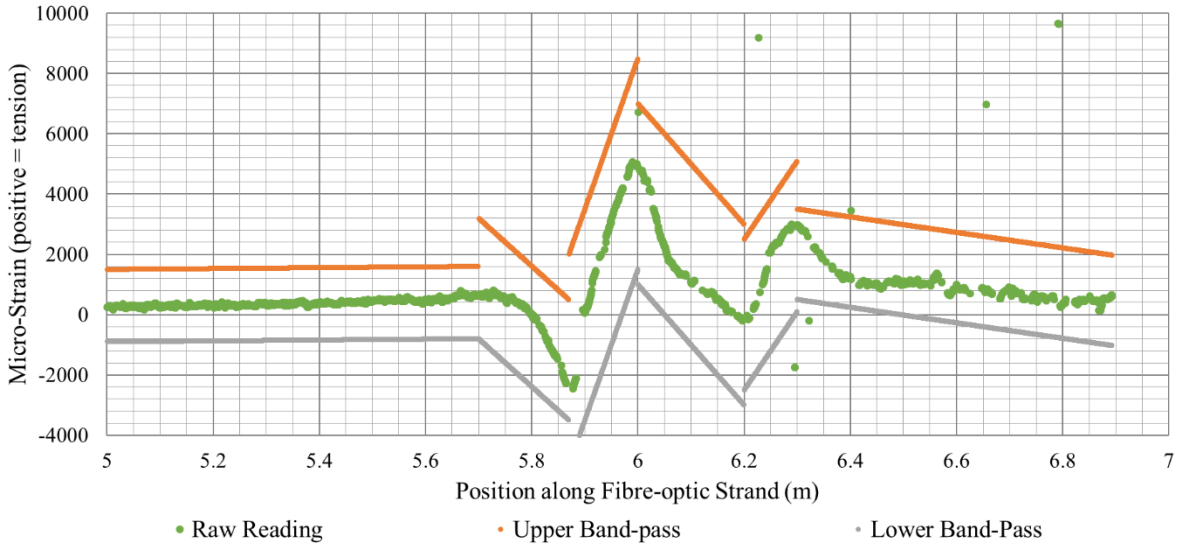

Figure C.25. Linear varying band pass filters relative to raw strain reading

Applying the filter and then averaging the results provides a much more continuous and clear strain profile. The example reading is shown in Figure C.26. As can be seen, the filtered and averaged strain profile has far less noise than the raw average.

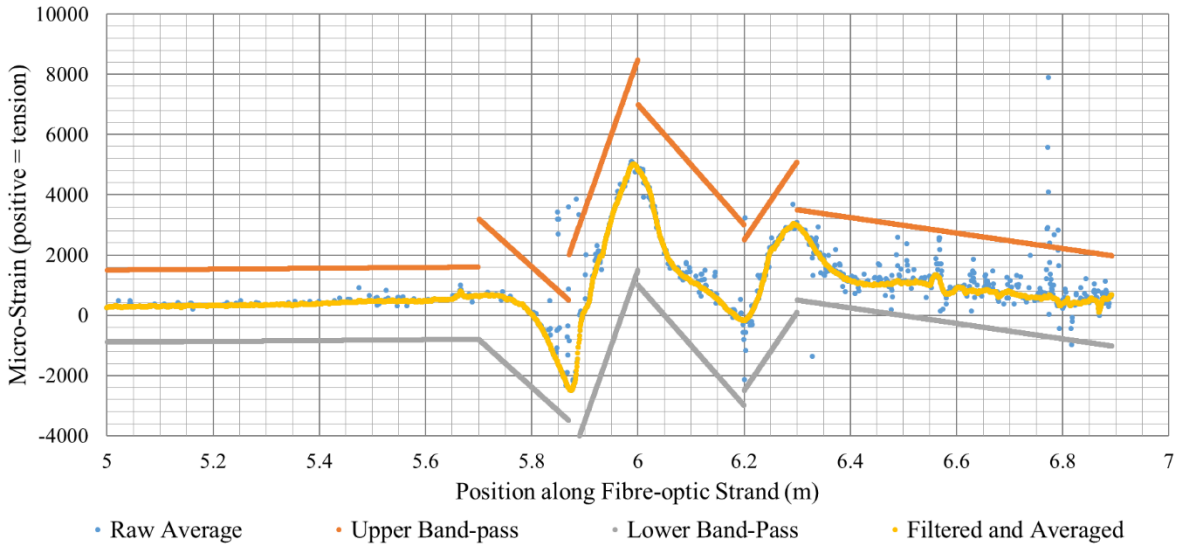

Figure C.26. Filtered and then averaged fibre optic strain profile and raw average of one hundred readings

Although filtering and averaging one hundred strain readings results in a nearly continuous strain profile, there can still be some "gaps" in the strain profile. The strain readings can be interpolated to some extent to further refine the results. For example, Figure C.27 shows that 5 strain reading were still unable to be calculated from over one hundred readings and needed to be interpolated.

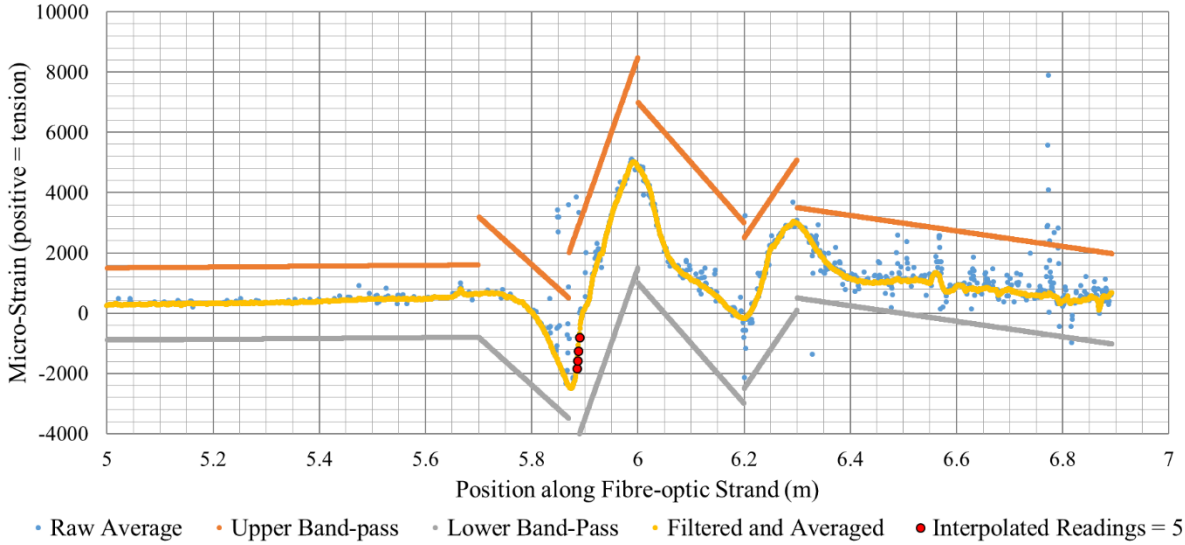

Figure C.27. Interpolated readings from filtered and averaged strain readings

Interpolating values is typically conducted by linear interpolation of missing strain values between two known strain values. This is a relatively simple process in theory, however it can be quite difficult using Excel logic arguments with the many strain values in a row are missing.

Figure C.28 shows three missing strain values in a row between two known strain values. Figure C.29 shows how linear interpolation can be used to approximate the missing values. The exact formulas and logic arguments used for this interpolation are dependent on the software used and how many consecutive strain values are missing.

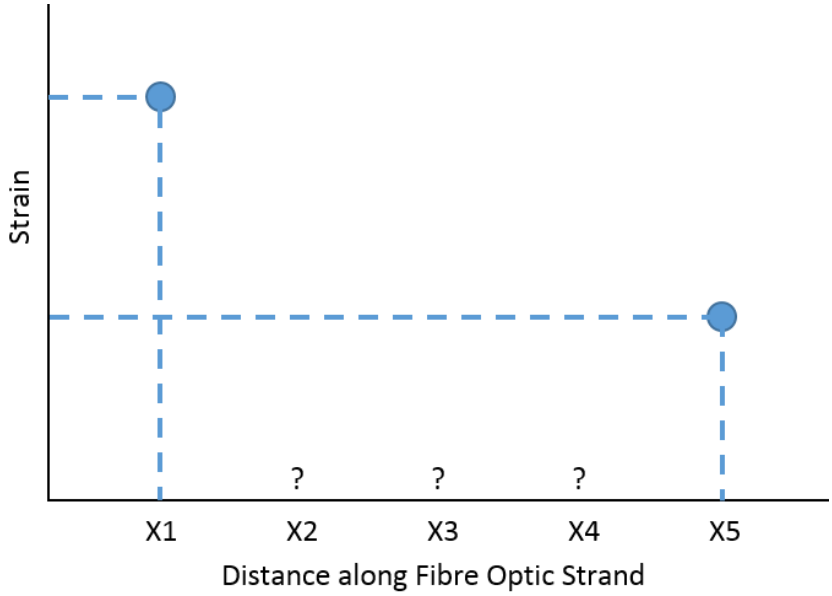

Figure C.28. An example of three missing strain values at distances of X2, X3, and X4 between known strain values at distances X1 and X5

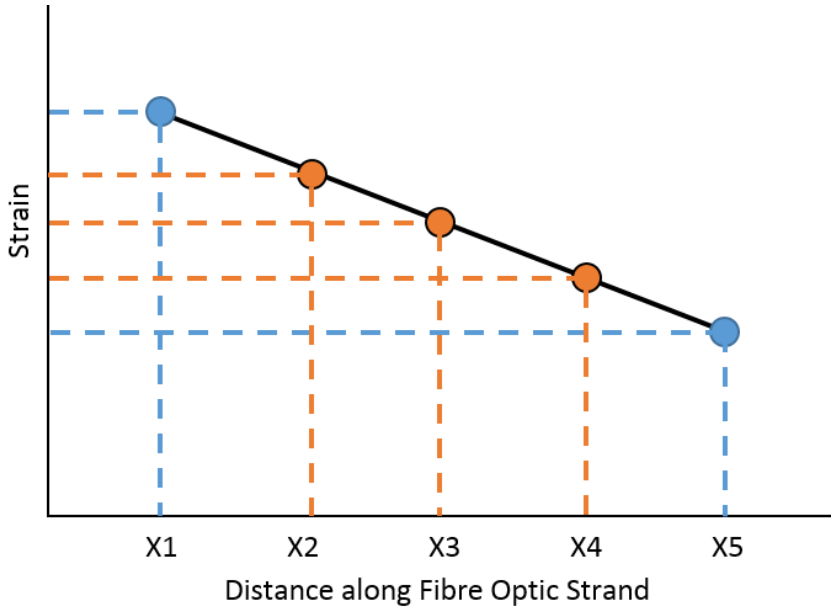

Figure C.29. Linear interpolation of three missing strain values

C.5.2 Superposition of Strain Readings

One more operation needs to be carried out on the fibre-optic data before a reliable analysis and interpretation can be conducted. A single fibre-optic strand is used to instrument the rebar by simply "wrapping" it down the rebar length two or three times. The strain readings from the fibre-optic strand must be lined-up so that two or three strain readings exist for each 0.65mm increment of the rebar length.

A diagram of a rebar rock bolt instrumented with a fibre-optic strand is shown in Figure C30. As shown, the fibre-optic strand is epoxied into three grooves around the circumference of the rebar. The fibre-optic strand starts at the head of the rock bolt and runs down its length. The fibre has a "turn-around" point at the end of the rebar and then it runs back up the rebar length. If the instrumented rebar is a "three-groove" type, then the strand has another "turn-around" point near the head of the bolt after which the strand passes down the rebar length for a third time.

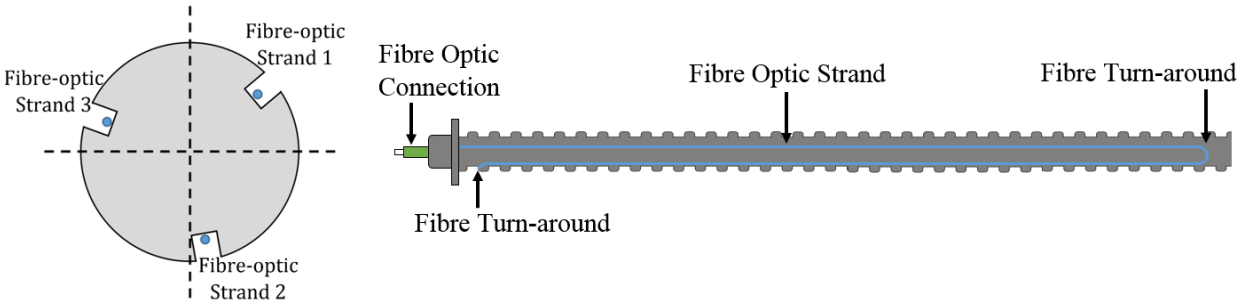

Figure C.30. Cross-section (left) and long-section (right) of fibre-optic instrumented rebar

The fibre-optic strand and its position along the rebar length can be defined by six points as shown in Figure C.31. These six points (1a, 1b, 2a, 2b, 3a, and 3b) represent a given length along the fibre-optic strand so that the operator can relate the strain readings recorded to their position along the rebar and relate one pass of the fibre-optic strand to the other passes. The six values are often provided by YieldPoint Inc., but if they are not, they can be experimentally determined fairly easily.

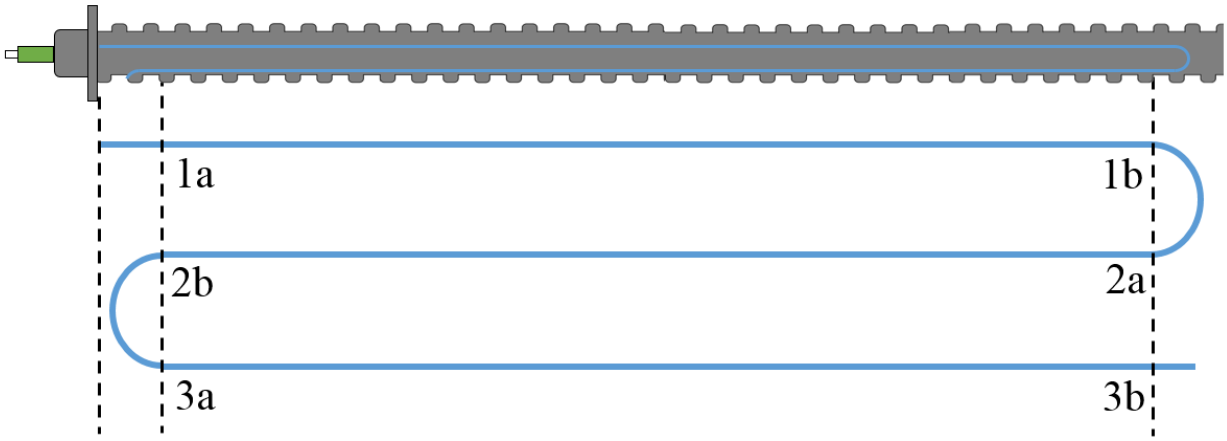

Figure C.31. Exploded long-section view of fibre-optic strand relative to instrumented rebar

To better explain how and why the strain readings must be “lined up”, consider the instrumented rebar shown in Figure C.32 that is subjected to some lateral forces and some tensile force. These forces will cause bending and stretching of the rebar, which will mean the fibre-optic instrumentation will measure some amount of strain along the rebar length.

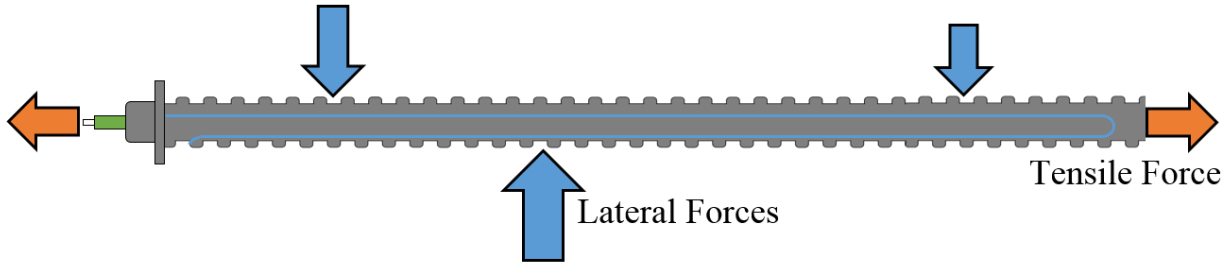

Figure C.32. Instrumented rebar subjected to some hypothetical lateral and tensile forces that causes internal tensile and bending strains

A hypothetical strain measurement is shown in Figure C.33. The positions of the six points (1a, 1b, 2a, etc.) are also shown as well as the "turn-around" points. The strain readings between each set of points, such as between 1a and 1b, are the strain readings of one pass of the fibre-optic. Theoretically, the distance between 1a and 1b should be equivalent to the distance between 2a and 2b as well as between 3a and 3b. However, these distances are often slightly different.

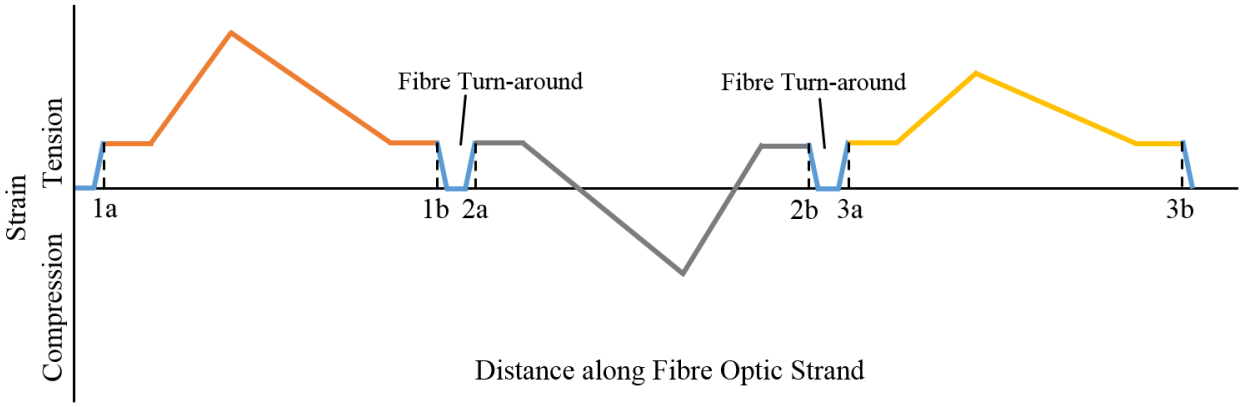

Figure C.33. Hypothetical strain readings from fibre-optic strand due to lateral and tensile forces acting on instrumented rebar

The strain readings between pass 1, pass 2, and pass 3 of the fibre-optic strand must be "lined up" or super-imposed so that there are three strain readings at each measurement increment. The strain readings at the very start of the fibre-optic strand, the very end of the strand, and at each turn-around point can be discarded as these values are erroneous.

Figure C.34 shows the hypothetical data from Figure C.33 after it has been lined up. Note that the data between 2a and 2b has been reversed! The second pass of the fibre-optic strand ran from the toe of the rock bolt towards the head, so the strain data must be reversed.

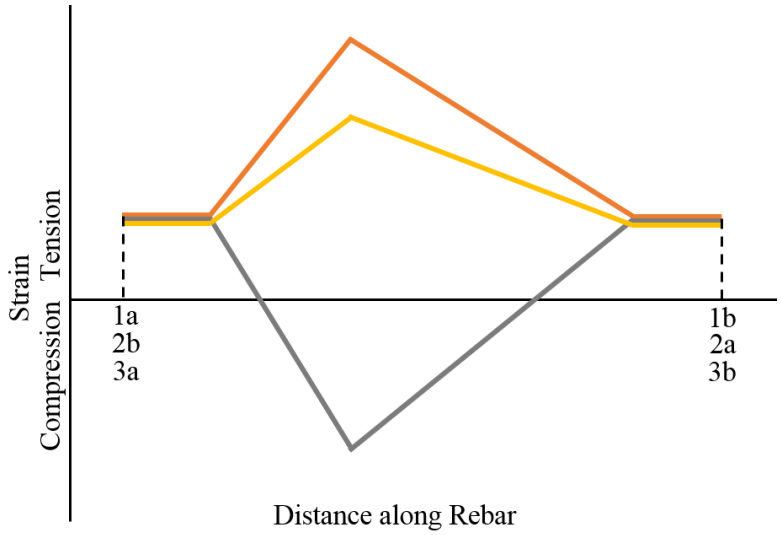

Figure C.34. Hypothetical strain readings after superposition by “lining up” points 1a, 2b, and 3a

Appendix D – Theoretical Derivation of the Area Moment of Inertia for a Slotted Rod

The following derivation was used to determine the Area Moment of Inertia of fibre-optic instrumented rebar. The fibre-optic instrumentation is installed by cutting two or three slots down the length of the rebar and using adhesive to attach the fibre-optic strand within the slot. Determining the Area Moment of Inertia of the instrumented rebar helped to evaluate the effect the instrumentation process has on the bending behaviour of the rebar. The Area Moment of Inertia also allows for calculation of the internal bending moment using the strain data collected with the fibre-optic instrumentation.

The Area Moment of Inertia for the instrumented rebar can be approximated by calculating the Area Moment of Inertia of the "un-notched" cylindrical rebar and subtracting the Area Moment of Inertia of the notches. This approach requires that Area Moment of Inertia of both the rebar and notches are evaluated about the same axis.

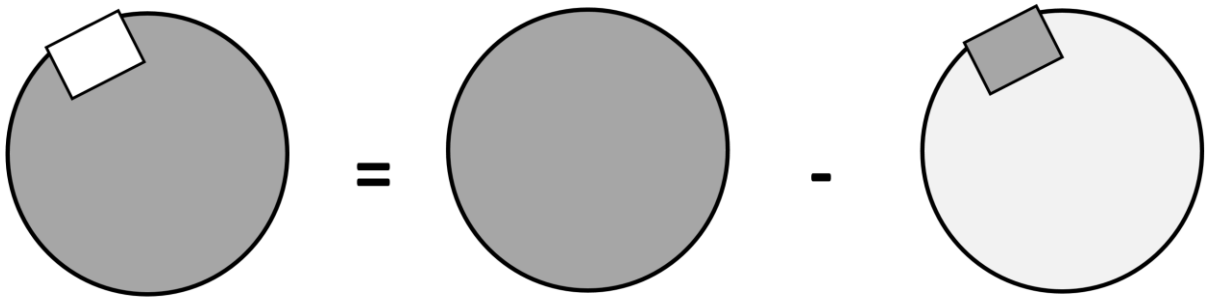

Figure D.1. Rebar cross-sections showing area contributing to and reducing the Area Moment of Inertia

$$I_{FORebar} = I_{Rebar} - I_{xNotch1} - I_{xNotch2} \cdots$$

Equation D.1

Where $I_{FORebar}$ is the Area Moment of Inertia of the fibre-optic instrumented rebar

I_{Rebar} is the Area Moment of Inertia of the solid cylindrical rebar with a circular cross-section

$I_{xNotch1}$ is the Area Moment of Inertia of a single notch cut into the rebar

The Area Moment of Inertia of a circular cross-section about its centroid can be calculated from the standardized equation:

$$I_{Rebar} = \frac{\pi d_{rebar}^4}{64}$$

Equation D.3

Where d_{rebar} is the minimum diameter of the rebar.

Now, the Area Moment of Inertia of the notches must be calculated. The notches can be oriented at any angle relative to the direction of bending. The notch and its orientation can be described by the parameters in the following figure:

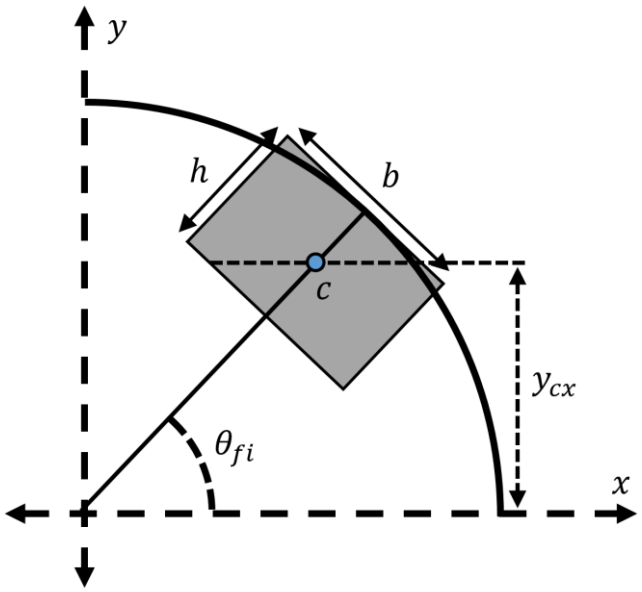

Figure D.2. Notch geometry and orientation in rebar cross-section

In the above figure, b is the width of the notch, h is the depth of the notch, θ is the angle of the notch from the centroidal axis of the rebar, c is the centroid of the notch, and y_{cx} distance from the centroidal axis of the rebar to the centroidal axis of the notch.

The Area Moment of Inertia of the notch is calculated about the notches centroid by the following equation for a rectangle at an angle:

$$I_{cNotch} = \frac{h\,b}{12}\left(b^2\ \text{SIN}^2\,\theta + h^2\ \text{COS}^2\,\theta\right)$$

Equation D.3

Where I_{cNotch} is the Area Moment of Inertia of the notch about the notches centroid

To calculate the Area Moment of Inertia about the rebars centroidal axis the parallel axis theorem must be used. The general equation of the parallel axis theorem is shown below:

$$I_{xNotch} = I_{cNotch} + y_{cx}^2 A_{Notch}$$

Equation D.4

Where y_{cx} is the distance from the rebars centroidal axis to the notches centroidal axis and A_{Notch} area of the notches cross-section.

Using geometry, the second term of EQ. B.4 can be determined to be:

$$y_{cx}^2 A_{Notch} = \left(\left(\frac{d_{rebar}}{2} - \frac{h}{2}\right) \text{SIN}^2\, \theta_{fi}\right)^2 \ (h\, b)$$

Equation D.5

By substitution and simplification, the Area Moment of Inertia of a single notch about the rebars centroidal axis can be calculated by:

$$I_{xNotch} = \frac{h\, b}{12}\left[b^2\ \text{SIN}^2\, \theta_{fi} + h^2\ \text{COS}^2\, \theta_{fi} + 3(d_{rebar} - h)^2\ \text{SIN}^2\, \theta_{fi}\right]$$

Equation D.6

The Area Moment of Inertia of instrumented rebar can now be calculated according to EQ. B.1. When rebar is instrumented with two strands of fibre-optic, then the Area Moment of Inertia can be calculated by:

$$\begin{aligned} I_{FORebar} = {} & \frac{\pi d_{rebar}^4}{64} - \frac{h\, b}{12}\left[h^2\ \text{SIN}^2\, \theta_{fi} + b^2\ \text{COS}^2\, \theta_{fi} + 3(d_{rebar} - h)^2\ \text{COS}^2\, \theta_1\right] \\ & - \frac{h\, b}{12}\left[h^2\ \text{SIN}^2\left(\theta_{fi} + \theta_{12}\right) + b^2\ \text{COS}^2\left(\theta_{fi} + \theta_{12}\right)\right. \\ & \left. + 3(d_{rebar} - h)^2\ \text{COS}^2\left(\theta_{fi} + \theta_{12}\right)\right] \end{aligned}$$

Equation D.7

Where θ_{fi} is the angle of the first fibre-optic strand from the centroidal axis of the rebar and θ_{12} is the counter-clockwise angle between the first fibre-optic strand and the second fibre-optic strand.

When the instrumented rebar has notches oriented diametrically opposed, then θ_{12} will be 180 degrees. This orientation also results in a symmetric rebar cross-section, so the centroid will not change position as a result of the instrumentation process.

Alternatively, the rebar can be instrumented with three strands of fibre-optic. In this case, the Area Moment of Inertia can be calculated by:

$$I_{FORebar} = \frac{\pi d_{rebar}^4}{64} - \frac{h\,b}{12}\left[h^2\,\text{SIN}^2\,\theta_{fi} + b^2\,\text{COS}^2\,\theta_{fi} + 3(d_{rebar} - h)^2\,\text{COS}^2\,\theta_1\right] - \frac{h\,b}{12}\left[h^2\,\text{SIN}^2\left(\theta_{fi} + \theta_{12}\right) + b^2\,\text{COS}^2\left(\theta_{fi} + \theta_{12}\right) + 3(d_{rebar} - h)^2\,\text{COS}^2\left(\theta_{fi} + \theta_{12}\right)\right] - \frac{h\,b}{12}\left[h^2\,\text{SIN}^2\left(\theta_{fi} + \theta_{12} + \theta_{23}\right) + b^2\,\text{COS}^2\left(\theta_{fi} + \theta_{12} + \theta_{23}\right) + 3(d_{rebar} - h)^2\,\text{COS}^2\left(\theta_{fi} + \theta_{12} + \theta_{23}\right)\right]$$

Equation D.8

Where θ_{23} is the counter-clockwise angle between the second fibre-optic strand and the third fibre-optic strand.

When the instrumented rebar has three notches oriented equally around the rebar, then θ_{12} and θ_{23} will be 120 degrees. This orientation results in a symmetric rebar cross-section, so the centroid will once again not change position as a result of the instrumentation process.

Errors in method of calculation

The area of the notch is approximated as a perfect rectangle. In reality, the notch has a curved outer surface matching the circular profile of the rebar, as shown below. This approximation will cause an over-estimation of the notch area and, as a result, an underestimation of the Area Moment of Inertia for the notched rebar.

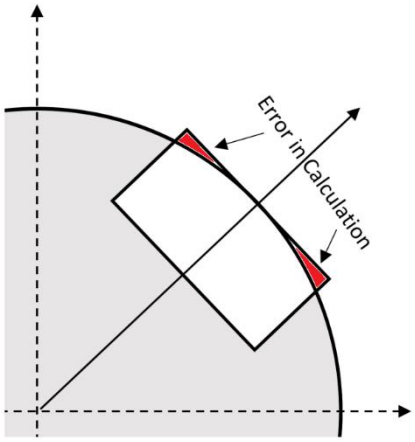

Figure D.3. Rebar cross-sections showing area contributing to and reducing the area moment of inertia

Appendix E – Derivations and Methods for Analyzing Fibre-optic Strain Gauge Data

The fibre-optic instrumented rebar provides a high resolution of strain readings along the length of the rebar. These strain readings can be difficult to interpret alone, but with some mathematical analysis a better understanding of the rebar behaviour can be gained.

The rebar instrumented with diametrically opposed fibre-optic strands only provides two strain readings at every 0.65 mm increment along the rebar. However, when the rebar is instrumented with three fibre-optic strands, then three strain measurements are acquired at each increment. These three strain readings can be used to determine significant information about the rebar behaviour. This section discusses and derives the analysis methods to do this.

Consider a hypothetical rebar rod instrumented with fibre-optic strain cables. The rod is then subjected to some combination of lateral forces and axial forces. These forces result in a combination of bending strains, axial strains, and shear strains that vary along the rods length.

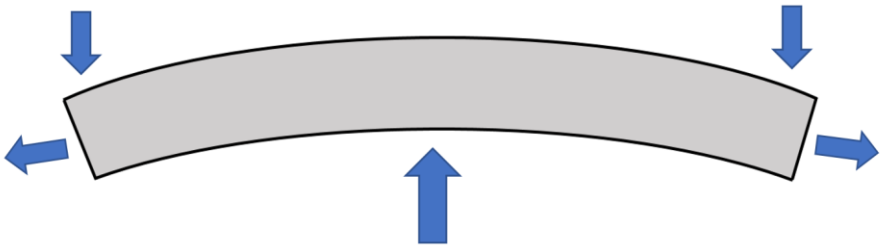

Figure E.1. Rebar cross-sections showing area contributing to and reducing the area moment of inertia

Now consider one cross-sectional segment of this rod. The cross-section will look something like the following; with the three fibre-optic strands at some random orientation and a neutral bending axis perpendicular to the directional of bending (the y-axis). The cross-sectional area of the rod is assumed to have some linear distribution of strains throughout its height (Euler-Bernoulli beam theory).

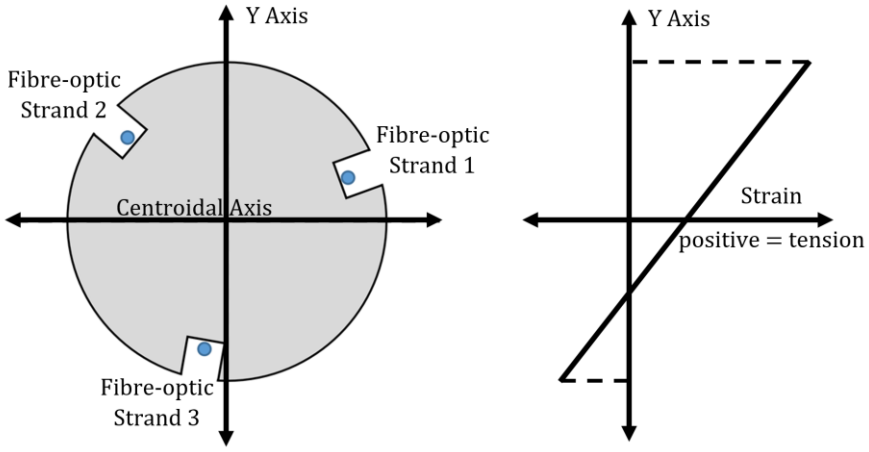

Figure E.2. Rebar cross-sections showing area contributing to and reducing the area moment of inertia

Some important characteristics of the cross-section must now be defined. The angle measured from the neutral bending axis to the first fibre-optic strand will be referred to as the angle of inclination, θ_{fi}. The angle from the first strand to the second and from the second to the third are defined by θ_{12} and θ_{23}, respectively. All fibre-optic strands are assumed to be an equal distance, r_{fo}, from the centre axis of the rod. Fibre-optic strands 1, 2, and 3 all measure a strain, defined as ε_1, ε_2, and ε_3.

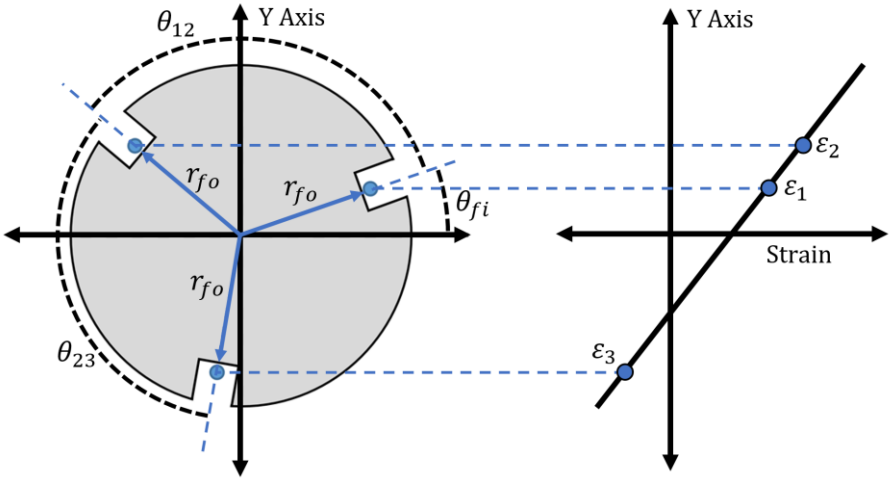

Figure E.3. Rebar cross-sections showing area contributing to and reducing the area moment of inertia

Using trigonometry, the following equations can be determined:

$$y_1 = r_{fo}\,\text{SIN}\,\theta_{fi} \qquad \text{Equation E.1}$$

$$y_2 = r_{fo}\,\text{SIN}(\theta_{fi} + \theta_{12}) \qquad \text{Equation E.2}$$

$$y_3 = r_{fo}\,\text{SIN}(\theta_{fi} + \theta_{12} + \theta_{23}) \qquad \text{Equation E.3}$$

Where y_1, y_2, and y_3 are the distances between the neutral bending axis and fibre-optic strands 1, 2, and 3, respectively.

Additionally, we can define three more characteristics of the cross-section. The axial strain, ε_{Axial}, at the centroidal axis and the strains, ε_{Top} and ε_{Bottom}, at either extreme edge of the rod (arbitrarily named the top and bottom).

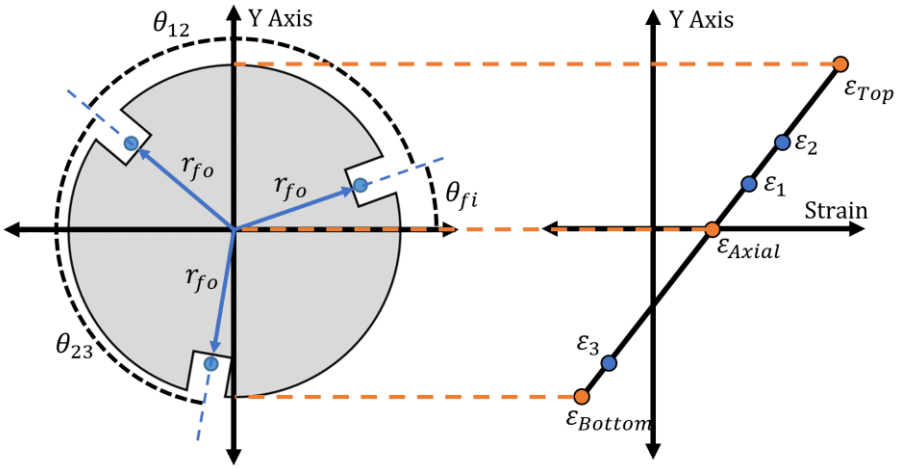

Figure E.4. Rebar cross-sections showing area contributing to and reducing the area moment of inertia

The strains measured by each fibre-optic strand can be related to their position by the following equations:

$$\varepsilon_1 = a_{strain}\,y_1 + \varepsilon_{Axial} \qquad \text{Equation E.4}$$

$$\varepsilon_2 = a_{strain}\,y_2 + \varepsilon_{Axial} \qquad \text{Equation E.5}$$

$$\varepsilon_3 = a_{strain}\,y_3 + \varepsilon_{Axial} \qquad \text{Equation E.6}$$

Where a_{strain} is the slope of the linear strain distribution within the cross-section.

Combining the six equations presented thus far yields:

$$\varepsilon_1 = a_{strain}\,r_{fo}\,\text{SIN}\,\theta_{fi} + \varepsilon_{Axial} \qquad \text{Equation E.7}$$

$$\varepsilon_2 = a_{strain}\,r_{fo}\,\text{SIN}(\theta_{fi} + \theta_{12}) + \varepsilon_{Axial} \qquad \text{Equation E.8}$$

$$\varepsilon_3 = a_{strain}\, r_{fo}\, \mathrm{SIN}\left(\theta_{fi} + \theta_{12} + \theta_{23}\right) + \varepsilon_{Axial}$$ Equation E.9

Next EQ. C.8 and EQ. C.9 are subtracted from EQ. C.7:

$$\varepsilon_1 - \varepsilon_2 = a_{strain}\, r_{fo}\, \mathrm{SIN}\, \theta_{fi} + \varepsilon_{Axial} - a_{strain}\, r_{fo}\, \mathrm{SIN}\left(\theta_{fi} + \theta_{12}\right) - \varepsilon_{Axial}$$

Equation E.10

$$\varepsilon_1 - \varepsilon_3 = a_{strain}\, r_{fo}\, \mathrm{SIN}\, \theta_{fi} + \varepsilon_{Axial} - a_{strain}\, r_{fo}\, \mathrm{SIN}\left(\theta_{fi} + \theta_{12} + \theta_{23}\right) - \varepsilon_{Axial}$$

Equation E.11

Simplification of these equations:

$$\varepsilon_1 - \varepsilon_2 = a_{strain}\, r_{fo}\left(\mathrm{SIN}\, \theta_{fi} - \mathrm{SIN}\left(\theta_{fi} + \theta_{12}\right)\right)$$ Equation E.12

$$\varepsilon_1 - \varepsilon_3 = a_{strain}\, r_{fo}\left(\mathrm{SIN}\, \theta_{fi} - \mathrm{SIN}\left(\theta_{fi} + \theta_{12} + \theta_{23}\right)\right)$$ Equation E.13

Division of EQ. C.12 by EQ. C.13 yields:

$$\frac{\varepsilon_1 - \varepsilon_2}{\varepsilon_1 - \varepsilon_3} = \frac{a_{strain}\, r_{fo}\left(\mathrm{SIN}\, \theta_{fi} - \mathrm{SIN}\left(\theta_{fi} + \theta_{12}\right)\right)}{a_{strain}\, r_{fo}\left(\mathrm{SIN}\, \theta_{fi} - \mathrm{SIN}\left(\theta_{fi} + \theta_{12} + \theta_{23}\right)\right)}$$ Equation E.14

Simplification:

$$\frac{\varepsilon_1 - \varepsilon_2}{\varepsilon_1 - \varepsilon_3} = \frac{\left(\mathrm{SIN}\, \theta_{fi} - \mathrm{SIN}\left(\theta_{fi} + \theta_{12}\right)\right)}{\left(\mathrm{SIN}\, \theta_{fi} - \mathrm{SIN}\left(\theta_{fi} + \theta_{12} + \theta_{23}\right)\right)}$$ Equation E.15

Expansion using the angle sum identity for sine:

$$\frac{\varepsilon_1 - \varepsilon_2}{\varepsilon_1 - \varepsilon_3} = \frac{\left(\mathrm{SIN}\, \theta_{fi} - \mathrm{SIN}\, \theta_{fi}\, \mathrm{COS}\, \theta_{12} - \mathrm{COS}\, \theta_{fi}\, \mathrm{SIN}\, \theta_{12}\right)}{\left(\mathrm{SIN}\, \theta_{fi} - \mathrm{SIN}\, \theta_{fi}\, \mathrm{COS}(\theta_{12} + \theta_{23}) - \mathrm{COS}\, \theta_{fi}\, \mathrm{SIN}(\theta_{12} + \theta_{23})\right)}$$ Equation E.16

Factoring of the common term:

$$\frac{\varepsilon_1 - \varepsilon_2}{\varepsilon_1 - \varepsilon_3} = \frac{\mathrm{SIN}\, \theta_{fi}\left(1 - \mathrm{COS}\, \theta_{12} - \mathrm{COT}\, \theta_{fi}\, \mathrm{SIN}\, \theta_{12}\right)}{\mathrm{SIN}\, \theta_{fi}\left(1 - \mathrm{COS}(\theta_{12} + \theta_{23}) - \mathrm{COT}\, \theta_{fi}\, \mathrm{SIN}(\theta_{12} + \theta_{23})\right)}$$ Equation E.17

And cancelling that term:

$$\frac{\varepsilon_1 - \varepsilon_2}{\varepsilon_1 - \varepsilon_3} = \frac{\left(1 - \mathrm{COS}\, \theta_{12} - \mathrm{COT}\, \theta_{fi}\, \mathrm{SIN}\, \theta_{12}\right)}{\left(1 - \mathrm{COS}(\theta_{12} + \theta_{23}) - \mathrm{COT}\, \theta_{fi}\, \mathrm{SIN}(\theta_{12} + \theta_{23})\right)}$$ Equation E.18

Multiplying by the denominator:

$$\frac{\varepsilon_1 - \varepsilon_2}{\varepsilon_1 - \varepsilon_3} - \frac{\varepsilon_1 - \varepsilon_2}{\varepsilon_1 - \varepsilon_3}\mathrm{COS}(\theta_{12} + \theta_{23}) - \frac{\varepsilon_1 - \varepsilon_2}{\varepsilon_1 - \varepsilon_3}\mathrm{COT}\, \theta_{fi}\, \mathrm{SIN}(\theta_{12} + \theta_{23}) = 1 - \mathrm{COS}\, \theta_{12} - \mathrm{COT}\, \theta_{fi}\, \mathrm{SIN}\, \theta_{12}$$

Equation E.19

Isolating terms with θ_{fi}:

$$\mathrm{COT}\, \theta_{fi}\, \mathrm{SIN}\, \theta_{12} - \frac{\varepsilon_1 - \varepsilon_2}{\varepsilon_1 - \varepsilon_3}\mathrm{COT}\, \theta_{fi}\, \mathrm{SIN}(\theta_{12} + \theta_{23}) = 1 - \mathrm{COS}\, \theta_{12} - \frac{\varepsilon_1 - \varepsilon_2}{\varepsilon_1 - \varepsilon_3} + \frac{\varepsilon_1 - \varepsilon_2}{\varepsilon_1 - \varepsilon_3}\mathrm{COS}(\theta_{12} + \theta_{23})$$

Equation E.20

Factoring:

$$\cot\theta_{fi}\left(\sin\theta_{12}-\frac{\varepsilon_1-\varepsilon_2}{\varepsilon_1-\varepsilon_3}\sin(\theta_{12}+\theta_{23})\right)=1-\cos\theta_{12}+\frac{\varepsilon_1-\varepsilon_2}{\varepsilon_1-\varepsilon_3}(\cos(\theta_{12}+\theta_{23})-1)$$

Equation E.21

Division:

$$\cot\theta_{fi}=\frac{\left(1-\cos\theta_{12}+\frac{\varepsilon_1-\varepsilon_2}{\varepsilon_1-\varepsilon_3}(\cos(\theta_{12}+\theta_{23})-1)\right)}{\left(\sin\theta_{12}-\frac{\varepsilon_1-\varepsilon_2}{\varepsilon_1-\varepsilon_3}\sin(\theta_{12}+\theta_{23})\right)}$$

Equation E.22

And solving for θ_{fi}:

$$\theta_{fi}=\tan^{-1}\left[\frac{\sin\theta_{12}-\frac{\varepsilon_1-\varepsilon_2}{\varepsilon_1-\varepsilon_3}\sin(\theta_{12}+\theta_{23})}{1-\cos\theta_{12}+\frac{\varepsilon_1-\varepsilon_2}{\varepsilon_1-\varepsilon_3}(\cos(\theta_{12}+\theta_{23})-1)}\right]$$

Equation E.23

Next, we calculate the slope of the strain distribution, a_{strain}. Knowing:

$$\varepsilon_1-\varepsilon_2=a_{strain}\,r_{fo}\left(\sin\theta_{fi}-\sin\left(\theta_{fi}+\theta_{12}\right)\right)$$

Equation E.24

Isolating for a_{strain}:

$$a_{strain}=\frac{\varepsilon_1-\varepsilon_2}{r_{fo}\left(\sin\theta_{fi}-\sin(\theta_{fi}+\theta_{12})\right)}$$

Equation E.25

Similarly, we can solve for the axial strain at the centroidal axis:

$$\varepsilon_{Axial}=\varepsilon_1-a_{strain}\,r_{fo}\sin\theta_{fi}$$

Equation E.26

If all three fibre-optic strands are spaced 120 degrees apart, then a somewhat simpler equation can be derived. Initially, the sum of the three fibre-optic strain readings must be set equal to the sum of their equivalents in Equations E.7, E.8 and E.9:

$$\varepsilon_1+\varepsilon_2+\varepsilon_3=a_{strain}\,r_{fo}\sin\theta_{fi}+a_{strain}\,r_{fo}\sin\left(\theta_{fi}+\theta_{12}\right)+a_{strain}\,r_{fo}\sin\left(\theta_{fi}+\theta_{12}+\theta_{23}\right)+3\,\varepsilon_{Axial}$$

Equation E.27

Then the terms are factored and rearranged:

$$\varepsilon_1+\varepsilon_2+\varepsilon_3=a_{strain}\,r_{fo}\left[\sin\theta_{fi}+\sin\left(\theta_{fi}+\theta_{12}\right)+\sin\left(\theta_{fi}+\theta_{12}+\theta_{23}\right)\right]+3\varepsilon_{Axial}$$

Equation E.28

$$\varepsilon_{Axial}=\left(\frac{\varepsilon_1+\varepsilon_2+\varepsilon_3}{3}\right)-\frac{a_{strain}\,r_{fo}}{3}\left[\sin\theta_{fi}+\sin\left(\theta_{fi}+\theta_{12}\right)+\sin\left(\theta_{fi}+\theta_{12}+\theta_{23}\right)\right]$$

Equation E.29

The trigonometric terms are expanded using trigonometric identities:

$$\varepsilon_{Axial} = \left(\frac{\varepsilon_1+\varepsilon_2+\varepsilon_3}{3}\right) - \frac{a_{strain}\, r_{fo}}{3}\left[\sin\theta_{fi} + \sin\theta_{fi}\cos\theta_{12} + \cos\theta_{fi}\sin\theta_{12} + \sin\theta_{fi}\cos(\theta_{12} + \theta_{23}) + \cos\theta_{fi}\sin(\theta_{12}+\theta_{23})\right]$$

Equation E.30

The angles between the fibre-optic strands are assumed to be 120 degrees:

$$\varepsilon_{Axial} = \left(\frac{\varepsilon_1+\varepsilon_2+\varepsilon_3}{3}\right) - \frac{a_{strain}\, r_{fo}}{3}\left[\sin\theta_{fi} + \sin\theta_{fi}\cos 120° + \cos\theta_{fi}\sin 120° + \sin\theta_{fi}\cos 240° + \cos\theta_{fi}\sin 240°\right]$$

Equation E.31

Lastly, similar terms are cancelled and we find the axial strain is equal to the average strain of all three strands so long as the strands are arranged 120 degrees apart:

$$\varepsilon_{Axial} = \left(\frac{\varepsilon_1+\varepsilon_2+\varepsilon_3}{3}\right) - \frac{a_{strain}\, r_{fo}}{3}\left[\sin\theta_{fi} - \frac{1}{2}\sin\theta_{fi} + \frac{\sqrt{3}}{2}\cos\theta_{fi} - \frac{1}{2}\sin\theta_{fi} - \frac{\sqrt{3}}{2}\cos\theta_{fi}\right]$$

Equation E.32

$$\varepsilon_{Axial} = \frac{\varepsilon_1+\varepsilon_2+\varepsilon_3}{3}$$ Equation E.33

Lastly, the strain at the extreme edges of the rod/rebar can be determined, knowing the radius of the rebar, r_{Rebar}.

$$\varepsilon_{Top} = a_{strain}\, r_{Rebar} + \varepsilon_{Axial}$$ Equation E.34

$$\varepsilon_{Bottom} = -a_{strain}\, r_{Rebar} + \varepsilon_{Axial}$$ Equation E.35

2-dimensional Position Reconstruction of Instrumented Rebar

If all bending along the rebar length occurs in the same direction, then all bending is two dimensional. Knowing the strain at very fine increments along the length of the rebar allows for the two dimensional axial position of the rebar to be determined. The following section describes the theoretical derivation of the equations to determine the two dimensional position of the rebar.

Consider an increment of the rebar with length, L_i, and radius, r. This increment, i, has a cross-section with two sides and a centerline as shown below:

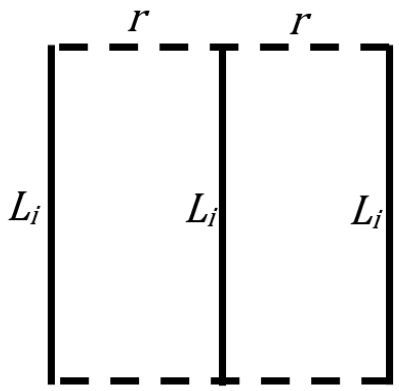

Figure E.5. Rebar cross-sections showing area contributing to and reducing the area moment of inertia

Now consider if the rebar increment is subjected to some arbitrary bending and axial forces. Using the derivation in the previous section, the fibre-optic instrumentation allows for calculation of the strain at either extreme fibre of the rebar (labelled top and bottom) as well as the axial strain. When combined with the initial increment length, the three strain values calculated provide new lengths for the increment at either edge and along the centerline:

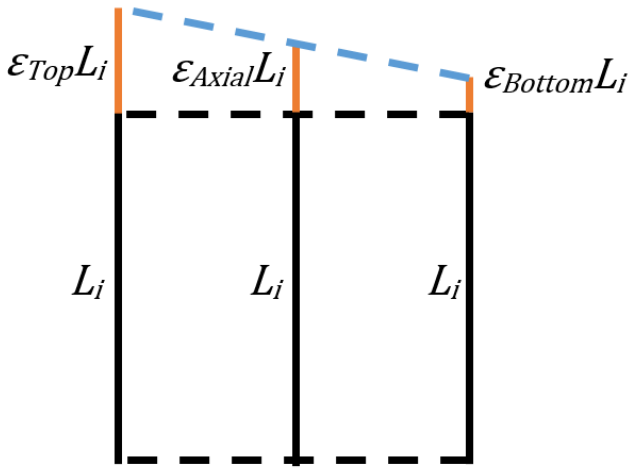

Figure E.6. Rebar cross-sections showing area contributing to and reducing the area moment of inertia

The three new lengths describe a curvature within the rebar. This curve can be defined by some angular change, $\Delta\phi_i$, and a radius of curvature, ρ_i. The centerline axis of the rebar at increment i will be said to start at a point in space, b_{i-1}, and end at another point, b_i.

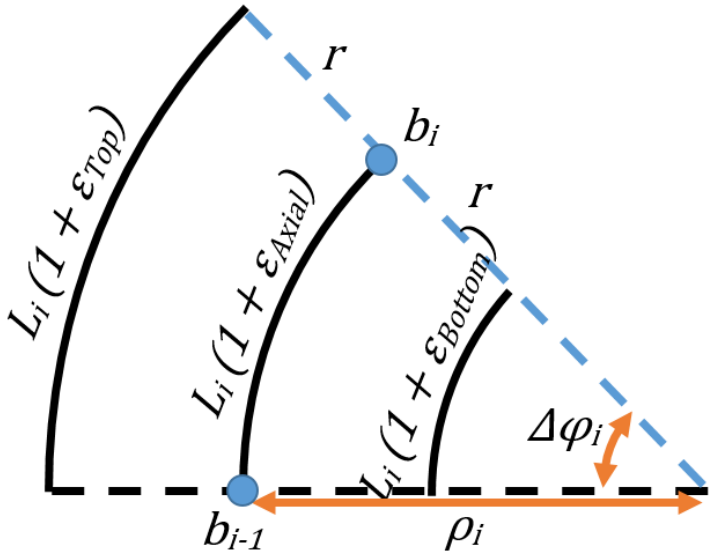

Figure E.7. Rebar cross-sections showing area contributing to and reducing the area moment of inertia

Applying the equation for an arc length yields:

$$\Delta\varphi_i\,(\rho_i + r) = L_i\big(1 + \varepsilon_{Top}\big) \qquad \text{Equation E.36}$$

And

$$\Delta\varphi_i\,(\rho_i - r) = L_i(1 + \varepsilon_{Bottom}) \qquad \text{Equation E.37}$$

Combining these equations and solving for the radius of curvature:

$$\frac{L_i(1+\varepsilon_{Top})}{(\rho_i+r)} = \frac{L_i(1+\varepsilon_{Bottom})}{(\rho_i-r)} \qquad \text{Equation E.38}$$

$$(\rho_i - r)\big(1 + \varepsilon_{Top}\big) = (\rho_i + r)(1 + \varepsilon_{Bottom}) \qquad \text{Equation E.39}$$

$$\varepsilon_{Top}\rho_i - \varepsilon_{Top}r = 2r + \varepsilon_{Bottom}\rho_i + \varepsilon_{Bottom}r \qquad \text{Equation E.40}$$

$$\big(\varepsilon_{Top} - \varepsilon_{Bottom}\big)\rho_i = r\left(\varepsilon_{Top} + \varepsilon_{Bottom} + 2\right) \qquad \text{Equation E.41}$$

$$\rho_i = \frac{r\,(\varepsilon_{Top}+\varepsilon_{Bottom}+2)}{(\varepsilon_{Top}-\varepsilon_{Bottom})} \qquad \text{Equation E.42}$$

Similarly, we can solve for the angular change:

$$\frac{L_i(1+\varepsilon_{Top})}{\Delta\varphi_i} - r = \frac{L_i(1+\varepsilon_{Bottom})}{\Delta\varphi_i} + r \qquad \text{Equation E.43}$$

$$L_i\big(1 + \varepsilon_{Top}\big) = L_i(1 + \varepsilon_{Bottom}) + 2r\,\Delta\varphi_i \qquad \text{Equation E.44}$$

$$2r\,\Delta\varphi_i = L_i\big(\varepsilon_{Top} - \varepsilon_{Bottom}\big) \qquad \text{Equation E.45}$$

$$\Delta\varphi_i = \frac{L_i}{2r}\big(\varepsilon_{Top} - \varepsilon_{Bottom}\big) \qquad \text{Equation E.46}$$

The goal here is to theoretically determine the shape of the instrumented rebar. The curve at increment *i* could begin at any orientation in two dimensional space. Let this beginning orientation be some angle, ϕ_{i-1}, measured from some reference axis (in this case, the vertical axis). The ending orientation of the incremental curve will be ϕ_i.

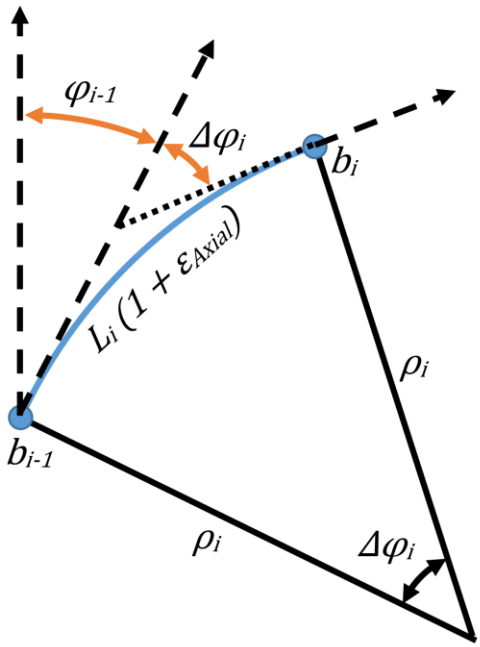

Figure E.8. Rebar cross-sections showing area contributing to and reducing the area moment of inertia

Since the curve has an angular change, the ending orientation of the curve can be found by:

$$\varphi_i = \varphi_{i-1} + \Delta\varphi_i \qquad \text{Equation E.47}$$

Now we will consider the change in location between b_{i-1} and b_i. The change in location will be defined by some vector, $\vec{c}_i$.

$$b_i = b_{i-1} + \vec{c}_i \qquad \text{Equation E.48}$$

We can determine the norm or magnitude of $\vec{c}_i$ using the geometry seen in the following figure:

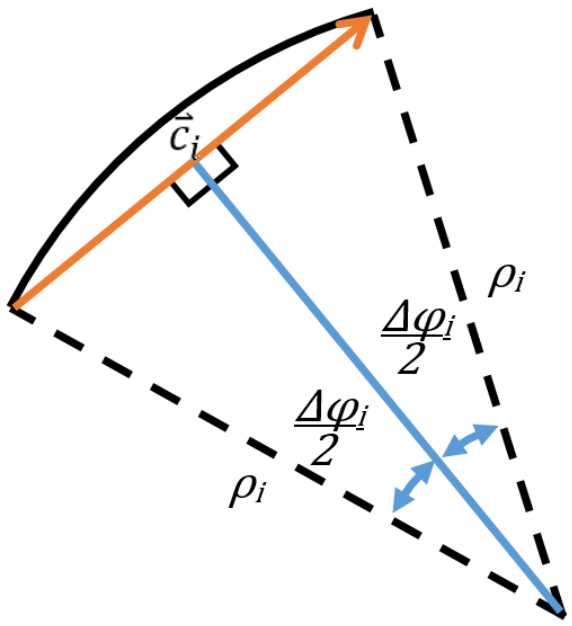

Figure E.9. Rebar cross-sections showing area contributing to and reducing the area moment of inertia

The following equation can be determined from trigonometry:

$$\text{SIN}\,\frac{\Delta\varphi_i}{2} = \frac{\|\vec{c}_i\|/_2}{\rho_i} \qquad \text{Equation E.49}$$

Where $\|\vec{c}_i\|$ represents the norm of vector $\vec{c}_i$.

By rearrangement we get:

$$\|\vec{c}_i\| = 2\,\rho_i\,\text{SIN}\,\frac{\Delta\varphi_i}{2} \qquad \text{Equation E.50}$$

The components of $\vec{c}_i$ can be determined knowing the magnitude and orientation of the vector, as in the following figure.

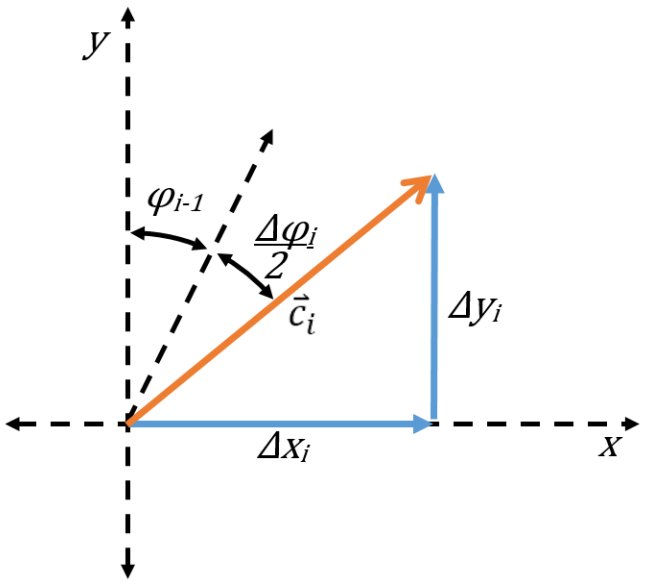

Figure E.10. Rebar cross-sections showing area contributing to and reducing the area moment of inertia

From this figure and trigonometry the following relations can be determined:

$$\Delta x_i = \|\vec{c}_i\| \sin\left(\varphi_{i-1} + \frac{\Delta\varphi_i}{2}\right) \quad \text{Equation E.51}$$

$$\Delta y_i = \|\vec{c}_i\| \cos\left(\varphi_{i-1} + \frac{\Delta\varphi_i}{2}\right) \quad \text{Equation E.52}$$

Applying the equations presented here starting with increment $i = 0$ to increment $i = n$ allows for a two dimensional series of discrete points that represent the axial position of the instrumented rebar. These points, from b_0 to b_n, correspond to each 0.65 mm increment at which strain was measured.

It is very important to note, that this 2-dimensional analysis method considers all bending to be within the 2-dimensional plane and is not "projected" onto the 2-D plane. This means the position and bending observed should be considered an upper-limit as, in many cases, some component of the bending will likely be out of this plane. In a laboratory setting where bending direction can be tightly controlled, this analysis method could prove useful. Unfortunately, in a field setting, bending of rebar often occurs in multiple directions simultaneously. For this type of bending, a 3-dimensional analysis must be considered.

3-dimensional Position Reconstruction of Instrumented Rebar

Bending of rebar is inherently a 3-dimensional problem, especially in in situ situations. The position of the centre axis of the rebar can be reconstructed in 3-dimensions similar to the 2-dimensional case previously analysed. However, this 3-dimensional analysis is significantly more complex to solve. The derivations of the relevant equations are presented here.

Consider one increment, i, of the rebar length. This incremental length begins at b_{i-1} and ends at b_i. The change in position between these two points can be described by some 3-dimensional vector $\vec{c}_i$, as in

$$\vec{c}_i = b_i - b_{i-1} \qquad \text{Equation E.53}$$

Where b_i is defined by x, y, and z coordinates:

$$b_i = \{x_i, y_i, z_i\} \qquad \text{Equation E.54}$$

And $\vec{c}_i$ has three components corresponding to the x, y, and z axis directions.

$$\vec{c}_i = c_{x\,i}\hat{\imath} + c_{y\,i}\hat{\jmath} + c_{z\,i}\hat{k} \qquad \text{Equation E.55}$$

All vectors and points are defined in a similar manner.

The direction of the centre axis of the rebar at b_{i-1} and b_i can be defined by directional vectors $\vec{d}_{i-1}$ and $\vec{d}_i$, respectively. The angle between these vectors (within their plane) can be defined by angle $\Delta\varphi_i$.

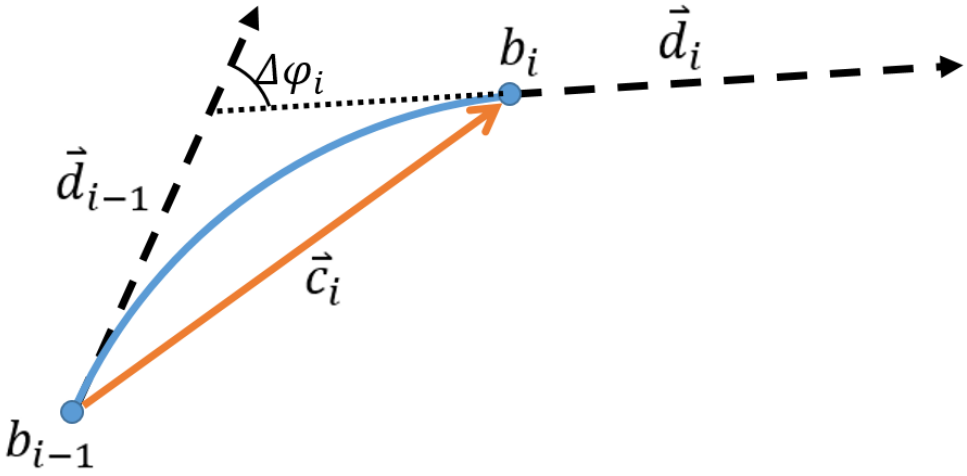

Figure E.11. Rebar cross-sections showing area contributing to and reducing the area moment of inertia

The cross-section of the rebar at b_{i-1} and b_i (perpendicular to $\vec{d}_{i-1}$ and $\vec{d}_i$) can be used to defined even more properties of the rebar geometry at each increment. The centroidal axis of each increment cross-section can be defined as a vector $\vec{n}_i$. The direction of this vector remains unchanged between b_{i-1} and b_i. The position of the first fibre-optic strand relative to the central axis of the rebar can be defined with a vector as well. However, due to the bend or curve of the rebar, the fibre-optic orientation vector is defined by $\vec{f}_{i-1}$ at b_{i-1} and $\vec{f}_i$ at b_i. At both of these positions, the first fibre-optic strand is an angle, θ_{fi} away from the neutral bending axis. This angle is the so-called angle of inclination as solved for previously. The cross-sectional view of these two points is shown below. Please note that in this figure, the $\vec{c}_i^{\,*}$ vector is out of the plane of the cross-section and is simply displayed projected onto the cross-section.

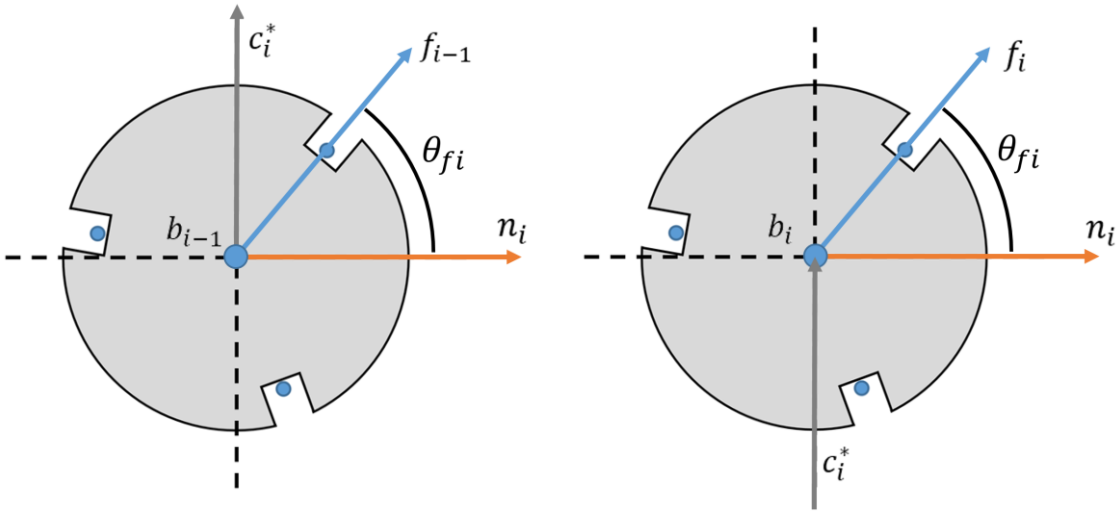

Figure E.12. Rebar cross-sections showing area contributing to and reducing the area moment of inertia

We will assume that at any increment, the following will be known:

- The position (x,y,z) of b_{i-1}
- The angle, θ_{fi}, between $\vec{n}_i$ and both $\vec{f}_{i-1}$ and $\vec{f}_i$
- The magnitude or length of $\vec{c}_i$
- The axial direction vector $\vec{d}_{i-1}$
- The angle, $\Delta\varphi_i$, between $\vec{d}_{i-1}$ and $\vec{d}_i$
- The fibre-optic orientation vector $\vec{f}_{i-1}$

Note that for the first increment, $i = 1$, the following can be assumed or changed in order to change the position and orientation of the rebar in virtual space:

$$b_0 = (0,0,0)$$

$$\vec{d}_{i-1} = (0,0,1)$$

$$\vec{f}_{i-1} = (1,0,0)$$

The first goal is to determine the vector components of $\vec{n}_i$.

Given the cross-product and right hand rule, we can derive the following equation at b_{i-1}:

$$\vec{n}_i \times \vec{f}_{i-1} = \|\vec{n}_i\|\left\|\vec{f}_{i-1}\right\| \text{SIN}\, \theta_{fi}\, \vec{d}_{i-1} \qquad \text{Equation E.56}$$

Since we only care about the direction of n_i and f_{i-1}, we can ensure the vectors are normalized at each increment and simplify this equation to:

$$\vec{n}_i \times \vec{f}_{i-1} = \text{SIN}\,\theta_{fi}\,\vec{d}_{i-1} \qquad \text{Equation E.57}$$

Also, according to the definition of the dot product:

$$\vec{n}_i \cdot \vec{f}_{i-1} = \|\vec{n}_i\|\|\vec{f}_{i-1}\|\,\text{COS}\,\theta_{fi} \qquad \text{Equation E.58}$$

Or

$$\vec{n}_i \cdot \vec{f}_{i-1} = \text{COS}\,\theta_{fi} \qquad \text{Equation E.59}$$

The cross-product equation above can be expanded into:

$$\left(n_{x\,i}\hat{\imath} + n_{y\,i}\hat{\jmath} + n_{z\,i}\hat{k}\right) \times \left(f_{x\,i-1}\hat{\imath} + f_{y\,i-1}\hat{\jmath} + f_{z\,i-1}\hat{k}\right) = \text{SIN}\,\theta_{fi}\left(d_{x\,i-1}\hat{\imath} + d_{y\,i-1}\hat{\jmath} + d_{z\,i-1}\hat{k}\right)$$

Equation E.60

$$\left(n_{y\,i}\,f_{z\,i-1} - n_{z\,i}\,f_{y\,i-1}\right)\hat{\imath} + \left(n_{z\,i}\,f_{x\,i-1} - n_{x\,i}\,f_{z\,i-1}\right)\hat{\jmath} + \left(n_{x\,i}\,f_{y\,i-1} - n_{y\,i}\,f_{x\,i-1}\right)\hat{k} = \text{SIN}\,\theta_{fi}\left(d_{x\,i-1}\hat{\imath} + d_{y\,i-1}\hat{\jmath} + d_{z\,i-1}\hat{k}\right)$$

Equation E.61

Then the following equations must be true

$$n_{y\,i}\,f_{z\,i-1} - n_{z\,i}\,f_{y\,i-1} = \text{SIN}\,\theta_{fi}\,d_{x\,i-1} \qquad \text{Equation E.62}$$

$$n_{z\,i}\,f_{x\,i-1} - n_{x\,i}\,f_{z\,i-1} = \text{SIN}\,\theta_{fi}\,d_{y\,i-1} \qquad \text{Equation E.63}$$

$$n_{x\,i}\,f_{y\,i-1} - n_{y\,i}\,f_{x\,i-1} = \text{SIN}\,\theta_{fi}\,d_{z\,i-1} \qquad \text{Equation E.64}$$

And from expanding the dot-product equation:

$$n_{x\,i}\,f_{x\,i-1} + n_{y\,i}\,f_{y\,i-1} + n_{z\,i}\,f_{z\,i-1} = \text{COS}\,\theta_{fi} \qquad \text{Equation E.65}$$

Since $\vec{f}_{i-1}$ and $\vec{d}_{i-1}$ are given, EQ. C.63 and EQ. C.64 are isolated for the y and z components of $\vec{n}_i$. We find n_{yi} and $n_{z\,i}$ in terms of n_{xi}.

$$n_{y\,i} = \frac{f_{y\,i-1}}{f_{x\,i-1}}n_{x\,i} - \frac{d_{z\,i-1}}{f_{x\,i-1}}\text{SIN}\,\theta_{fi} \qquad \text{Equation E.66}$$

$$n_{z\,i} = \frac{f_{z\,i-1}}{f_{x\,i-1}}n_{x\,i} + \frac{d_{y\,i-1}}{f_{x\,i-1}}\text{SIN}\,\theta_{fi} \qquad \text{Equation E.67}$$

Then by substitution of EQ. C.66 and EQ. C.67 into EQ. C.65 and arithmetic:

$$n_{x\,i}\,f_{x\,i-1} + \frac{{f_{y\,i-1}}^2}{f_{x\,i-1}}n_{x\,i} - \frac{f_{y\,i-1}\,d_{z\,i-1}}{f_{x\,i-1}}\text{SIN}\,\theta_{fi} + \frac{{f_{z\,i-1}}^2}{f_{x\,i-1}}n_{x\,i} + \frac{f_{z\,i-1}\,d_{y\,i-1}}{f_{x\,i-1}}\text{SIN}\,\theta_{fi} = \text{COS}\,\theta_{fi}$$

Equation E.68

$$\left({f_{x\,i-1}}^2 + {f_{y\,i-1}}^2 + {f_{z\,i-1}}^2\right)n_{x\,i} = f_{x\,i-1}\,\text{COS}\,\theta_{fi} + f_{y\,i-1}\,d_{z\,i-1}\,\text{SIN}\,\theta_{fi} - f_{z\,i-1}\,d_{y\,i-1}\,\text{SIN}\,\theta_{fi}$$

Equation E.69

$$n_{x\,i} = \frac{f_{x\,i-1}\,\cos\theta_{fi} + f_{y\,i-1}\,d_{z\,i-1}\,\sin\theta_{fi} - f_{z\,i-1}\,d_{y\,i-1}\,\sin\theta_{fi}}{\left(f_{x\,i-1}{}^2 + f_{y\,i-1}{}^2 + f_{z\,i-1}{}^2\right)} \qquad \text{Equation E.70}$$

Similarly, the following can be determined:

$$n_{y\,i} = \frac{f_{y\,i-1}\,\cos\theta_{fi} + f_{z\,i-1}\,d_{x\,i-1}\,\sin\theta_{fi} - f_{x\,i-1}\,d_{z\,i-1}\,\sin\theta_{fi}}{\left(f_{x\,i-1}{}^2 + f_{y\,i-1}{}^2 + f_{z\,i-1}{}^2\right)} \qquad \text{Equation E.71}$$

$$n_{z\,i} = \frac{f_{z\,i-1}\,\cos\theta_{fi} + f_{x\,i-1}\,d_{y\,i-1}\,\sin\theta_{fi} - f_{y\,i-1}\,d_{x\,i-1}\,\sin\theta_{fi}}{\left(f_{x\,i-1}{}^2 + f_{y\,i-1}{}^2 + f_{z\,i-1}{}^2\right)} \qquad \text{Equation E.72}$$

Now we must determine the vector $\vec{c}_i$. As before, it can be found:

$$\vec{c}_i \times \vec{d}_{i-1} = \|\vec{c}_i\|\left\|\vec{d}_{i-1}\right\| \sin\frac{\varphi_i}{2}\vec{n}_i \qquad \text{Equation E.73}$$

$$\vec{c}_i \cdot \vec{d}_{i-1} = \|\vec{c}_i\|\left\|\vec{d}_{i-1}\right\| \cos\frac{\varphi_i}{2} \qquad \text{Equation E.74}$$

$\vec{d}_{i-1}$ can still be assumed to be a unit vector of length 1, however $\vec{c}_i$ is not. Therefore, the above equations simplify to:

$$\vec{c}_i \times \vec{d}_{i-1} = \|\vec{c}_i\| \sin\frac{\varphi_i}{2}\vec{n}_i \qquad \text{Equation E.75}$$

$$\vec{c}_i \cdot \vec{d}_{i-1} = \|\vec{c}_i\| \cos\frac{\varphi_i}{2} \qquad \text{Equation E.76}$$

Substitution and isolation proceeds as before and we arrive at the following equations:

$$\frac{c_{x\,i}}{\|\vec{c}_i\|} = \frac{d_{x\,i-1}\cos\frac{\varphi_i}{2} + d_{y\,i-1}\,n_{z\,i-1}\sin\frac{\varphi_i}{2} - d_{z\,i-1}\,n_{y\,i-1}\sin\frac{\varphi_i}{2}}{\left(d_{x\,i-1}{}^2 + d_{y\,i-1}{}^2 + d_{z\,i-1}{}^2\right)} \qquad \text{Equation E.77}$$

$$\frac{c_{y\,i}}{\|\vec{c}_i\|} = \frac{d_{y\,i-1}\cos\frac{\varphi_i}{2} + d_{z\,i-1}\,n_{x\,i-1}\sin\frac{\varphi_i}{2} - d_{x\,i-1}\,n_{z\,i-1}\sin\frac{\varphi_i}{2}}{\left(d_{x\,i-1}{}^2 + d_{y\,i-1}{}^2 + d_{z\,i-1}{}^2\right)} \qquad \text{Equation E.78}$$

$$\frac{c_{z\,i}}{\|\vec{c}_i\|} = \frac{d_{z\,i-1}\cos\frac{\varphi_i}{2} + d_{x\,i-1}\,n_{y\,i-1}\sin\frac{\varphi_i}{2} - d_{y\,i-1}\,n_{x\,i-1}\sin\frac{\varphi_i}{2}}{\left(d_{x\,i-1}{}^2 + d_{y\,i-1}{}^2 + d_{z\,i-1}{}^2\right)} \qquad \text{Equation E.79}$$

Knowing the components of $\vec{c}_i$, we can determine the position of b_i by:

$$b_i = b_{i-1} + \vec{c}_i \qquad \text{Equation E.80}$$

To determine the position of b_{i+1}, we must now determine the axial direction vector $\vec{d}_i$ and the new fibre-optic direction $\vec{f}_i$. Using the exact same method as before, we know:

$$\vec{d}_i \times \vec{c}_i = \|\vec{c}_i\| \sin\frac{\varphi_i}{2}\vec{n}_i \qquad \text{Equation E.81}$$

$$\vec{d}_i \cdot \vec{c}_{i-1} = \|\vec{c}_i\| \cos\frac{\varphi_i}{2} \qquad \text{Equation E.82}$$

And can solve for $\vec{d}_i$:

$$d_{x\,i} = \frac{\frac{c_{x\,i}}{\|\vec{c}_i\|}\cos\frac{\varphi_i}{2} + \frac{c_{y\,i}}{\|\vec{c}_i\|}n_{z\,i-1}\sin\frac{\varphi_i}{2} - \frac{c_{z\,i}}{\|\vec{c}_i\|}n_{y\,i-1}\sin\frac{\varphi_i}{2}}{\left(\left(\frac{c_{x\,i}}{\|\vec{c}_i\|}\right)^2 + \left(\frac{c_{y\,i}}{\|\vec{c}_i\|}\right)^2 + \left(\frac{c_{z\,i}}{\|\vec{c}_i\|}\right)^2\right)} \qquad \text{Equation E.83}$$

$$d_{y\,i} = \frac{\frac{c_{y\,i}}{\|\vec{c}_i\|}\cos\frac{\varphi_i}{2} + \frac{c_{z\,i}}{\|\vec{c}_i\|}n_{x\,i-1}\sin\frac{\varphi_i}{2} - \frac{c_{x\,i}}{\|\vec{c}_i\|}n_{z\,i-1}\sin\frac{\varphi_i}{2}}{\left(\left(\frac{c_{x\,i}}{\|\vec{c}_i\|}\right)^2 + \left(\frac{c_{y\,i}}{\|\vec{c}_i\|}\right)^2 + \left(\frac{c_{z\,i}}{\|\vec{c}_i\|}\right)^2\right)} \qquad \text{Equation E.84}$$

$$d_{z\,i} = \frac{\frac{c_{z\,i}}{\|\vec{c}_i\|}\cos\frac{\varphi_i}{2} + \frac{c_{x\,i}}{\|\vec{c}_i\|}n_{y\,i-1}\sin\frac{\varphi_i}{2} - \frac{c_{y\,i}}{\|\vec{c}_i\|}n_{x\,i-1}\sin\frac{\varphi_i}{2}}{\left(\left(\frac{c_{x\,i}}{\|\vec{c}_i\|}\right)^2 + \left(\frac{c_{y\,i}}{\|\vec{c}_i\|}\right)^2 + \left(\frac{c_{z\,i}}{\|\vec{c}_i\|}\right)^2\right)} \qquad \text{Equation E.85}$$

Lastly, the new orientation of the fibre-optic, $\vec{f}_i$, can be solved for from:

$$\vec{n}_i \times \vec{f}_i = \sin\theta_{fi}\,\vec{d}_i \qquad \text{Equation E.86}$$

$$\vec{n}_i \cdot \vec{f}_i = \cos\theta_{fi} \qquad \text{Equation E.87}$$

By substitution and rearrangement:

$$f_{x\,i} = \frac{n_{x\,i}\cos\theta_{fi} + n_{y\,i}\,d_{z\,i}\sin\theta_{fi} - n_{z\,i}\,d_{y\,i}\sin\theta_{fi}}{\left({f_{x\,i}}^2 + {f_{y\,i}}^2 + {f_{z\,i}}^2\right)} \qquad \text{Equation E.88}$$

$$f_{y\,i} = \frac{n_{y\,i}\cos\theta_{fi} + n_{z\,i}\,d_{x\,i-1}\sin\theta_{fi} - n_{x\,i}\,d_{z\,i}\sin\theta_{fi}}{\left({f_{x\,i}}^2 + {f_{y\,i}}^2 + {f_{z\,i}}^2\right)} \qquad \text{Equation E.89}$$

$$f_{z\,i} = \frac{n_{z\,i}\cos\theta_{fi} + n_{x\,i-1}\,d_{y\,i}\sin\theta_{fi} - n_{y\,i}\,d_{x\,i}\sin\theta_{fi}}{\left({f_{x\,i}}^2 + {f_{y\,i}}^2 + {f_{z\,i}}^2\right)} \qquad \text{Equation E.90}$$

The same process, starting with determining $\vec{n}_i$, can then be applied to increments *i+1*, *i+2*, etc. Thus, a series of points (b_1, b_2, b_3…), each with an x, y, and z component, can be generated to theoretically reconstruct the shape of the instrumented rebar.

It should also be noted that most of the vectors used are unit vectors and have a theoretical length of 1. However, if using a program like Microsoft Excel, the vector components will be rounded after a certain number of significant figures. This is insignificant after one iteration of the process presented here, but after many thousand operations the errors can compile and the position plot can drift. To prevent this, it is important to normalize the vectors every time they are calculated.

Appendix F – Lateral Pull Testing Apparatus Drawings and Installation Procedure

Drawings for the lateral pull testing apparatus are presented below. These drawings were delivered to the machinists at the University of Saskatchewan Machine Shops for construction of the apparatus. A procedure for installation of the apparatus and test setup in the field is also presented in the section.

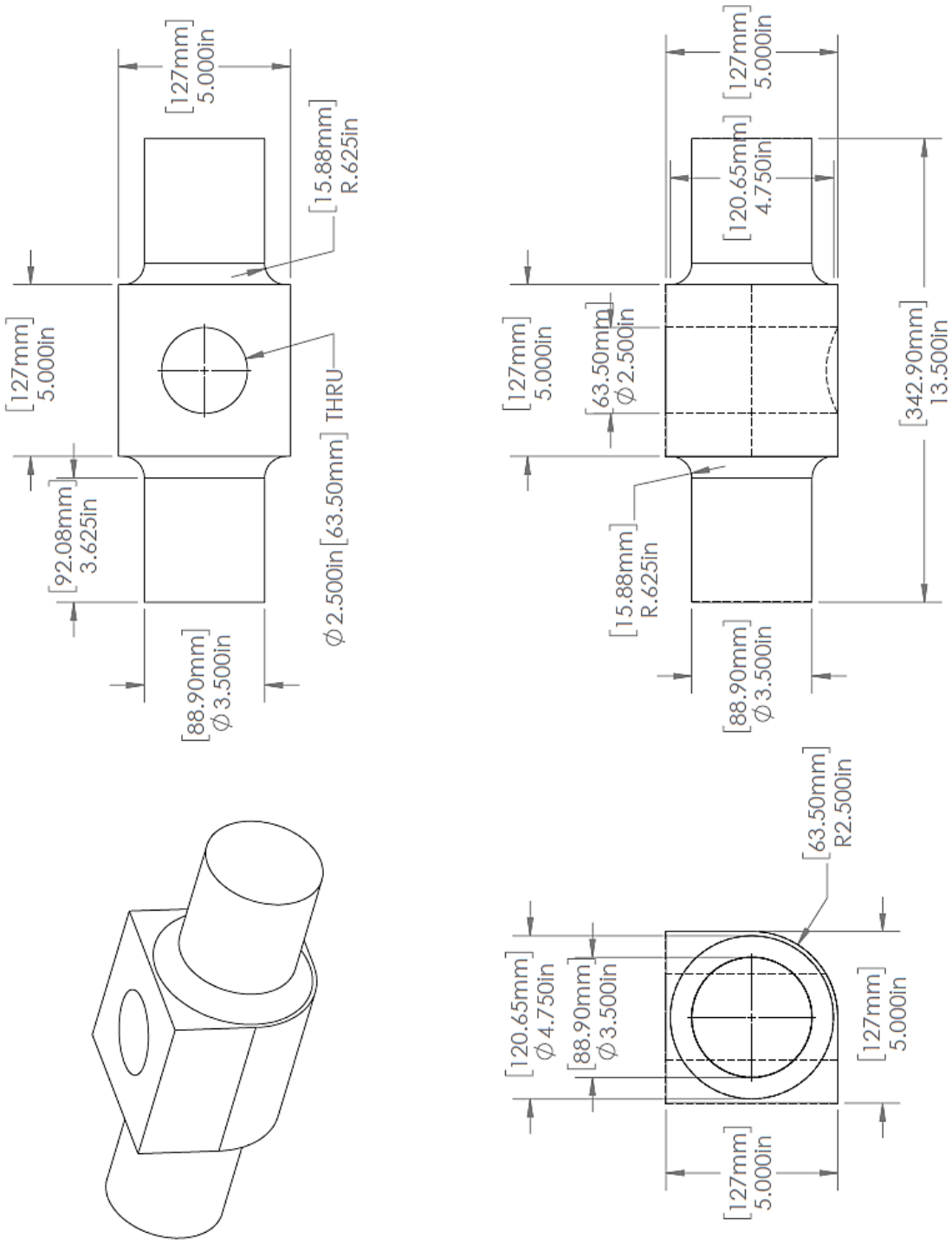

LPT Testing Apparatus – Chassis Design

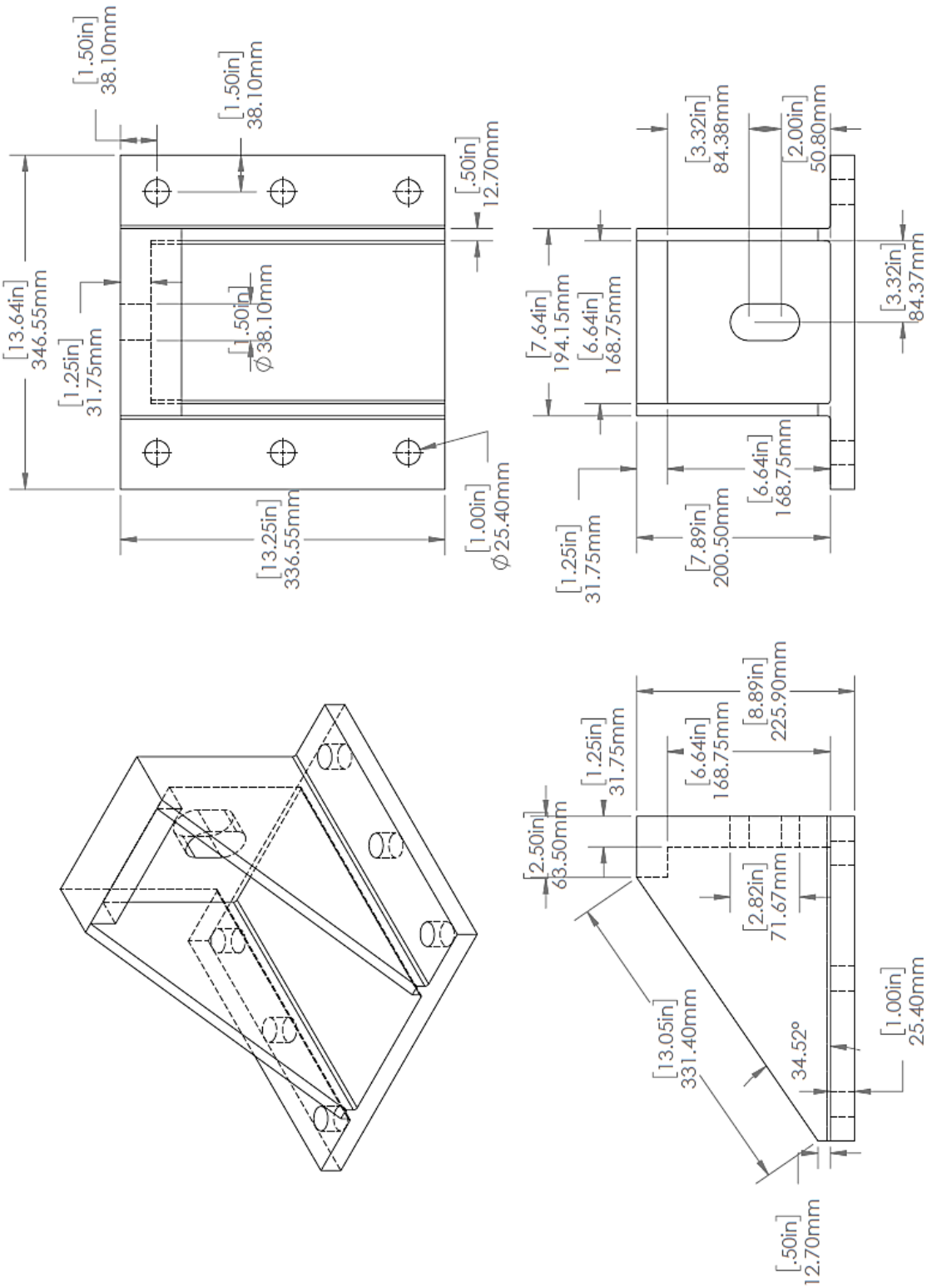

LPT Testing Apparatus – L-Bracket Design

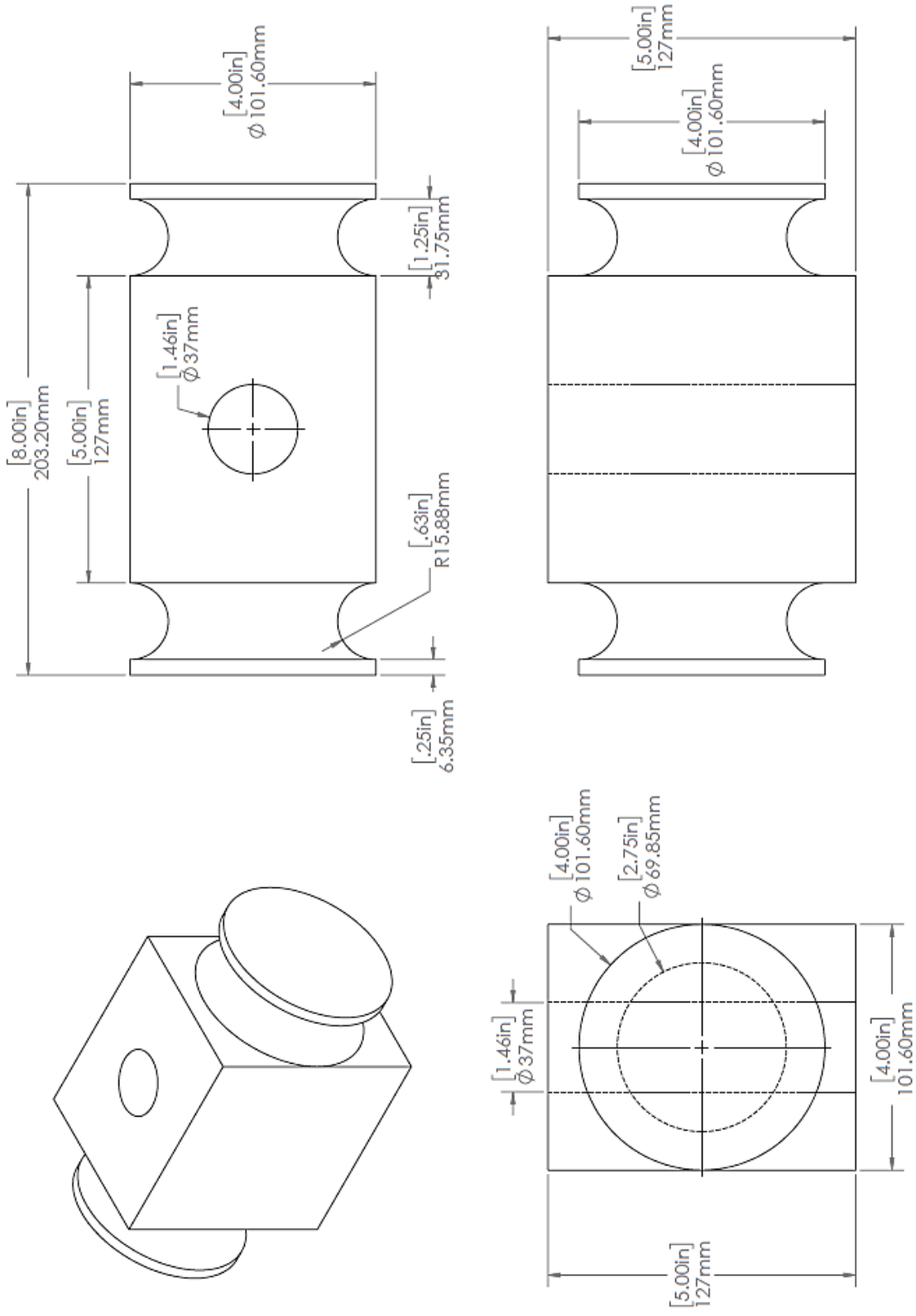

LPT Testing Apparatus – Spreader Block Design

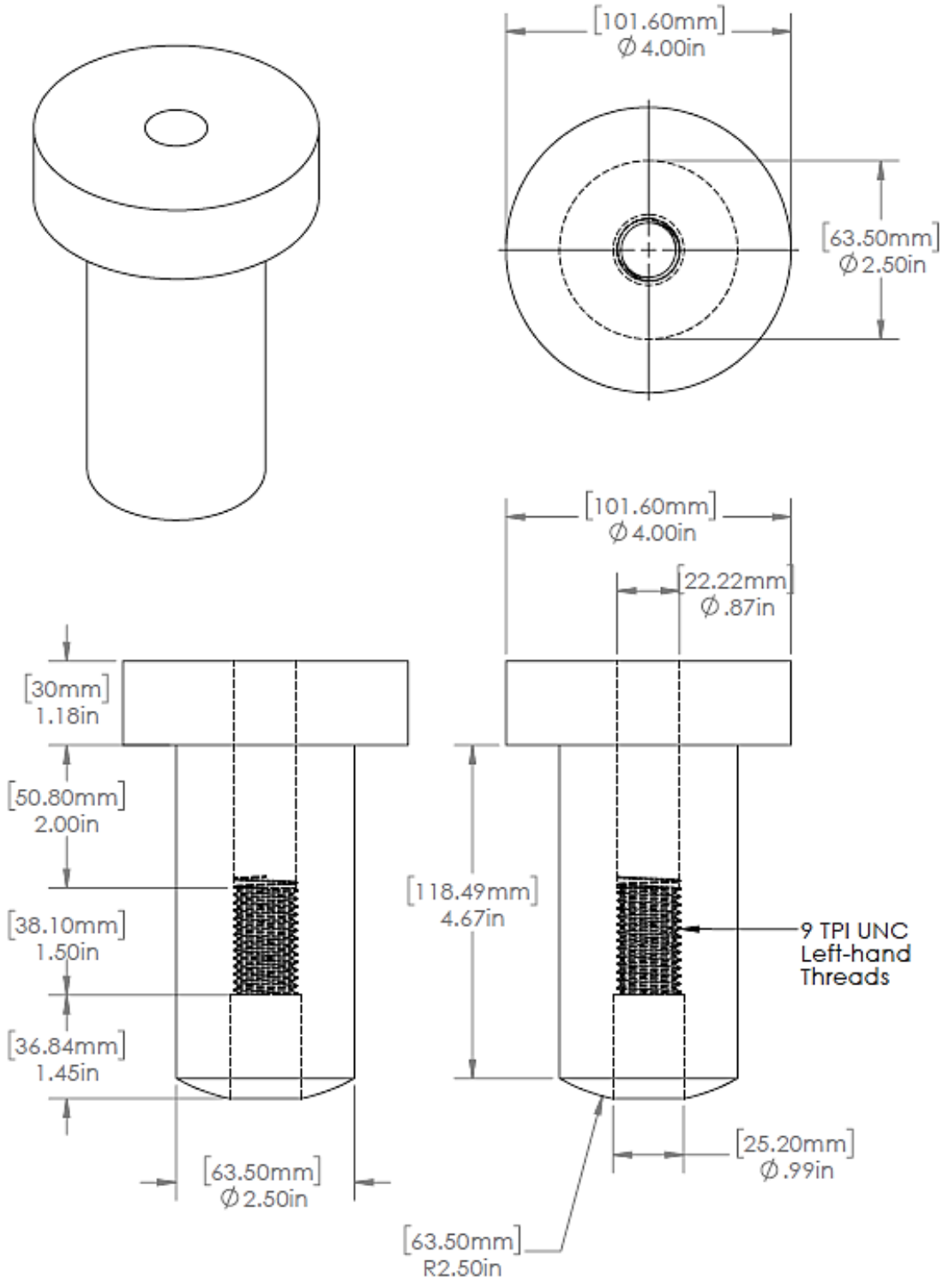

LPT Testing Apparatus – Threaded Insert Design for 22M (#7) Rebar

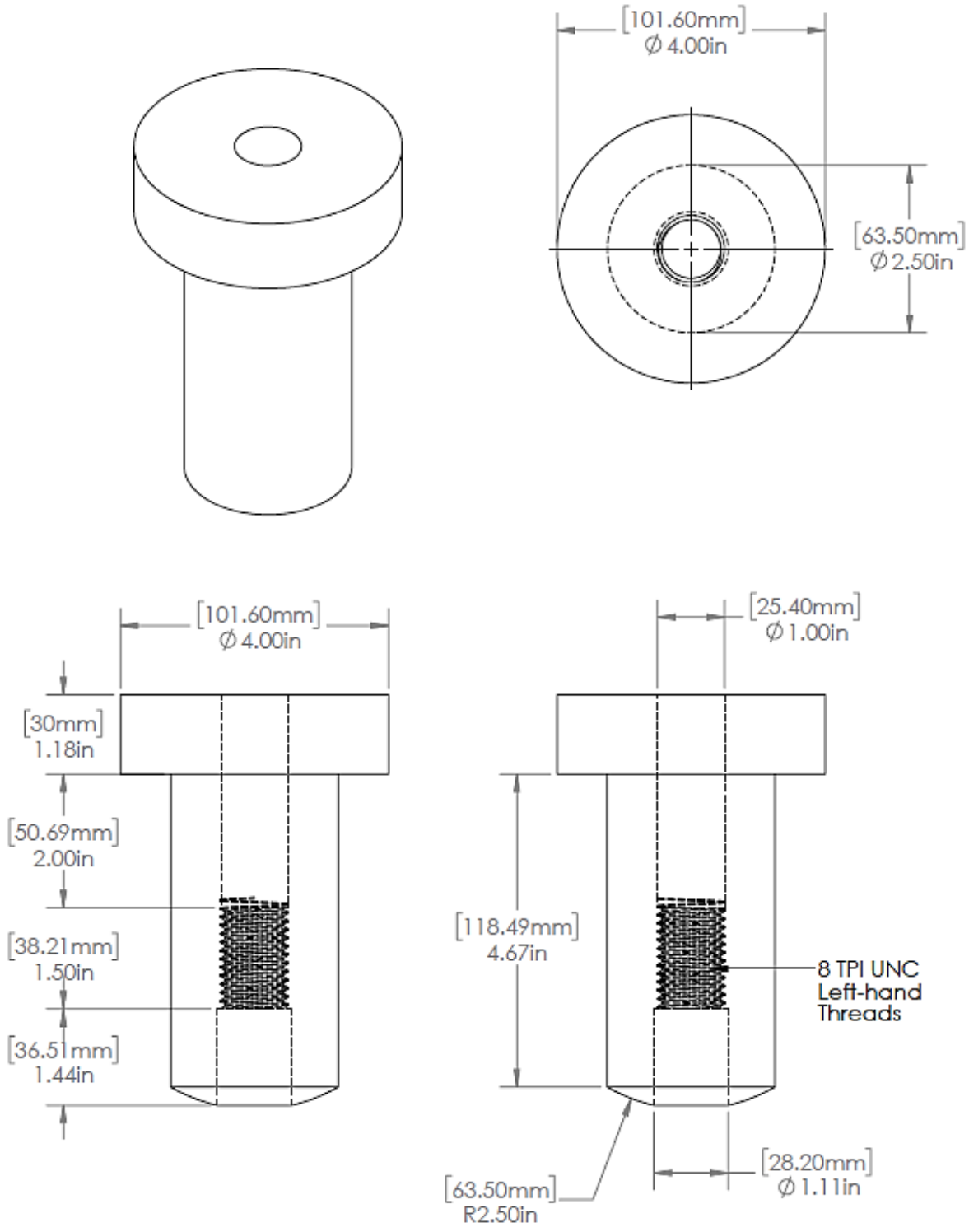

LPT Testing Apparatus – Threaded Insert Design for 25M (#8) Rebar

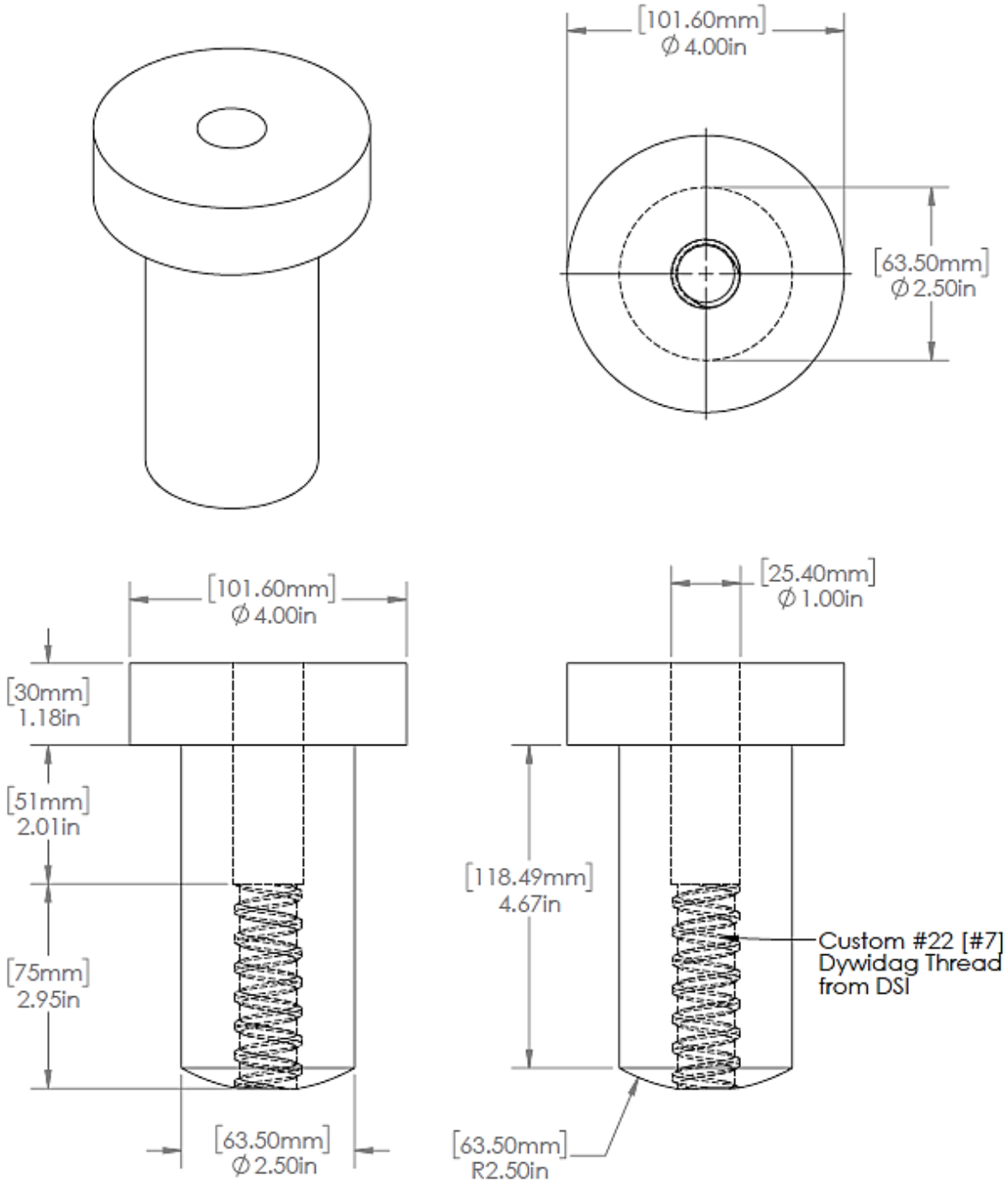

LPT Testing Apparatus – Threaded Insert Design for 22M (#7) Dywidag Threadbar

The procedure for installing the lateral pull testing apparatus and performing a test is described here.

1. A testing area of approximately 3 m long and 1.5 m wide is required. The rock surface must competent, have a representative mineralogy of the rock type under investigation, and.be flat and planar to ensure a valid test is achieved. Due to the weight of the testing apparatus, tests conducted in the floor of a drift are much more practical.
2. Rebar will first be installed at one end of this testing area. Drill the proper sized hole into the floor with a "plugger" or "sinker" drill (similar to a stoper). Take care not to ream the hole to a larger diameter than desired. Check the hole depth against the rebar length to ensure the rebar threads sit about 25 mm (1 in.) above the potash surface. The hole may need to be over drilled slightly to account for cuttings falling back into the hole.
3. Insert resin cartridges to fill the hole. Test the resin to make sure it hardens properly and is not expired.
4. Spin the rebar into the hole and resin with the plugger. Fully insert it into the hole and then spin as per manufacturer's instructions which was 6 seconds in this program. Scrape away excess resin from the collar of the hole to make a flat resin surface in line with the potash surface.

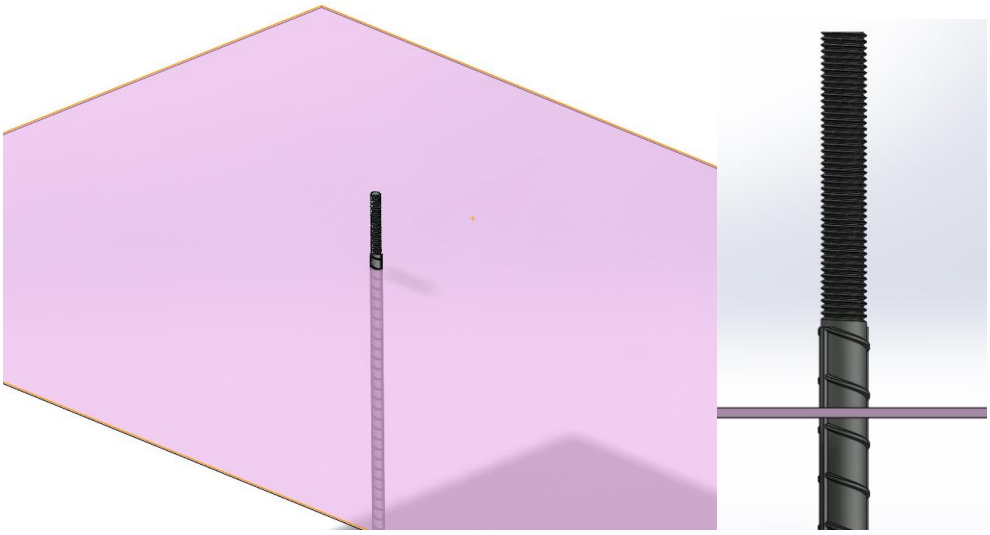

Figure F.1. Rebar installed in potash surface for lateral pull testing

5. Place the skid plates on either side of the rebar. They should be about 337 mm (13.25 in.) apart centred around the rebar.

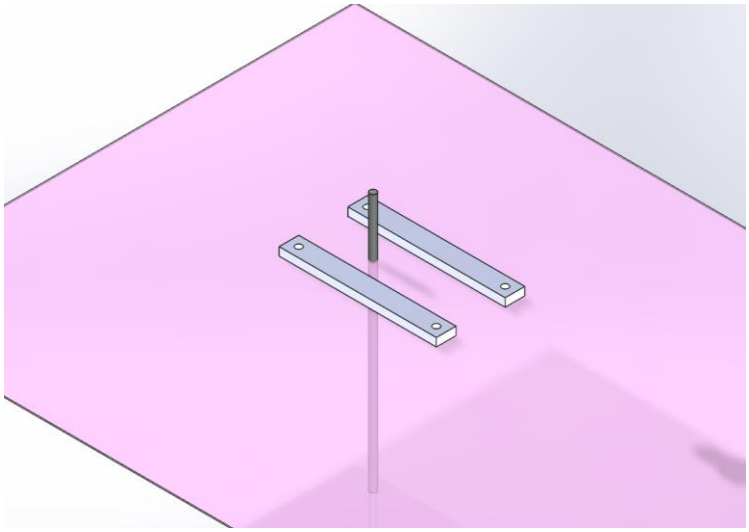

Figure F.2. Skid plates parallel to the rebar

6. Place the master links on each cylindrical arm of the apparatus chassis and bolt on the end disks. Apply ample grease to between the master links and the chassis arms.

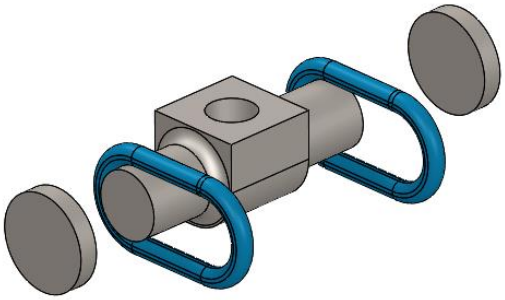

Figure F.3. Apparatus chassis assembly

7. Place the chassis assembly around the installed rebar so that the cylindrical arms rest on the skid plates. Apply ample grease between the chassis arms and the skid plates, as well as a bead along the skid plates.

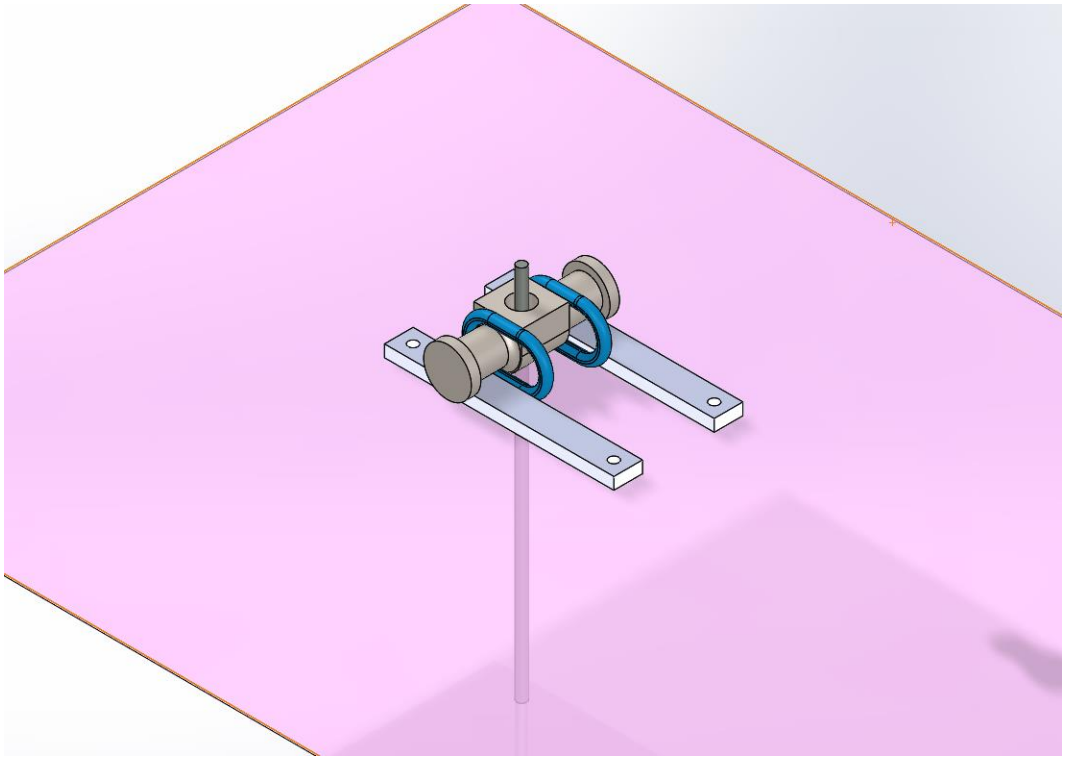

Figure F.4. Apparatus chassis resting on skid plates

8. Tighten the threaded insert onto the rebar until the chassis sits firmly against the skid plates.

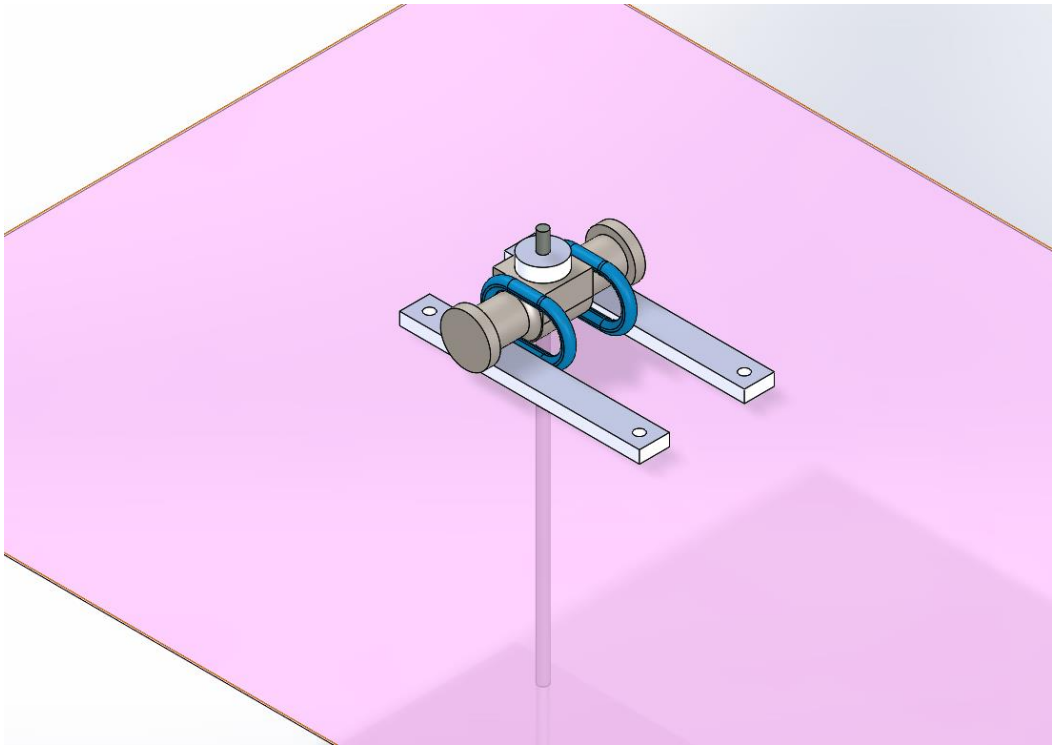

Figure F.5. Threaded insert tightened onto rebar

9. Carefully position the skid plates to be parallel and 337 mm (13.25 in.) apart. Take special care to ensure the plates are centred around the rebar. Having the chassis and threaded insert on the rebar helps with this since a 3.2 mm (0.125 in.) gap needs to be left between the end discs of the chassis and the skid plates. Install the mining screws one at a time, measuring the position and adjusting the skid plates after ever screw installation.

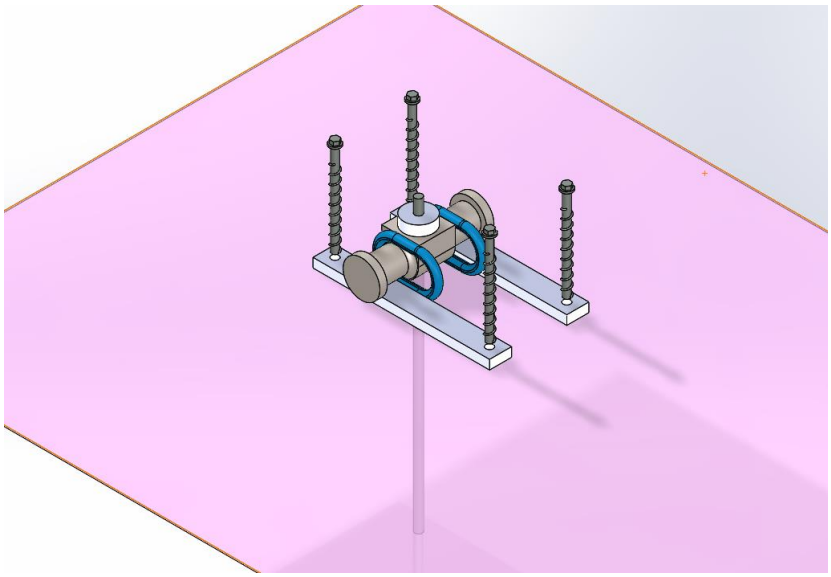

Figure F.6. Anchoring skid plates with mining screws

10. Attached the turnbuckles to the master links on the chassis. Lengthen the turnbuckles fully.

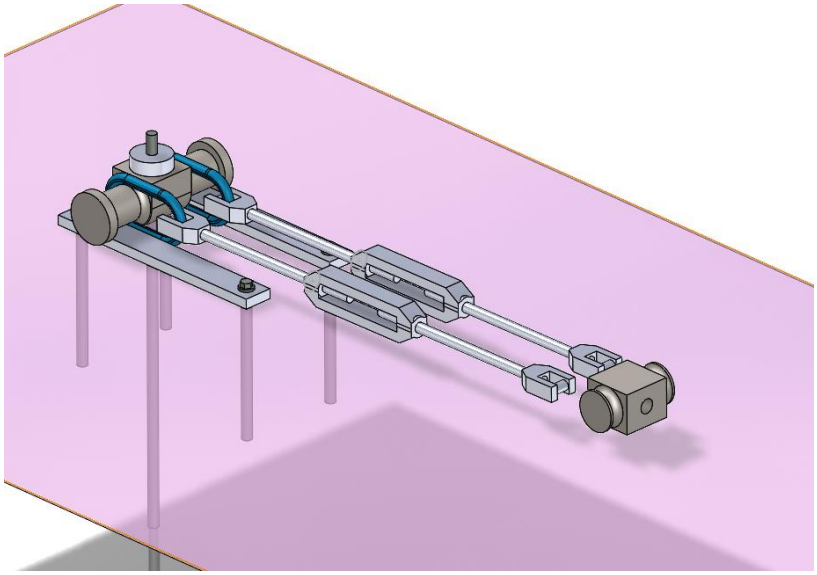

Figure F.7. Turnbuckles attached to master links on apparatus chassis

11. Attach the master links between the turnbuckle and the spreader block.

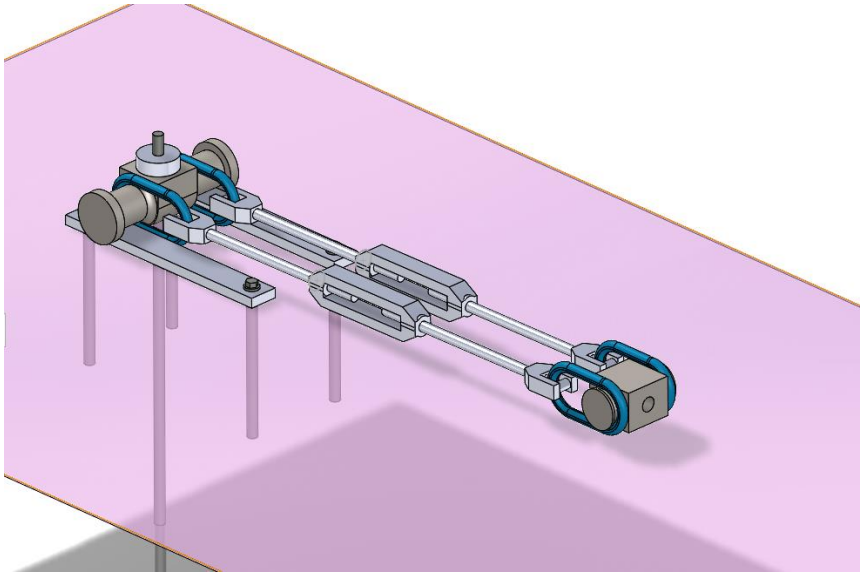

Figure F.8. Master links attached between turnbuckles and spreader block

12. Place the L-bracket between 6 ft and 8 ft from the rebar. Special care needs to be taken to align the bracket with the parallel skid plates.

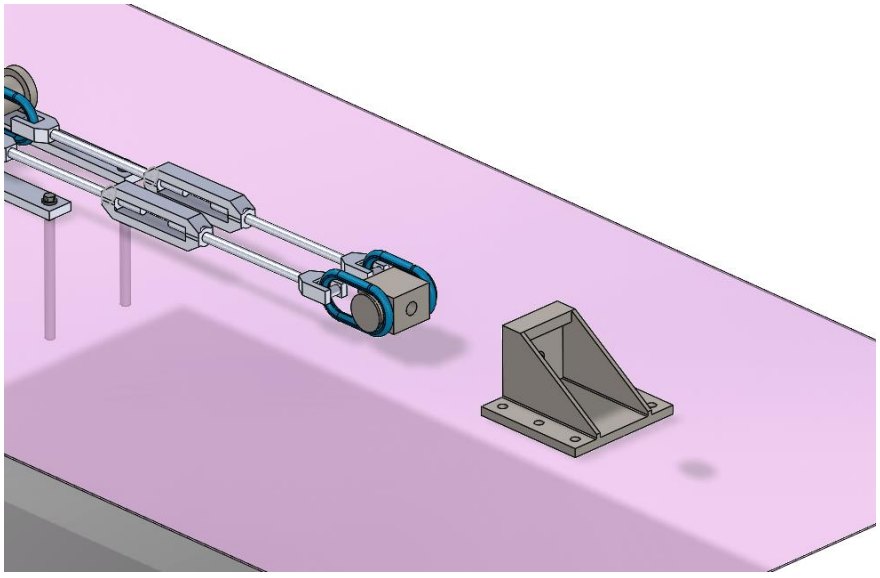

Figure F.9. L-bracket aligned with skid plates

13. Place the hydraulic cylinder in the bracket.

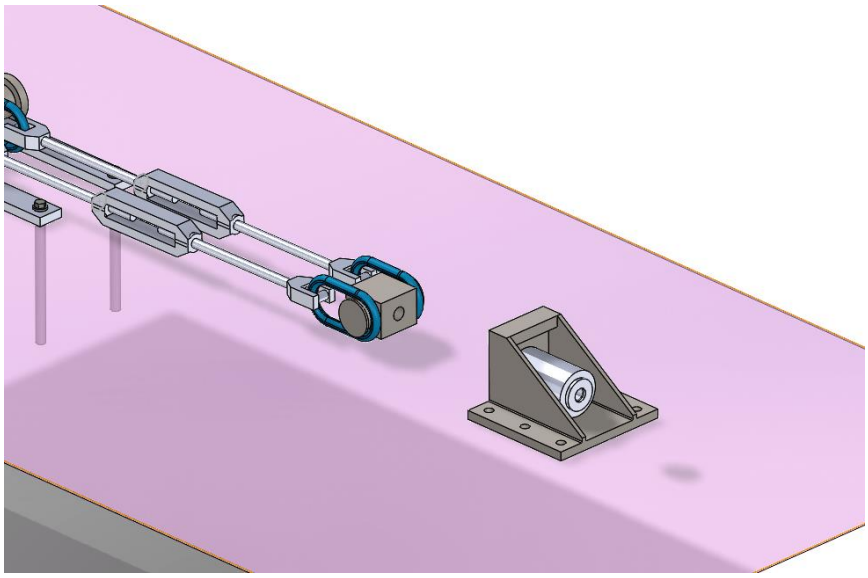

Figure F.10. Hydraulic cylinder in L-bracket

14. Pass the threaded rod through the hydraulic cylinder and the spreader block. Ensure this rod had a yield strength higher than the failure strength expected from the rebar being tested. 25M (#8) dywidag threadbar was used in this testing.
15. Place nuts on either end of the threaded rod and lightly tighten them.

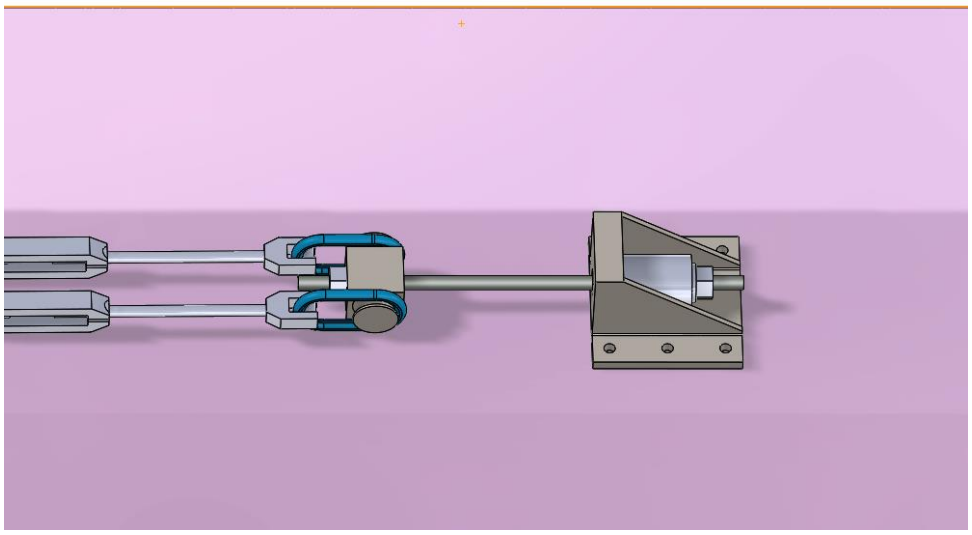

Figure F.11. Passing threaded rod through hydraulic cylinder and spreader block

16. Anchor the L-bracket to the potash surface with mining screws.

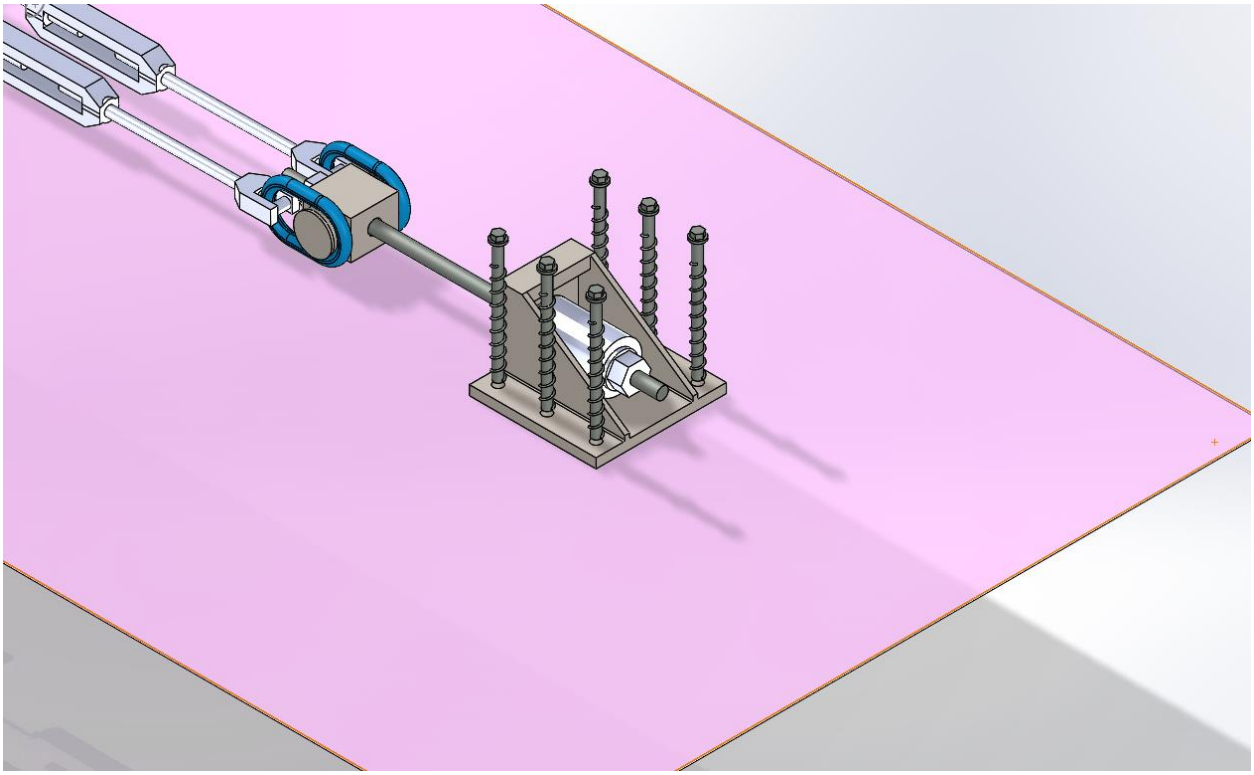

Figure F.12. Anchoring the L-bracket with mining screws

17. Fully tighten the turnbuckles to remove any slack within the test setup.

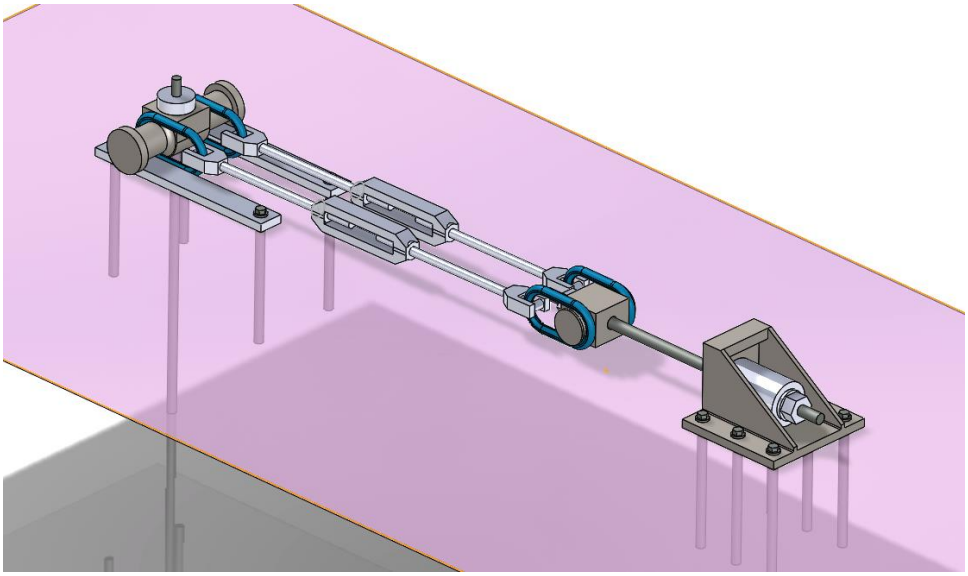

Figure F.13. Lateral Pull Testing setup

18. Chain the L-bracket to the either end of the threaded rod using shackles and eye-nuts. Pass this chain through the turnbuckles and master links as well.
19. Chain the skid plates to the apparatus chassis and threaded insert using shackles. This is a crucial step since the rebar is expected to break and the chassis and threaded insert will have significant kinetic energy.
20. Measure the angle forwards and sideways from horizontal of the chassis and skid plates. Record these angles.
21. Connect the string-pots to the chassis using steel tie-wire. Connect them at the upper corner of the chassis and the front side of the curve on the chassis. Ensure the string pots are level with the chassis. Measure and record the distance between the chassis and the string pots.

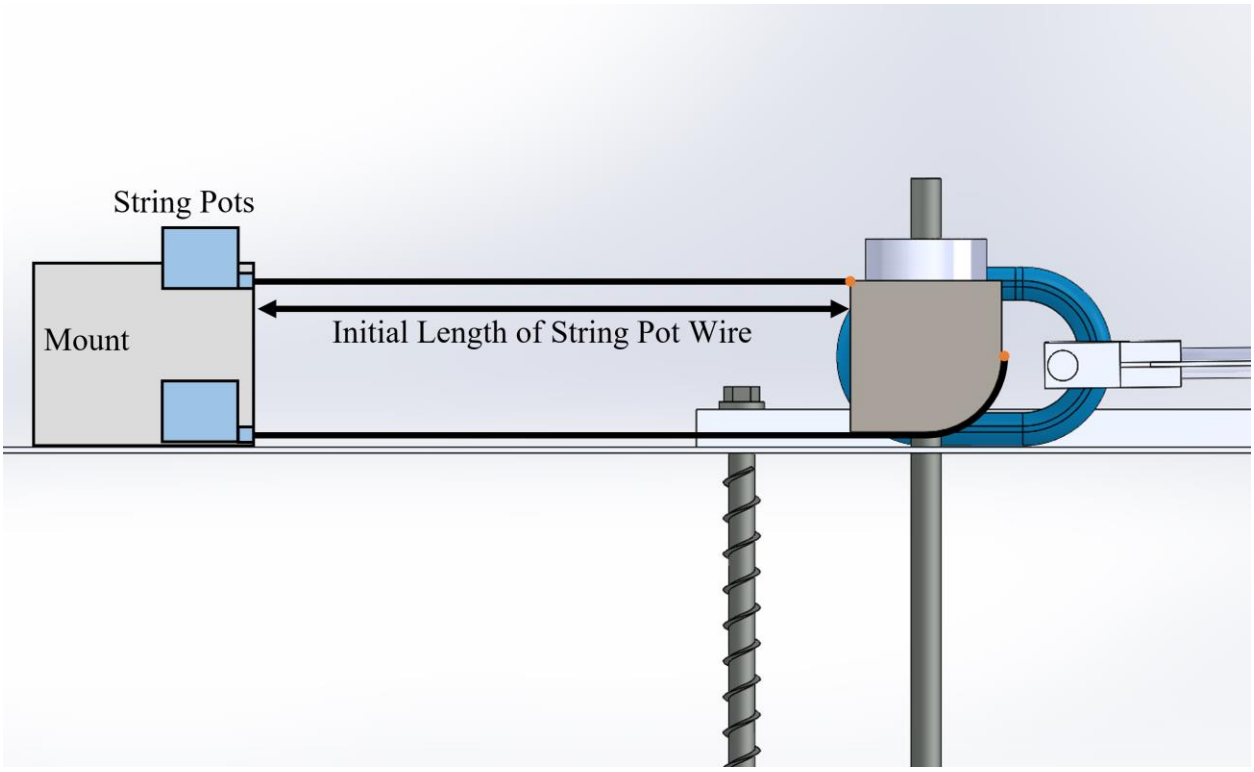

Figure F.14. Initial string pot position

22. Connect the hand pump to the hydraulic cylinder. Top up reservoir with hydraulic fluid.
23. Connect the pressure transducer to the hydraulic line. Make sure there is no pressure on the hydraulic line and that the pressure release valve is fully open.
24. Connect all instrumentation to the pc and open YieldPoint Pulltest software.
25. Ensure all instrumentation is operating correctly.
26. Retreat to a minimum distance of 10 m away. Ensure this point is to the side of the test setup.
27. Begin pumping hand pump to increase the load on the hydraulic cylinder. Continue increasing the load until the rebar fails.
28. After failure, release all pressure from the hydraulic line and make sure the hydraulic cylinder fully collapses. An extended cylinder could be indicative of residual pressure in the hydraulics.

Appendix G – Theoretical Derivation of Equations for Analyzing the Lateral Pull Test Data

The goal of the string potentiometers in the lateral pull testing were to record the displacement and rotation of the apparatus and rebar as the lateral load is applies. The string pot measurements and load are recorded continuously by YieldPoint pull testing software.

It was originally planned to use a tiltmeter with one string pot to record the rotation and displacement, respectively. However, YieldPoint's pull testing software is incompatible with their tiltmeters. Instead, two string pots are used and math is used to determine the displacement and rotation from the string pot data. The derivation of the mathematical relations are shown here.

The two string pots are glued to the apparatus at the top and bottom. Both strings run approximately horizontal and parallel. The initial distance between the apparatus and the string pots, Li, is measured manually. The figure shows the initial distance involved in the test.

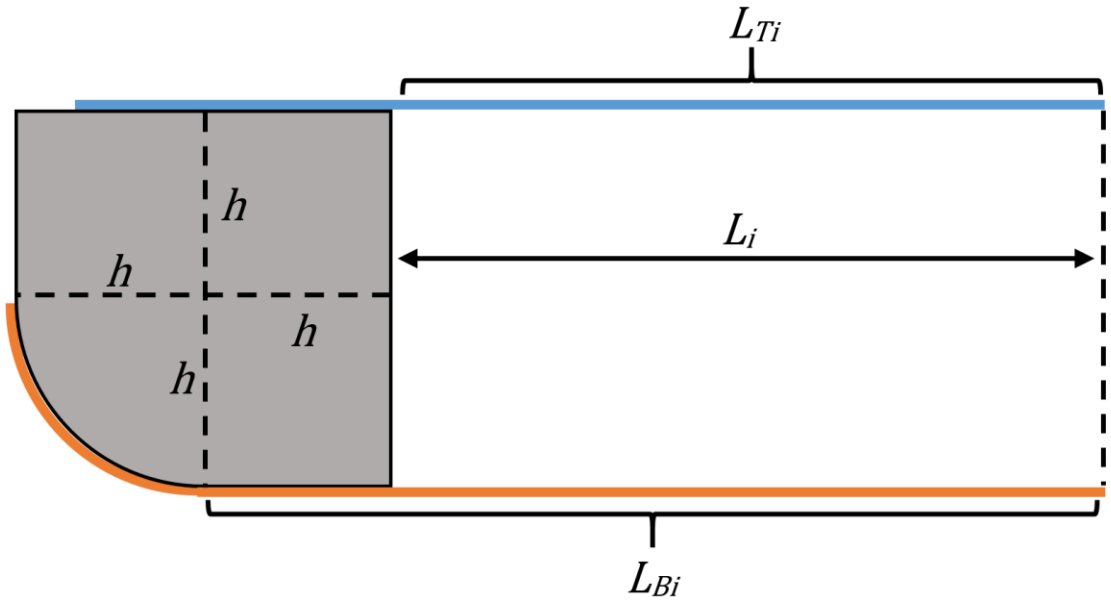

Figure G.1. Initial string-pot and LPT chassis geometry

From this figure, the following equations should be clear:

$$L_{Bi} = L_i + h \qquad \text{Equation G.1}$$

$$L_{Ti} = L_i \qquad \text{Equation G.2}$$

As testing progresses, the apparatus will exhibit a displacement, d, and a rotation, $\theta_{Rotation}$.

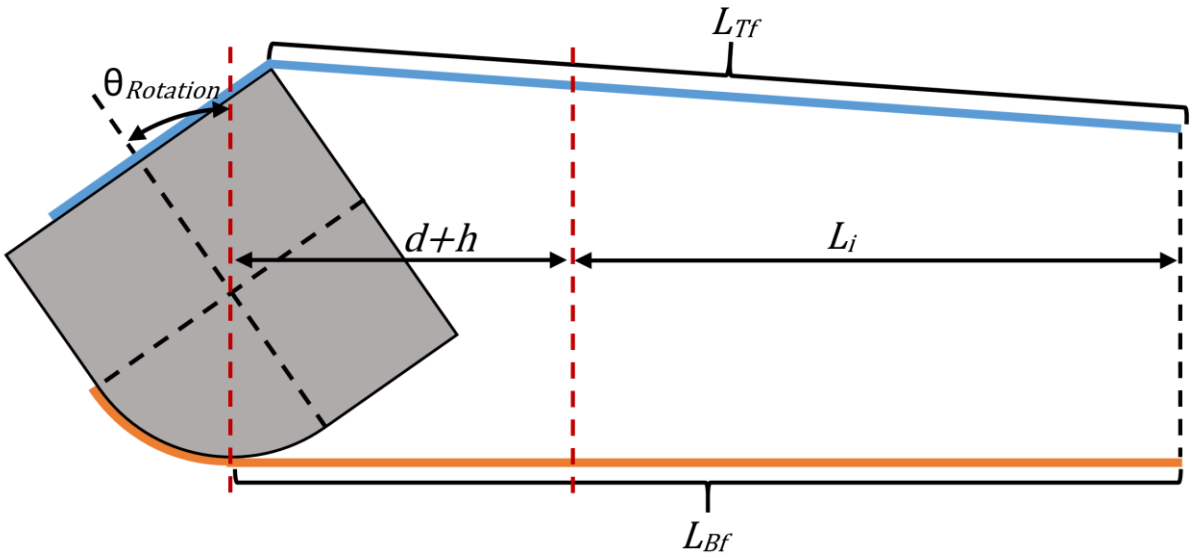

Figure 0.2. String-pot and LPT chassis geometry during test

The displacement of the apparatus can be defined by:

$$d = L_{Bf} - L_{Bi} \qquad \text{Equation G.3}$$

The final lengths of the top and bottom strings can be further broken down as in the following figure and equations.

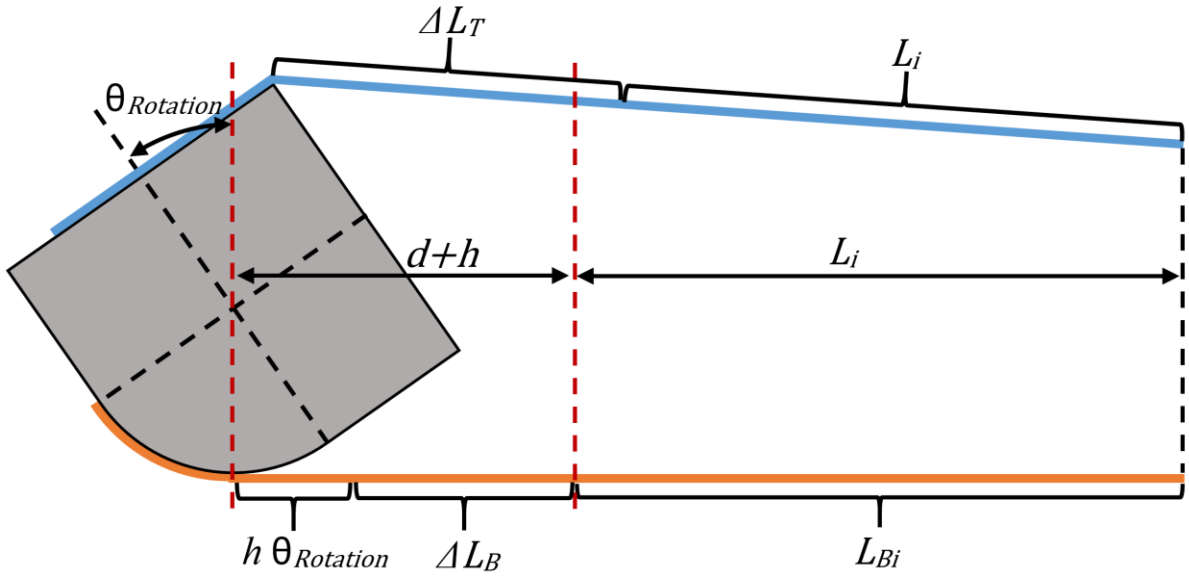

Figure 0.3. Breakdown of string-pot lengths after chassis rotation and displacement has occurred

$$L_{Bf} = L_{Bi} + (\theta_{Rotation} h) + \Delta L_B \quad \text{Equation G.4}$$

$$L_{Tf} = \Delta L_T + L_{Ti} \quad \text{Equation G.5}$$

Substitution lets us derive the following equation:

$$d = (L_{Bi} + (\theta_{Rotation} h) + \Delta L_B) - L_{Bi} \quad \text{Equation G.6}$$

$$d = (\theta_{Rotation} h) + \Delta L_B \quad \text{Equation G.7}$$

And rearrangement yields:

$$\theta_{Rotation} = \frac{d - \Delta L_B}{h} \quad \text{Equation G.8}$$

Further analysis of the top string requires a closer look at what happens as the apparatus rotates. As shown in the below figure, rotation results in a change in vertical position of the strings attachment point on the apparatus, Δy_T. Rotation also results in a change in horizontal position of the strings attachment point, Δx_{TR}.

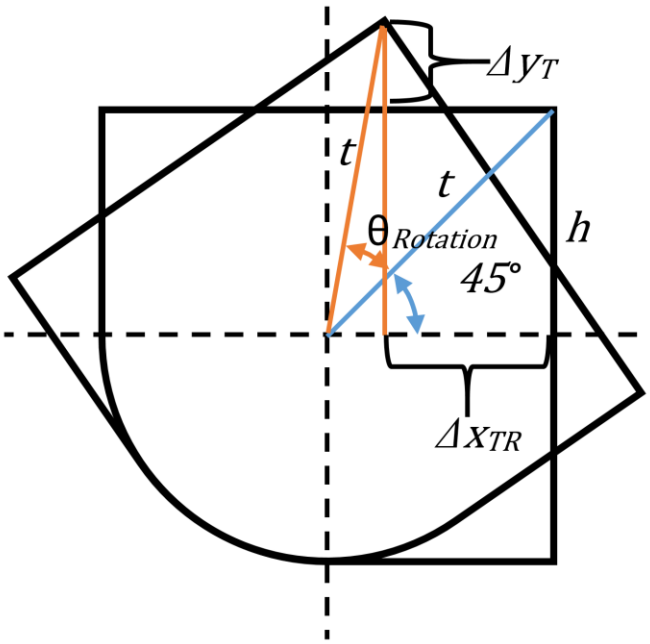

Figure G.4. Trigonometric relationships for chassis rotation

The above figure shows the constant, t, which can be calculated by:

$$t = \sqrt{h^2 + h^2} \quad \text{Equation G.9}$$

$$t = h\sqrt{2} \quad \text{Equation G.10}$$

The values Δy_T and Δx_{TR} can be calculated by:

$$\Delta y_T = t\cos(45° - \theta_{Rotation}) - h \quad \text{Equation G.11}$$

$$\Delta x_{TR} = h - t\cos(45° + \theta_{Rotation}) \quad \text{Equation G.12}$$

The attachment point will also change horizontal position due to the displacement of the apparatus. This component of the horizontal position change is called Δx_{Td} and is equal to the displacement of the apparatus:

$$\Delta x_{Td} = d \quad \text{Equation G.13}$$

The total horizontal position change of the string attachment point is then:

$$\Delta x_T = \Delta x_{TR} + \Delta x_{Td} \quad \text{Equation G.14}$$

The change in vertical position and horizontal position lead to geometry shown in the following figure:

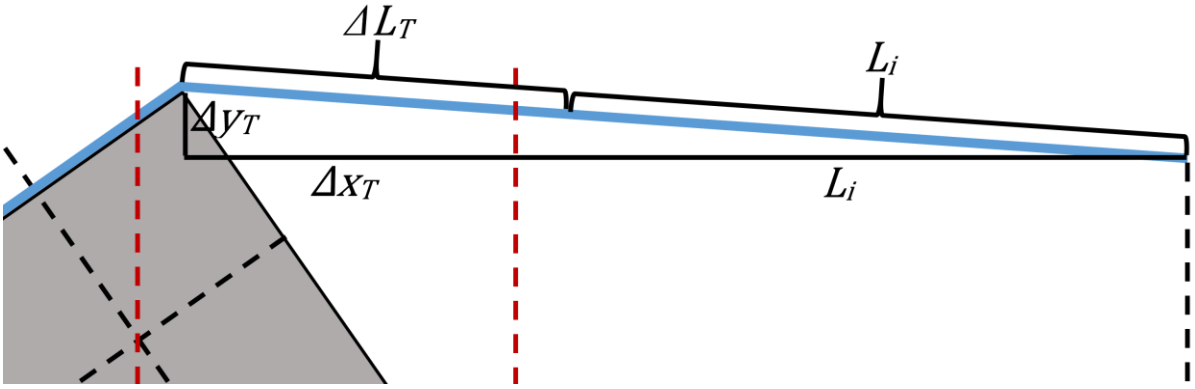

Figure G.5. Detailed breakdown of upper string-pot and the effect of chassis displacement and rotation on its length

The triangular geometry leads to the relationship:

$$(L_{Tf})^2 = (L_{Ti} + \Delta x_T)^2 + (\Delta y_T)^2 \quad \text{Equation G.15}$$

Substitution yields:

$$(L_{Ti} + \Delta L_T)^2 = (L_i + \Delta x_T)^2 + (\Delta y_T)^2$$

Equation G.16

$$(L_i + \Delta L_T)^2 = (L_i + \Delta x_{TRotation} + \Delta x_{Td})^2 + (t\cos(45° - \theta_{Rotation}) - h)^2$$

Equation G.17

$$(L_i + \Delta L_T)^2 = (L_i + h - t\cos(45° + \theta_{Rotation}) + d)^2 + (t\cos(45° - \theta_{Rotation}) - h)^2$$

Equation G.18

$$(L_i + \Delta L_T)^2 = \left(L_i + h - h\sqrt{2}\cos(45° + \theta_{Rotation}) + d\right)^2 + \left(h\sqrt{2}\cos(45° - \theta_{Rotation}) - h\right)^2$$

Equation G.19

Using trigonometric relationships we can expand some terms:

$$\left(L_i + h - h\sqrt{2}(\cos 45° \cos\theta_{Rotation} - \sin 45° \sin\theta_{Rotation}) + d\right)^2$$
$$= (L_i + \Delta L_T)^2 - \left(h\sqrt{2}(\sin 45° \sin\theta_{Rotation} + \cos 45° \cos\theta_{Rotation}) - h\right)^2$$

Equation G.20

We then isolate the displacement variable:

$$(L_i + h - h(\cos\theta_{Rotation} - \sin\theta_{Rotation}) + d)^2$$
$$= (L_i + \Delta L_T)^2 - (h(\sin\theta_{Rotation} + \cos\theta_{Rotation}) - h)^2$$

Equation G.21

$$d = +h(\cos\theta_{Rotation} - \sin\theta_{Rotation}) - L_i - h$$
$$+ \sqrt{(L_i + \Delta L_T)^2 - (h(\sin\theta_{Rotation} + \cos\theta_{Rotation}) - h)^2}$$

Equation G.22

We now have two independent equations with the displacement and rotation. Although the equations cannot be easily solved for the displacement and rotation terms, the displacement and rotation variables can be iteratively solved until the unique values for displacement and rotation are determined.

Appendix H – Rebar Geometries

The rebar tested in this project can be broadly divided into two types: Grade 400 (Grade 60) rebar and Grade 500 (Grade 75) dywidag threadbar. Although the two rebar types both have a solid cylindrical core, they both have different surface deformation patterns. The Grade 400 rebar has rib deformations and two diametrically opposed line deformations down the length, as seen in Figure G.1. The Grade 500 dywidag has rib deformations that create a rough thread. The dywidag also lacks the two line deformations down its length, as seen in Figure G.1.

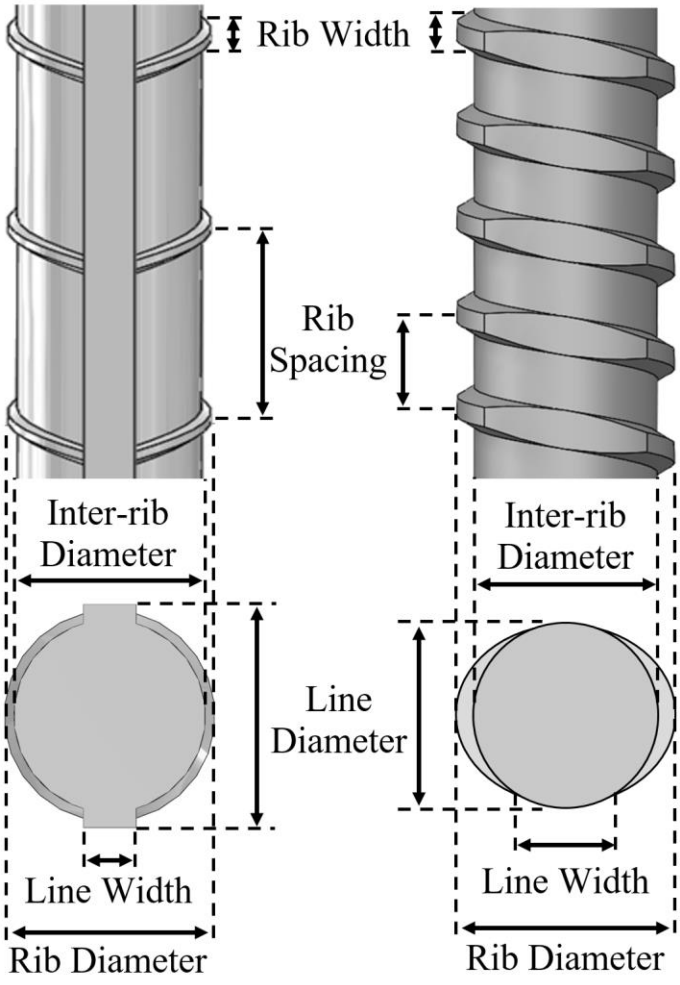

Figure H.1. General geometries of the Grade 400 rebar (left) and the Grade 500 dywidag threadbar (right)

The Grade 400 rebar tested were of two sizes: 22M (#7) and 25M (#8). Only size 22M (#7) of the dywidag threadbar was tested. The geometries of the rebar were quantified according to the six characteristics shown in Figure H.1. A total of nine measurements were made with calipers on three separate samples of each rebar type and size. The mean value of these measurements are shown in Table H.1.

Table H.1. Geometry of the three rebars tested – mean of nine measurements across three different samples

	Inter-rib Diameter (mm)	Line Diameter (mm)	Rib Diameter (mm)	Line Width (mm)	Rib Width (mm)	Rib Spacing (mm)
22M (#7) Grade 400 (Grade 60) Rebar	21.1*	24.5	23.5	5.9	3.6	12.7
25M (#8) Grade 400 (Grade 60) Rebar	23.1*	27.7	26.5	3.6	3.9	16.6
22M (#7) Grade 500 (Grade 75) Dywidag Threadbar	21.5	21.0*	24.4	7.7	4.4	10.7

*Minimum rebar diameter

The angle between Strand 1 and the neutral bending axis was calculated for every incremental distance along the rebar's length using **Error! Reference source not found.**. The results for test BB-8R-00-FO at 1995 N applied load are plotted in Figure I.1. Since the first fibre-optic strand was oriented nearly horizontal and the load was applied vertically downwards the angle between strand 1 and the centroidal axis is near to zero. The calculated angle becomes very scattered near the ends of the rebar because no bending occurs beyond the outer supports and instrumentation noise governs the resulting angle.

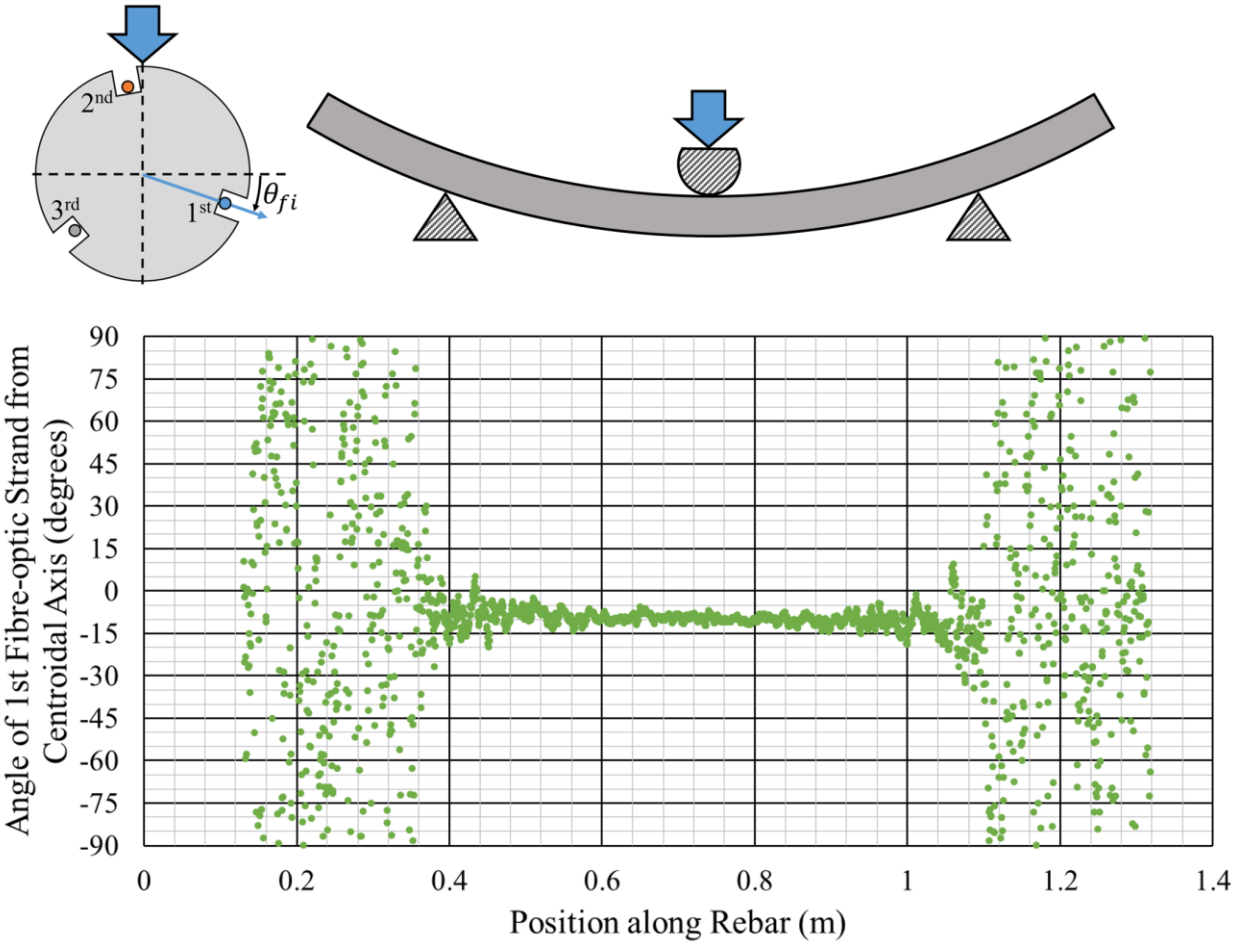

Figure I.1. Angle of bending of rebar calculated from fibre-optic instrumentation in beam bending test BB-8R-00-FO with 1995 N applied

Figure I.2 plots the load calculated from the fibre-optic instrumentation as a percent of the measured load for all beam bending tests on fibre-optic instrumented rebar. This figure depicts the under-estimation of the calculated load from the fibre-optics very well.

Figure I.3 plots the deflection calculated from the fibre-optic instrumentation as a percent of the measured load for all beam bending tests on fibre-optic instrument rebar. This figure also shows the under-estimation of calculated deflection, but shows the calculated deflection converges on the measured deflection as the amount of bending increases.

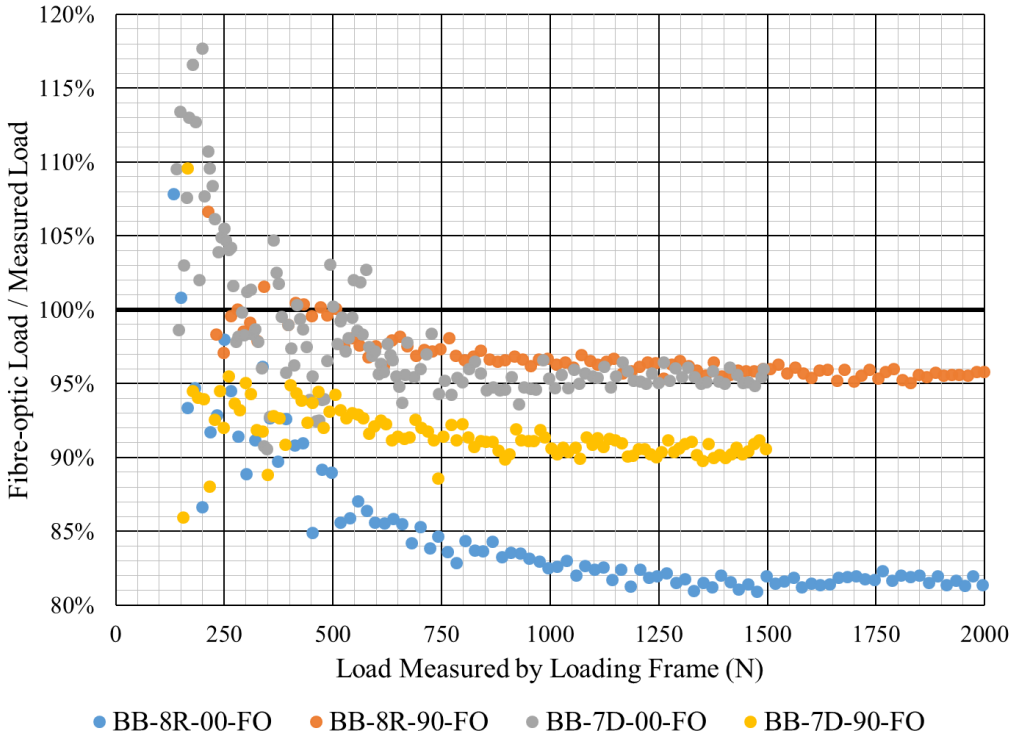

Figure I.2. Ratio of load calculated from fibre-optic to load measured by loading frame

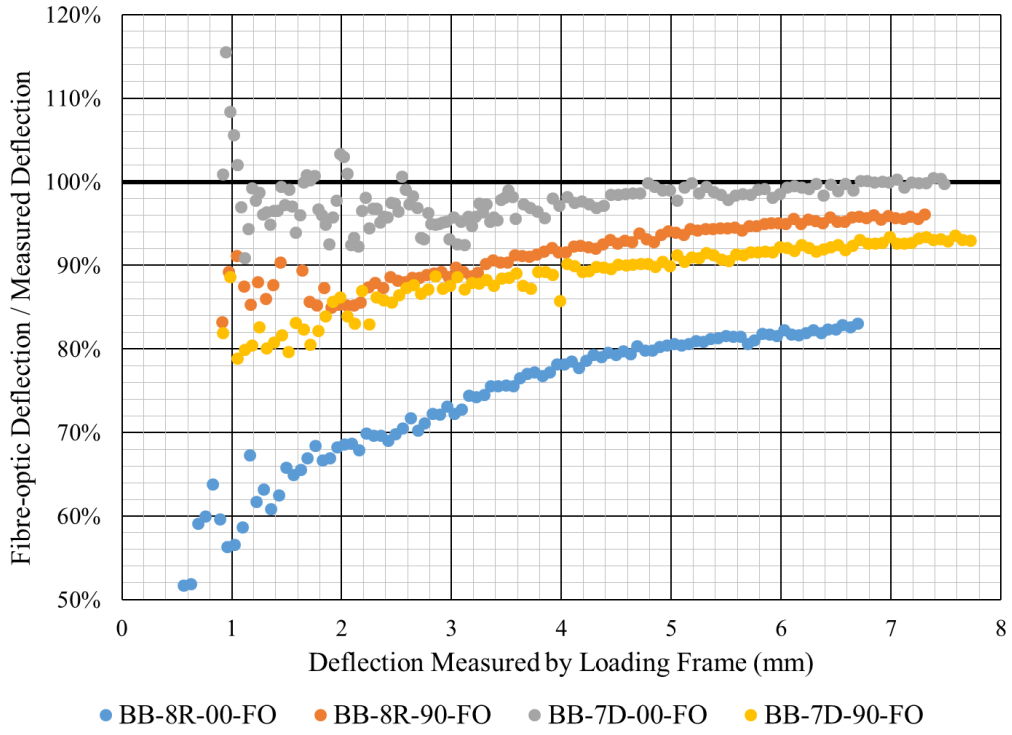

Figure I.3. Ratio of fibre-optic calculated deflection to deflection measured by loading frame

Appendix J – Additional Data, Plots, and Discussion of Double Shear Test Results

The direction of bending can be calculated from the strain readings of the three "strands" or "wraps". The angle of the first strand from the centroidal axis, θ_{fi} (measured counter-clockwise), was calculated. Generally, this angle remains similar along the rebar length for all instrumented double shear tests since all bending occurs in the same plane.

The angle of the first strand is plotted in Figure J.1**Error! Reference source not found.** for test DS-8R-320-FO with 148 kN applied. The angle of the first fibre-optic strand from the centroidal axis ranges from -15 degrees to +5 degrees. The sample was tested with the first fibre-optic strand oriented approximately horizontal relative to the rebars centroid and the load was applied downward. The calculated angle of the first fibre-optic strand is, therefore, in close agreement with the qualitative observations made during the test. Note that the scatter in data at either end of the rebar length is simply because there is no prominent bending and noise in the strain readings dominates the resulting angle.

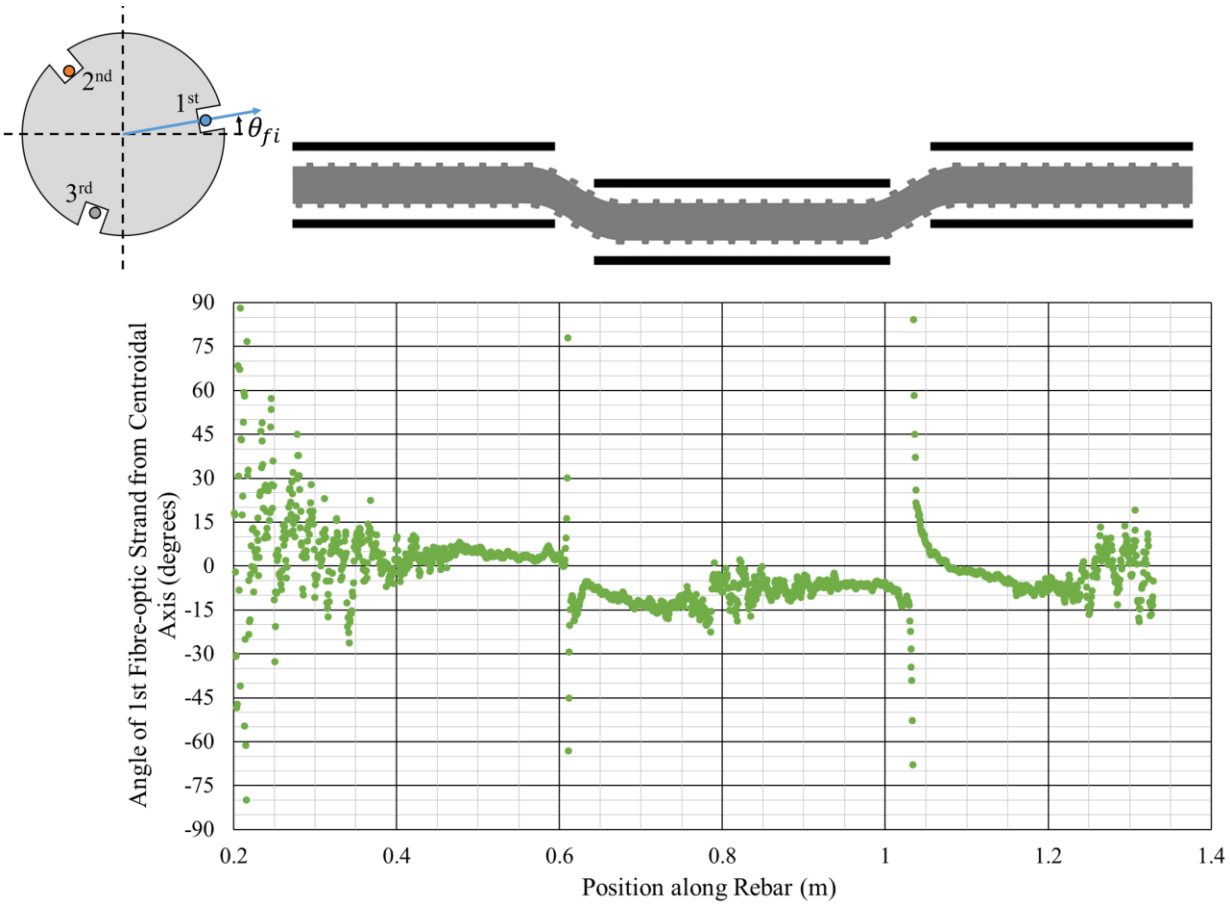

Figure J.1. Angle between first fibre-optic strand and the neutral bending axis for double shear test DS-8R-320-FO at 330 seconds with 148 kN total applied load

Using the strain readings from the fibre-optic instrumentation, the direction of the bending, the diameter of the rebar, and assuming the fibre-optic strand are 120 degrees apart and embedded 3 mm into the surface of the rebar, the strain at the extreme edges and the centroidal axis of the rebar can be calculated. The results of this calculation are displayed in Figure J.2 for double shear test DS-8R-320-FO.

The strains shown in Figure J.2 still exhibit the same shear planes and sample behaviour that was identified previously. This figure also shows that the rebar is actually starting to exhibit yielding at the extreme edges of the rebar. Tensile testing, included in Appendix B, showed 25M Grade

400 rebar begins to yield at approximately 2,000 micro-strain. The strain at the extreme edges of this sample has just begun to surpass this strain threshold.

A total applied load of 148 kN or 74 kN per shear plane was measured when the strains shown in Figure J.2 were measured. This is slightly lower than the yield point of 88 kN that was identified for this test from Figure 3.16. The fibre-optic strain readings and the calculations made with them suggest the apparent yield points identified for the load-displacement plots are actually where the substantial yield has begun to occur in the rebar steel. The same finding can be made from the other double shear tests on instrumented rebar.

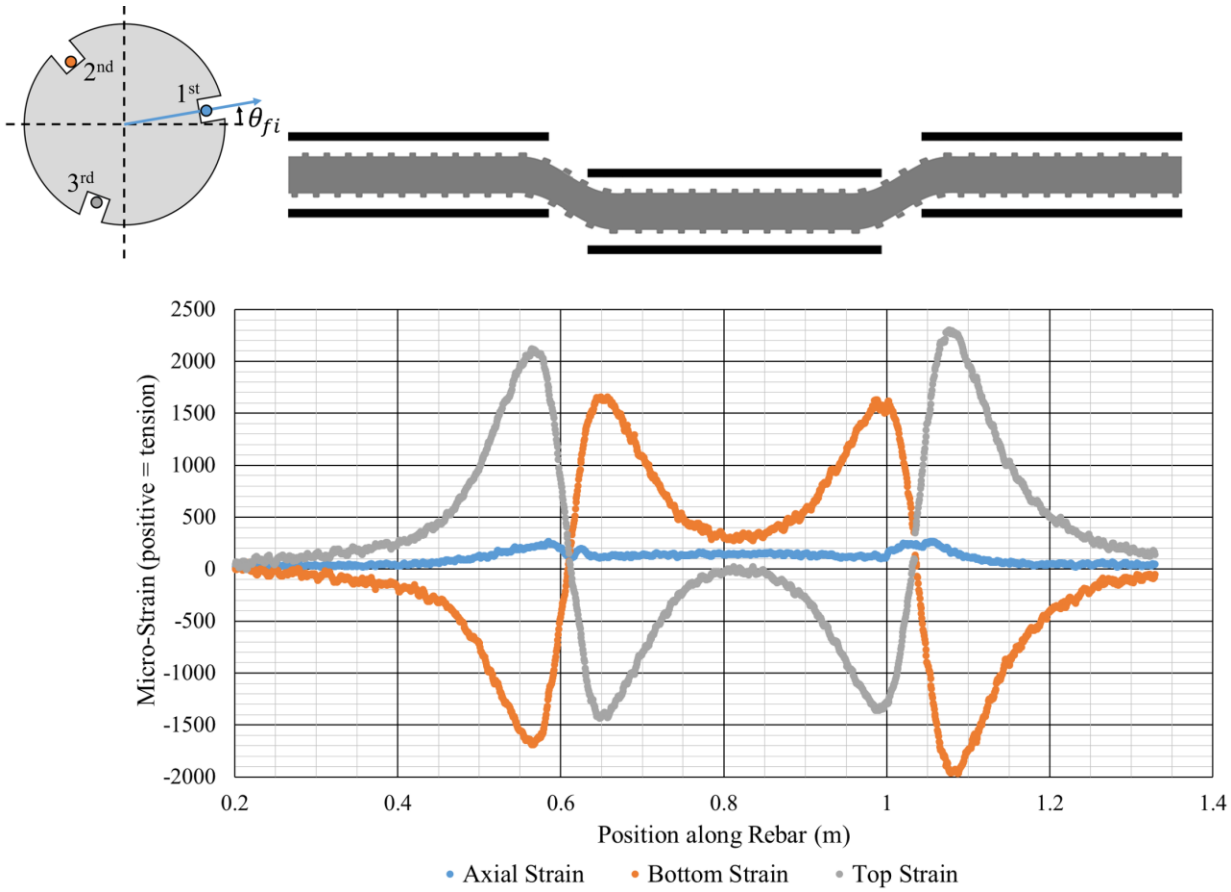

Figure J.2. Strain calculated from fibre-optic instrumentation for double shear test DS-8R-320-FO at 330 seconds with 148 kN total applied load

This analysis on DS-8R-320-FO provides the ideal case of analyzing the fibre-optic instrumented rebar tested in the double shear setup. However, tests DS-8R-305-FO, DS-7D-105-FO, and DS-7D-120-FO all showed an anomalous strain distribution throughout the tests. There is an unexpected “jump” in strain near the shear planes.

An example of the “jump” in strain values can be seen in **Error! Reference source not found.** which plots the strain readings (top) and resulting bending moment diagram (bottom) for double shear test DS-7D-105-FO at 100 seconds. The test sample had 75 kN total applied load and 1.4 mm displacement. The reason for these jumps in strain readings are not clear but could be an indication of an issue with the test setup or fibre-optic instrumentation.

The shear loads were still calculated for the tests exhibiting this erroneous behaviour despite the “jumps” in the bending moment diagrams. The linear trendline was simply fitted to avoid the “jump”, as seen in Figure J.3 (bottom).

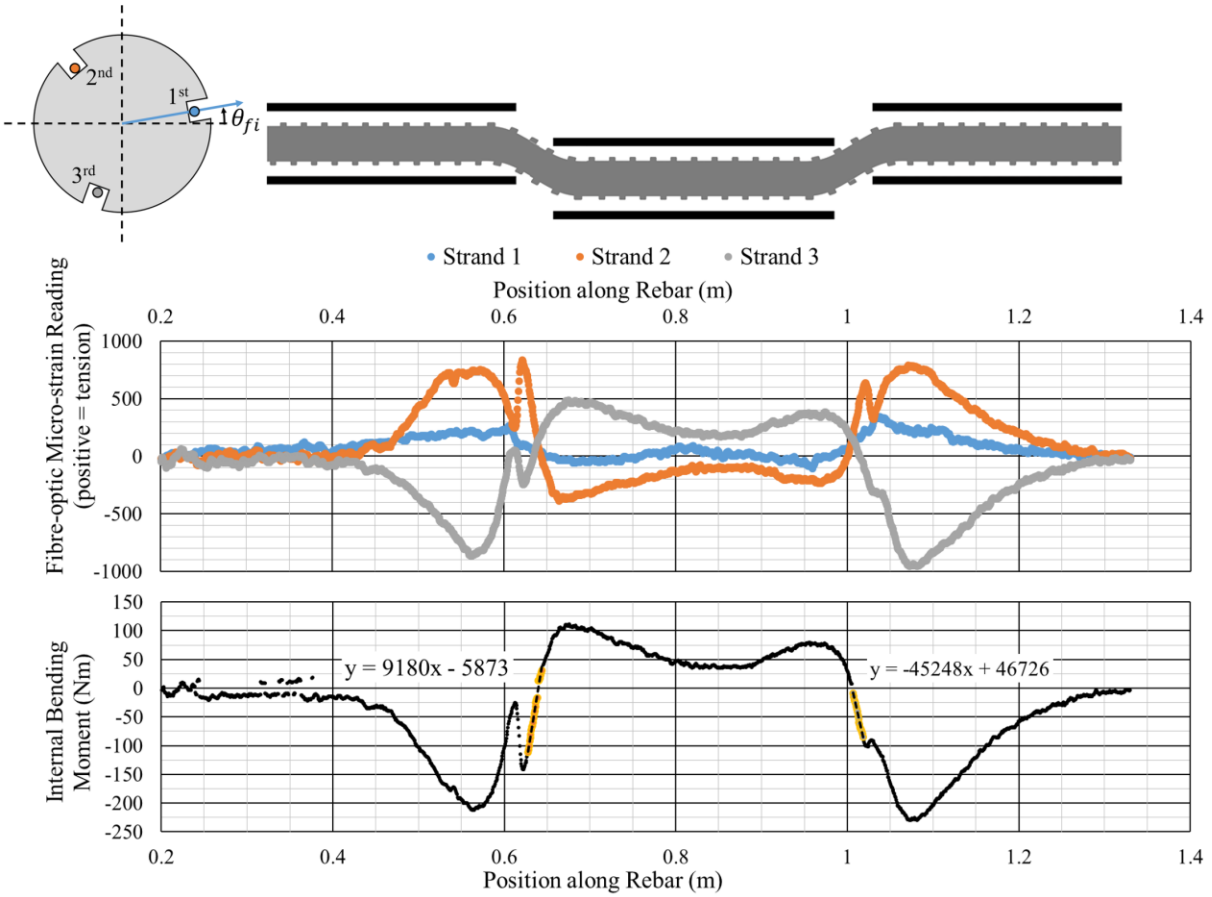

Figure J.3. Fibre-optic strain readings (top) and resulting bending moment diagram (bottom) for double shear test DS-7D-105-FO at 100 seconds with 75 kN total applied load

Figure J.4 shows the position of the rebars centroidal axis as calculated from the fibre-optic strain readings for double shear test DS-8R-320-FO with 148 kN total load applied. An unexpected observation made from this figure is the downward slope of the outer sections of the rebar relative to the centre segment. One should also note that there is significant vertical exaggeration in this plot so the downward deflection of the outer segments is not nearly as pronounced. Regardless, this could be a result of the clamping system applied to the outer pipe segments which, there same mechanism causing the increased bending moments observable at the start of the tests.

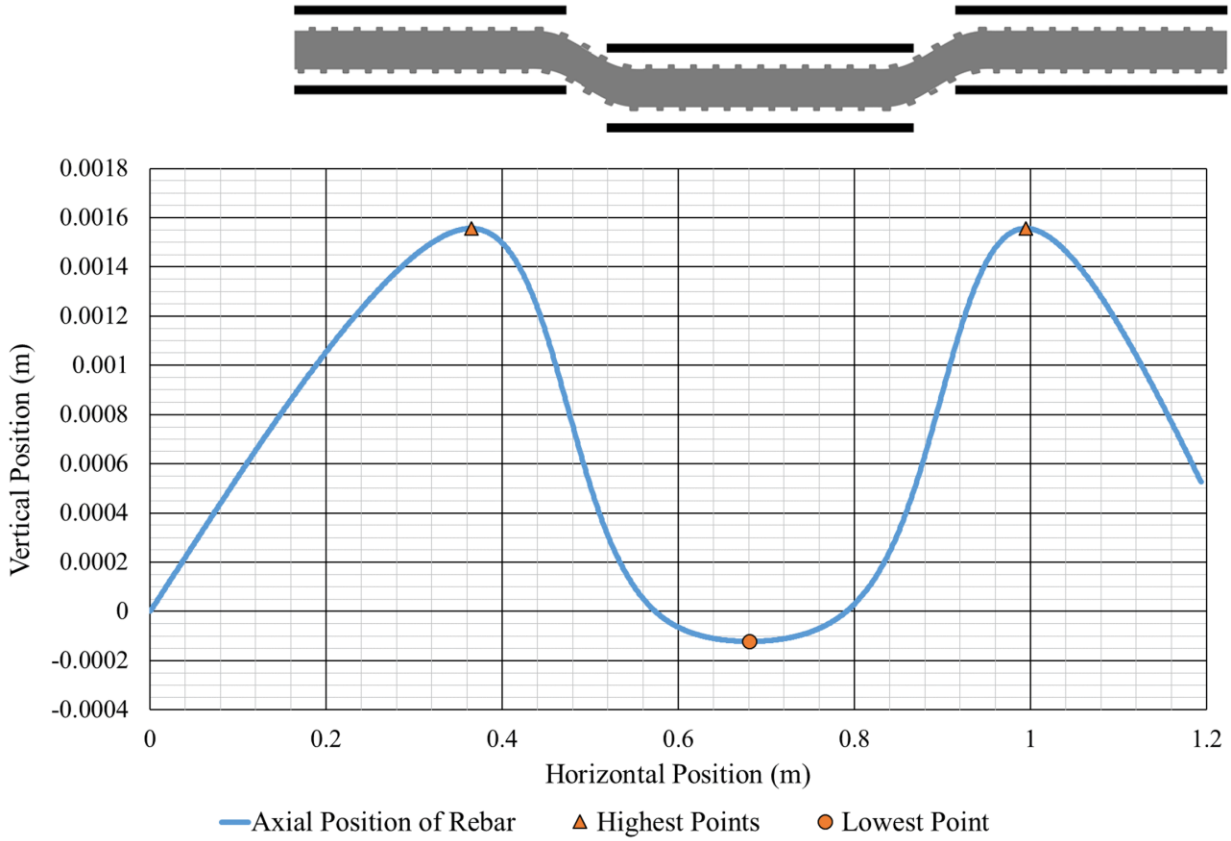

Figure J.4. Axial position of rebar calculated from fibre-optic instrumentation for double shear test DS-8R-320-FO at 330 seconds with 148 kN total applied load

Appendix K – Additional Data, Plots, and Discussion of Lateral Pull Tests

A series of plots are included in this section that present additional data not included in the main body of this report. These plots show the load-rotation and rotation-displacement relationships of the LPT tests on various rebar samples.

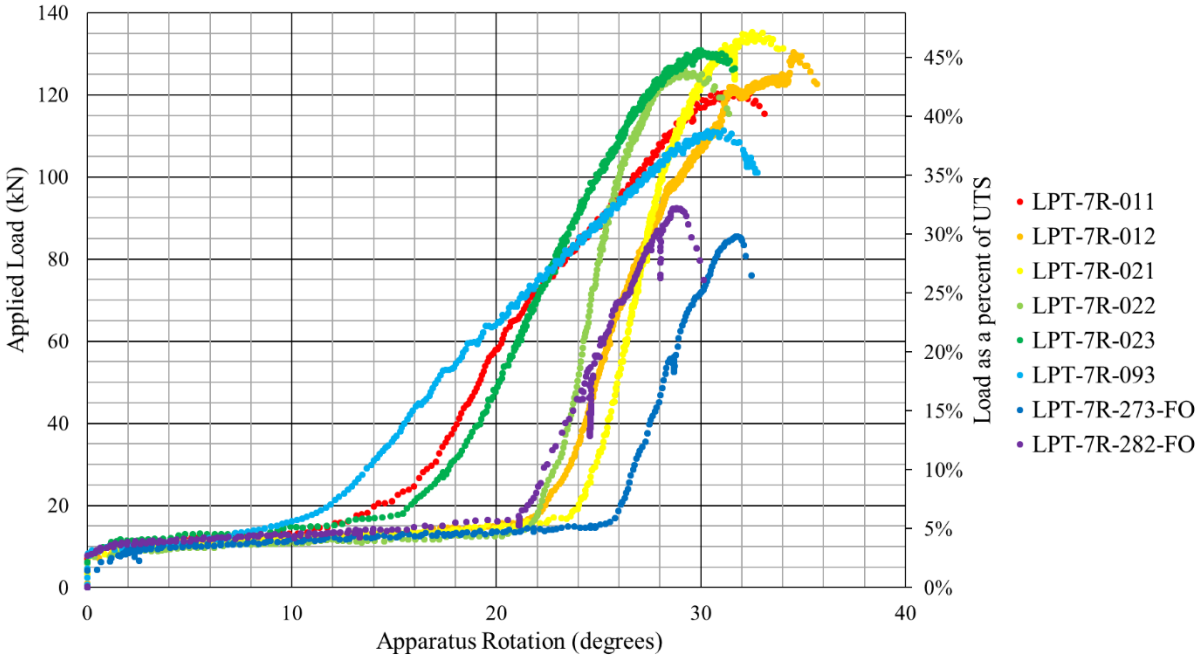

Figure K.1. Applied load vs rotation for lateral pull tests on 22M (#7) Grade 400 rebar

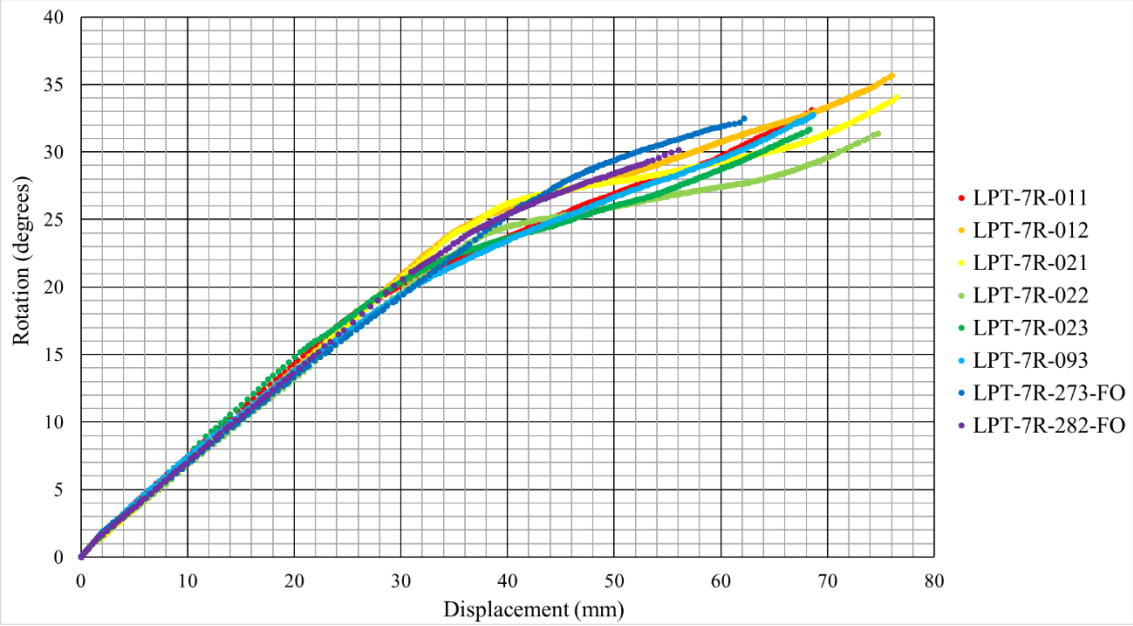

Figure K.2. Rebar Rotation vs displacement for lateral pull tests on 22M (#7) Grade 400 rebar

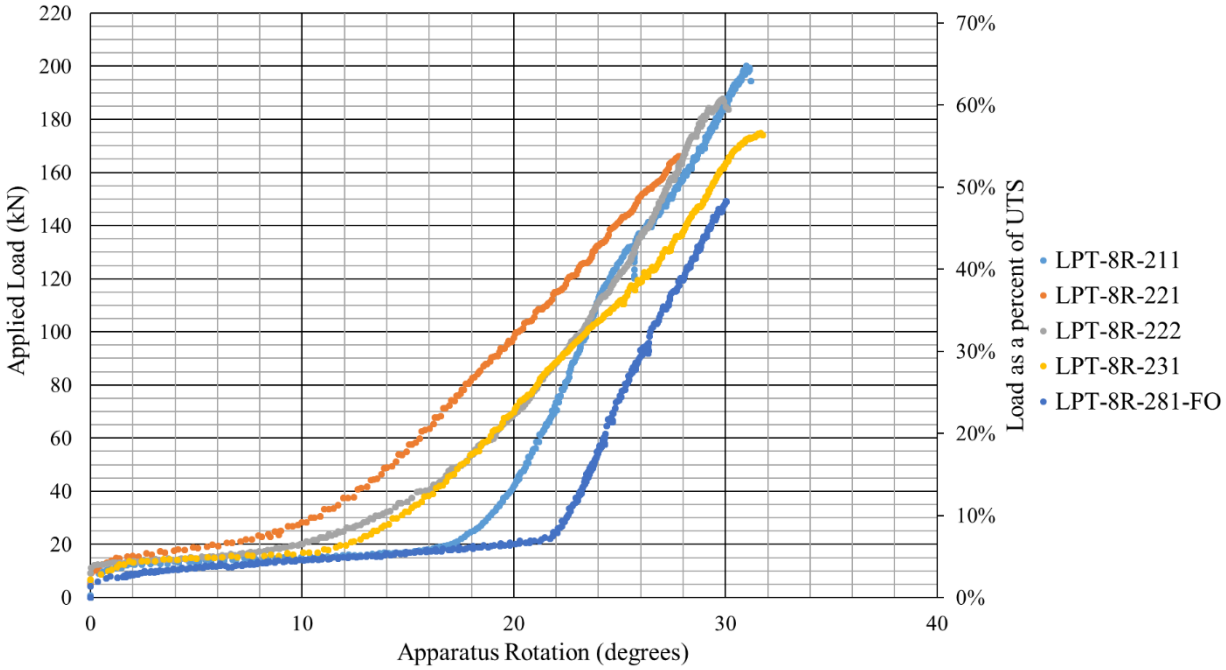

Figure K.3. Applied load vs rotation for lateral pull tests on 25M (#8) Grade 400 rebar

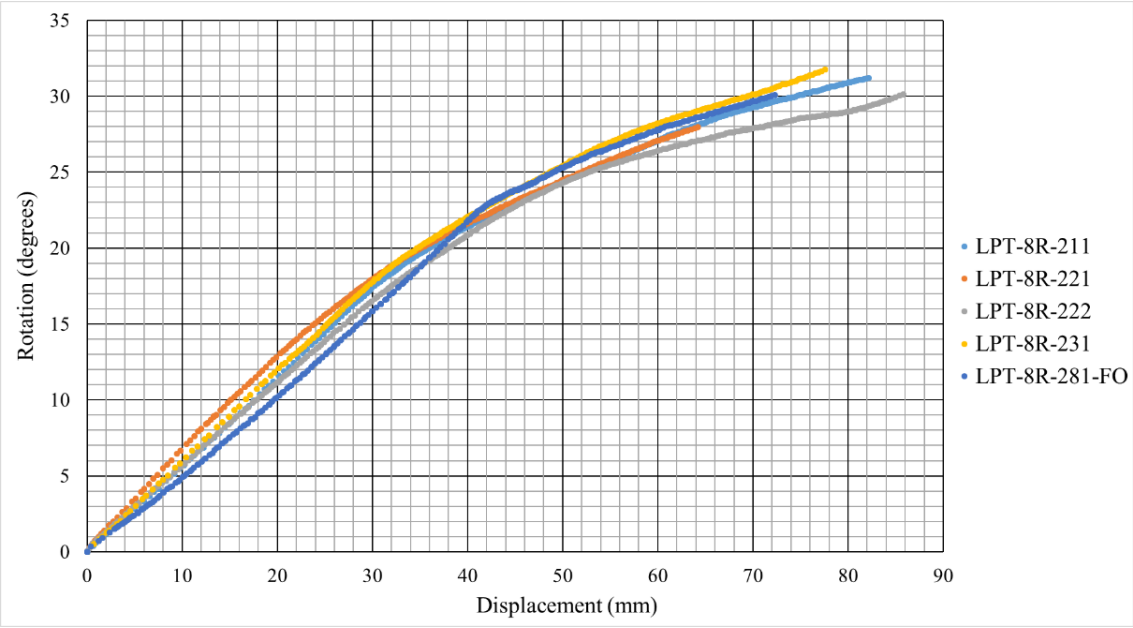

Figure K.4. Rebar Rotation vs displacement for lateral pull tests on 25M (#8) Grade 400 rebar

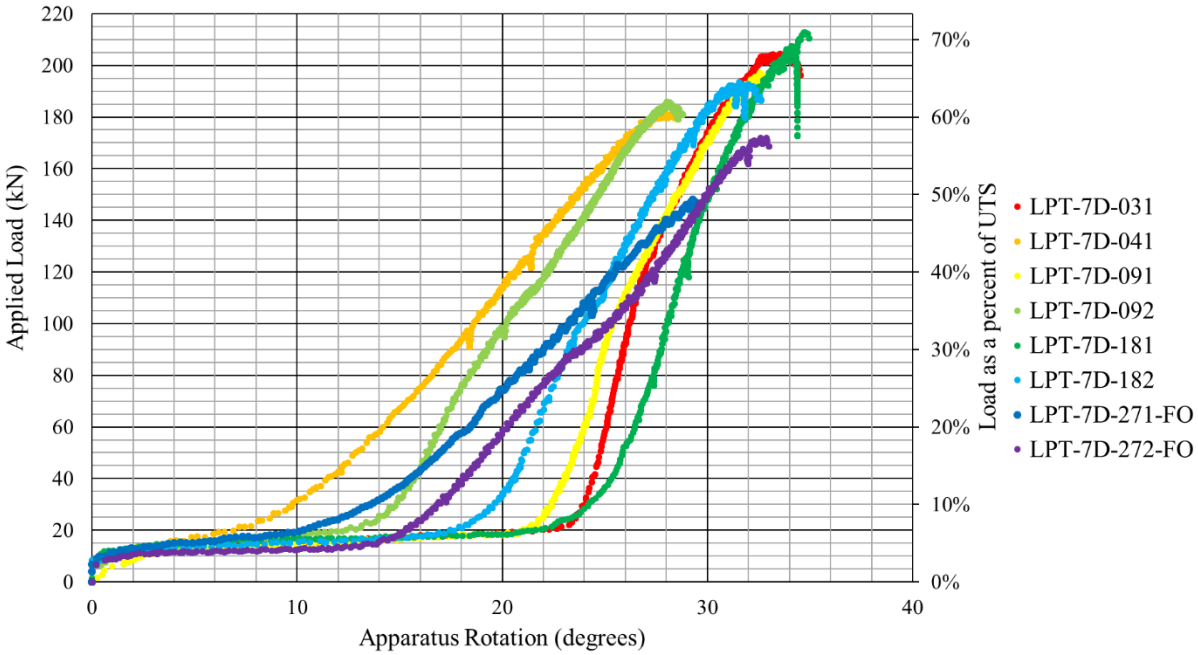

Figure K.5. Applied Load vs rotation for lateral pull tests on 22M (#7) Grade 500 dywidag

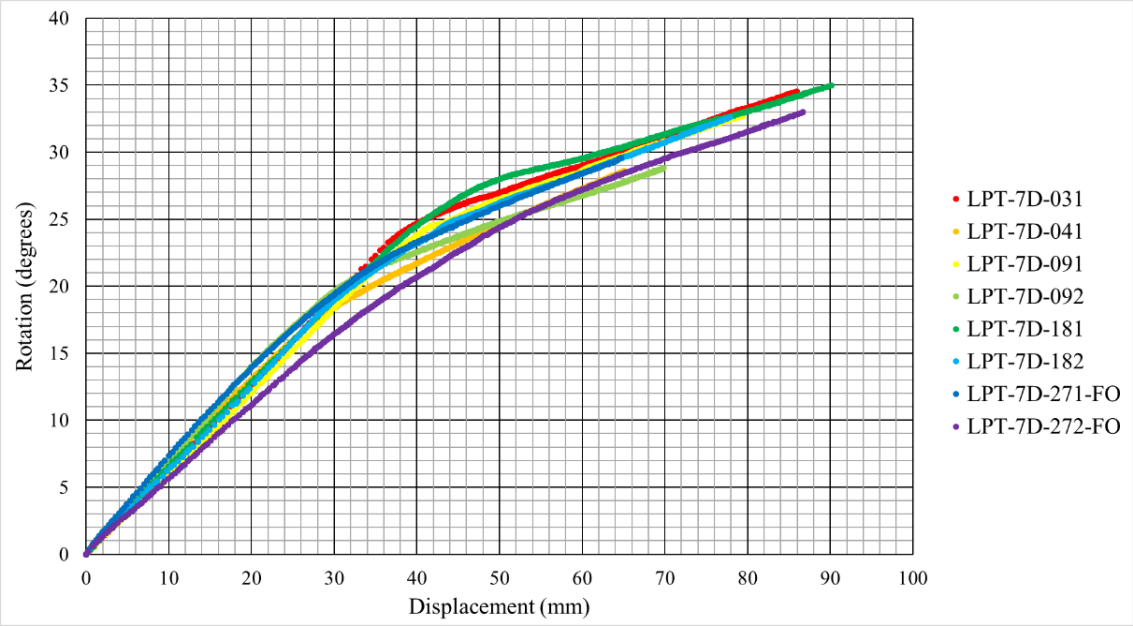

Figure K.6. Rebar Rotation vs displacement for lateral pull tests on 22M (#7) Grade 500 dywidag

The position plots for five readings from test LPT-7D-271-FO are shown in Figure K.7. The axial position of the rebar was calculated using the fibre-optic strain readings from the rebar. The equations for these calculations are derived in Appendix E.

These position plots help demonstrate the increasing bending of the rebar with increasing lateral loads. The deformation is isolated to one plane and is also fairly localised to the length of rebar in the upper several centimeters of its embedment.

Figure K.7 demonstrates initial strain and bending in the rebar before any load has been applied by the hydraulic cylinder. This is an important factor to note since it suggests the measured displacement of the rebar, which is relative to the initial position of the apparatus, is not an accurate measure of the true displacement.

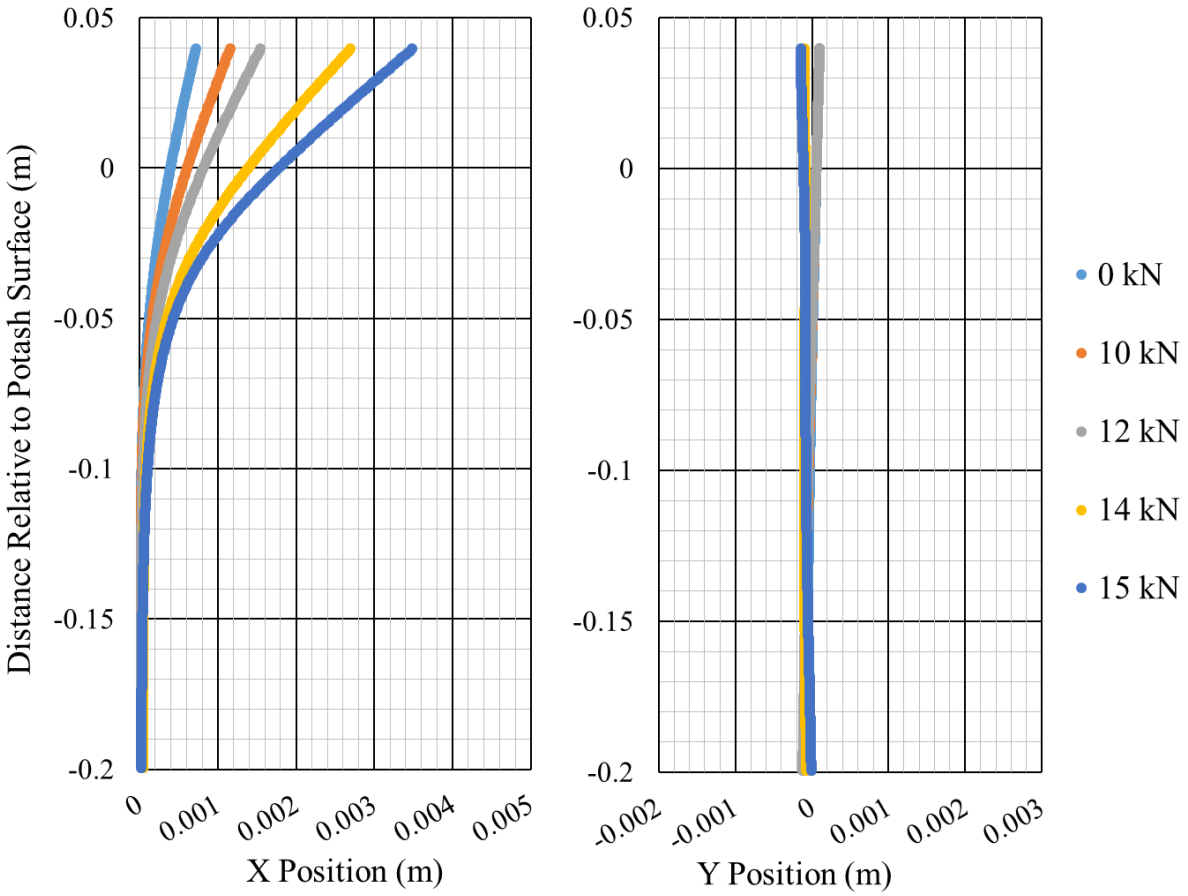

Figure K.7. Axial position plot calculated from fibre-optic instrumentation for various loads in test LPT-7D-271-FO

Appendix L – Additional Data, Plots, and Discussion of In Situ Instrumentation

The internal bending moments were calculated from the strain distribution at each point along the rebar. The internal bending moments for the 25M (#8) Grade 400 (60) rebar were calculated and are displayed in Figure L.1. As expected, the bending moment magnitudes are increased and opposite on each side of the shear planes. Due to the relatively close spacing of the shear planes, the bending moment is not able to return to zero for any significant length between the shear planes. This suggests the two shear planes are interfering with one another and could alter the behaviour of the rebar.

One may also notice that the slope of the internal bending moment becomes zero in the upper shear plane at 222 days. This is a result of the rebar being fully yielded in the shear plane. Due to the highly plastic behaviour of steel after yielding, very little bending moment can be supported by the rebar.

The axial force was calculated in Figure L.2. Similar to what was seen from the axial strain, there is no significant axial force within the rebar between the collar of the hole and the lower shear plane. There is however a substantial increase in axial force at the upper shear plane near 1.65 m. This axial force is large enough to fully yield the rebar in tension.

The relatively constant axial force, especially in early readings, above the upper shear plane between 1.65 m and 2 m could suggest the rebar has a poor bond strength in this area. As a result, the rebar is not able to dissipate this axial force into the surrounding rock. The axial force does eventually decrease near the toe of the hole so the rebar will be assumed to be performing adequately in this upper region.

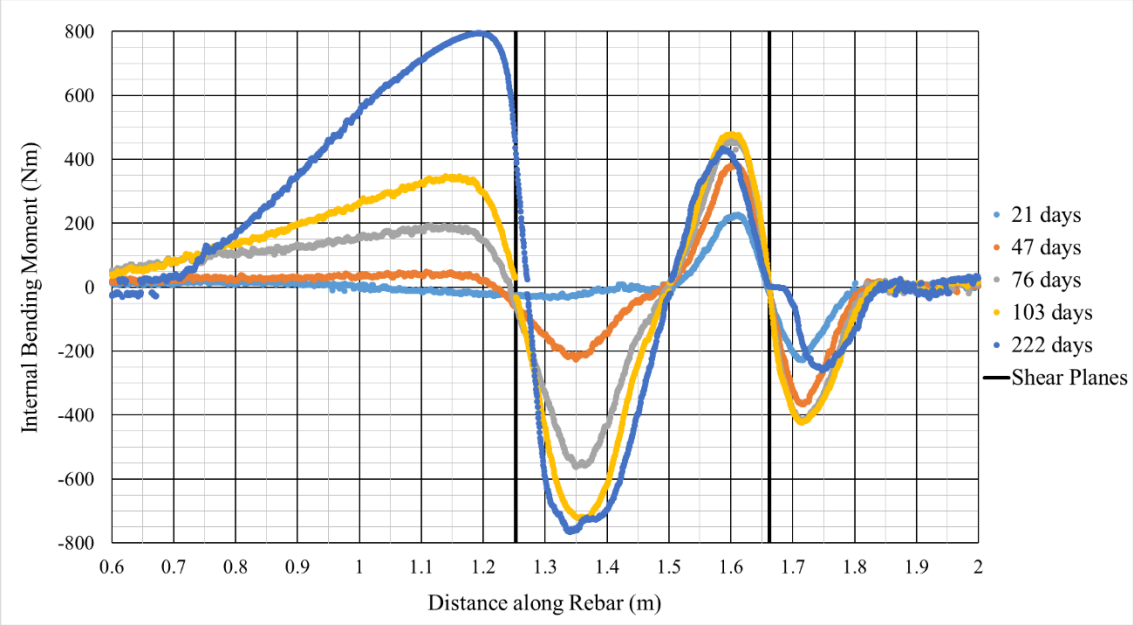

Figure L.1. Rebar Internal bending moment calculated from fibre-optic instrumentation in 25M Grade 400 rebar at Mosaic Colonsay

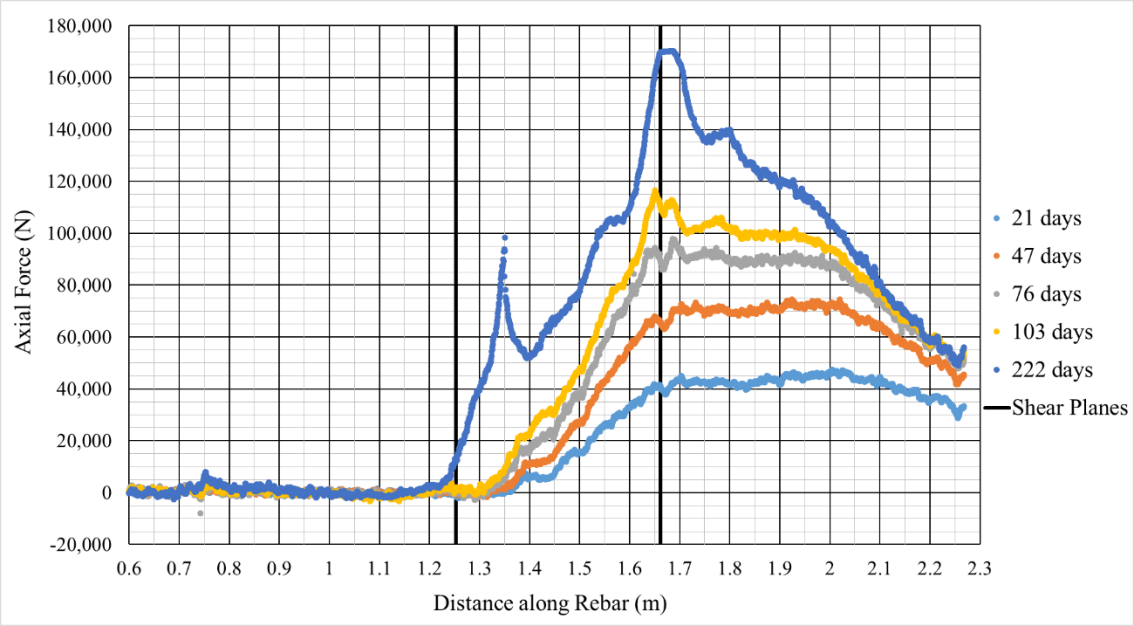

Figure L.2. Rebar Axial force calculated from fibre-optic instrumentation in 25M Grade 400 rebar at Mosaic Colonsay

Figure L.3 shows the internal bending moments calculated from the fibre-optic readings for the 22M (#7) Grade 500 (75) dywidag. The bending moments are large and opposite on either side of the shear planes. The maximum magnitudes of bending moments do not increase substantially as time goes on. This apparent approach to a limit can be attributed to a plastic hinge beginning to form within the dywidag.

Once again, the internal bending moment is not reduced to zero for a substantial length between the two shear planes. The close vicinity of the shear planes means the dywidag behaviour at each shear plane is partially influenced by the other shear plane. Also, the internal bending moment "plateaus" at each shear plane, as seen before. This anomaly can, again, be attributed to the full tensile yield of the dywidag at the shear planes. This yielding prevents the dywidag from supporting any substantial internal bending moments.

The calculated axial force for the 22M (#7) dywidag is shown in Figure L.4. The axial force is substantially increased in the vicinity of each shear plane. As time progressed and further shear occurred, the axial force extends further from the shear planes. After 222 days, the axial force appears to have fully yielded the dywidag in tension.

The axial force decreases significantly near the collar and toe of the hole. However, the axial force remains quite high between the two shear planes and above the upper shear plane; 1.3 m to 2 m. The high axial force, especially at later readings, could suggest damage to the resin/bond due to high axial displacements or poor bond strength to begin with.

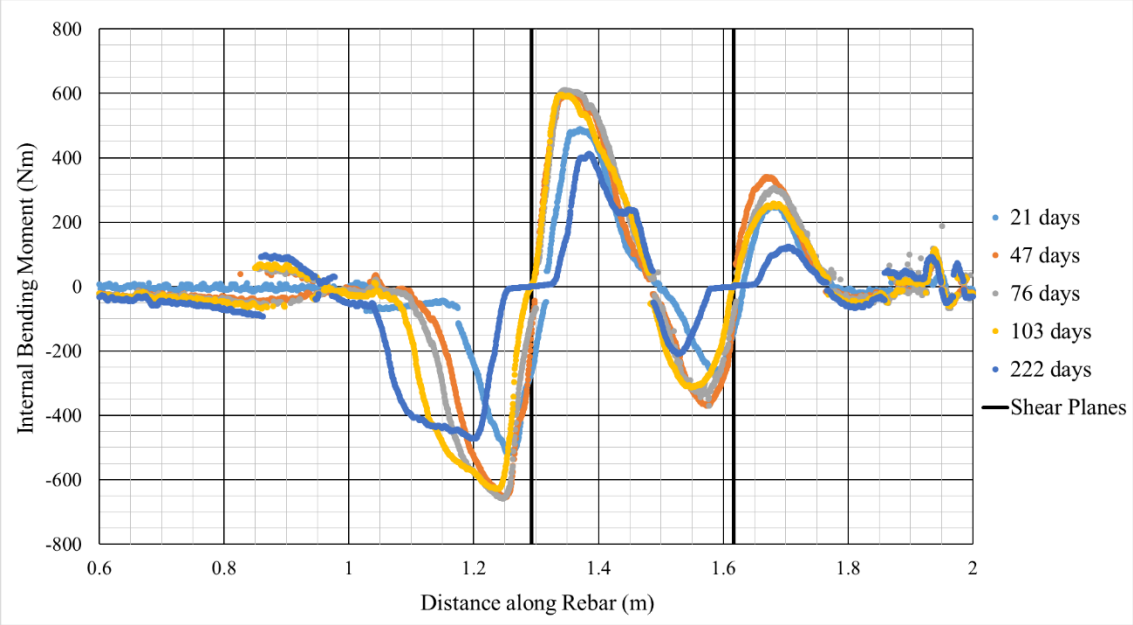

Figure L.3. Rebar Internal bending moment calculated from fibre-optic instrumentation in 22M Grade 500 dywidag at Mosaic Colonsay

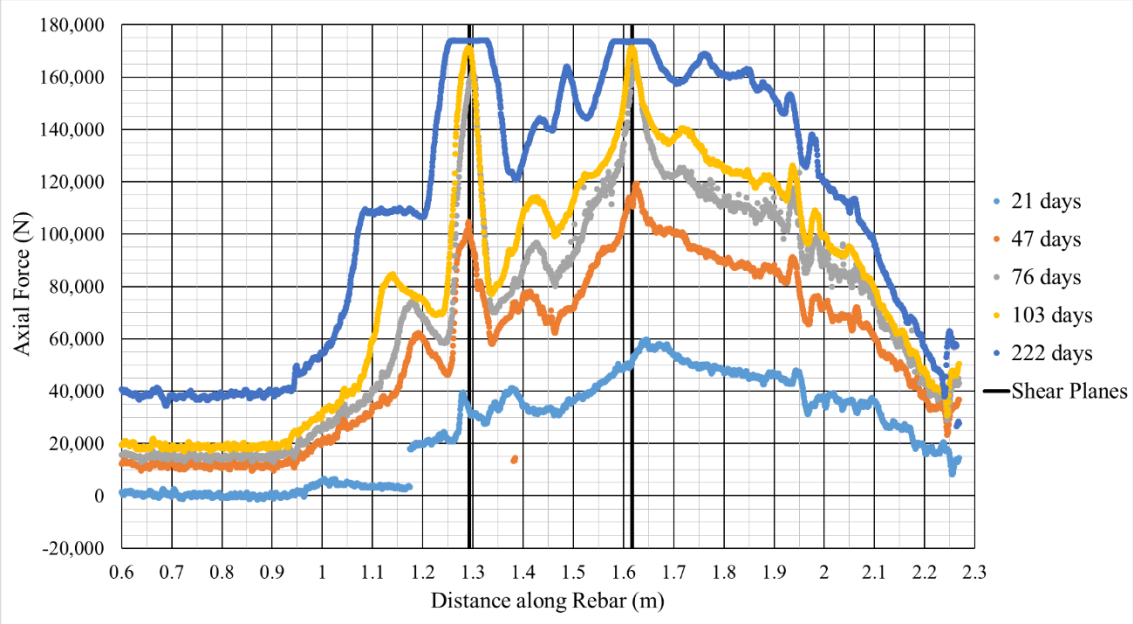

Figure L.4. Rebar Axial force calculated from fibre-optic instrumentation in 22M Grade 500 dywidag at Mosaic Colonsay

The shear force in each shear plane was calculated by fitting a linear trendline to the slope of the internal bending moment diagrams at each shear plane. The slopes of these trendlines were taken to equal the shear force within the rebars. The axial forces were taken as an average in the small area of the shear planes for the axial forces presented previously.

Figure L.5 presents the calculated shear forces and axial forces for the 25M (#8) rebar plotted against the time of the readings since the installation of the rebar. As was seen previously, the axial force at the lower shear plane remains very low due to poor bond at the lower portion of the rebar. The axial force at the upper shear plane increases substantially as time, and shear displacement, progresses. The shear forces for both shear planes trends upwards with time, with the exception of the final reading on the upper shear plane.

The shear forces and axial forces for the 22M (#7) dywidag are presented in Figure L.6 plotted against the time since it was installed. Similar to the 25M (#8) rebar, the axial forces increases over time. The shear force increases dramatically initially, but appears to reduce to some residual value after a set amount of time. This reduction in shear force is likely due to yield of the dywidag and the development of plastic hinges.

The lateral pressure that the resin and potash applied to the instrumented rebar was calculated by fitting a parabolic trendline to the bending moments on either side of each shear plane. The lateral pressure was determined for each rebar type, at every reading time. Figure L.7 shows the lateral pressures determined for the 25M (#8) Grade 400 (60) rebar at Mosaic Colonsay. Figure L.8 shows the lateral pressures determined for the 22M (#7) Grade 500 (75) dywidag.

There are no clear trends present in Figure L.7 or Figure L.8**Error! Reference source not found.**. The objective of these plots was to determine a single value of lateral pressure representative of the resin and potash strength, or to identify a decreasing trend that could be indicative of the visco-plastic behaviour of potash. Neither of these characteristics are easily identifiable from the figures. This could be a limit to the fibre-optic instrumentation, or simply due to the natural variability and uncontrolled parameters involved with in situ testing.

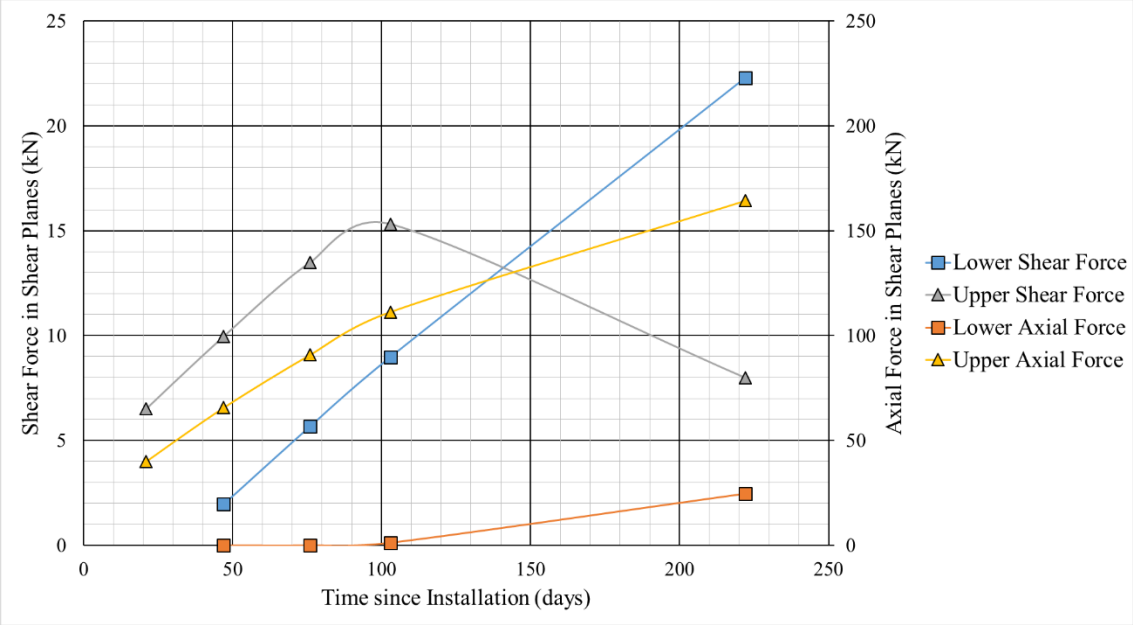

Figure L.5. Rebar Axial and shear forces near lower and upper shear planes calculated from fibre-optic instrumentation in 25M Grade 400 rebar at Mosaic Colonsay

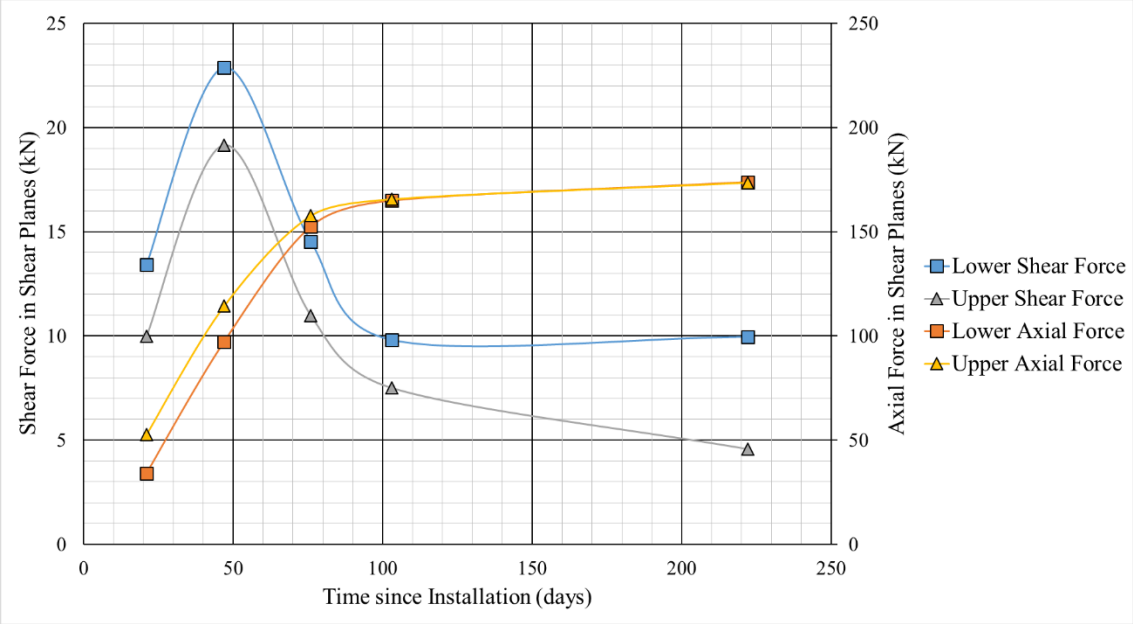

Figure L.6. Rebar Axial and shear forces near lower and upper shear planes calculated from fibre-optic instrumentation in 22M Grade 500 dywidag at Mosaic Colonsay

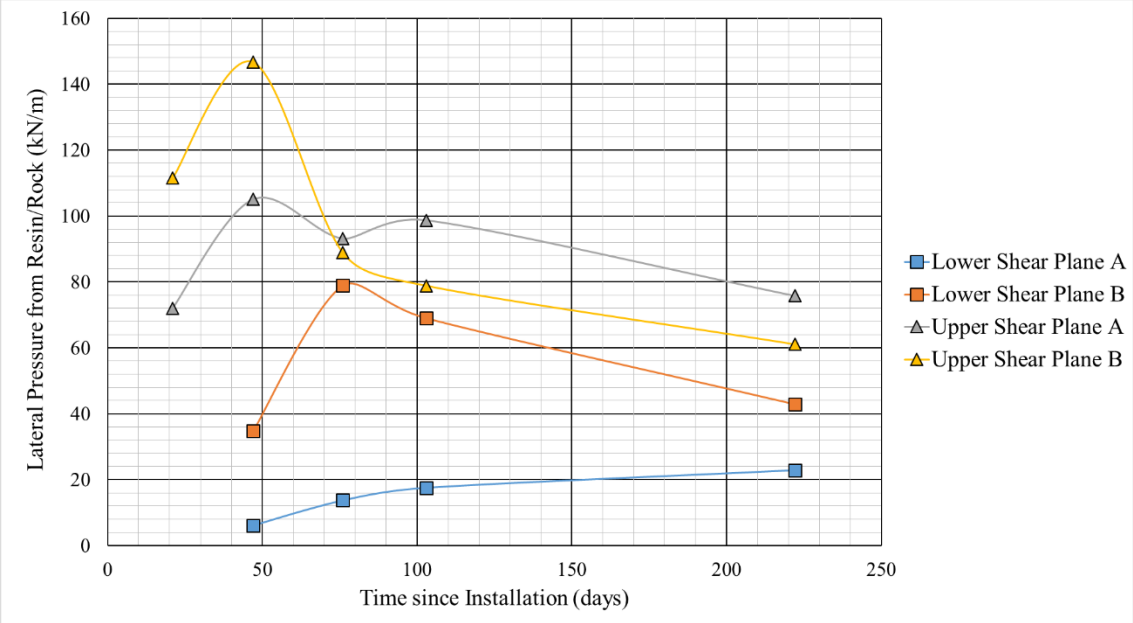

Figure L.7. Rebar Lateral pressure of resin and potash on either side of the lower and upper shear planes calculated from fibre-optic instrumentation in 25M Grade 400 rebar at Mosaic Colonsay

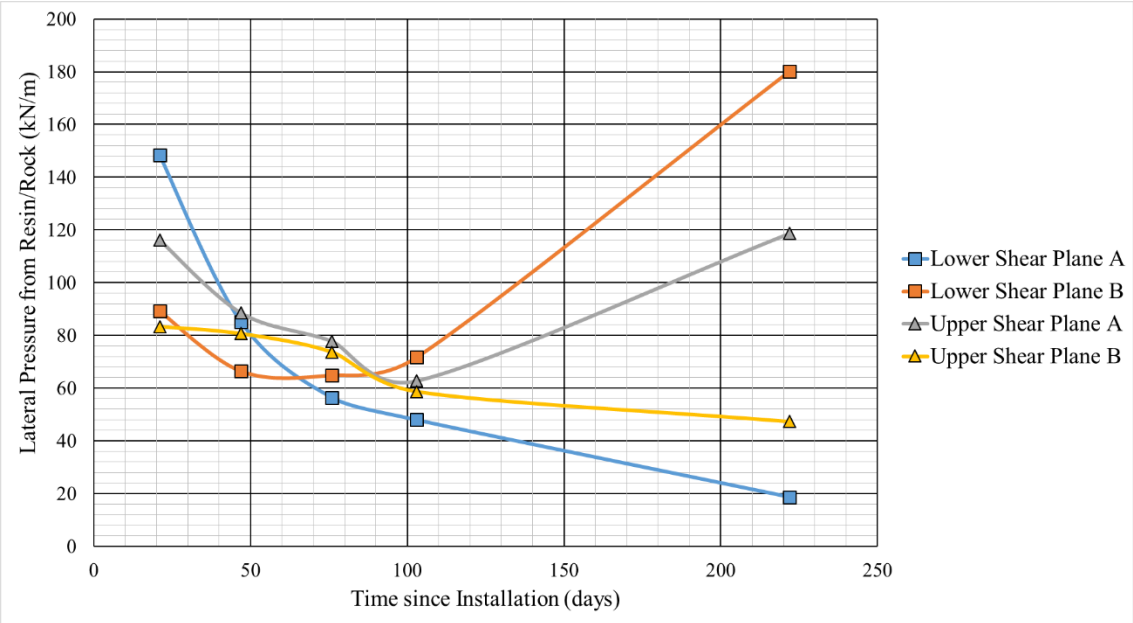

Figure L.8. Rebar Lateral pressure of resin and potash on either side of the lower and upper shear planes calculated from fibre-optic instrumentation in 22M Grade 500 dywidag at Mosaic Colonsay

The centroidal axis position of the 25M Grade 400 rebar is shown in Figure L.9. The position in the arbitrary “x” direction and “y” direction is shown where the “x” direction is perpendicular to the slot cut and the “y” direction is parallel to the slot cut. As can be seen, most of the movement occurs in the “x” direction. The position of the shear planes, identified previously, are shown in the plots as well as multiple points along the rebar where the strain readings seemed relatively unaffected by the shear planes.

The centroidal position plots and subsequent analysis were excluded from the main body of this report due to the subjectivity in generating the plots. The centroidal position had to be determined by iteratively changing the assumed rebar orientation until a reasonable estimate is attained. This process is not considered scientifically rigorous without additional instrumentation or surveying the rebar orientation.

The strain readings and position plots from the instrumented 25M rebar indicate a lower shear plane at 0.9 m into the back and an upper shear plan at 1.3 m into the back, as seen in Figure L.9. The position plot shows a shear movement and bending of the rebar on either side of both shear planes. Below the lower shear plane, the rebar appears to have a long gradual bend. This is unexpected but, as was pointed out from **Error! Reference source not found.**, could be due to poor bonding or anomalous potash behaviour.

A similar plot was generated for the 22M Grade 500 dywidag at Colonsay and is shown in Figure L.10. Once again, most of the movement of the dywidag axis is in the “x” direction. The shear planes identified are also shown on this plot along with points along the dywidag where the effect of the shear planes has ended.

The instrumented 22M dywidag exhibits symptoms of a lower shear plane at 0.95 m into the back and the symptoms of an upper shear plane at 1.27 m into the back. Although most of the bending due to shear movement can be seen in the “x” direction, the “y” direction also appears to show some amount of shear deformation.

Note that these position plots used the fibre-optic readings tared against the initial strain measurements. This removes any slight bending caused when the rebar was installed and made the effect of shear movement identifiable. Also, the orientation of the rebar had to be assumed. This was done manually with several iterations until the effect of shear appeared increasing and consistently in one direction across the several readings.

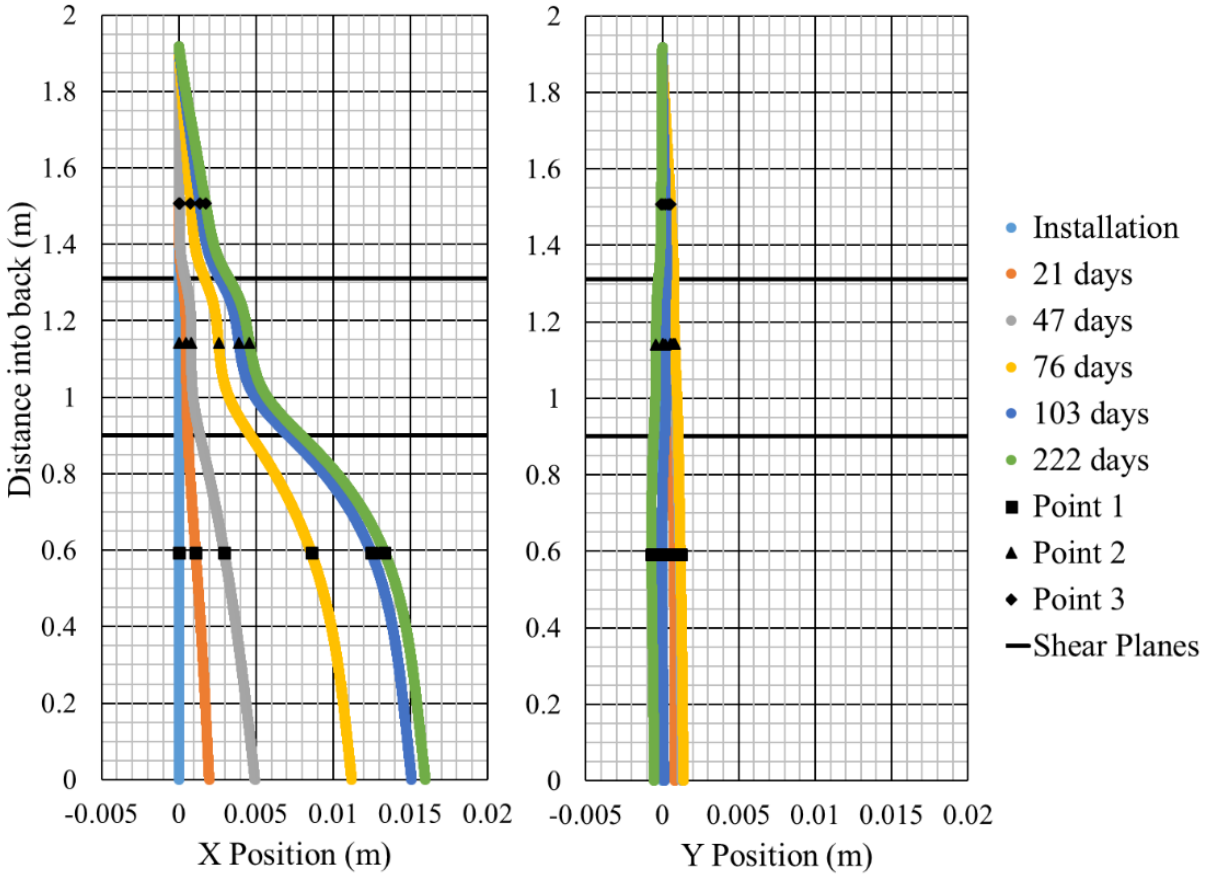

Figure L.9. Position of centroidal axis calculated from fibre-optic instrumentation in 25M Grade 400 rebar at Mosaic Colonsay showing identified shear planes and reference points to estimate shear displacement

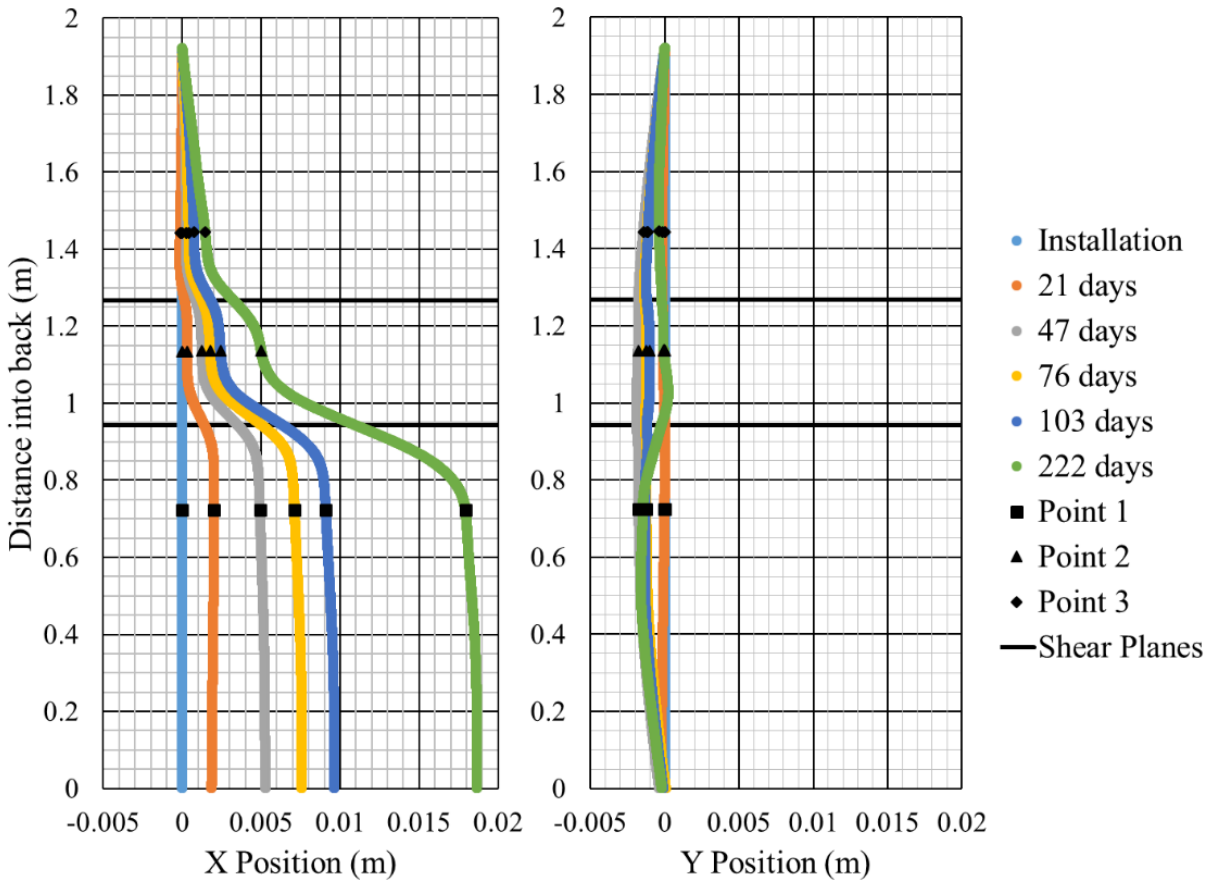

Figure L.10. Position of centroidal axis calculated from fibre-optic instrumentation in 22M Grade 500 dywidag at Mosaic Colonsay showing identified shear planes and reference points to estimate shear displacement

The three points picked in Figure L.9 and Figure L.10 were used to approximate the shear displacement across the shear planes. Since most shear displacement appeared to occur in the x-direction, only the relative displacements in this direction were considered. The displacements for both instrumented rebar at Mosaic Colonsay are shown in Figure L.11 plotted against the time since the rebars were installed.

If the lower shear planes are assumed to be the same shear plane for both rebar, and a similar assumption is made for the upper shear planes, then the displacements calculated for both instrumented rebar should be the same. As seen in Figure L.11, the displacements are generally similar. A linear trend line was fitted to the displacements for each of the two shear planes showing the approximately constant rate of shear displacement that each shear plane exhibits.

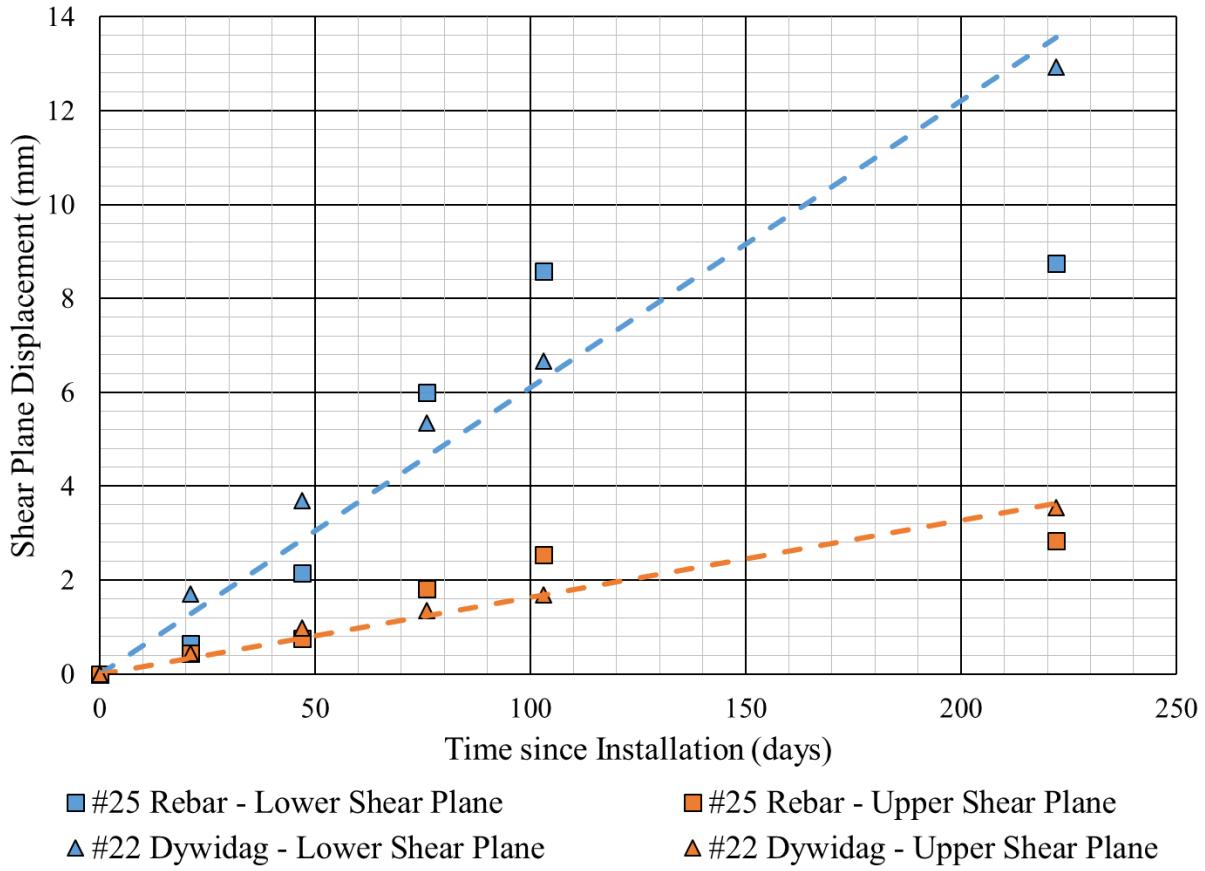

Figure L.11. X direction displacement across lower and upper shear planes as calculated from points 1, 2, and 3 in position plots of fibre-optic instrumented rebar at Mosaic Colonsay

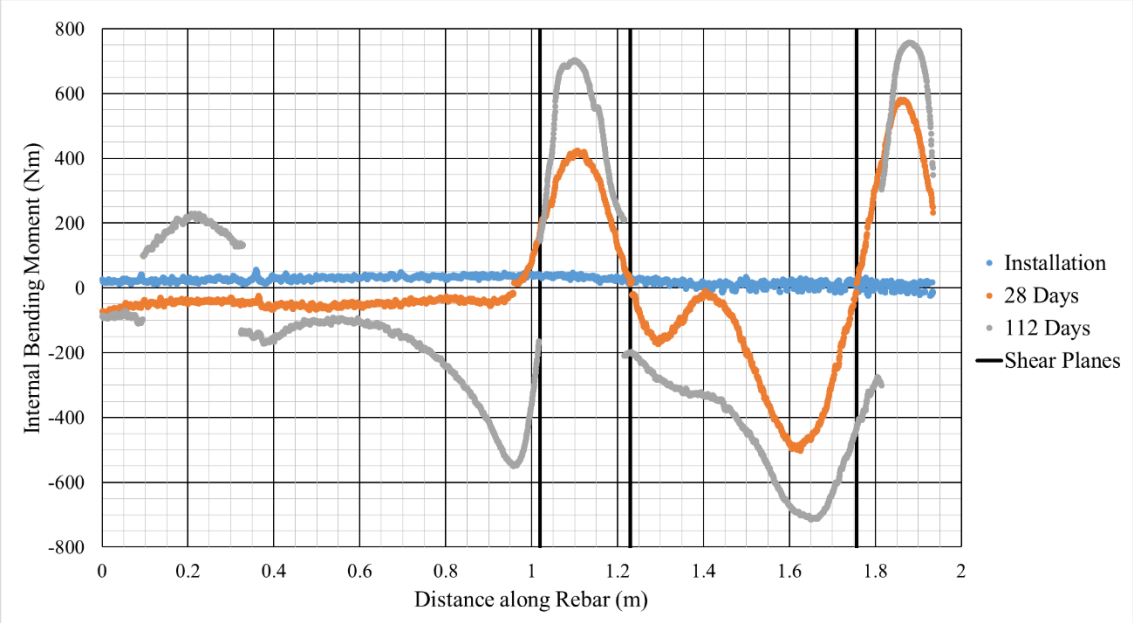

Figure L.12. Rebar internal bending moment calculated from fibre-optic instrumentation in 25M Grade 400 rebar at Nutrien Vanscoy

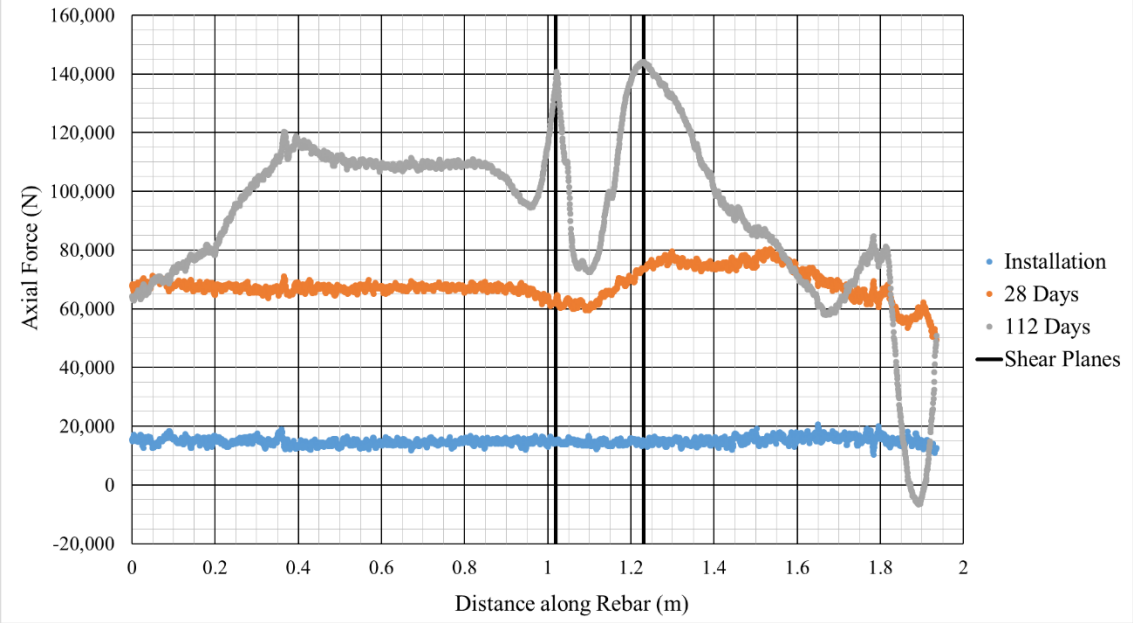

Figure L.13. Rebar axial force calculated from fibre-optic instrumentation in 22M Grade 500 dywidag at Nutrien Vanscoy

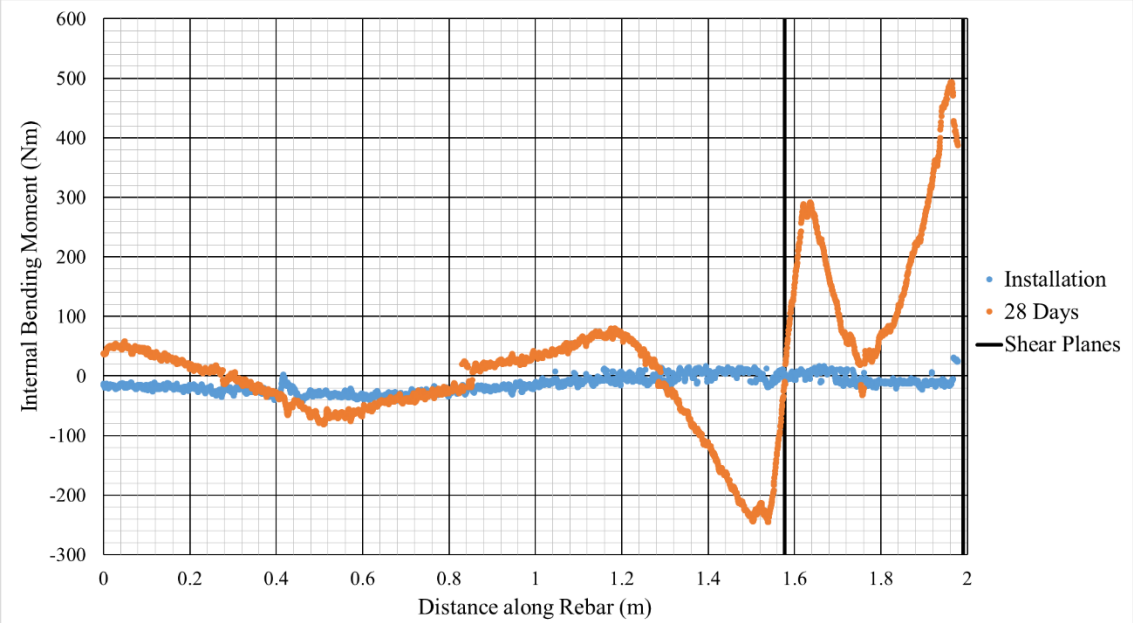

Figure L.14. Rebar internal bending moment calculated from fibre-optic instrumentation in 25M Grade 400 rebar at Nutrien Vanscoy

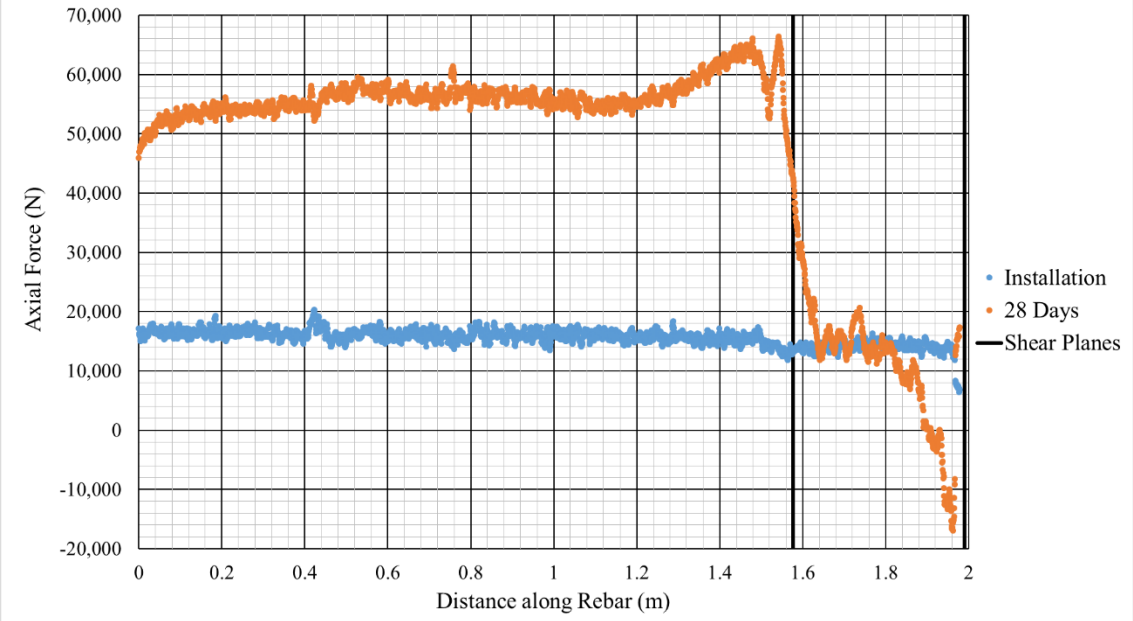

Figure L.15. Rebar axial force calculated from fibre-optic instrumentation in 22M Grade 500 dywidag at Nutrien Vanscoy

The axial position of the 25M Grade 400 rebar was calculated and is plotted in Figure L.16. Apparent shear in both the “x” direction and the “y” direction speaks to the complex nature of the shear deformation encountered here.

The position of the centre axis of the 22M Grade 500 dywidag installed at Nutrien Vanscoy is shown in Figure L.17. Most of the rebar deformation is exhibited in the “x” direction. Once again, the deformation appears to be very complex.

The position plots in Figure L.16 and Figure L.17 are very difficult to interpret. The clearly defined shear planes seen at Mosaic Colonsay and correlation of shear movement with clay seams are not present here. A few possible shear planes have been highlighted in the figures.

The issues seen in these results may be due to poor bonding between the rebar and the potash, progressive degradation of the potash, or bulk movement and deformation of the potash as opposed to movement along discrete shear planes.

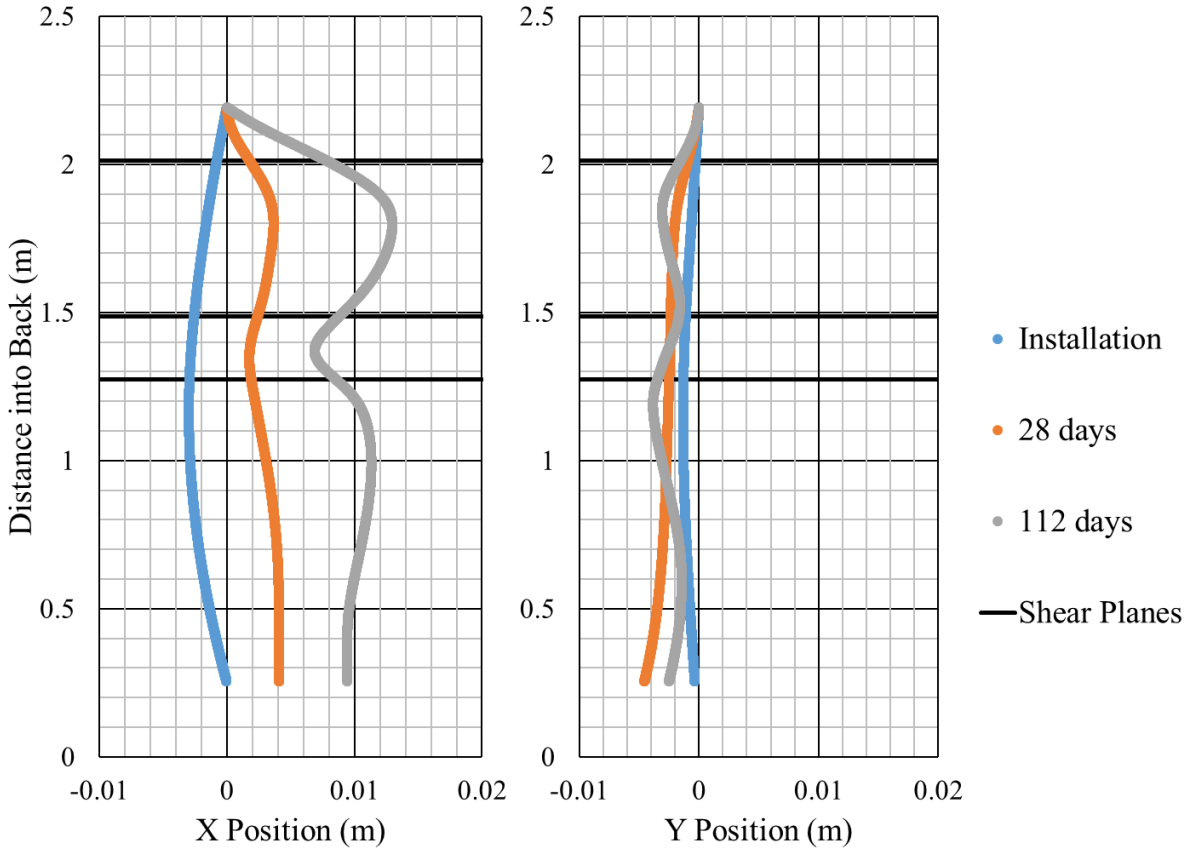

Figure L.16. Axial position plot calculated from fibre-optic instrumentation in 25M Grade 400 rebar at Nutrien Vanscoy

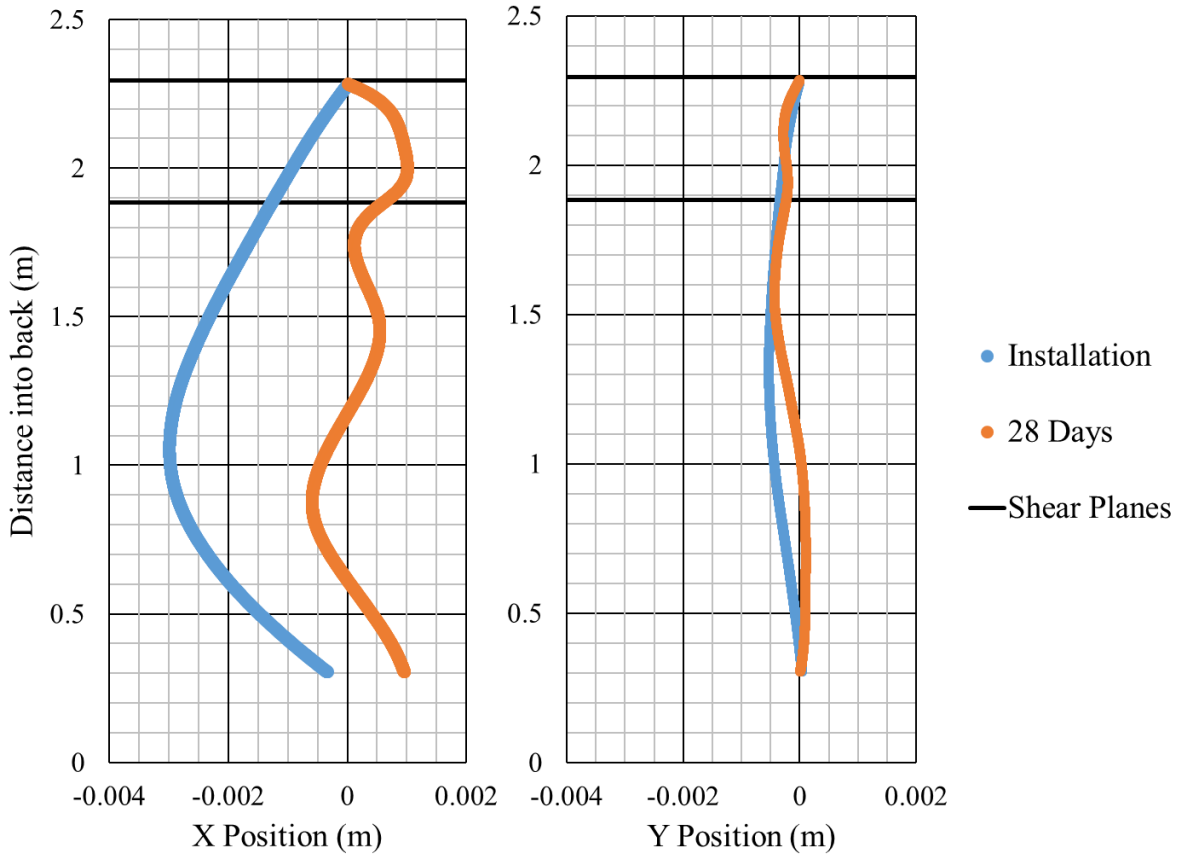

Figure L.17. Axial position plot calculated from fibre-optic instrumentation in 22M Grade 500 dywidag at Nutrien Vanscoy

The strain measurements form the fibre-optic instrumentation was used to calculate the axial position of the rebar. This position is displayed in an “x” direction and a “y” direction in Figure L.18. Most of the bending deformation within the rebar is present in the “x” direction.

From the position plot in the “x” direction, two possible shear planes are identifiable: at 1.05 m and at 2.05 m into the back. The two shear planes correspond to 1.23 m and 2.25 m along the rebar. The position plot exhibits an unexpected lateral displacement between 1.2 m and 1.9 m into the back. The reason for this is not clear but could be due to poor bonding strengths in this area or the bulk deformation of the potash instead of shear movement along a discrete plane.

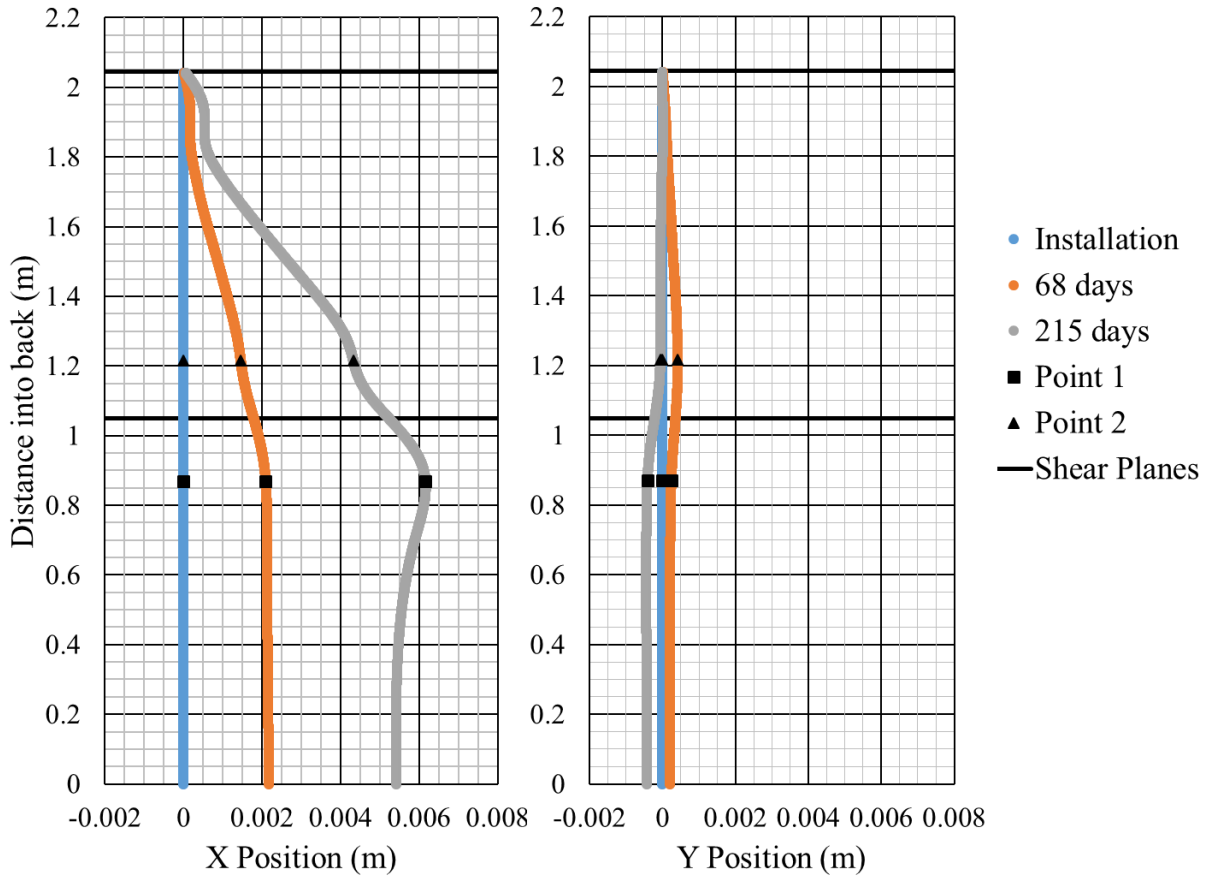

Figure L.18. Axial position plot calculated from fibre-optic instrumentation in 25M Grade 400 rebar at Nutrien Allan

Assuming the position plots in Figure L.18 are accurate, two points can be chosen on either side of the shear plane at 1.05 m into the back. These points are chosen where the bending strains due to shear are negligible. The shear displacement across the shear plane was then approximated from the “x” position plot. The shear displacements are plotted against the time since the rebar was installed in Figure L.19 and suggest a constant rate of movement.

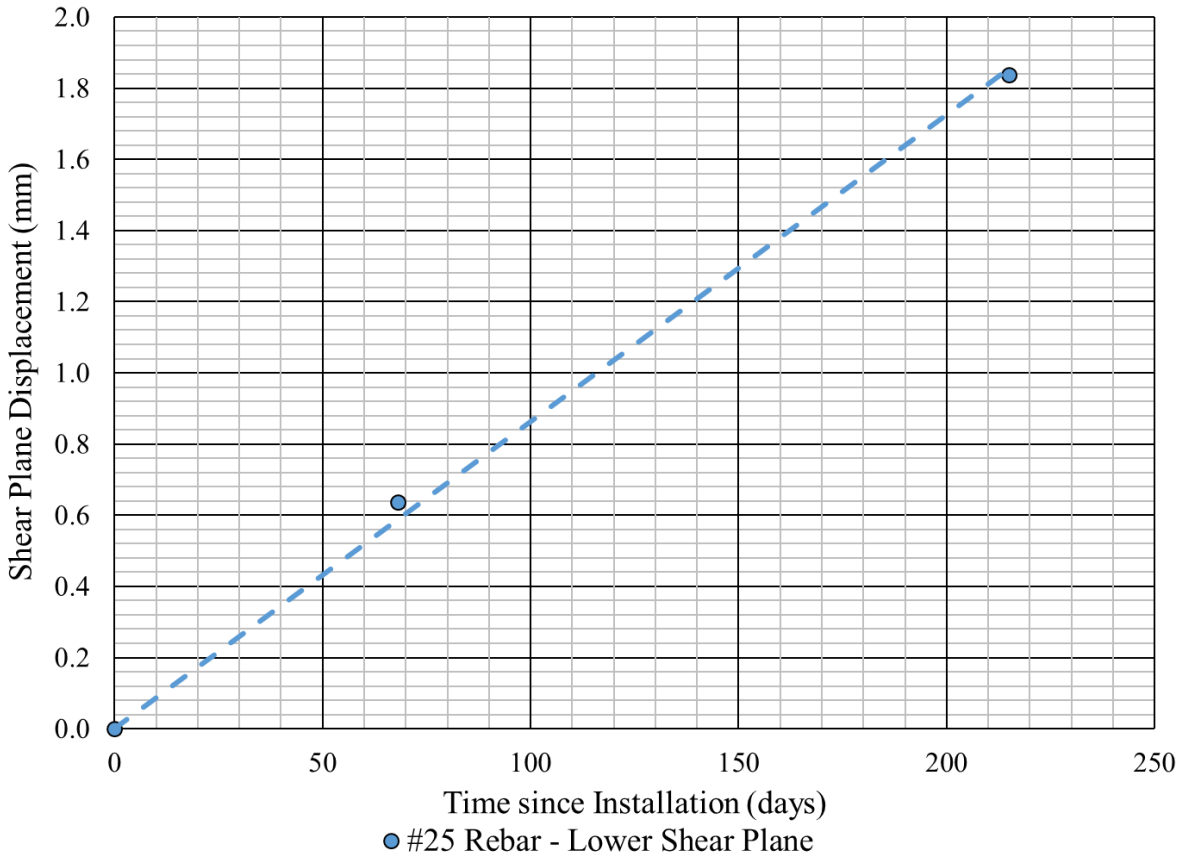

Figure L.19. X-direction displacement across lower shear plane as calculated from points 1 and 2 in position plots of fibre-optic instrumented rebar at Nutrien Allan